Low-level visual processing and its relation to neurological disease

Marc Mason Himmelberg

PhD

University of York

Psychology

March 2019

Abstract

Retinal neurons extract changes in image intensity across space, time, and wavelength. Retinal signal is transmitted to the early visual cortex, where the processing of low-level visual information occurs. The fundamental nature of these early visual pathways means that they are often compromised by neurological disease. This thesis had two aims. First, it aimed to investigate changes in visual processing in response to Parkinson's disease (PD) by using electrophysiological recordings from animal models. Second, it aimed to use functional magnetic resonance imaging (fMRI) to investigate how low-level visual processes are represented in healthy human visual cortex, focusing on two pathways often compromised in disease; the magnocellular pathway and chromatic S-cone pathway. First, we identified a pathological mechanism of excitotoxicity in the visual system of *Drosophila* PD models. Next, we found that we could apply machine learning classifiers to multivariate visual response profiles recorded from the eye and brain of *Drosophila* and rodent PD models to accurately classify these animals into their correct class. Using fMRI and psychophysics, found that measurements of temporal contrast sensitivity differ as a function of visual space, with peripherally tuned voxels in early visual areas showing increased contrast sensitivity at a high temporal frequency. Finally, we used 7T fMRI to investigate systematic differences in achromatic and S-cone population receptive field (pRF) size estimates in the visual cortex of healthy humans. Unfortunately, we could not replicate the fundamental effect of pRF size increasing with eccentricity, indicating complications with our data and stimulus.

Table of Contents

List of Tables

List of Figures

peaks at multiples of the input frequency. In A) we present an averaged time-domain SSVEP response from a w^- fly to 99% contrast reversing sine grating over 1000ms, modulating at 8Hz, whilst B) shows Fourier amplitudes decomposed from Fourier transform the 8Hz waveform in A, with peaks occurring at multiples of our input frequency (8Hz, 16Hz, 24Hz, 32Hz, 40Hz). The same is shown in C) and D) for a PINK15 PD-mutant fly. 91

Figure 3.2 Analysis path for Linear Discriminant Analysis (LDA). The raw ERG (electroretinogram) response to 64 different stimuli is collected – here from a control (wild-type) w^- fly and an EOPD (PINK15) fly (A). For each stimulus, Fourier analysis is used to measure the response of the fly at the second harmonic (2f) (B). Each fly is exposed to 64 stimuli – each with a known contrast and temporal frequency. The heat map (C) represents the amplitude of the second harmonic at each stimulus condition. In this simple case, with just 2 genotypes at one time point, the LDA is applied to the data from both genotypes, and determines the equation that best separates the data into two classes based on the 64 responses. Three outcomes could be envisaged – an optimal separation of the data. Di) a clear line separates the data, or a partial separation (Dii), or no difference (Diii), all the data are mixed). In this portrayal, the graph plots 'X' and 'Y' which will be calculated from the 64 Fourier results by the LDA algorithm. In the more complex dataset explored below, 5 genotypes and 5 ages were sampled, leading to a multi-dimensional 'cloud' of data which can still be separated by a (more complex) set of linear equations. 92

Figure 3.3 We use the ERG to obtain accurate SSVEP measurements from both wild-type and PD *Drosophila* mutants at different contrasts and ages. In A-F we present exemplar ERG responses at 8Hz obtained from w^- and *PINK1*^{5} PD mutants at 1 and 28 days of age, and at 64% and 99% contrast. SSVEP waveform peak amplitude increases with increasing contrast. 94

Figure 3.4 EOPD mutants show steeper response amplitudes at 1 day of age. A-E) Mean response amplitudes from all *Drosophila* genotypes (n=10 for each genotype). *Drosophila* exhibit visual tuning to temporal frequency and contrast, with peak sensitivity at 6-8Hz temporal frequency and 99% contrast. Further, the maps appear to show subtle differences outside of peak regions between 12-36Hz at 1-8% contrast. Profiles indicate that EOPD mutants have larger response amplitudes at

List of Equations

Acknowledgements

Foremost, I would like to express my gratitude to my supervisor, Prof. Alex Wade. I have been incredibly privileged to have Alex's guidance throughout my PhD. His optimism, encouragement, dedication, and most of all patience, have made my PhD enjoyable from start to finish. Thank you for taking a chance on me and giving me the opportunity to do something that I enjoy, as well as dedicating so much of your time to teaching me. It might not seem like it, but it something that I don't take for granted.

I would like to thank Heidi Baseler, Dan Baker, and Tony Morland for their thoughtful insights and encouragement during my TAP meetings. I would also like to thank Scott Cairney who has provided me with encouragement and advice over the past three years, and has, when necessary, kept me in check. You have all helped me to begin to foster confidence in myself. Additionally, I'd like to thank Tony for always being generous in investing in me to attend so many conferences and workshops, I've learnt a lot and had a good time in the process. My thanks also go to Chris Elliott and Ryan West for their guidance in the fly lab and helping me find my feet, and Jelle van Dijk for assisting in scanning at Spinoza.

I have been very lucky to have met so many people in the Department of Psychology and NextGenVis who have been a positive influence in both my research and my life. Special thanks to Mark Carey, Barbar Moltz, Junior Whiteley, Adam Eggleston, Kirstie Wailes-Newson, Milena Kaestner, Alessandro Grillini, Jan Kurzawski, Mladen Sormaz, and even Alex Reid. Your camaraderie means a lot to me and I'm glad to have met you all.

Finally, I need to thank my mum and dad for their unwavering support. Even though they are on other side of the world and have to pretend to understand what I am doing, they have always driven me to do my best and provided me with every opportunity possible so that I can achieve my goals. I can't thank you both enough; I am really proud to have you both as my parents and I hope I can make you proud, too.

Declaration

I declare that the work presented in this thesis is original and I am the sole author. This work was carried out under the supervision of Professor Alex Wade. This work has not been submitted to this or any other University for a degree. All sources are acknowledged as References.

Rodent data collection presented in Chapter 4 were collected in collaboration with Lundbeck A/S, Copenhagen, by Freja Gam Østergaard. All of the reported data analyses, experimental design, creation of the stimuli, and all other data collection were performed by myself, under supervision from Professor Alex Wade.

Data presented in Chapter 3 were published in:

Himmelberg, M.M., West, R.J.H, Elliott, C.J.H, & Wade, A.R. (2017). Abnormal visual gain control & excitotoxicity in early-onset Parkinson's disease *Drosophila* models, *Journal of Neurophysiology*, *119*(3), 957-970. doi:10.1152/jn.00681.2017

Data presented in Chapter 4 are included in:

Østergaard, F. G., Laursen, B., Himmelberg, M. M., Wade, A. R., Siebner, H. R., & Christensen, K. V. (in prep). A visual assay for detection of α-synuclein-related pathology in a rat model of Parkinson's disease.

Data presented in Chapter 5 were published in:

Himmelberg, M.M. & Wade, A.R. (2019). Eccentricity-dependent temporal contrast tuning in human visual cortex measured using fMRI, *NeuroImage*, 184, 462-474. doi:10.1016/j.neuroimage.2018.09.049

Data from Chapter 5 were presented at OSA Fall Vision Meeting, Washington D.C, USA (October 2017) and published in abstract form:

Himmelberg, M.M. & Wade, A.R. (2017). Measuring temporal contrast sensitivity across the visual field & visual cortex using fMRI, *Journal of Vision, 17*(15), doi:10.1167/17.15.18.

Data from Chapter 5 were also presented at Vision Sciences Society, St Pete Beach, Florida, USA (May 2018) and published in abstract form:

Himmelberg, M.M. & Wade, A.R. (2018) fMRI measurements of neural temporal contrast sensitivity across population receptive field eccentricity & size, *Journal of Vision, 18*(10), doi:10.1167/18.10.251.

Chapter 1

Introduction.

1.1 Thesis overview

Low-level visual processing is driven primarily by visual-input to the retinal photoreceptors. Here, retinal neurons extract changes in image intensity across space, time, and wavelength. These retinal signals are transmitted to the early visual cortex, where the processing of low-level visual information occurs before being interpreted in higher-order visual areas. We are still learning how low-level visual signals associated with pre-cortical pathways are represented in the early visual cortex. This is an important stream of research, as the fundamental nature of these pathways means that they are often compromised by neurological disease.

The experiments presented in this thesis come under at two themes. First, we use electrophysiological measurements to investigate how visual processing changes in response to Parkinson's disease (PD), using *Drosophila* and rodent PD models. Investigating visual perturbations in PD models allows us to use vision as a window into expanding our understanding of the aetiology of PD and to identify new visual biomarkers. Second, we use functional magnetic resonance imaging (fMRI) to investigate how low-level visual processes associated with pre-cortical pathways are represented in the healthy human cortex. Only once we understand how low-level vision is represented in the healthy human brain can we can start to assess how these

parameters change in response to neurological disease. We focus on two key pre-cortical pathways that are often compromised in disease; the magnocellular pathway, that is primarily driven by transient, achromatic inputs, and the chromatic S-cone pathway, that is sensitive to relatively sustained, blue-yellow opponent colour signals.

This thesis asks the following questions:

- Can we use measurements of low-level vision to identify visual biomarkers in animal models of PD?
- How are eccentricity-dependent pre-cortical pathways that are sensitive to temporal frequency and contrast represented in the human cortex, and how do such sensitives align with behavioural measurements?
- How are the spatial and physiological properties of the chromatic S-cone pathway represented in human primary visual cortex?

A range of methods were used to answer these questions, including electrophysiological steady state visually evoked potential (SSVEP) recordings from *Drosophila* and rodent models of PD, machine learning classification techniques, 3T and 7T functional magnetic resonance imaging (fMRI), and visual psychophysics.

The aim of this chapter is to introduce the key ideas that pertain to the experiments in the thesis. This includes an overview of the human visual

system, from retina to cortex, and low-level visual sensitivities, followed by an overview of Parkinson's disease and its effects on human vision. This is followed by an overview of *Drosophila* as a disease model, a breakdown of the *Drosophila* visual system, and the key features of the rodent visual system.

1.2 Human Visual System

1.2.1 The photoreceptors

The first stage of low-level visual processing begins at the retinal photoreceptors. First, light passes through cornea, lens, and inert materials of the eye. The lens focuses light onto the retina, which is ~0.5mm thick, and contains cells that segregate visual signals into parallel, neural pathways that are specialised for different visual tasks. The retina contains two types of light-sensitive photoreceptors – the cones and rods. There are 3 types of cones that have differing sensitivities to light wavelength and eventually give rise to the perception of colour (further discussed in 1.2.5 *The perception of colour*), while the rods are specialized for scotopic, low-light vision. Photoreceptors contain photopigment that absorbs light energy and phototransduction occurs via changes in the ionic conductance of the surface membrane of the outer segment of the upper photoreceptor. Conductance changes result in ionic movements, which shift the electrical potential across the photoreceptor surface membrane. This shift spreads to the synaptic ending of the photoreceptor, which then modulates the secretion of the synaptic transmitter (Ebrey & Koutalos, 2001). Notably, it has been found that peripheral cones tend to show increased response kinetics to light when compared to more

foveal cones (Sinha et al., 2017). As presented in Figure 1.1, the resulting signal is sent to the second-order neurons in the retina; the bipolar, horizonal, and amacrine cells, then to the retinal ganglion cells (RGCs).

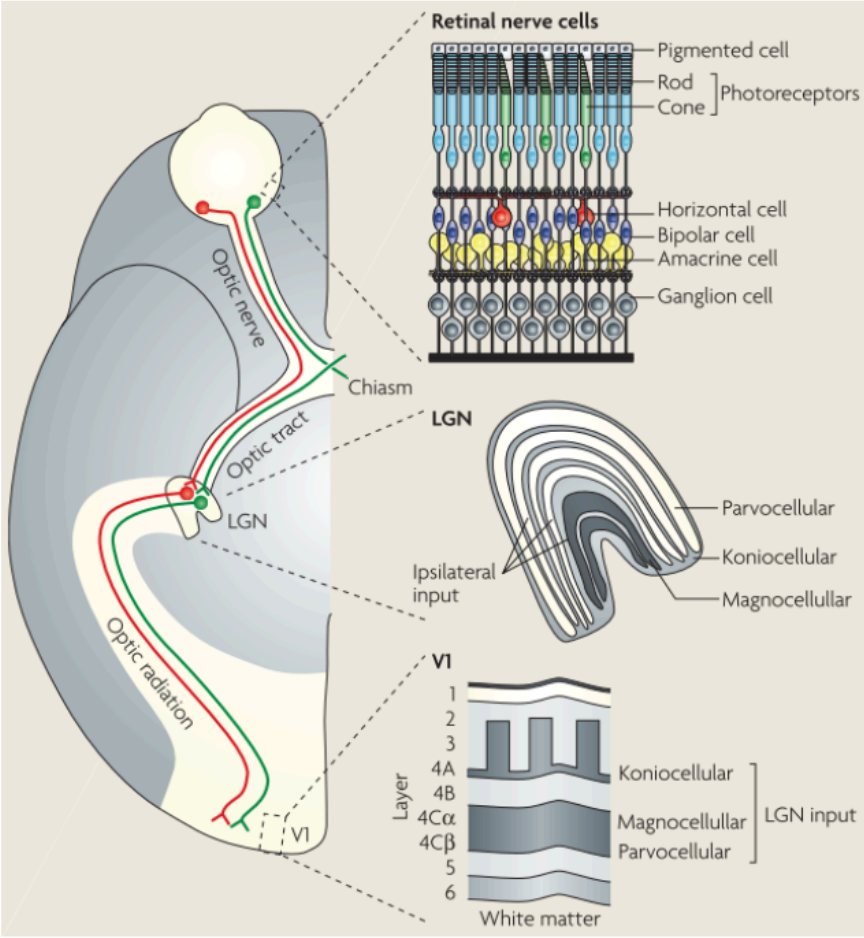

Figure 1.1 The primary visual pathway in humans. Visual signal passes through the retinal nerve cells. Next, the signal is projected to the LGN – nasal projections pass to the contralateral hemisphere while temporal projections pass to the ipsilateral hemisphere. This signal is received in the LGN, where signal is segregated into different layers corresponding to the PC, MC, and KC pathways. Signal is then sent through the optic radiation to primary visual cortex (V1), where signal again is initially segregated into separate laminae (Solomon & Lennie, 2007).

1.2.2 The retinal ganglion cells

In the primate eye, the RGC layer contains over 20 types of ganglion cells that vary in their shape, size, and function (Sanes & Masland, 2015). For the purpose of this thesis we are interested in two types of RGCs; midget and parasol cells. Midget cells are abundant in the primate retina. They are more populous around the fovea and have small and dense dendritic trees that contact a single bipolar cell (and usually a single photoreceptor cone). On average, the dendritic field size of midget RGCs increases with retinal eccentricity. Conversely, parasol RGCs have a larger and less dense dendritic trees than midget cells, and again, the average size of these dendritic trees increases with retinal eccentricity (Polyak, 1941). Importantly, the proportion of parasol to midget RGCs increases with increasing retinal eccentricity, with parasol cells comprising of 5% of all RGCs in the retina, increasing to 15% in the peripheral retina (Connolly & van Essen, 1984; Dacey, 1993, 1994; Dacey & Petersen, 1992; De Monasterio & Gouras, 1975; Marshak, 2010).

Midget and parasol RGCs are the beginning of two separate visual streams; the parvocellular (PC) and magnocellular (MC) pathways (see *1.2.4 Magnocellular, parvocellular, and koniocellular pathways*). The smaller size of midget RGCs means that they receive input from less photoreceptors, while the larger size of parasol RGCs means that they receive input from more photoreceptors. The size of the region of the retina (i.e. more photoreceptors cover a larger region, less photoreceptors cover a smaller region) that provides visual information to a RGC corresponds to the size of the region of

visual space that the RGC reads information from. This is termed a cell's 'receptive field' (Hartline, 1938). Midget cells have small receptive fields that are condensed towards the fovea. This allows for high spatial resolution (up to 60 cycles per degree (cpd)) in the central visual field. Conversely, parasol cells have larger receptive fields and are able to resolve spatial frequencies up to 20 cpd (Wandell, 1995). Following this, signals are carried down the axons of the RGCs which form the optic nerve of each eye. Responses from the nasal and temporal regions of the retina of each eye are separated; nasal inputs cross to the contralateral hemisphere at the optic chiasm while temporal inputs pass to the ipsilateral hemisphere (see Figure 1.1). The two optic nerves then meet at the optic chiasm, and from here signal is passed down the optic tract to the dorsal lateral geniculate nucleus (LGN) of the thalamus.

1.2.3 The lateral geniculate nucleus (LGN)

The LGN is a small, bi-lateral structure that receives input from each eye representing the contralateral half of the visual field. It consists of six distinct laminae that process segregated information input from different classes of RGCs, effectively segregating the magnocellular (MC), parvocellular (PC), and koniocellular pathways. The axons of the midget RGCs terminate in the four superficial (upper) layers, called the parvocellular layers, while the axons of the parasol RGCs terminate in the two deeper (lower) layers, called the magnocellular layers. Axons from small bistratified RGCs connect to cell bodies in layers ventral to each of the magnocellular and parvocellular layers, called the koniocellular layers (Jeffries, Killian, & Pezaris,

2014). Axons from RGCs that are on the left side of the visual field send information to the right side of the LGN, and RGCs that read from the right side of the visual field send information to the left side of the LGN. Thus, each side of the LGN contains visual signal from both eyes, but only one half of the visual field. Next, the magnocellular and parvocellular pathway project from the LGN via the optic radiation and enter layer 4C of primary visual cortex (V1), while the koniocellular pathway projects to layer 1 and to the cytochrome-oxidase (CO) 'blobs' in the superficial layers of V1 (Hendry & Reid, 2000).

1.2.4 Magnocellular, parvocellular, and koniocellular pathways

The magnocellular (MC), parvocellular (PC), and koniocellular (KC) pathways derive their inputs from weighted combinations of the cone photoreceptors. The MC pathway is derived from the summed outputs of long and middle wavelength sensitive cones, via parasol RGCs, and feeds into the MC layers of the LGN. The MC pathway has a high response gain to achromatic contrast (see Figure 1.2), prefers high temporal frequencies, and low spatial frequencies. The MC pathway receives most input from parasol cells, which are more populous in the periphery of the retina and read from larger regions of the visual field, when compared to midget cells. The PC pathway is derived from cells that respond to long – middle wavelength sensitive cones (colour opponent red-green) and gives a linear response to contrast (see Figure 1.2). The PC pathway has a slow temporal resolution but a high spatial resolution due to the smaller receptive fields of midget cells that feed into the pathway (Wandell, 1995). Finally, the KC pathway receives input

exclusively from the short wavelength sensitive cone photoreceptors that feed into small bistratified ganglion cells. The sparse arrangement of S-cone photoreceptors means that the koniocellular pathway has a lower spatial resolution than the other MC and PC pathways (Hendry & Reid, 2000).

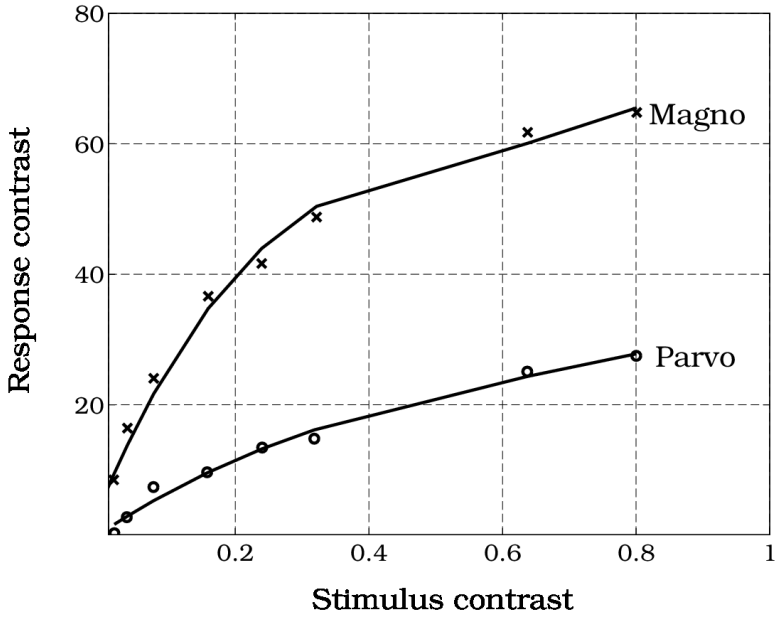

Figure 1.2 Contrast response functions of neurons in the LGN. MC cells show a rapid contrast gain at low contrasts while PC cells show a fairly linear response to contrast. This difference can be traced to midget and parasol cells in the retina (Wandell, 1995).

1.2.5 The perception of colour

The three types of cone photoreceptors in the retina can be classified based on the sensitivity of their photopigment to light wavelength. The three types of photoreceptors are the L (long) cones, M (middle) cones, and the S (short) cones, due to their sensitivity to long, middle, and short wavelengths. As illustrated in Figure 1.3, the normalized peak sensitivity of these three cone

types falls around 570nm, 545nm, and 440nm, for L, M, and S cones, respectively (D.H. Brainard & Stockman, 2010; Wandell, 1995).

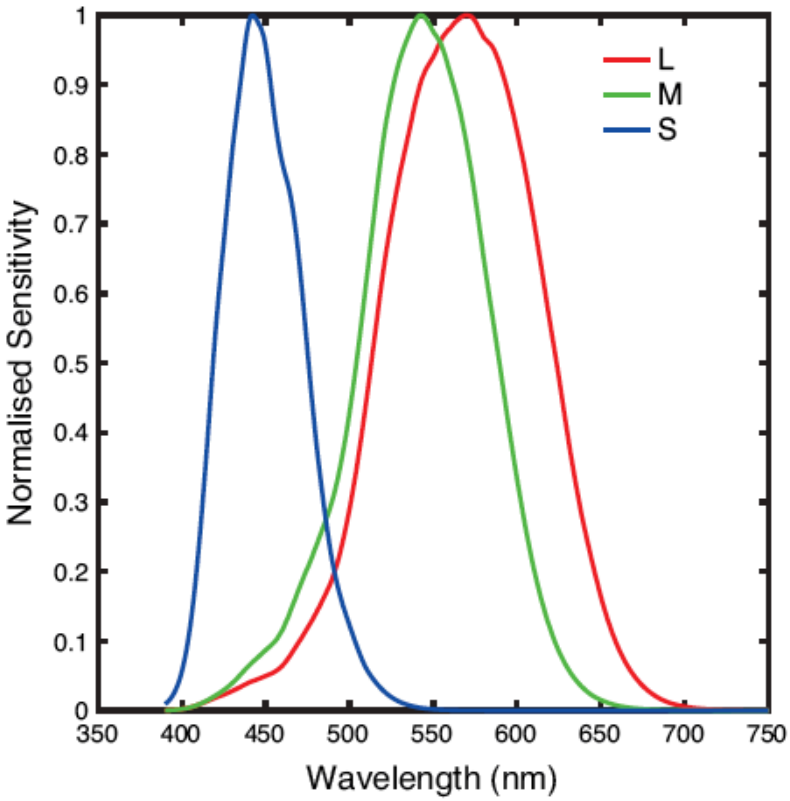

Figure 1.3 Normalized spectral sensitivity of the S, M and L cones, plotted as a function of wavelength (Stockman & Sharpe, 2000).

The count and spatial density of these cones differs. The spatial density of L and M cones is greatest towards the fovea and declines with increasing retinal eccentricity. Further, the ratio of L to M cones varies considerably when comparing between individual retinas (Carroll, Neitz, & Neitz, 2002). Conversely, S-cones account for only ~4% of total cones and have a spatial density of 0 in the central 0.1mm of the fovea, increasing to a maximum density around 1° retinal eccentricity, then declining again towards the more peripheral regions of the retina (Roorda & Williams, 1999).

Spectral sensitivity at the photoreceptoral level is dictated by antagonistic interactions between input signals from the three different cone types, referred to as colour-opponency. Each cone synoptically connects (directly or indirectly) with bipolar and horizontal cells, which then connect to the RGCs. Each bipolar cell receives input from a small localised area of cones in the retina that process visual information from its receptive field, which is organised in a centre-surround fashion. The centre of the receptive field receives input from the cones, and the surround received information from the horizontal cells. These cells have opposing signal responses (i.e. on/off centre-surround, or off/on centre-surround organisation). This centre-surround organisation allows the cell to compare the cone activation between the centre and surround regions of the cell (Stockman & Brainard, 2010). Similar organisation exists in the RGCs, where different bipolar and amacrine cells contribute to centre-surround inputs. The type of photoreceptor input into a centre-surround cell determines the opponency of the cell.

This results in three colour-opponent pathways. The luminance (L+M) pathway is driven by the summed output of the L and M-cones and is insensitive to wavelength and responds strongly to achromatic contrast. Conversely, the 'red-green' (L-M) pathway is driven by the output of colour opponent L-M cones and responds to red-green contrast, while the 'blue-yellow (S-(L+M), or S-cone) pathway is driven predominantly by S-cones (Stockman & Brainard, 2010; Wandell, 1995).

1.2.6 Primary visual cortex (V1)

After visual signal is passed from the retina to the LGN, it arrives at the primary visual cortex (V1), located within the calcarine sulcus in the occipital lobe. V1 is 2mm thick and is comprised of six cortical layers (see Figure 1) based on the relative density of neurons, axons, and synapses (Wandell, 1995). Layers 1-3 are grouped together and are referred to as the 'superficial layers' of the cortex. Information from different classes of RGC are segregated upon entry to V1. The MC and PC layers of the LGN project signals to layer 4C of V1; the MC pathway projects to the upper subdivision, layer 4Cα, while the PC pathway projects to the lower subdivision, layer 4Cβ. Layer 5 sends major output to the superior colliculus, while layer 6 sends feedback to the LGN (Wandell, 1995). It has been suggested that feedforward connections to higher order visual areas extend from the upper layers, while feedback is received in the deeper layers (Fellman & Van Essen, 1991; Rockland & Pandya, 1979). The koniocellular layers of the LGN do not strictly respect lamina bodies of V1, however it has been found that they have major projections to layer 4A, and importantly, CO blobs in superficial layers 2 and 3 (see Figure 1.1). The cells within these CO blobs are chromatically selective and are thought to be involved in the processing of chromatic information (Lennie, Krauskopf, & Sclar, 1990; Livingstone & Hubel, 1984).

Neurons in V1 are classified in two categories: simple cells and complex cells. Simple cells tend to have distinct on/off excitatory and inhibitory subregions within a receptive field and show a predictable linear spatial

summation within these regions. When a stimulus covers both subregions, the neuronal response is cancelled. Conversely, complex cells are selective for spatio-temporal orientation; however, they have no clear on/off regions and their maximal response tends to be independent of the exact stimulus position within the receptive field (Carandini, 2006; Hubel & Wiesel, 1962). Further, the receptive field properties of complex cells tend to be broader, as their spatial tuning is independent of receptive field size (Movshon, Thompson, & Tolhurst, 1978).

1.2.7 Retinotopic organisation

The spatial organisation of the retinal photoreceptors is maintained in the LGN. This spatial organisation is further maintained in neurons within the visual cortex. In V1, neurons whose receptive field centres are near to fovea (i.e. they read information from the centre of the visual field) are located towards the posterior calcarine sulcus. The spatial tuning of visual neurons becomes increasingly more eccentric as one moves towards increasingly anterior regions of the calcarine sulcus (Fellman & Van Essen, 1991; Wandell, Dumoulin, & Brewer, 2007; Wandell, 1995). Further, each hemisphere of V1 contains information from one visual hemifield. The left hemisphere of V1 contains neurons with receptive fields that read information from the right hemifield, while the right hemisphere contains neurons with receptive fields that read information from the left hemifield. Further, neurons that are dorsal in V1 read from their respective lower quadrant of a hemifield, while neurons that are ventral read from the upper quadrant. This effectively reverses and

flips a map of visual space onto the cortex. This spatial organisation of cortical cells is referred to as 'retinotopic organisation' because it follows the topographic organisation of receptive fields in the LGN, and subsequently the retina, and is common through further higher order visual field maps, although the exact organisation of these maps is known to change (Amano, Wandell, & Dumoulin, 2009; Tyler et al., 2005; Wandell et al., 2007; Wandell, Brewer, & Dougherty, 2005).

1.2.8 Higher order areas

Visual information leaves V1 and spreads up the visual hierarchy. Extrastriate cortex is comprised of visual field maps that are similarly organised around retinal spatial coordinates. As one progresses up the visual hierarchy, these field maps are linked to functional specialisations as they are tuned to increasingly higher-order visual properties, such as faces and form, and become increasingly less concerned to low-level visual properties (Avidan et al., 2002; Fellman & Van Essen, 1991; Grill-Spector et al., 1999; Kanwisher, 2010; Perry & Fallah, 2014; Vernon, Gouws, Lawrence, Wade, & Morland, 2016). However, two higher-order regions that are important to low-level vision are hV4 and human middle temporal cortex (hMT+). Research has suggested the existence of millimetre-large colour modules, coined 'globs', in visual area hV4 and inferior temporal (IT) cortex; an extension upon the CO blobs identified in the upper layers of V1 (Conway, Moeller, & Tsao, 2007). Similar to blobs, globs are thought to be involved in colour processing, specifically elaborating on the perception of hue, and project this information for higher-

order processing in IT (Bohon, Hermann, Hansen, & Conway, 2016; Conway et al., 2007). Conversely, hMT+ is a well-accepted homologue of the macaque motion sensitive area MT (Dubner & Zeki, 1971). Neurons in MT tend to be velocity-selective, exhibit a high contrast sensitivity, and have a larger receptive field size, thus lower spatial sensitivity (Movshon & Newsome, 1996).

1.2.9 Spatiotemporal Contrast Sensitivity

Perception requires the visual system to differentiate between different features in the environment. These features contain luminance, which is subjectively perceived as brightness, and is defined as the measurable intensity of light emitted from a source or reflected from a surface. The visual system is sensitive to information based on differences in luminance, termed luminance contrast. In vision science, we often use sine wave gratings as our stimulus, for which contrast is defined using the Michelson contrast formula presented in Equation 1.1, where L_{max} represents the highest measured luminance in the image (i.e. the luminance of the light bars of the grating) and L_{min} represents the lowest measured luminance (i.e. the dark bars of the grating), and C returns a value between 0 and 1 that reflects the contrast in the image (Michelson, 1927):

$$C = \frac{(L_{max} - L_{min})}{(L_{max} + L_{min})}$$

Equation 1.1. Equation for calculating Michaelson contrast of a sine wave grating

Contrast is a fundamental visual cue. Contrast sensitivity, that is derived from both retinal and cortical factors, often changes in response to disease (Bodis-wollner et al., 1987; Cadenhead, Dobkins, McGovern, & Shafer, 2013; Campbell & Green, 1965; Ming, Palidis, Spering, & McKeown, 2016; Pelli & Bex, 2013; Weil et al., 2016; Wolkstein, Atkin, & Bodis-Wollner, 1980). Psychophysical measurements of contrast sensitivity output a contrast threshold, the level of contrast required to perceive a target stimulus. The reciprocal of this threshold is a measurement of contrast sensitivity.

There are multiple channels in vision that are selective to different bands of spatial frequencies, thus we can measure contrast sensitivity as a function of spatial frequency (Campbell & Robson, 1968). The contrast sensitivity function (CSF) is formed from measuring multiple contrast detection thresholds at many spatial frequencies (Pelli & Bex, 2013). Typically, the achromatic CSF has a band pass filter, peaking ~4 cpd (see Figure 1.4). The fovea is more sensitive to higher spatial frequencies, while more eccentric regions of the visual field show increased contrast sensitivity at lower spatial frequencies (Wandell, 1995). Generally, contrast sensitivity declines with increasing eccentricity, and this decline is more rapid at high spatial frequencies (~6cpd) than low (~2cpd) (Wright & Johnston, 1983). Similarly, the temporal contrast sensitivity function (TCSF) measures contrast sensitivity as a function of temporal frequency flicker at a single spatial frequency. The TCSF has a band pass filter, peaking ~8Hz (see Figure 1.4), and this peak

sensitivity is similar across eccentricity, indicating that behavioural sensitivity to temporal modulations of contrast is homogenous across the visual field (Koenderink, Bouman, Bueno, & Slappendel, 1978; Virsu, Rovamo, Laurinen, & Näsänen, 1982; Wright & Johnston, 1983). Overall, psychophysical evidence indicates that contrast sensitivity differs as a function of spatial frequency and temporal frequency (i.e. it is not space-time separable), however contrast sensitivity does differ across the visual field as a function of temporal frequency (Robson, 1966a).

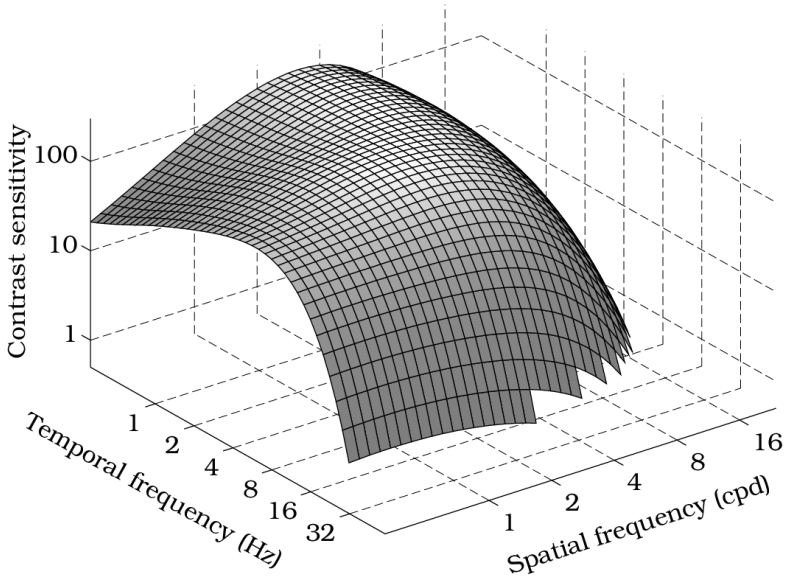

Figure 1.4. Human spatiotemporal contrast sensitivity function where contrast sensitivity is plotted as a function of both spatial and temporal frequency. On a mean background luminance of 1000 trolands, spatial contrast sensitivity peaks around 4cpd, while temporal contrast sensitivity peaks around 8Hz (Wandell, 1995).

1.3 Parkinson's disease

Parkinson's disease (PD) is a progressive neurodegenerative disorder of the central nervous system that is characterized by the progressive loss of dopaminergic neurons in the substantia nigra pars compacta (SNc). The disease was first described in 1817 by Dr James Parkinson as a 'shaking palsy' due to the classical motor symptoms (tremor, bradykinesia, and muscular rigidity) associated with dopaminergic loss that typically occur in mid to late stages of the disease (Parkinson, 2002). However, PD is also characterized by non-motor symptoms in the visual, olfactory, sleep, and cognitive domains, indicating perturbations in typically nondopaminergic areas (Anatal, Bandini, Keri, & Bodis-Wollner, 1998). Many of these non-motor changes occur before the onset of motor symptoms, suggesting the potential for identifying prodromal biomarkers for PD.

The etiology of PD is thought to be multifactorial, resulting from an interaction between environmental and genetic factors. Recent advances in genetic research have led to the identification of monogenic forms of PD caused by a single mutation in dominantly or recessively inherited genes and associated genetic risk factors. It is thought that such monogenic forms of PD account for ~30% of familial and ~5% of sporadic cases of the disease (Klien & Westenberger, 2012). Further, evidence for the function (and dysfunction) of genes associated with PD suggest that mitochondrial dysfunction and oxidative stress play a central role in disease pathogenesis (Bogaerts,

Theuns, & Van Broeckhoven, 2008; Büeler, 2009; Henchcliffe & Beal, 2008; Schapira, 2008)

The animal studies in this thesis pertain to three genes linked to early-onset PD; *PINK1*, *DJ-1*, and *SNCA*. Please see *1.4.2 Drosophila as a model of Parkinson's disease* for a discussion of *Drosophila* PD mutations in *PINK1* and *DJ-1*. Please see *1.5.2 SNCA and α-synuclein* or a discussion of *SNCA* and α-synuclein.

1.3.1 Visual abnormalities in PD

Dopamine is found in the human retinal amacrine cells and the inner border of the inner nuclear layer of the retina (Andretic, Kim, Jones, Han, & Greenspan, 2008; Dowling, 1979). Dopamine appears to play some role in the moderation of photoreceptor signalling, and is responsible for light adaptation and contour perception (Crooks & Kolb, 1992; Witkovsky, 2004). It has been postulated that many low-level visual symptoms in PD are a sequela of altered intraretinal dopaminergic synaptic activity.

PD patients report a number of visual symptoms that affect their ability to navigate their everyday environment and contribute to a reduction in quality of life. For the purpose of this thesis we will focus on changes in low-level vision. PD patients often experience a reduction in low contrast visual acuity which is thought to be a result of retinal dopamine loss (Jones & Donaldson, 1995; Jones, Donaldson, & Timmings, 1992). Next, measurements of

psychophysical contrast sensitivity in PD patients are decreased at high and intermediate spatial frequencies, and contrast sensitivity tends to further decrease with disease progression (Bodis-wollner et al., 1987; Bulens, Meerwaldt, Van Der Wildt, & Keemink, 1986; Hutton, Morris, & Elias, 1993). Such changes have been found to occur at both foveal and peripheral locations of visual field (Silva et al., 2005). L-3,4-dihydroxyphenylalanine (L-dopa) therapy tends to improve contrast sensitivity to that of healthy controls, suggesting that dopamine plays some role in contrast sensitivity (Bulens, Meerwaldt, Van der Wildt, & Van Deursen, 1987).

Further, PD patients report changes in the S-cone colour vision pathway. Visually evoked potential (VEP) responses show decreased amplitudes and increased latency for all chromatic stimuli, but these perturbations are largest in response to blue-yellow stimuli (Sartucci et al., 2012). Further, VEP responses to coloured patterns are more sensitive to L-dopa therapy, supporting the idea that dopamine may play some modulatory role of the retinal colour system (Barbato, Rinalduzzi, Laurenti, Ruggieri, & Accornero, 1994).

If changes in low-level visual processes are linked to altered intraretinal dopaminergic synaptic activity that occurs in response to PD, this may allow us to establish a sensitive visual biomarker for PD that can assist in early diagnosis, monitoring disease progression, and testing the effectivity of new drug therapies. One way establishing such biomarkers is by taking

measurements of retinal signalling in response to low-level visual stimuli from animal models of PD.

1.4 *Drosophila Melanogaster*

Drosophila melanogaster are a well-studied and highly tractable genetic model organism that are often used to explore the cellular mechanisms underlying neurodegenerative disease. Several traits make *Drosophila* an attractive disease model. First, the fly genome has been completely sequenced, encoding over 14,000 genes on only four chromosomes (Adams et al., 2000). Second, 75% of human disease-relate genes have a functional homologue in the fly, with well conserved gene pathways, and the expression of these genes often showing similarities to human disease (Reiter, Potocki, Chien, Gribskov, & Bier, 2001). Third, *Drosophila* are inexpensive to propagate, with a single mating pair producing hundreds of genetically homogenous offspring within ~10 days (Powell, 2013). Finally, *Drosophila* make disease progression easy to study, with a life cycle of ~30 days, with 10 days to the adult stage (see Figure 1.5) (Ong, Yung, Cai, Bay, & Baeg, 2015; Roote & Prokop, 2013).

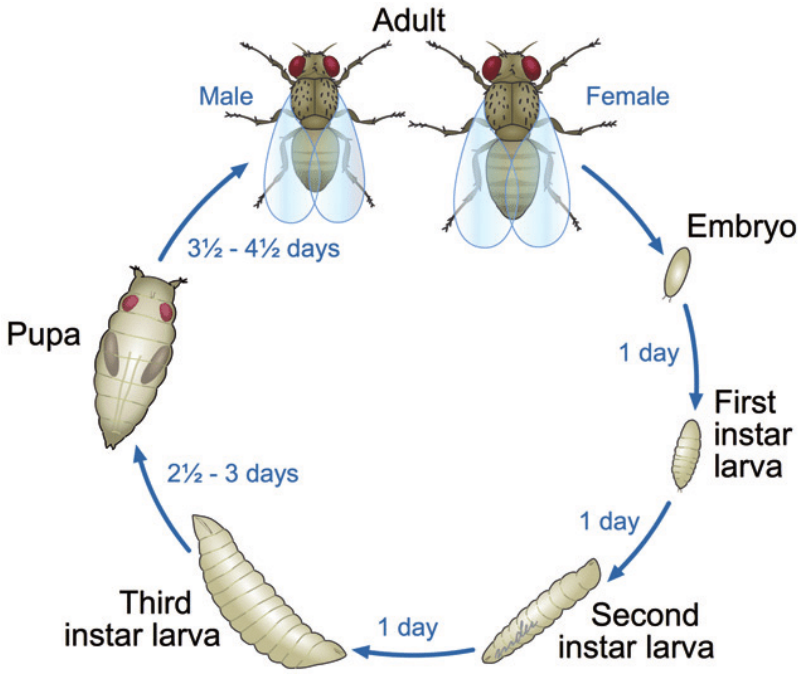

Figure 1.5 Cycle of Drosophila from conception to adulthood. Fertilized females lay hundreds of eggs over several days. At 25°, there are 3 stages of larvae development over 5 days. Metamorphosis occurs during pupal stages, where all organs degenerate and restructure into adult form. ~10 days after egg-lay, the adult flies emerge from the pupal case and require 8 hours to sexually mature (Ong et al., 2015).

Adult *Drosophila* have a relatively simple central nervous system (CNS), however many structures show homologies to the mammalian organs and circuits. Further, this simple CNS can still mediate complex behaviours including sleep, learning, memory, courtship, and feeding. Although humans and flies differ in their large-scale morphological and cellular features, the molecular mechanisms that drive cellular and physiological processes appear to be conserved between the two organisms (Pandey & Nichols, 2011; Ugur, Chen, & Bellen, 2016). Superficially, the *Drosophila* and human visual system

differ as *Drosophila* have a compound eye, however, there are many underlying homologies in visual circuitry. An overview of the *Drosophila* visual system will now be discussed.

1.4.1 Drosophila visual system

The adult fly visual system contains ~15,000 neurons, and similar to humans, visual information is initially received by the retina and is processed in the optic lobes. Here, computations occur in regard to shape, colour, motion, and orientation, which are then further transmitted to the central brain (Nériec & Desplan, 2016). The following is a description of the *Drosophila* visual system from photoreceptors to the optic lobe. See Figure 1.6 for visualization of anatomy of the fly visual system.

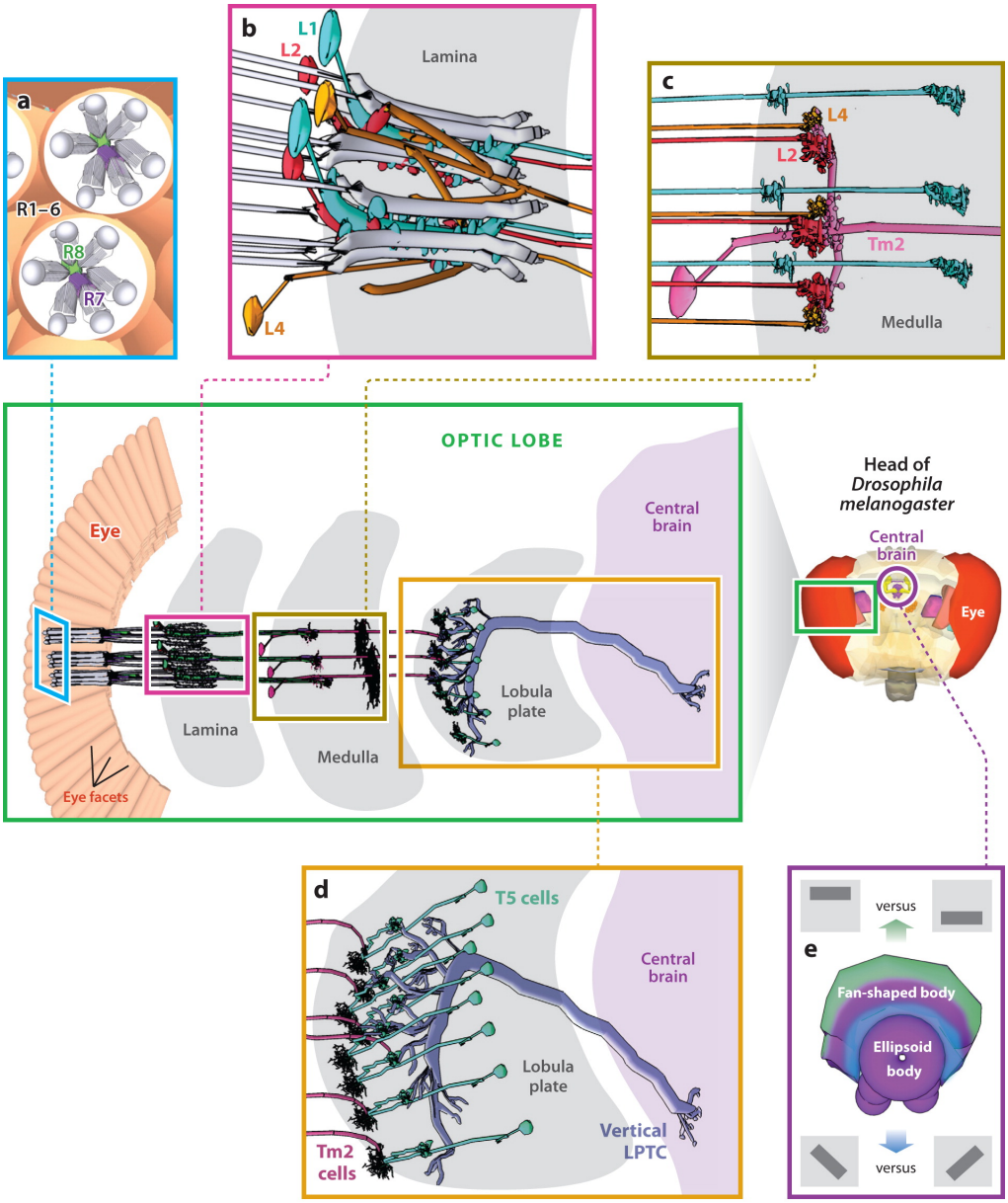

Figure 1.6 The anatomy of the fly visual system comprises of the photoreceptors, the lamina, medulla, and lobula complex. A) Light enters the eye via individual ommatidia that contain 8 photoreceptors (R1-R8), B) the R1-R6 photoreceptors input to the lamina. The motion circuitry is comprised of neurons L1, L2, and L4, that project synapses to the medulla. C) The medulla is organised into compartments and receives synaptic input from the lamina neurons which then project to the lobula complex (Paulk, Millard, & van Swinderen, 2013).

1.4.1.1 Fly eyes and photoreceptors

The adult *Drosophila* eye is comprised of an array of ommatidia, ~750 independent unit eyes, which are analogous to ~750 pixels in the *Drosophila* visual field (Nériec & Desplan, 2016; Paulk et al., 2013). The fly visual system must successfully filter, sample, and integrate the image transmitted by each individual ommatidium to contribute to an overall image across the entire eye. Each ommatidium possesses its own lens and houses eight photoreceptor neurons (R1-R8) that contain rhodopsin (light absorbing pigment), and like humans, these photoreceptors are responsible for the transduction of light signal (Hardie, 1985).

1.4.1.2 Phototransduction

Phototransduction in the *Drosophila* photoreceptors is different from that of humans, yet surprisingly similar to mammalian intrinsically photosensitive retinal ganglion cells (ipRGCs) (Qiu et al., 2005). In *Drosophila*, phototransduction occurs through a pathway that links rhodopsin to phospholipase C (PLC), which opens two Ca^{2+}-permeable transient receptor potential (TRP) channels (Montell, 2012). This subsequently leads to photoreceptor depolarization. A read out of the phototransduction process, as well as downstream processes in the optic lobe, can be recorded using the *Drosophila* electroretinogram, as discussed in *2.1.4 Drosophila electroretinogram*.

Phototransduction in *Drosophila* differs to that of humans. Fly photoreceptors depolarize in response to light, as the TRP channels open in response to light, while human photoreceptors hyperpolarize. Further, fly phototransduction is much faster than phototransduction in humans – the response of a fly photoreceptor to a photon of light is 10-100x faster than a vertebrate photoreceptor. Finally, although human rods saturate with increasing light intensity, fly photoreceptors can adapt over the entire environmental range of light, up to 106 photons per second (Hardie & Raghu, 2001a).

1.4.1.3 The optic lobe

The *Drosophila* optic lobe contains 60,000 neurons that are grouped into four neuropiles: the lamina, medulla, lobula, and lobula plate (Morante & Desplan, 2004). These structures are comprised of individual sampling units. Photoreceptors R1-R6, located on the outer region of the ommatidia project to individual lamina cartridges, which form the first synapses with downstream neurons involved with motion processing (Fischbach & Dittrich, 1989; Rister et al., 2007). Photoreceptors R7-R8, located in the inner region of the ommatidia, bypass the lamina and project further downstream to segregated columns in the medulla neuropil which form the first synapses for colour vision, and the second synapses for the motion processing pathway (Fischbach & Dittrich, 1989; Paulk et al., 2013). The majority of neurons in these regions of the optic lobe are retinotopic. Next, neurons project from the medulla to the lobula complex (the lobula and the lobula plate), where this retinotopic map is

roughly maintained (Rister et al., 2007). The lobula plate contains large neurons responsible for motion detection (Hofbauer & Campos-Ortega, 1990). Surprisingly, input neurons to the lobula plate appear to maintain retinotopic organisation, however the neurons that output to the central brain do not (Strausfeld, 1976). All projections from the lobula merge at the neck of the lobula plate, to form a single fibre tract that connects the lobula to the central brain, where visual information is processed (Otsuna & Ito, 2006; Paulk et al., 2013).

1.4.2 Drosophila as a model of Parkinson's Disease

The identification of genes associated with familial forms of PD have revolutionised how we can study the aetiology of PD (Hernandez, Reed, & Singleton, 2016). This has led to studies using *Drosophila* as an animal model for genetic PD, where we can gain insight into the pathological mechanisms underlying PD and how the disease develops over time. The following is a discussion of three *Drosophila* PD mutations in genes whose human homologues are associated with recessive, early-onset (< 50 years of age) PD; *DJ-1*α*, DJ-1*β and *PINK1*.

Drosophila DJ-1α and *DJ-1*β are homologous to human *DJ-1*. In flies, the expression of *DJ-1*α is restricted to the testis, while *DJ-1*β is expressed ubiquitously, and more closely resembles the expression of human *DJ-1* (Meulener et al., 2005). *DJ-1* is mutated in 1-2% of early-onset PD cases and is considered to be rare, thus few cases are reported in literature relating to

human forms of the mutation (Pankratz et al., 2006). *DJ-1* encodes a small protein that inhibits the aggregation of α-synuclein, a protein implicated in PD pathogenesis, and is thought to be protective against oxidative stress and assist in mitochondrial regulation by functioning as a cellular sensor of oxidative stress (Canet-Avilés et al., 2004; Oswald et al., 2016; Shendelman, Jonason, Martinat, Leete, & Abeliovich, 2004). Loss-of-function mutations in *DJ-1* lead to an increase cell death in response to increased oxidative stress as their neuroprotective function and antioxidant activity becomes reduced (Anderson & Daggett, 2008; Malgieri & Eliezer, 2008).

PINK1 (PTEN-induced Kinase 1) is a protein kinase with a mitochondrial targeting sequence, and is thought to maintain mitochondrial homeostasis in dopaminergic neurons (Park et al., 2006). Mutations on the *PINK1* gene are the second most common cause of autosomal recessive early-onset PD, with a frequency of 1-9%, varying greatly across ethnic groups (Bonifati et al., 2005; Rogaeva et al., 2004). It is thought that *PINK1* may act on a pathway which senses and selectively eliminates damaged mitochondria from the mitochondrial network (Klien & Westenberger, 2012). Studies of loss-of-function mutations in *PINK1* animal models have found evidence for abnormal mitochondrial morphology, reduced ATP signalling, impaired dopamine release and locomotor deficits (Clark et al., 2006a; Kitada et al., 2007; Park et al., 2006).

Overall, the protein products of *DJ-1* and *PINK1* appear to impact mitochondrial functioning and oxidative stress responses, supporting the theory that mitochondrial impairment plays a role in the pathogenesis of genetic PD (Mandemakers, Morais, & Strooper, 2007).

1.5 Rodent visual system

Rats have become a model system in vision research for two reasons. First, advances in rodent genetics allow us to manipulate neuronal activity in a controlled manner (Luo, Callaway, & Svoboda, 2008; Zhang, Aravanis, Adamantidis, de Lecea, & Deisseroth, 2007). Second, research has demonstrated that the rodent visual system possesses similar functional features seen in higher-order animals, making them a viable higher-order model of the visual system (Niell & Stryker, 2008; Prusky & Douglas, 2004). Like primates, visual input is processed in the retina, passes through the LGN, and is eventually projected to V1. Rodent V1 contains receptive fields that are tuned to basic spatial features such as orientation, direction, spatial frequency, and temporal frequency (Niell & Stryker, 2008; Smith & Häusser, 2010). However, in the rodent there is no real evidence for functional architecture beyond basic retinotopy, with a diverse arrangement sensitivity across local receptive fields, and a stronger influence of geniculocortical feed forward and feedback connections from other cortical areas (Bonin, Histed, Yurgenson, & Reid, 2011). Further, the superior colliculus has heightened importance in the rodent due to the high projection rate of RGCs to this structure (Ellis, Gauvain, Sivyer, & Murphy, 2016). The following will briefly cover rodent V1 and superior

colliculus, two cortical areas investigated in *Chapter 4: Classification of α-synuclein Parkinson's disease rodents using chromatic SSVEP measurements*.

1.5.1 Key features of the rodent visual system

The rat is widely used to study aspects of vision, usually as a model for retinal disease. The rats eyes are laterally directed and provide a panoramic view of the visual space, with centrally overlapping visual fields that gives them central binocular vision (Adams & Forrester, 1968). While the human retina contains L-, M-, and S-cones, rats only have M- and S-cones, with the sensitivity of S-cones shifted towards ultraviolet wavelengths (Deegan & Jacobs, 1993). Further, the rodent retina is dominated by rods, leading to desaturated colour vision and poor visual acuity (Wells, 1934). In the retina, RGCs primarily project to the contralateral hemisphere, although 5-10% project to the ipsilateral hemisphere.

There are two major regions that receive direct visual signal from the retina; the dorsolateral geniculate nucleus (dLGN) and the superior colliculus (SC) (Seabrook, Burbridge, Crair, & Huberman, 2017). The circuitry between these areas is intricate, with many feedforward and feedback connections, as well as connections to other higher visual areas (see Figure 1.7). Similar to humans, the dLGN is the primary relay station of the visual system, however it is thought to be a homogenous structure with no clear lamina organisation.

dLGN axons terminate in the ipsilateral layer 4 and layer 6 of V1 (also called area 17).

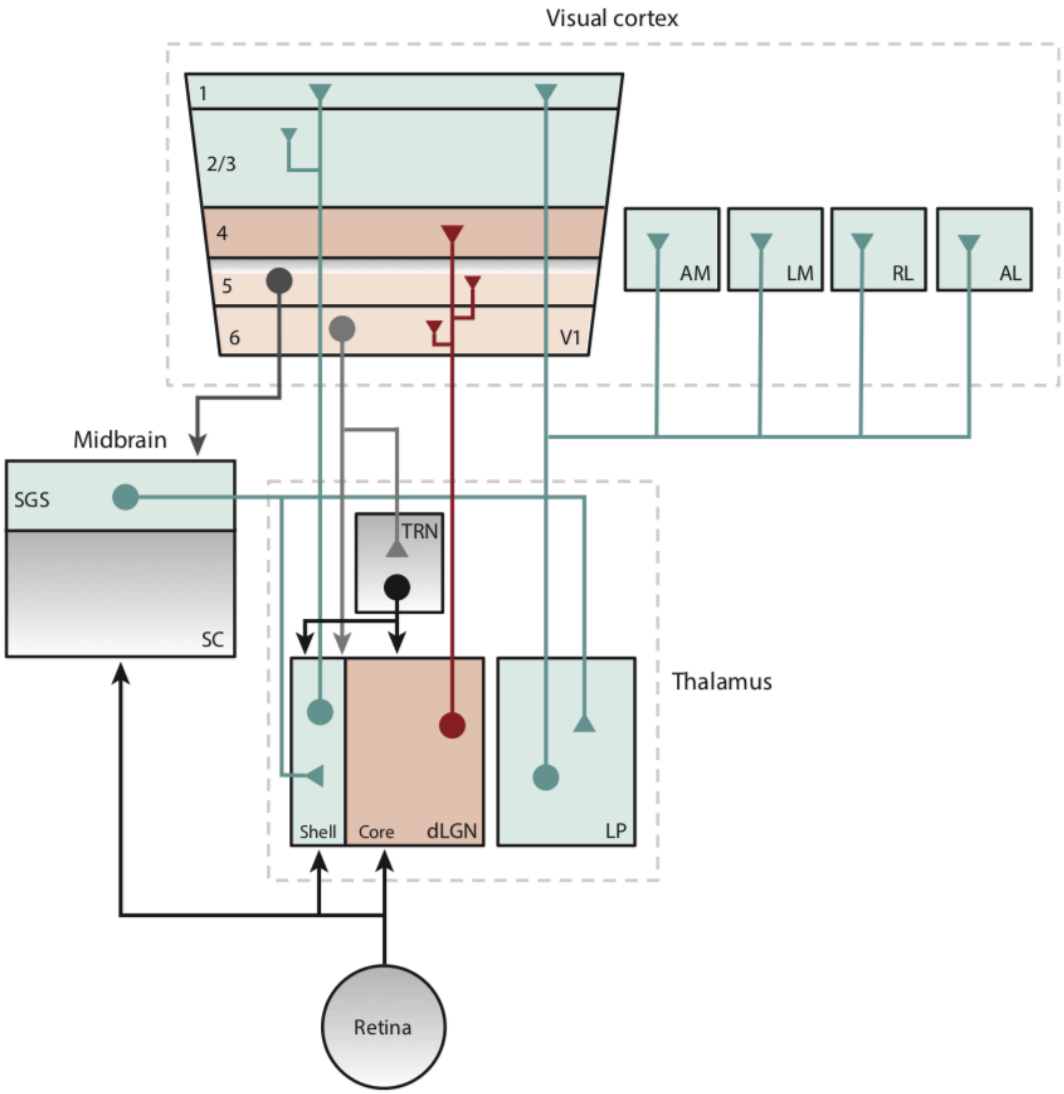

Figure 1.7 Retinorecipient targets in the rodent visual pathway. The retina sends visual signal to the dLGN. Here, neurons in the shell of the dLGN project to layers 1 and 2/3 of V1, while those from the core dLGN project to layer 4 of V1. Signal from layer 6 of V1 is fed back into the core dLGN. The retina also sends signal to the SC, which then indirectly connects to V1 via the lateral posterior nucleus (LP) and the dLGN. Signal from layer 5 of V1 is fed back into the SC (Seabrook et al., 2017).

Rodent V1 is 1.5mm thick, elliptical in shape, covers ~8mm^2, and carries a retinotopic map of the contralateral visual field (Espinoza & Hardy, 1983). It does not receive any direct input from the retina and is instead driven by geniculocortical feed forward and feedback connections from other cortical areas implicated in vision and cognition (Angelucci & Bressloff, 2006; Glickfeld, Reid, & Andermann, 2014). Overall, rodent V1 is thought to have less involvement in visual processing when compared to higher order animals. However, like humans, V1 is split into 6 cortical layers with the primary input being into a granular layer 4.

The SC is thought to be the most prominent retinal target in the rodent, with superficial laminae of the stratum griseum superficiale (SGS) receiving direct retinal input from ~90% of RGCs (conversely, only ~10% of primate RGCs project to the SC) (Ellis et al., 2016; Hofbauer & Dräger, 1985; Humphrey, 1968; Lupeng Wang, Sarnaik, Rangarajan, Liu, & Cang, 2010). The rodent SC is organised into several synaptic laminae, with different RGC types projecting to different regions of the SGS, adhering to retinotopic organisation (Ito & Feldheim, 2018). SC neurons are thought to be 'feature detectors', with specific neurons preferring certain types of stimulus in their receptive field (Ito & Feldheim, 2018).

1.5.2 SNCA and α-synuclein

The past two decades have seen a rapid increase in research towards the genetics of PD, with the identification of 20 loci and 15 disease-causing genes in relation to sporadic and familial parkinsonism (Deng & Yuan, 2014). The *SNCA* gene is one of the most intensely investigated due the importance of overexpressed α-synuclein, the protein which *SNCA* encodes, in the Lewy body clusters typically associated with PD.

SNCA was the first gene to be identified with mutations that cause autosomal-dominant early-onset PD (Klien & Westenberger, 2012). Such mutations are rare, and the disease itself presents with rapid progression, with Lewy bodies found in the superior colliculus, locus coeruleus, hypothalamus, and cerebral cortex (Polymeropoulos et al., 1996). The *SNCA* gene encodes α-synuclein, a protein localised in neuronal mitochondria, and although it's exact function is still ambiguous, it has been implicated in the regulation of dopamine release (Siddiqui, Pervaiz, & Abbasi, 2016). α-synuclein itself is a major component of Lewy bodies; intracellular protein aggregates that are a neuropathic feature in some variants of PD (Siddiqui et al., 2016). α-synuclein-induced neurotoxicity aggregates form within neurons and then spread across connected regions of the brain via interneuronal transmission, with the mass accumulation of such pathological aggregations inducing toxicity in the brain (Lücking & Brice, 2000; Recasens & Dehay, 2014). Several toxic pathways have been postulated, such as the disruption of α-synuclein release, where the protein acts as a regulator of dopamine release, the impairment of

mitochondrial structure, and the impairment of protein-degradation mechanisms – all leading to cell injury and death (Abeliovich et al., 2000; G. Liu et al., 2009; Martin et al., 2006; Martinez-Vicente & Vila, 2013; Murphy, Rueter, Trojanowski, & Lee, 2000; Nakamura et al., 2011).

1.6 Outline of the thesis

The following thesis contains four experiments organised into individual empirical papers. First, *Chapter 2* provides a detailed overview of the methods used across the four experimental chapters. In *Chapter 3*, we use *Drosophila* PD models to investigate changes in visual sensitivity to temporal frequency and contrast to identify a visual biomarker for PD; in *Chapter 4*, we similarly ask whether we can use measurements of low-level vision to identify a visual biomarker in rodent models of PD; in *Chapter 5*, we use fMRI to investigate how cortical sensitivity to achromatic contrast changes as a function of temporal frequency and visual field eccentricity in the human brain; and in *Chapter 6* we use population receptive field (pRF) mapping methods to investigate the representation of the spatial properties of the S-cone pathway in primary visual cortex, resolved using sub-millimetre fMRI. *Chapter 7* summarises the conclusions of these four experiments, as well as describing directions for future studies.

Chapter 2

Methodologies.

The following is a review of key methods used in the thesis, that are not covered in the experimental chapters themselves. This includes *Drosophila* culture and the electroretinogram (ERG), steady state visually evoked potentials (SSVEPs) and Fourier analysis, machine learning classification methods, principles of neuroimaging, and population receptive field mapping.

2.1 *Drosophila* culture and electroretinogram

2.1.1 Food

The diet of the fly is of importance when measuring visual response. The level of carotenoid in the food is associated with the concentration of rhodopsin in the fly eye (Goldsmith, Barker, & Cohen, 1964). *Drosophila* experiments in this thesis utilized standard food containing agar (1% w/v), cornmeal (3.9%), yeast (3.7%), and sucrose (9.4%), and nipagin (0.1% w/v). Nipagin was used to avoid fungal contamination in the *Drosophila* vials. This food mixture is poured into a small plastic vial or a half-pint bottle. In our study, fly stocks were bred in half-pint bottles. Upon hatching, only female flies were transferred into small plastic vials that were later bred with males during genetic crossing. Approximate ~30 flies are kept in each vial, where they reproduce and lay eggs within the food.

2.1.2 Drosophila Stock Contamination

The two main organisms that can contaminate *Drosophila* stocks in the laboratory are mold and mites. Mites can lead to the reduction in the number of offspring and can destroy *Drosophila* stocks by consuming the eggs (Sang, 1982). Although mould is not directly harmful to flies, it produces toxins which may affect the *Drosophila* CNS and this can affect visual response. No *Drosophila* stocks were found to be contaminated by mites in the thesis experiments, however any stocks that were affected by mold were discarded.

2.1.3 Adult flies

Physical differences between male and female *Drosophila* allow them to be distinguished at birth. Males are small, with 5 abdominal segments and a black tip at the end of the abdomen and have bristles along their foreleg (known as the sex comb). Conversely, females are larger (especially at birth), with 7 abdominal segments and do not have a black tip or a sex comb.

In *Drosophila* research it is essential to use female virgins when conducing genotypic crosses, especially during outcrossing, as female flies have the ability to store sperm after mating. This means that if the female is not a virgin, we cannot identify the genotype of the male used in the crossing. Flies do not mate until ~8 hours after eclosion and virgin flies are physically distinct from mature adults. Virgin females are larger than older females and have a light colouration. Early after eclosure, there is a visible dark green spot

(the meconium) on the underside of the virgin abdomen which are the remains of the larval gut (Sang, 1982). This was used to identify virgin flies for breeding.

2.1.4 Drosophila electroretinogram

The *Drosophila* electroretinogram (ERG) has been used for over 40 years and allows one to record signal produced by the fly eye in response to a visual stimulus. The method uses an extracellular electrode to record a compound field potential produced by fly photoreceptors and downstream lamina and medulla neurons within the fly eye and brain (Dolph, Nair, & Raghu, 2011). A reference electrode is placed elsewhere on the fly (the thorax, or the proboscis) and upon visual stimulation, the voltage difference between these two electrodes is measured in real time. Within this signal, the transient spike that occurs at the onset of visual stimulation represents the hyperpolarization of the lamina neurons, which are the synaptic targets of photoreceptors R1-R6. Chloride-permeable ionotropic histamine receptors are opened in response to the release of histamine neurotransmitters by the photoreceptors. Following this is a sustained negative potential that occurs during the stimulus presentation represents the depolarization of photoreceptor cells, providing a read-out of the phototransduction process (Hardie & Raghu, 2001b; Craig Montell, 1999). The amplitude of this negative potential is proportional to the intensity of the stimulus. The transient spike that occurs at the offset of the visual stimulus reflects the repolarization of the lamina neurons after photoreceptors cessation of histamine neurotransmitters (Hardie & Raghu, 2001b).

ERG recordings were first adapted to assess changes in the visual response of mutant disease *Drosophila* in the late 1960s (Hotta & Benzer, 1969). In such models of disease, genetic mutations may affect intracellular signalling, synaptic transmission, or neural functioning (Ugur et al., 2016). In turn, this may impair phototransduction, which then affects the ERG waveform – for example, reduced/increased depolarization amplitudes, changes in on/off transients, or shifts response latency (Afsari et al., 2014; Chouhan et al., 2016; Himmelberg, West, Elliott, & Wade, 2018; Hotta & Benzer, 1969; Pak, 1966). Thus, comparison between ERG response from mutant diseased and wild-type *Drosophila* may allow us to assess whether visual response to different stimulus parameters can be used as a biomarker for a range of diseases.

The visual stimulus used to produce this response is typically triggered by a single stimulus presentation (usually a flash of light) to produce a VEP (visually evoked potential) or a repeated train of stimulus presentation to produce a SSVEP (steady state visually evoked potential). This stimulus is typically used in human electroencephalogram; however, it has been found that SSVEPs can be accurately measured in *Drosophila* using spatial SSVEP stimuli rather than flash SSVEP stimuli. A general overview on how SSVEPs are measured will now be discussed.

2.2. Measuring steady state visual evoked potentials

2.2.1 Overview

Visual stimulation generates electrophysiological potentials in the brain, referred to as visually evoked potentials (VEPs). When a stimulus parameter is periodically modulated as a function of time it evokes VEPs with a periodic time course. A repeated train of periodically modulated stimuli presented at a fixed rate will generate repeated multiple VEP responses that have similar amplitude and phase over time. These responses are referred to as steady-state visually evoked potentials, or SSVEPs (Regan, 1966). The SSVEP response occurs at periodic intervals and is confined to multiples of the input frequency. Thus, it is logical to analyse SSVEP recordings in the frequency domain rather than the time domain (Norcia, Appelbaum, Ales, Cottereau, & Rossion, 2015). The relationship between periodic signals and the frequency domain can be seen in Figure 2.1. A sine wave modulated at a frequency of 2Hz will produce a single spectral component at 2Hz in the frequency domain, representing response amplitude (Figure 2.1A). SSVEPs also output a response phase, related to integration times and temporal processing of the visual system. Phase is coded as a circular variable in which 0 phase is located by a vector angled horizontally to the right (Figure 2.1C). A delay in temporal processing will be represented as a phase shift, which is then represented as a rotation of the vector per the waveforms temporal delay.

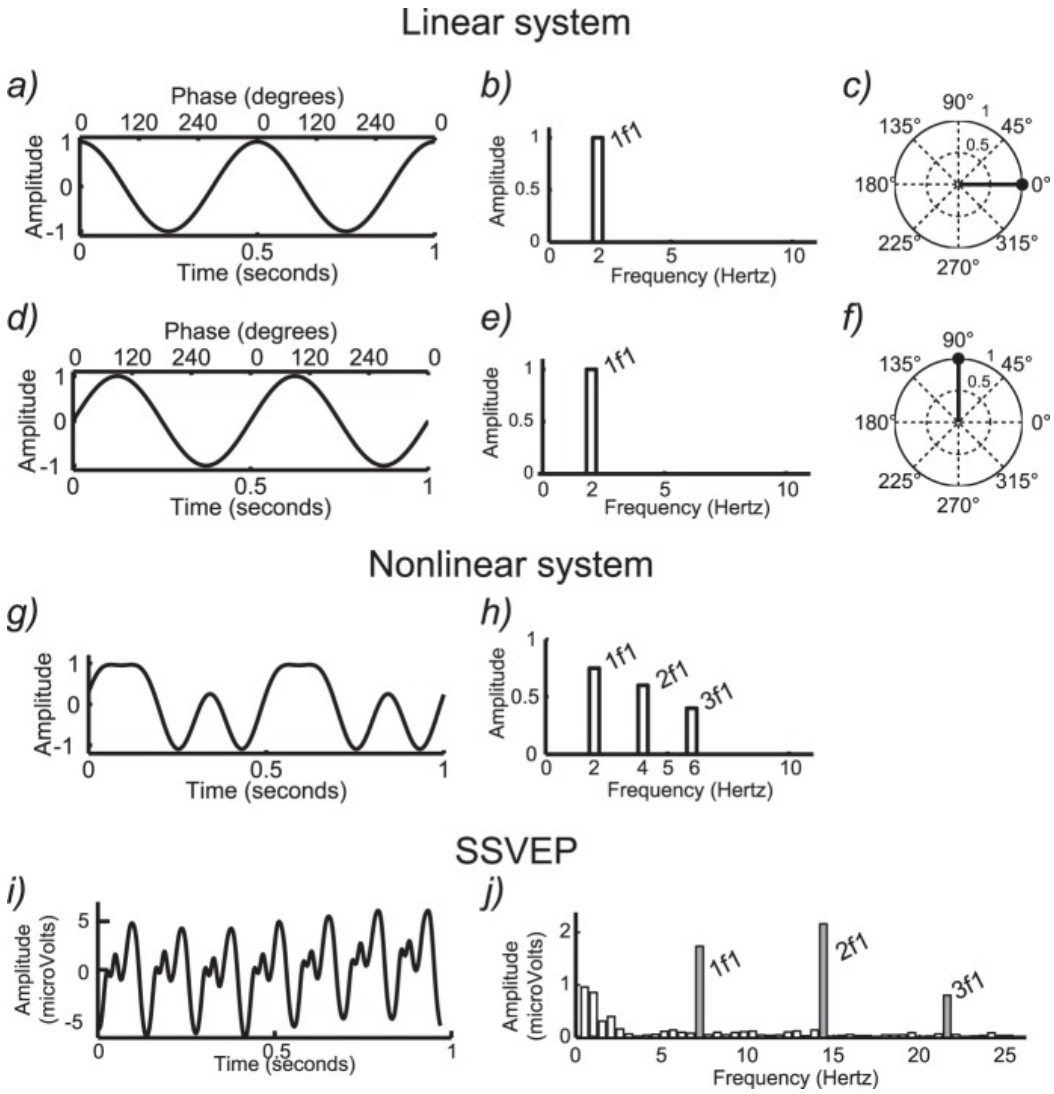

Figure 2.1 SSVEP responses in time and frequency domains. (A) A 2Hz pure sine wave response in the time domain with (B) as this transformed into the frequency domain. (C) shows phase of (A), set to 0° phase. Temporal delay resulting in a cosine wave (D) results in a 90° shift in phase. A nonlinear system (G) in the time domain produces responses at multiple harmonics in the frequency domain (H). SSVEP response from a 7.2Hz modulating stimuli and responses amplitudes in the frequency domain (J) (Norcia et al., 2015).

When a stimulus contains multiple temporal frequencies, or the system is non-linear (as is visual response), SSVEP responses will contain activity in

harmonics occurring at integer multiples of the input frequency. For example, an input frequency of 2Hz in a non-linear system will produce frequency responses at 2Hz, 4Hz, and 6Hz (Figure 2.1H). A SSVEP recording will always produce a periodic non-linear response (Figure 2.1I), and the subsequent response in the frequency domain is represented at the input frequency and higher harmonics (Figure 2.1J). SSVEP analysis of data in the frequency domain results in a high signal-to-noise ratio as overall experimental noise is confined into bins that are not of interest based on experimental conditions.

Stimuli for measuring SSVEPs can be presented as an on/off modulating pattern or a contrast reversing pattern. In on/off modulating patterns, a stimulus alternates between a structured stimulus and a uniform field of the same luminance (Figure 2.2A). Here, the response will be present at input frequency and higher harmonics. In contrast reversing patterns (those used in this thesis), a patterns luminance is alternated with the 'light' and 'dark' parts of the pattern reversing at the rate of stimulating temporal frequency. This spatial alternation evokes equivalent neuronal responses, producing equivalent responses at each reversal (Figure 2.2B). Further, the spatial phase in one pattern reversal is symmetrical to the subsequently presented reversal. This results in frequency responses at even harmonics (Figure 2.2C). The modulation rate of contrast reversing stimuli is defined by the number of reversals per second (i.e. a 10Hz contrast reversing pattern will present 10 alternations in 1 second).

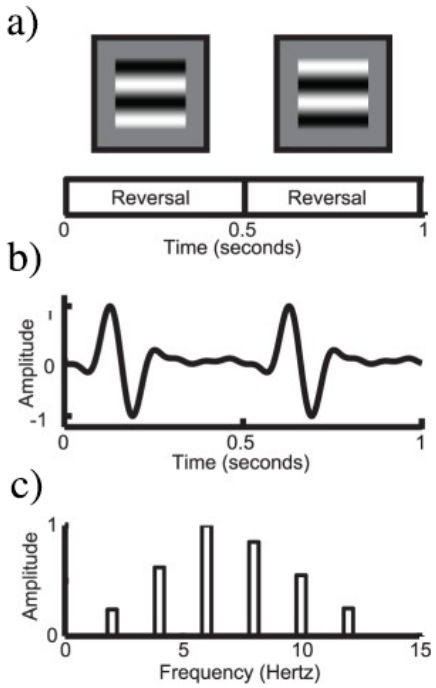

Figure 2.2 (A) Contrast reversing stimuli with a 180 shift in spatial phase at each reversal. (B) illustrates the response to a single pattern reversal, with this response producing only even harmonics of the stimulus frequency in the frequency domain (C) (Norcia et al., 2015).

2.2.2 Fourier Transform

SSVEP signals are analysed using the Fourier transform. The Fourier transform is a mathematical technique that converts SSVEP signal from the time domain into its corresponding components in the frequency domain. The waveform generated by the SSVEP is a result of the stimulus input frequency and multiples thereof, as well as general noise within the visual system. The Fourier transform decomposes a signal and returns information about the frequency of all the sine waves included within.

The Discrete Fourier transform:

$$X_k = \sum_{n=0}^{N-1} x_n \ . e^{-i2\pi kn/n}$$

Equation 2.1 Equation for the discrete Fourier transform.

Where X_k is a complex number (of amplitude and phase) representing the amount of frequency *k* in the signal, *k* is the current frequency under consideration (from 0-N-1 Hz), *N* is the number of time samples, *n* is the current value, x_n is value of the signal at time n, $e^{-i2\pi k}$ is how far we have moved along our circular path for a speed/time, and n/n is the percentile of time we have gone through. To summarise, to find the energy at a frequency we spin our signal around a circle at that frequency and average the points along the path.

To find the complex value of a signal at time *n*, we use the following formula:

$$x_n = \frac{1}{N} \sum_{k=0}^{N-1} x_k \ . e^{i2\pi kn/n}$$

Equation 2.2 Equation for finding the complex value of a signal at a specific time.

As a result of this, from an SSVEP assay we derive complex number that contains two components; a response amplitude and a response phase. The response amplitude is related to the height, or energy, of the response, while the phase is the offset of a frequency and is related to processing speed of the visual system. Amplitude and phase are typically represented as a vector in a polar coordinate system, with the length of the vector representing the amplitude and the polar angle representing the phase (See Figure 2.1C and F). The experiments in this thesis are concerned with the amplitude of the SSVEP, rather than the phase.

2.3 Machine learning classification

2.3.1 Overview

Machine learning classification is a form of predictive modelling where we aim to accurately predict a class or category based on a set of given data points. Generally, classification is a form of supervised learning where the classes are known and provided with a given data points (i.e. the data belongs to class A or class B). A classifier will use training data to learn how the given data points relate to their assigned class and can then be used to classify untrained data from an unknown class. The primary goal of modern machine learning classifiers is to produce highly accurate, data driven predictions on test data, typically using very large datasets. The experiments in this thesis apply these classification methods to multivariate data sets, with the aim to identify unique visual biomarkers for PD. The ability to accurately classify disease in such way opens avenues for assessing disease progression and

prognosis, as well as novel methods for testing newly developed therapeutic treatments that target disease related genes.

We make use of two types of classifiers; a linear discriminant analysis (LDA) is used in *Chapter 3: Abnormal visual gain control and excitotoxicity in early-onset Parkinson's disease Drosophila models*, and a support vector machine (SVM) classifier is used in *Chapter 4: Classification of α-synuclein Parkinson's disease rodents using chromatic SSVEP measurements*.

2.3.2 Linear discriminant analysis

We used LDA as a tool to accurately classify flies into their correct PD genotype based on multivariate visual response profiles that were collected via ERG, in response to 64 unique combinations of temporal frequency flicker and contrast. The 'Linear Discriminant' was first developed by Ronald A. Fisher in 1936 and was initially designed to work with binary classifications, however this generalized to a 'multi-class LDA' by C. R. Rao in 1948 to utilize multiple measurements in biological classification (Fisher, 1936; Radhakrishna, 1948). LDA is most commonly used as a dimensionally reduction technique and is closely related to principal components analysis (PCA) as they both search for linear combinations of variables that best explain the input data. However, LDA differs in that it explicitly attempts to model the difference between two or more classes of data by finding the axes (or 'linear discriminants') that maximize separation between multiple classes. This allows for the most accurate classification of new data. Further, LDA

works under the assumption that unique classes generate unique Gaussian distributions (Izenman, 2008).

LDA predicts the probability that new input data belongs in each class. The class that is assigned the highest probability (i.e. the class with the smallest misclassification cost) for the new input data is the predicted class. Typically, this is achieved using Bayes Theorem to estimate probabilities, in which we estimate the probability of output class given the input using the probability of each class, in addition to the probability of the data belonging to each class.

2.3.2.1 Model cross-validation methods

With smaller sample sizes, a more useful way of assessing the accuracy of an LDA model is perform a cross-validated LDA. Cross validation is a method for estimating generalisation errors. Here, rather than using new test data, we split our training data into two groups – a cross validation training set and a cross-validation test set. Thus, by employing cross validation on the predicted groups, we get a sense of how the model would perform on new observations. Two forms of cross validation used in the current thesis are k-fold and leave-one-out cross validation.

In k-fold cross validation, the data points randomly organised and split into k equal sized samples, with a single sample retained as the test data set for testing the model, while the remaining $k - 1$ sample are used in as the

training data for the LDA. We fit the LDA model to the training data and evaluate the model using the test data set. This cross-validation process is then repeated *k* times, with each of the subsamples used once as the validation data. Each data point is assigned to one of *k* samples and stays within this sample throughout the entire cross-validation processes (Inezman, 2008; James, Witten, Hastie, & Tibshirani, 2013). We can then look at the *k*-fold loss estimate, or the predictive inaccuracy of the model. Here, the lower the loss, the better the prediction. The value of *k* must be chosen to ensure that each sample is statistically representative of the broader dataset (Kuhn & Johnson, 2013). When *k* = n (or the size of the entire dataset), a leave-one-out cross validation is occurring. In leave-one-out cross validation, the classification function is determined using all but one of the labelled data points (i.e. the test set is a single observation and the training set is all other data). The classification function is then used to predict the class of the omitted data point. This is then repeated for all data points and the generalisation error is averaged to obtain an overall model accuracy.

2.3.3 Support vector machine

We used support vector machine (SVM) as a tool to classify α-synuclein and control rodents into their correct genotypic class based on a dataset of SSVEPs recorded from different light wavelengths. The SVM is a popular and robust supervised learning model that is based on statistical learning theory, as developed and first implemented by Vladimir Vapnik (Vapnik, 1995). Currently, SVMs are considered to be one of the most efficient methods of

classification in real world applications and are most prevalently used for binary classifications. The SVM aims to find the hyperplane (that acts as a decision boundary) in a *N*-dimensional space, where *N* is the number of features included in the analysis, that best separates two classes in order to distinctly classify observed data points. There are many possible hyperplanes that separate data, thus, the SVM aims to find the hyperplane that has the maximum distance between the 'support vectors', that is, the data points closest to the hyperplane, in order increase the accuracy of our decision boundary.

SVM can use a technique called the kernel trick to overcome non-linear data separation problems. A kernel function is a measure of similarity between two sets of features. These kernels functions transform data from low dimensional input space into higher dimensional space. For example, a polynomial, gaussian kernel will calculate the hyperplane in a higher dimension that a linear kernel. The dimensionality of the dataset does not need to be preserved when undergoing this transformation. This is done by computing the inner products, or the dot products, between all pairs of data in the N-dimensional feature space. Thus, we use instances of 'neighbourhood', or similarity, of instances of data in our transformation – we transform to a basis where each component is the similarity to a known instance of data. Finally, we can use regularization to optimize the SVM by dictating how much we want to avoid misclassification. An SVM with low regularization will look for the largest margin (i.e. distance between the support vectors and hyperplane)

separating hyperplane, even if this results in misclassifications, while an SVM with high regularization will choose a smaller margin hyperplane that is more accurate in classifying the training data. High regularization may result in overfitting the data, as will be discussed next. Finally, SVM itself does not provide probability estimates. As such, classification accuracy is commonly achieved through cross-validation techniques and bootstrapping methods.

2.3.4 Radial Basis Function Kernel

In *Chapter 4: Classification of α-synuclein Parkinson's disease rodents using chromatic SSVEP measurements*, we employ a Radial Basis Function (RBF) kernel function for our hyperplane. Kernels are used to port low-dimensional data into a higher dimensional space. This makes it easier to define a hyperplane separating the data. The RBF is a standard kernel function that transforms the input data, that is in finite dimensional space, into infinite dimensional space. The RBF kernel assumes that an instance of data is a characteristic of a gaussian distribution (i.e. the mean), and we assess the probability that that another instance of data falls within the distribution. The RBF kernel has one free parameter that we can tune, gamma, which is related to the variance of the gaussian distribution.

2.3.5 Issues: Overfitting

Overfitting occurs when a model/hyperplane is fit too closely to a particular training dataset (i.e. it is too dependent on the detail and noise of the data) and may have a higher error rate when attempting to classify new,

unseen data. Thus, the model may struggle to be generalized outside the training dataset. Machine learning algorithms include parameters that constrain how much detail the model can learn in order to overcome any problems of overfitting. Alternatively, resampling techniques (such as *k*-fold validation) can be used to estimate model accuracy. In *Chapter 4: Classification of α-synuclein Parkinson's disease rodents using chromatic SSVEP measurements*, we bootstrap our SSVEP data itself to produce unique, synthetic rats that are included in 1000 bootstrapped iterations of a bootstrapped SVM, effectively overcoming any overfitting problems that may occur.

2.3. Neuroimaging

2.3.1 Magnetic resonance imaging

Magnetic resonance imaging (MRI) measures how radio frequency waves affect nuclei within in a magnetic field. When imaging the brain, the MR signal arises from hydrogen nuclei, that make up ~60% of the human body. The MR signal reflects how the dipoles of hydrogen nuclei transition between energy states. In the absence of a magnetic field, hydrogen nuclei are randomly orientated on their axes and have a net magnetization of 0 (M0). When a subject is placed within the static magnetic field (vector B0) of a MR scanner, these hydrogen nuclei are polarized. Roughly half the nuclei enter a low energy state and align parallel with B0, whilst the other half enter a high-energy state and align antiparallel to B0. In this state, the precession, or phase, of the nuclei is random.

A radiofrequency (RF) pulse is sent to momentarily excite the tissue, which flips the low-energy nuclei within the tissue away from their resting state into a high-energy state. This excitation is only effective at a resonance frequency known as the Larmor frequency. The Larmor frequency is the rate of precession, or spin, of a proton around the external magnetic field, and is proportional to B0 and the gyromagnetic ratio (the ratio of magnetic moment to angular momentum) of the hydrogen nucleus. A gradient coil is used to control spatial inhomogeneity in the magnetic field. As consequence, the RF pulse selectively excite nuclei within a magnetically aligned field. This RF pulse causes the hydrogen nuclei to resonate by absorbing energy emitted by the pulse. Further, the RF pulse causes hydrogen nuclei to coherently align in their precession phase. Once the RF pulse is terminated and nuclei begin to return to their equilibrium state. During this process, they release the absorbed RF pulse energy whilst undergoing precession to de-phase. A receiver coil is placed in the transverse plane to receive current from nuclei precession. This current is converted into MR signal.

The current induced in the receiver coil is reduced after the RF pulse is terminated and the de-phasing process begins. After receiving a 90-degree RF pulse, the time that it takes for transverse magnetization of nuclei to decay by 63% of its maximum value is referred to as T2 relaxation, whereas the time it takes for magnetization to recover 63% of its maximum value is T1 relaxation when realigning to the magnetic field. Thus, T1 relaxation time is always longer or equal to the T2 relaxation time. T1 and T2 relaxation times are different for

different tissues. Relaxation times are shorter in fat and longer in water. This difference in relaxation time results in tissue contrast in MR images. T1 and T2 images can be differentiated by the cerebral spinal fluid (CSF). In T1-weighted images, CSF is dark as relaxation time is longer in water/CSF, whereas in T2-weighted images CSF is bright. Finally, there is a faster relaxation process referred to as T2* relaxation. Here, T2* relaxation is due to local inhomogeneity of the magnetic field and molecular interactions due to the difference of deoxyhemoglobin and oxyhaemoglobin in tissue during metabolic processes.

2.3.2 Functional magnetic resonance imaging

2.3.2.1 The BOLD Signal

Functional Magnetic Resonance imaging (fMRI) is used to non-invasively measure blood-oxygen dependent changes in the brain. The biochemical reactions involved in the transmittance of neural information require energy in the form of ATP, which is produced from glucose through the processes of oxidative phosphorylation. This process requires oxygen, which is transported through the blood in a protein called haemoglobin. When an oxygen molecule is bound to haemoglobin, it is oxyhemoglobin (or oxygenated blood), and conversely when no oxygen molecule is bound it is deoxyhemoglobin (or deoxygenated blood). The relative levels of oxyhaemoglobin and deoxyhaemoglobin have differential magnetic susceptibility as deoxyhaemoglobin is a paramagnetic molecule (i.e. it is slightly attracted to a magnet). The presence of deoxyhaemoglobin causes a

susceptibility difference between a blood vessel and its surrounding tissue. This results in a dephasing of the hydrogen nuclei, a reduction in the T2* relaxation time, and a subsequent 'darkening' in voxels that contain deoxyhaemoglobin. Conversely, oxyhaemoglobin does result in dephasing of hydrogen nuclei as it is a diamagnetic molecule (i.e. it is slightly rebelled by a magnet). Therefore, as the concentration of deoxyhaemoglobin decreases, the signal increases. This signal is the blood oxygenation level dependent signal (BOLD signal). This lays on the assumption that neural activity results in increased blood blow, which is in turn indicative of metabolic activity.

2.3.2.2 The hemodynamic response function (HRF)

The time course of the BOLD signal is called the hemodynamic response (see Figure 2.3). An increase in neural activity is met by a metabolic demand for oxygen. As metabolism occurs, oxygen is extracted from the blood and the haemoglobin becomes paramagnetic, creating an initial dip in the HRF signal time course. This is followed by an increase in signal due to compensatory blood flow, increasing the ratio of oxyhaemoglobin to deoxyhaemoglobin. This increase peaks at about 4-8 seconds, with the peak denoting the primary neural response. If neural activity continues, the BOLD signal will plateau. After a stimulus is removed, the BOLD signal then returns to baseline over 7-11 seconds and is followed by a signal undershoot.

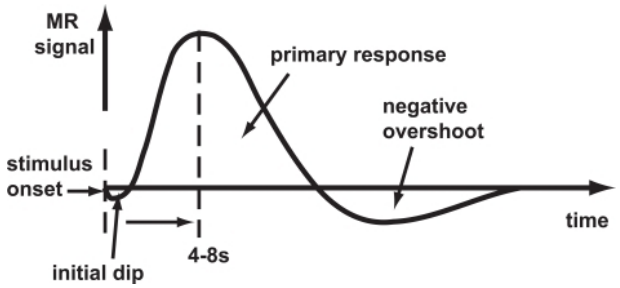

Figure 2.3 The BOLD Hemodynamic response. Stimulus onset causes an initial dip, followed by an increase in MR signal that peaks at 4-8 seconds, followed by a negative overshoot and return to baseline.

2.3.2.3 High resolution fMRI

The advent of high field (7T) fMRI allows for submillimetre resolution acquisition of MR data and the application of computational models at the mesoscopic scale. Thus, high resolution fMRI allows for more accurate mapping of brain processes and structures that were previously contained within a single voxel (i.e. orientation and ocular dominance columns in V1). Importantly, we are now able to resolve cortical layers in humans and investigate lamina-segregated processes, such as feedforward vs feedback processes, that occur within the cortex. The goal of high-field fMRI is to increase spatial resolution of images by increasing SNR and BOLD signal of images obtained during scanning. The SNR increases with the strength of B0, as the polarization of the proton signal increases linearly with field strength. Therefore, the magnitude of the imaging signal at 7T is approximately 2 times higher than the imaging signal at standard 3T. Similarly, the contrast-to-noise (CNR) is also increased with field strength. This is then translated into increased spatial resolution and image contrast. However, this technique is

not without its limitations, with increases in physiological noise, motion sensitivity and geometric distortion, and limitations on gradient strength.

A typical 3T voxel is 3 mm^3 isotropic and covers the entire cortical thickness including multiple cortical columns and laminae. However, a 7T voxel can occur at an isotropic resolution of 0.6-0.8 mm^3, allowing for distinction in responses when comparing between cortical layers and columns. For example, the cortex is divided into six functionally and structurally distinct layers. In V1, information enters the cortex in layer 4 and is then spread across further layers. Thus, we can use high-field fMRI to aid the investigation of local neural circuitry in that occurs during early-visual processes. It should be noted that higher resolution is not always better – different scientific questions are best addressed at different resolutions and many questions about neural processing can be answered at a lower resolution.

2.3.3 Retinotopy and population receptive field (pRF) mapping using fMRI

The visual receptive field of a neuron can be defined as the area of visual field upon which stimulation elicits a response (Hubel & Wiesel, 1962). Receptive fields have been typically modelled using single unit electrophysiology (Carandini, Heeger, & Movshon, 1997; Derrington & Lennie, 1984; Hubel & Wiesel, 1962; Levitt, Schumer, Sherman, Spear, & Movshon, 2001; Wandell, Winawer, & Kay, 2015). Recording from a single neuron informs us about not only the neuron itself, but the feed-forward and feedback projections from millions of other neighbouring neurons in the brain. Recent

developments in fMRI allow us to model the underlying characteristics of cortical visual receptive fields at both 3T and 7T, albeit at a courser resolution than single unit electrophysiology (Dumoulin & Wandell, 2008; Fracasso, Petridou, & Dumoulin, 2016). The human cortex contains ~50,000 neurons per mm^3. A typical $2mm^3$ isotropic voxel contains ~400,000 neurons. Therefore, our measured BOLD response tells us about the computations of a large network of neurons within a voxel that may be tuned to varying stimuli parameters. In population receptive field (pRF) mapping, this pooled neuronal response is conceptualised as a 'population receptive field', which refers to the aggregate properties of many neurons that share similar features due to the topographic organisation of visual cortex (Wandell & Winawer, 2015). Therefore, the pRF response can be considered a reflection of the mean tuning of the collective neurons within an individual voxel. Notably, the pRF estimates are usually made in response to high-contrast achromatic stimuli, thus neurons sensitive to such parameters will be predominately activated during a pRF experiment.

Retinotopic maps within the visual cortex can be derived using similar fMRI 'retinotopic mapping' techniques (Engel et al., 1997; Engel et al., 1994). This technique is based on periodic stimuli that generate travelling waves of activity in primary visual cortex. The visual field is mapped by measuring BOLD response to stimuli consisting of rotating wedges that extend into different directions and provide estimates of polar angle maps and expanding rings that increase in radius and provide estimates of eccentricity maps (see figure 2.4A

and B). A change in the BOLD response of a voxel is indicative of brain activity given a presented stimulus (Wandell, 1995). As such, the phase-difference between these periodic stimuli and the recorded BOLD response can be used to estimate the visual field location that produces the largest fMRI response in each voxel as indicative of the region of the visual field that each voxel is attuned too. We typically develop quantitative models of functional responses within these specific cortical maps, as different maps are responsible for different forms of visual processes (i.e. colour, motion, and form selective maps). Additionally, such techniques can be used to investigate the existence of new maps in human visual cortex that are homologues of non-human primate maps.

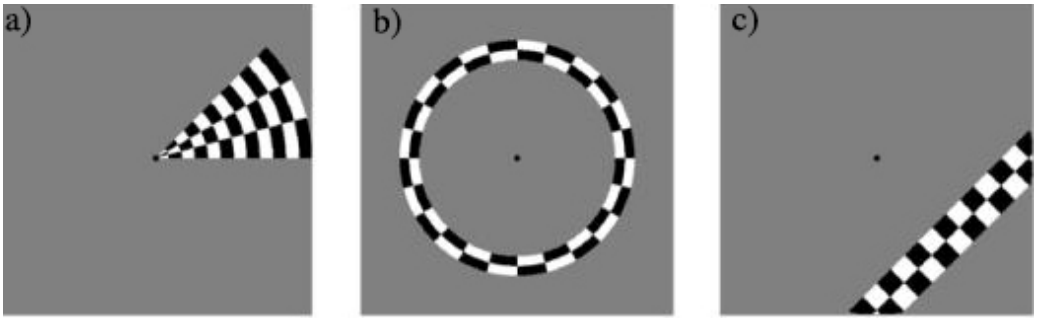

Figure 2.4 Examples of retinotopy stimuli. In A) we present the rotating wedge stimulus used to map out polar angle tuning, in B) we present the expanding ring stimulus used to map out eccentricity tuning, and in C) we present the standard pRF stimulus bar that drifts across the screen in 8 directions. In these examples, all stimuli are high-contrast achromatic checkerboards.

Population receptive field mapping (pRF) is a class of fMRI measurement that expands upon retinotopic mapping by estimating traditional retinotopic parameters (i.e. visual field location) and additional receptive field

properties (i.e. receptive field size) (Dumoulin & Wandell, 2008). In pRF mapping, the receptive field that elicits a voxel response is defined as an isotropic Gaussian. This Gaussian can be defined through three key parameters; visual field location (x_0 and y_0) and pRF size (σ). These parameters can be predicted using a fMRI time series in response to either traditional retinotopic mapping stimuli, or a drifting bar stimulus (see Figure 2.4C).

The pRF model uses a linear spatiotemporal model of fMRI response, which can be defined as:

$$y(t) = p(t)\beta + e$$

Equation 2.1 Equation for spatiotemporal linear model of fMRI response

Where p(t) is the predicted fMRI signal, β is the response strength scaling factor that accounts for unknown units of the fMRI signal, and e is noise. The predicted fMRI signal is calculated using a 2D Gaussian model of the population receptive field, which can be defined as:

$$g(x,y) = \exp - \left(\frac{(x - x_0)^2 + (y - y_0)^2}{2\sigma^2} \right)$$

Equation 2.2 Equation for Gaussian model of pRF used to calculate p(t).

Where $(x_0 y_0)$ is the Gaussian centre (or the pRF centre) and σ is the standard deviation (or the pRF spread).

Overall, the pRF model aims to find and fit the optimal pRF parameters to each voxel by minimizing the residual sum of squares between the prediction and the fMRI time course. This is completed using two stage, coarse-to-fine approach. In the first stage, the data are smoothed using a 5mm full-width at half-maximum Gaussian kernel to remove high frequency noise and improve spatial correlation amongst neighbouring voxels. Next, the optimum is found using brute force search. Here, 100,000 time series predictions are generated, and the best fit is estimated for every other voxel. In the second stage, unsmoothed voxels from the first stage whose fits explained over 15% of variance in that voxels time course are retained. These data are then refit using an optimization algorithm. Using these fits, x_0, y_0, and σ are estimated for each voxel. From these three values we can deduce three key values; the eccentricity value of a voxel (how far away from the centre of visual space a neuron is tuned too), the polar angle value (the radial angle), and the receptive field size (the size, in degrees, of space a neuron receives input from).

Chapter 3

Abnormal visual gain control and excitotoxicity in early-onset Parkinson's disease *Drosophila* models.

3.1 Abstract

The excitotoxic theory of Parkinson's disease (PD) hypothesises that a pathophysiological degeneration of dopaminergic neurons stems from neural hyperactivity at early stages of disease. This leads to mitochondrial stress and cell death. Recent research has harnessed the visual system of *Drosophila* PD models to probe this hypothesis. Here, we investigate whether abnormal visual sensitivity and excitotoxicity occur in early-onset PD (EOPD) *Drosophila* models *DJ-1*$\alpha^{\Delta 72}$, *DJ-1*$\beta^{\Delta 93}$, and *PINK1*^{5}. We used an electroretinogram (ERG) to record steady state visually evoked potentials (SSVEPs) driven by temporal contrast stimuli. At 1 day of age, all EOPD mutants had a twofold increase in response amplitudes when compared to w^{-} controls. Further, we found that excitotoxicity occurs in older EOPD models after increased neural activity is triggered by visual stimulation. In an additional analysis, we used a linear discriminant analysis (LDA) to test whether there were subtle variations in neural gain control that could be used to classify *Drosophila* into their correct age and genotype. The discriminant analysis was highly accurate, classifying *Drosophila* into their correct genotypic class at all age groups at 50-70% accuracy (20% chance baseline). Differences in cellular processes link to subtle alterations in neural network operation in young flies – all of which lead

to the same pathogenic outcome. Our data are the first to quantify abnormal gain control and excitotoxicity in EOPD *Drosophila* mutants. We conclude that EOPD mutations may be linked to more sensitive neuronal signalling in prodromal animals that may cause the expression of PD symptomologies later in life.

3.2 Introduction

Parkinson's Disease (PD) is the second most common progressive neurodegenerative disease, affecting ~0.2-3% of the population, with an increased prevalence in those aged over 50 (Clarke, 2007; de Rijk et al., 1997). PD is thought to stem from the pathophysiologic degeneration and subsequent loss of dopaminergic neurons within the pars compacta of the substantia nigra, a basal ganglia structure that plays a key role in movement (Clarke, 2007). It is hypothesised that neuronal death in PD is caused by an excitotoxic mechanism in which neuronal hyperactivity leads to neurodegeneration. Neuronal hyperactivity causes an increase in demand for ATP from mitochondria, leading to oxidative stress and eventual neuronal death (Beal et al., 1993; Surmeier, Obeso, & Halliday, 2017). The neuronal responses in both mammals and invertebrates are regulated by a tightly-linked network of excitatory and inhibitory gain control mechanisms that, collectively, we refer to as 'normalization' (Carandini & Heeger, 1994; Carandini, Heeger, & Movshon, 1997; Carandini & Heeger, 2011; Single, Haag, & Borst, 1997). Normalization mechanisms can be measured across the animal kingdom using a range of methods, including steady state visually evoked potential

(SSVEP) recordings, a sensitive technique commonly used to measure the amplitude of neural population responses to periodic flickering stimuli (Busse, Wade, & Carandini, 2009; Norcia et al., 2015; Regan, 1966; Tyler, Apkarian, & Nakayama, 1978).

In *Drosophila*, SSVEP recordings are collected from the surface of the eye and can be made in both healthy and PD mutant strains (Afsari et al., 2014; West, Elliott, & Wade, 2015). Previously we have shown that young flies carrying the late-onset gain-of-function PD mutation *LRRK2-G2019S* showed increased visual contrast sensitivity to full field flicker stimuli, reflecting a failure in regulation of neural activity (i.e. abnormal gain control or normalization) at one day of age (Afsari et al., 2014). This regulatory failure is followed by a decline in visual function over time, with physiological and anatomical degeneration in older *LRRK2-G2019S Drosophila* (Hindle et al., 2013; Mortiboys et al., 2015).

Feeding *LRRK2-G2019S Drosophila* with BMPPB-32, a kinase inhibitor specifically targeted at *LRRK2*, restored normal contrast sensitivity at both 1 and 14 days of age, indicating that both the early neuronal hypersensitivity and the subsequent neurodegeneration are due to abnormal kinase domain activity (Afsari et al., 2014). Vision loss was accelerated by increasing neural activity via photic stimulation of the *Drosophila* visual system using flashing LED lights. Together, these findings support an excitotoxicity theory of the *LRRK2-G2019S* form of PD. This excitotoxicity theory of PD has also found

support in rodent models of the *G2019S* mutation (Longo, Russo, Shimshek, Greggio, & Morari, 2014; Matikainen-Ankney et al., 2016; Ponzo et al., 2017; Sloan et al., 2016; Volta et al., 2017).

We have previously demonstrated that linear discriminant analysis (LDA) is a useful tool in the analysis of SSVEP data obtained from *Drosophila* (West et al., 2015). Here, our findings indicated differences in SSVEP amplitude both between and within wild type flies and EOPD mutants, in response to spatiotemporal patterns. These differences had enough statistical regularity for LDA to accurately discriminate between genotypes. When compared to wild-type controls, qualitative observations indicated an elevation in SSVEP response in 1-day old EOPD flies. Although LDA has diagnostic utility, it does not allow for the quantification of directional differences in such responses. Having established this method, we now seek to expand upon this and investigate abnormal gain control and excitotoxicity in EOPD models.

Is excitotoxicity a general feature of all *Drosophila* PD mutants? If so, it would suggest that rather than being an epiphenomenon of some metabolic dysfunction that causes PD, the excitotoxicity itself is central to the disease. In the current paper, we use SSVEP techniques combined with principal components analysis, general linear modelling, and LDA, to investigate abnormal gain control and excitotoxicity in EOPD *Drosophila* models. We hypothesised that abnormal gain control would occur in young *Drosophila* carrying EOPD mutations due to disease related changes in retinal

dopaminergic neurons, reflected by increased SSVEP amplitudes in 1-day old EOPD mutants. We also hypothesised that abnormal gain control would cause an excitotoxic cascade in older EOPD mutants. Consequently, we expect to observe a decrease in SSVEP amplitudes at later ages. Finally, we wondered if all mutations affected neuronal gain control in the exact same manner or if there were subtle mechanistic variations that could be used to differentiate the genotypes. To address this, we used a LDA based on SSVEP responses to a range of temporal modulation rates and contrast levels to classify flies into their correct genotypic class at different points throughout their lifespan. The greater the differences in the gain control profiles across genotypes, the greater the accuracy we expected from this classification.

We found that SSVEP response amplitudes to spatial stimuli are significantly increased in EOPD mutants at 1 day of age – indicating that neuronal gain control is abnormal in these animals. Generating additional neuronal stress by exposing flies to randomly pulsating light for 7 days resulted in a profound loss of vision in all PD mutants, supporting the excitotoxicity model of PD. Finally, there are robust differences between the temporal contrast response profiles of the different PD mutants which allow our multivariate classification algorithms to classify flies into their respective genotypes at well above chance levels throughout their lifespan.

3.3 Materials and Methods

3.3.1 Drosophila stocks and maintenance

Drosophila were raised in a 12hr:12hr light:dark (LD) cycle at 25°C on standard food consisting of agar (1% w/v), cornmeal (3.9%), yeast (3.7%), and sucrose (9.4%). All flies were outcrossed and stabilised where appropriate to remove any naturally occurring mutations. Three EOPD mutations (*DJ-1*$\alpha^{\Delta 72}$, *DJ-1*$\beta^{\Delta 93}$, and *PINK1*^{5}), one knockout of the fly LRRK2 homologue (*dLRRK*^{ex1}), and one wild-type control genotype (*w*^{1118}, herein *w*$^{-}$) were deployed. *w*$^{-}$ strains were gifted by Sean Sweeney. *PINK1*^{5} and *dLRRK*^{ex1} strains were obtained from the Bloomington *Drosophila* Stock Centre (Indiana, USA), whilst *DJ-1*$\alpha^{\Delta 72}$ and *DJ-1*$\beta^{\Delta 93}$ strains were kind gifts from Alex Whitworth. Male flies all had white eyes, and were tested at 1, 7, 14, 21, and 28 days post eclosion.

3.3.2 Preparation of Drosophila for Testing

Male flies were collected within 8 hours of eclosion and transferred to a new vial of standard food that additionally contained nipagin (0.1% w/v). Flies were maintained in these vials and transferred to fresh food weekly. Flies were kept in a 12hr:12hr LD cycle at 25°C until they had reached appropriate age for testing.

3.3.3 Photic stress

To explore as to whether an increase in neural demand resulted in a decrease in SSVEP amplitudes, all *Drosophila* genotypes were exposed to a photic stressor condition (Afsari et al., 2014; Hindle et al., 2013). Male flies

were collected within 8 hours of eclosion and transferred to a new vial of standard food containing nipagin. These flies were maintained within a 29°C incubator with irregularly pulsating LED lights at ~1.5s intervals to force the *Drosophila* visual system to adapt to new light levels and increase photoreceptor response. Flies were maintained here for 7 days, as this was the age at which *G2019S* mutants had previously shown visual loss (Hindle et al., 2013). Ten flies of each genotype tested (except for *DJ-1*$\alpha^{\Delta 72}$, where eight were tested) (N=48).

3.3.4 Preparation for Electroretinogram

On the day of testing, flies were collected using a pooter and aspirated into a shortened pipette. Once the fly's head was protruding from the tip of the pipette, it was restrained by placing a small layer of nail varnish on the back of the fly's neck. Two pipettes at a time were mounted onto a customised *Drosophila* electroretinogram (ERG) recording system, with both flies placed 22cm away from the dual display monitors (West et al., 2015). ERG recordings were made through hollow drawn-glass electrodes containing simple saline (130mM, NcCl, 4.7 mM KCl, 1.9mM CaCl2) connected to a high-impedance amplifier (LF356 op-amp in the circuit [Fig.7] of (Ogden, 1994)) via thin silver wires. The reference electrode was inserted gently onto the *Drosophila* proboscis, and the recording electrode was placed on the surface of the right eye. Ten unique flies of each genotype at each age were tested (N=250).

3.3.5 Stimuli

Stimuli were contrast-reversing achromatic sine wave gratings with a range of Michelson contrasts (Michelson, 1927) and temporal frequencies. Spatial frequency was held at 0.056 cycles per degree as this had previously been found to be the optimal spatial frequency to measure SSVEP recordings from *Drosophila* (West et al., 2015). Stimuli were generated using the Psychophysics Toolbox on a Windows 7 PC and were displayed on dual 144Hz LCD monitors (XL240T, BenQ, Tiwam). Stimuli swept through unique combinations of 8 levels of temporal frequency (1, 2, 4, 6, 8, 12, 18, and 36 Hz) and 8 levels of contrast (1, 4, 8, 16, 32, 64, 99%) to generate 64 different combinations of temporal contrast stimuli. Parameter combinations were presented in a random order for an 11 second trial, with a 4 second inter-stimulus interval. The first second of each trial was removed prior to analysis to remove onset transients. Each parameter combination was presented 3 times per fly to create a ~1-hour recording session.

3.3.6 Analysis

3.3.6.1 Steady state visually evoked potentials

The periodic modulation of a contrast reversing grating evokes steady-state visually evoked potentials (SSVEPs) with a phase-locked, periodic time course which is analysed most conveniently in the frequency domain (see Figure 3.1A and C for examples of SSVEP response from w^- and *PINK1*^{5} mutants). For a single contrast reversing grating, the ERG records responses from both the photoreceptors and the subsequent neuronal signalling

pathways (Afsari et al., 2014). Individual photoreceptors track the luminance modulations of the grating bars at the input frequency (*F*1), but, because the signal elicited by a grating is a population average of photoreceptors driven by different transition polarities (some dark -> light, some light -> dark) the overall photoreceptor contribution is largely self-cancelling. Residual responses at *F*1 arise from asymmetries in photoreceptor sampling of the relatively low spatial frequency grating. The majority of the signal is composed of the transient responses arising from the visual neurons which are confined to even multiples of the input frequency. Of these responses, the second harmonic is by far the largest and we restrict our analyses to 2*f* for each input frequency. A coherently averaged (phase-sensitive) Fourier amplitude was calculated for each temporal frequency and contrast combination by averaging complex frequency-domain data obtained for each condition over 3 runs (see Figure 3.1B and D for examples of Fourier amplitudes from w^{-} and *PINK1*^{5} mutants). Due to the phase-locked nature of VEPs, coherent averaging preserves the signal while phase-randomized noise sums to zero (Norcia et al., 2015). This results in a high signal to noise (SNR) ratio for SSVEP recordings.

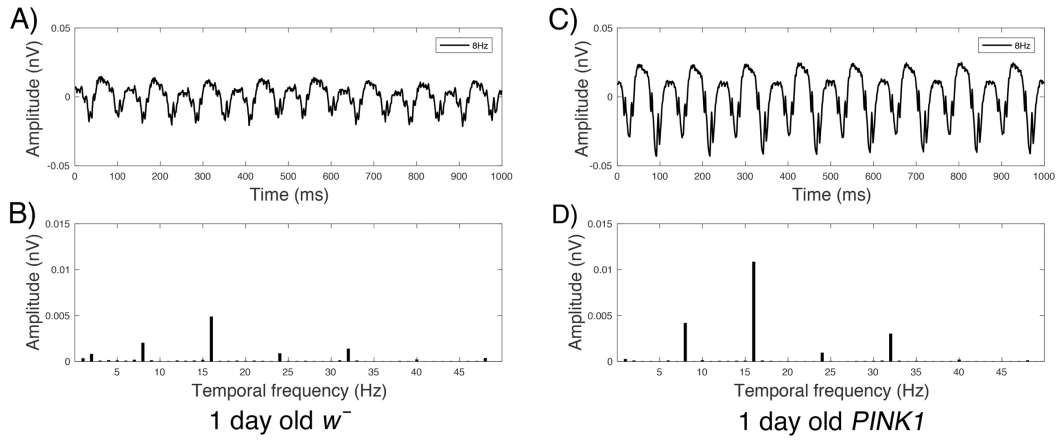

Figure 3.1 Time-domain SSVEP with a stimulus input frequency of 8Hz contains 16 'reversals' / second and can be decomposed into a SSVEP response spectrum with peaks at multiples of the input frequency. In A) we present an averaged time-domain SSVEP response from a w^- fly to 99% contrast reversing sine grating over 1000ms, modulating at 8Hz, whilst B) shows Fourier amplitudes decomposed from Fourier transform the 8Hz waveform in A, with peaks occurring at multiples of our input frequency (8Hz, 16Hz, 24Hz, 32Hz, 40Hz). The same is shown in C) and D) for a PINK15 PD-mutant fly.

3.3.6.2 Linear discriminant analysis

We assessed LDA as a tool to accurately assign flies into their correct genotype based on multivariate visual response profiles. We used ERG measurements recorded in response to 64 combinations of contrast and temporal frequency, thus, providing a 64-dimensional dataset to input into the LDA. Each fly was therefore located in a 64-dimensional space. Flies that showed similar responses to these combinations of contrast and temporal frequency clustered together in this space. Thus, if different classes showed

different visual responses, unique clusters for each class would form in this 64-dimensional space. The LDA algorithm then attempted to identify a single linear boundary between these clusters and classified each fly into its correct class by asking which side of this linear boundary the fly was situated. The accuracy of the LDA algorithm depends on the degree of separation between the genotypic clusters in the multidimensional feature space. This is further expanded upon in Figure 3.2, where we illustrate the process of raw data collection through to a range of possible classifications.

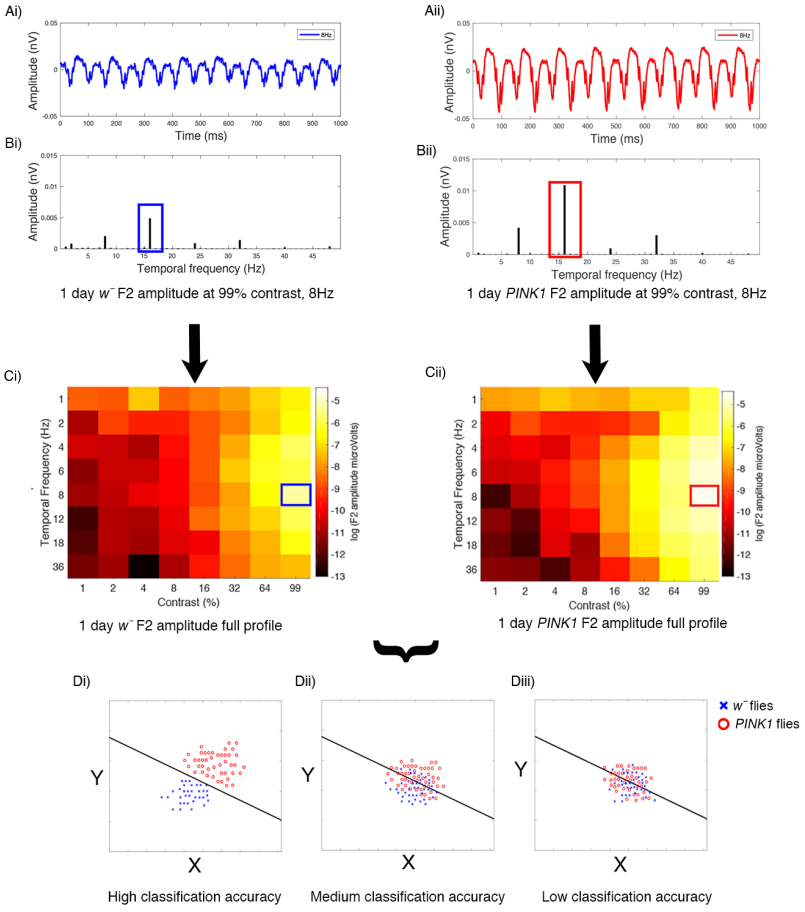

Figure 3.2 Analysis path for Linear Discriminant Analysis (LDA). The raw ERG (electroretinogram) response to 64 different stimuli is collected – here from a control (wild-type) w^- fly and an EOPD (*PINK1*^{5}) fly (A). For each stimulus, Fourier analysis is used to measure the response of the fly at the second

harmonic (2f) (B). Each fly is exposed to 64 stimuli – each with a known contrast and temporal frequency. The heat map (C) represents the amplitude of the second harmonic at each stimulus condition. In this simple case, with just 2 genotypes at one time point, the LDA is applied to the data from both genotypes, and determines the equation that best separates the data into two classes based on the 64 responses. Three outcomes could be envisaged – an optimal separation of the data. Di) a clear line separates the data, or a partial separation (Dii), or no difference (Diii), all the data are mixed). In this portrayal, the graph plots 'X' and 'Y' which will be calculated from the 64 Fourier results by the LDA algorithm. In the more complex dataset explored below, 5 genotypes and 5 ages were sampled, leading to a multi-dimensional 'cloud' of data which can still be separated by a (more complex) set of linear equations.

3.4 Results

3.4.1 Early-onset PD temporal contrast profile amplitudes are larger than controls

A series of exemplar raw SSVEP responses from both w^- and *PINK1*^{5} mutants at different ages and stimulus contrasts are illustrated in Figure 3.3. Average Fourier amplitudes at 2*f* for each temporal contrast combination for each genotype are illustrated in Figure 3.4. Higher peak response amplitudes are represented by lighter colours whilst lower amplitudes are represented by darker colours. Visual response changes as a function of both contrast and temporal frequency, with responses in both wild-type and EOPD models

peaking at high contrast (99%) and an intermediate temporal frequency (6-8Hz).

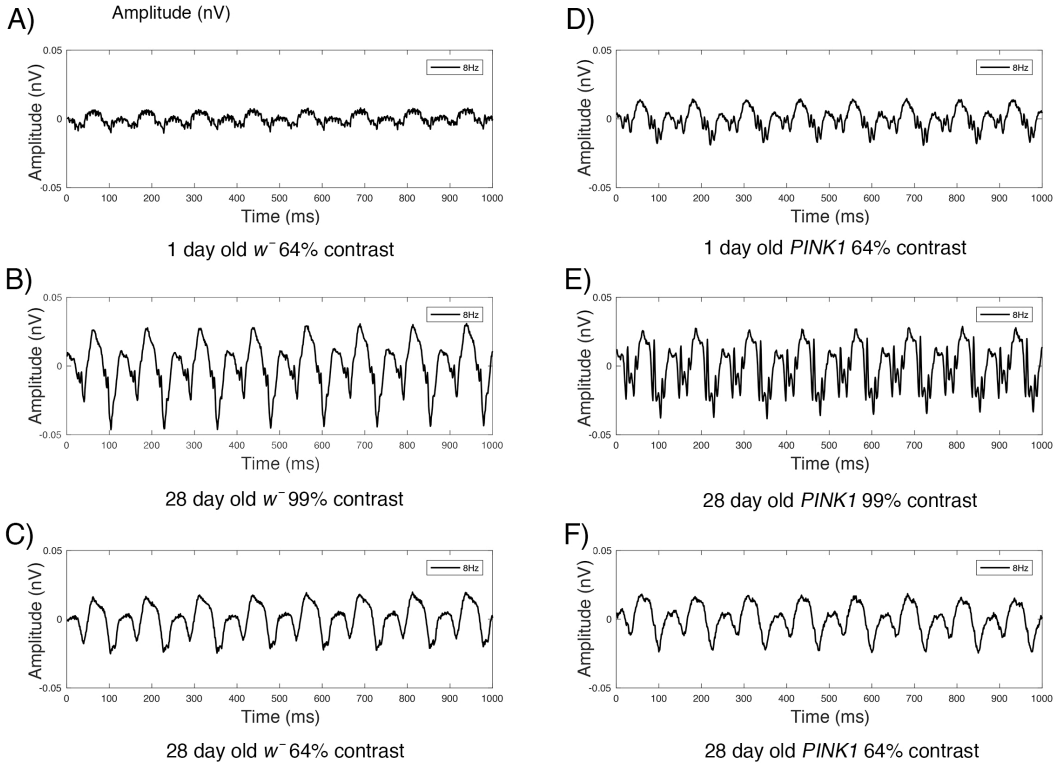

Figure 3.3 We use the ERG to obtain accurate SSVEP measurements from both wild-type and PD *Drosophila* mutants at different contrasts and ages. In A-F we present exemplar ERG responses at 8Hz obtained from $w^{-}$and *PINK1*^{5} PD mutants at 1 and 28 days of age, and at 64% and 99% contrast. SSVEP waveform peak amplitude increases with increasing contrast.

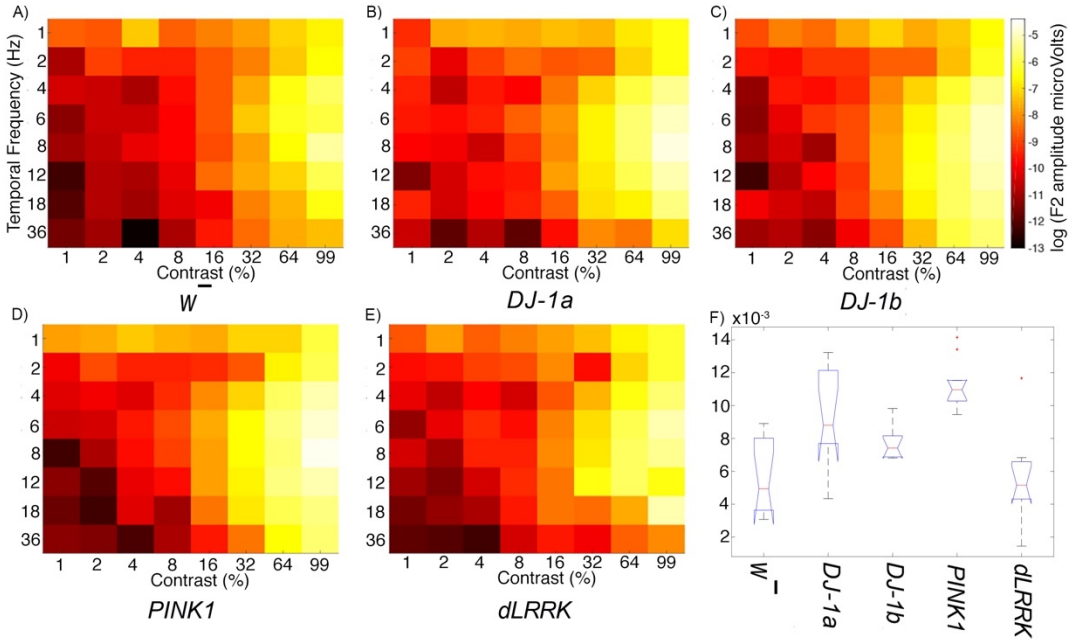

Figure 3.4 EOPD mutants show steeper response amplitudes at 1 day of age. A-E) Mean response amplitudes from all *Drosophila* genotypes (n=10 for each genotype). *Drosophila* exhibit visual tuning to temporal frequency and contrast, with peak amplitude at 6-8Hz temporal frequency and 99% contrast. Further, the maps appear to show subtle differences outside of peak regions between 12-36Hz at 1-8% contrast. Profiles indicate that EOPD mutants have larger response amplitudes at 'peak sensitivity' regions. F) Boxplot of the 2f peak response at 99% contrast and 8Hz for each genotype.

3.4.2 Principal Components Analysis

To decompose our complex, multivariate data, a single Principal Components Analysis (PCA) was computed on the full dataset (N=250) (See Figure 3.5). This allowed us to retain just those principal components (PCs) that explain significant amounts of the overall variance, simplifying our 64-dimensional data (Jolliffe & Cadima, 2016; West et al., 2015). Our first PC

explained 89.9% of total variance within the dataset and the univariate analysis that follows is based on the amplitude of this component, while the multivariate analysis later in the paper is performed on the full dataset.

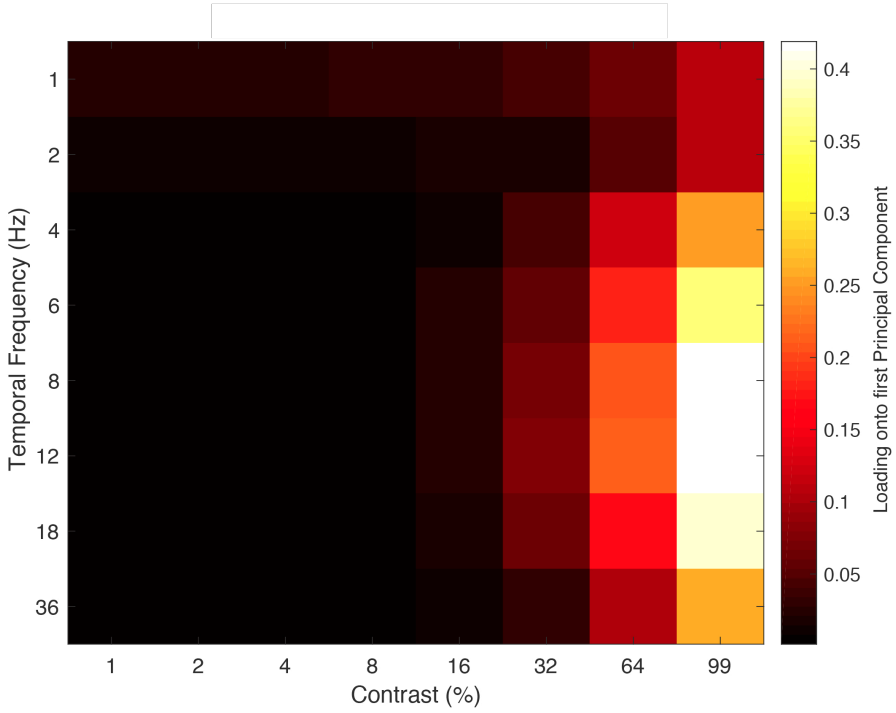

Figure 3.5 High contrast (99%) and intermediate temporal frequency combinations (6-18Hz) conditions exhibit the strongest loading onto the first principal component. The entire dataset (N=250) is run through the PCA simultaneously to ensure that it is scaled by the same eigenvalue. Brighter colours represented a higher loading onto the first PC, whilst darker colours represent a lower loading.

3.4.3 Main effects

A 5x5 between groups ANOVA was performed on the first principal component score (representing SSVEP amplitude) to assess if there was a difference in SSVEP amplitudes between *Drosophila* genotypes or ages. The

analysis found a significant main effect of genotype, $F(4,225) = 21.428$, $p < .001$, indicating a difference in response amplitude between the five genotypes, when collapsed across age. The analysis also found a significant main effect of age $F(4,225) = 5,558$, $p < .001$, indicating a difference in response amplitude between the 5 ages, when collapsed over genotype. Finally, there was a significant interaction effect $F(16,225) = 2.984$, $p < .001$, indicating that response amplitude differed between genotype depending on age. A simple effects analysis was performed to tease out differences in our conditions and explore our interaction effect.

3.4.4 Simple effects analysis comparing between genotypes within each age group

A simple effects analysis was undertaken to explore differences in the SSVEP amplitudes of *Drosophila* genotypes within each age group, with Sidak corrections applied to all possible comparisons. The SSVEP amplitudes of each genotype as a function of age are illustrated in Figure 3.6, whilst all corresponding *p* values are presented in Appendix A3 Tables A3.1 - A3.6. Analysis revealed that at 1 day of age, all EOPD mutants (i.e. excluding *dLRRK*^{ex1}) had significantly higher SSVEP amplitudes when compared to w^- control flies, ($p < .01$). When comparing between 1-day old PD mutants, *PINK1*^{5} produced significantly higher SSVEP amplitudes when compared to both *DJ-1*$\alpha^{\Delta 72}$ ($p < .05$) and *dLRRK*^{ex1} mutants ($p < .01$). There were no other significant differences in the SSVEP amplitudes of PD mutants. The larger amplitudes of EOPD mutants did not hold over later ages as wild type

response increased at 7 days of age (see Figure 3.6). However, differences between the SSVEP amplitudes of PD mutants was found at these later ages. At 7 days of age *PINK1*^{5} mutants produced significantly higher amplitudes when compared to *dLRRK*^{ex1} ($p < .005$), whilst at 14 days of age *DJ-1*$\beta^{\Delta 93}$ had significantly higher amplitudes when compared to *DJ-1*$\alpha^{\Delta 72}$ ($p < .001$) and *dLRRK*^{ex1} ($p < .001$) mutants. This trend continued at 21 days of age, with *DJ-1*$\beta^{\Delta 93}$ continuing to show higher SSVEP amplitudes when compared to *DJ-1*$\alpha^{\Delta 72}$ ($p < .01$) and *dLRRK*^{ex1} ($p < .05$). At 28 days of age, *DJ-1*$\beta^{\Delta 93}$ ($p < .01$) and *PINK1*^{5} ($p = .01$) produced significantly higher SSVEP amplitudes when compared to *DJ-1*$\alpha^{\Delta 72}$.

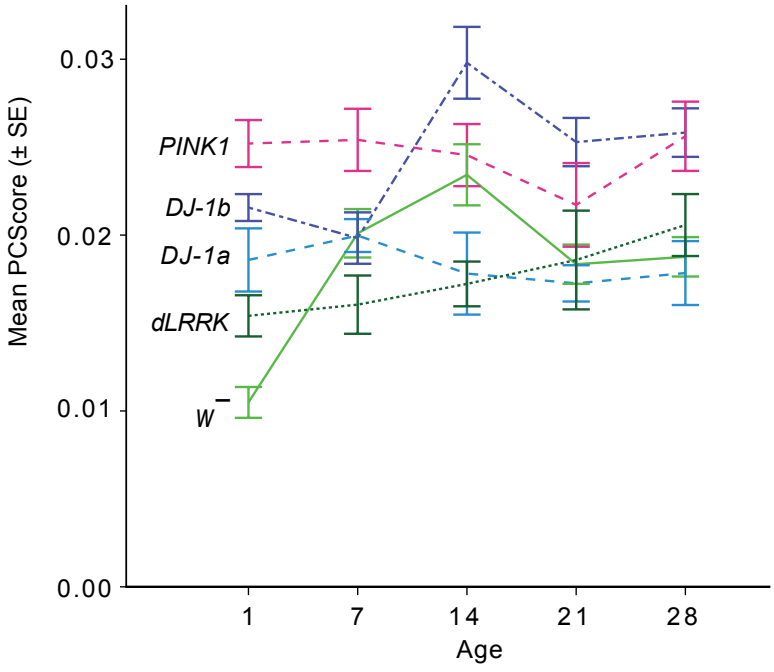

Figure 3.6 One day old EOPD flies show increased SSVEP response amplitudes when compared to control flies (w^{-}). Mean PC Score (representing response amplitude) as a function of age for five *Drosophila* genotypes (n=10 for each genotype/age group). Error bars show ±1SE.

3.4.5 Simple effects analysis comparing between age group within each genotype

A simple main effects analysis was undertaken to explore differences in the SSVEP amplitudes within each *Drosophila* genotype over its lifespan, with Sidak corrections applied to all possible comparisons. The *p* values for all simple effects are presented in Appendix A3 Tables A3.5 - A3.10. Analysis revealed that w^- response amplitudes increased between 1 and 7 days of age ($p = .001$), however there was no significant difference when comparing between further consecutive ages within this genotype, thus, visual response held stable between 7 to 28 days of age. There was a significant increase in *DJ-1*$\beta^{\Delta 93}$ response amplitudes between 7 and 14 days of age ($p < .001$), which then held steady from 14 to 28 days of age. There was no significant difference in response amplitudes within *DJ-1*$\alpha^{\Delta 72}$, *PINK1*^{5} or *dLRRK*^{ex1} at any consecutive ages between 1 and 28 days.

3.4.6 Increased demand for energy in the visual system leads to loss of visual response in old PD flies

While we demonstrated that abnormal gain control occurs in 1-day old EOPD mutants, at later ages, responses were comparable to those of wild-type flies (w^-). This represents a difference between EOPD mutant flies and flies mimicking the late-onset LRRK2-*G2019S* mutation, where responses fall to zero at later ages (Hindle et al., 2013). We hypothesized that maintaining our *Drosophila* stocks at 25°C and a 12:12 LD cycle did not produce enough neuronal demand on the visual system to see any effect. To test this

hypothesis, we increase the demand for energy by exposing *Drosophila* to irregular ~1.5s flashes of light of at random periodic intervals over seven days. Here, we hypothesise that the abnormal gain we have observed in young EOPD flies will interact with a visually induced increase in neural demand to cause an excitotoxic cascade.

Observation of temporal contrast response profiles (see Figure 3.7) indicated a profound reduction in SSVEP amplitudes across temporal frequency and contrast combinations for PD mutants (but not wild-type flies) after seven days exposure to photic stress.

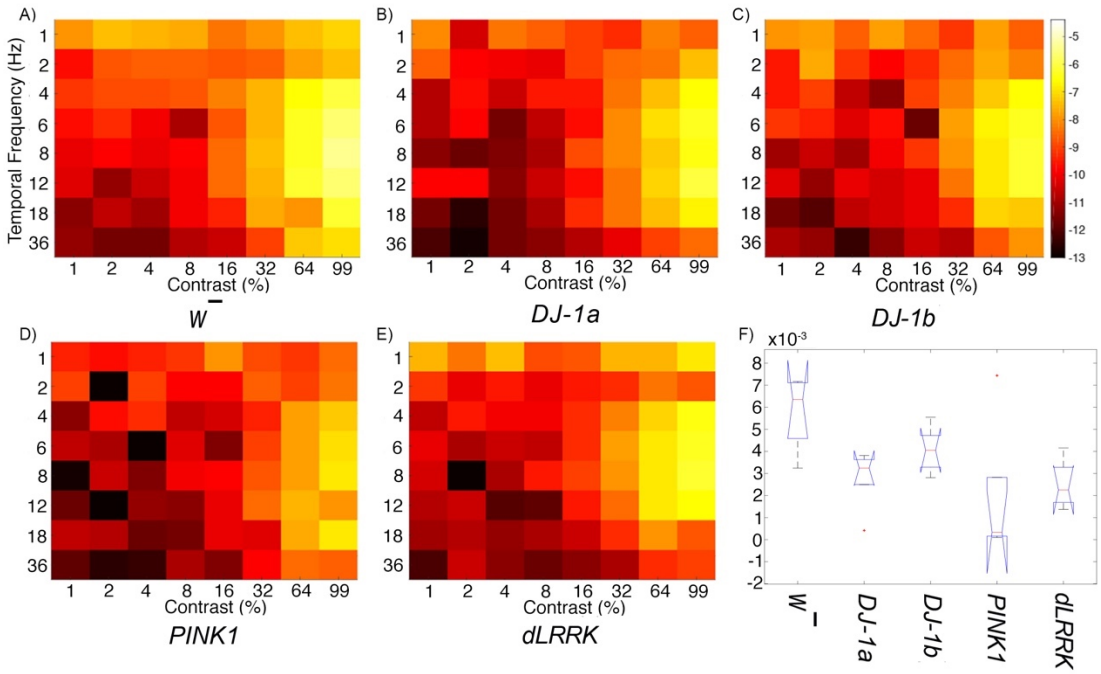

Figure 3.7 All EOPD mutants show perturbations in response amplitudes after exposure to pulsating light, indicating a decrease in temporal contrast sensitivity (n=10 per genotype). A-E) Mean response amplitudes from all *Drosophila* genotypes after 7 days of visual stimulation (each genotype n=10,

except *DJ-1α*$^{\Delta 72}$ n=8). Same scale as Figure 3.3. F) Boxplot of the 2*f* peak response at 99% contrast and 8Hz.

A one way between groups ANOVA was performed on the first principal component score (representing SSVEP amplitude) extracted via the PCA analysis to assess if there was a significant difference in visual response between five *Drosophila* genotypes after they had been exposed to seven days of photic stress. The analysis found a significant main effect of genotype, $F(1,43) = 5.965$, $p = .001$, $\eta^2 = .357$, indicating a difference in response amplitude between the five genotypes. Pairwise comparisons revealed that all PD mutants produced significantly lower SSVEP amplitudes when compared to w^- control flies ($p < .05$), indicating an interaction between visual stimulation and *Drosophila* genotype on visual response amplitudes (see Figure 3.8). There was no significant difference between the PD mutants' SSVEP responses.

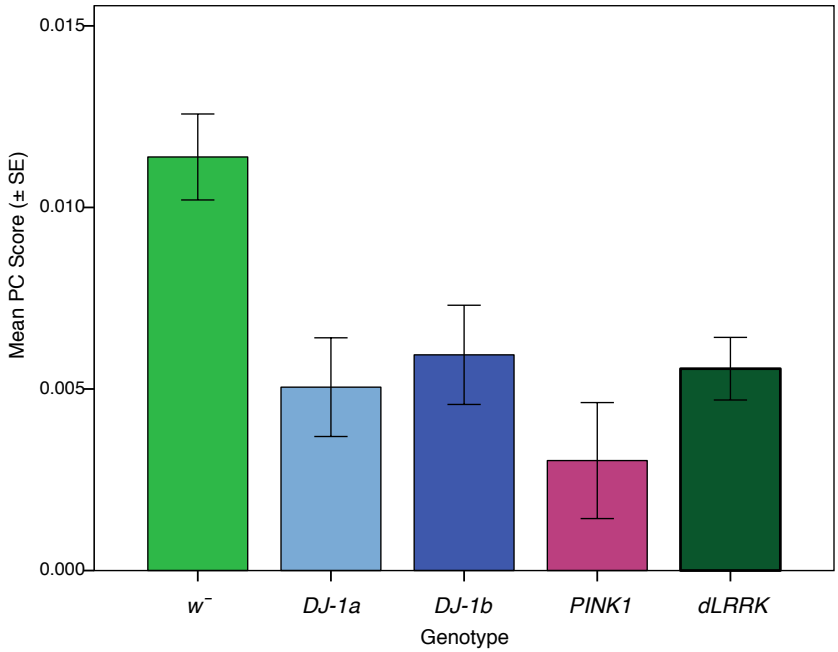

Figure 3.8 Visual loss occurs in all PD mutants after 7 days of exposure to pulsating light. Mean PC Score of 5 *Drosophila* genotypes after 7 days exposure (each genotype n=10, except *DJ-1*$\alpha^{\Delta 72}$ n=8).

3.4.7 Linear discriminant analysis classifies flies into their correct genotypic class

Thus, all EOPD mutants show both an early increased visual response and a loss of vision after 7 days of visual stimulation, compared to w^- control flies. In the presentation of our data so far, we utilized PCA to reduce the dimensionality in our data to a single variable, thereby removing any nuanced differences between full *Drosophila* temporal contrast profiles. We now explore how linear discriminant analysis can use the additional small, but significant sources of variation in our SSVEP data to classify *Drosophila* into their correct genotypic class and age group.

Linear discriminant analysis (LDA) classification is a statistical method that aims to answer both binary and multi-class classification problems. It seeks linear combinations of variables that best explain the variance within the data, working under the assumption that unique classes generate unique Gaussian distributions (Izenman, 2008). We assess the accuracy of our LDA in two ways. First, we use a standard linear classifier as implemented in MATLAB's (2017a, Mathworks, MA) 'classify' function to conduct a leave-one-out (LOO) analysis, where the classifier receives training data from all flies to be assessed except one, then we measure the classifiers accuracy in classifying the excluded fly (Fisher, 1936). This fly is resubstituted, and the classification is repeated for every fly in the dataset to return a generalized LOO accuracy. Second, we use MATLAB's classification function 'fitcdiscr' to fit an LDA model to our raw 64-dimensional data. We then use Monte Carlo resampling methods to produce 3 estimates of accuracy – an overall model accuracy, an N-way classification accuracy (the accuracy of correctly classifying a fly into one of the 5 genotypes at each age group or 5 age groups for each genotype) and a pair-wise classification accuracy (the accuracy of correctly classifying a fly into one of two correct genotypes at each age group). See *Chapter 2 Section 2.3.1 Linear discriminant analysis* for more information on this technique.

Here, we hypothesise that *Drosophila* will be classified into their correct genotypic class at above-chance levels based on temporal contrast profiles, in line with previous findings using spatiotemporal profiles (West et al., 2015).

3.4.8 Overall Model Discrimination Accuracy

We first ran our full dataset of 25 classes through the LDA to assess how well it could classify *Drosophila* when considering both their genotype and age. In this case, baseline (chance) performance was 4% (1/25). Next, to assess how well we could discriminate between *Drosophila* genotypes within each age group, our data were partitioned into 5 genotypes and LDA was applied with a 20% chance baseline (1/5). Finally, to assess how well we could classify between *Drosophila* at different ages within each genotype, our data were divided into 5 age groups within each genotype and analysed using LDA, again with a 20% chance baseline (1/5).

The full overall classification accuracies for both LOO analysis and Monte Carlo resampling analysis for all 3 sets of data are presented in Table 3.1. The overall accuracy of our model in classifying *Drosophila* into their correct genotypic class differed depending on the age of the genotypes included in the model. The highest classifications occurred at 1 and 28 days of age. Although there was a slight decrease in accuracies when classifying *Drosophila* into their correct age within a genotype, the algorithm still performed above 20% chance baseline for all genotypes.

Table 3.1 Classification accuracy differs when flies are grouped by age and classified into genotype, and when they are grouped by genotype and classified into age. Generally, both LOO and Monte Carlo resampling methods provide similar classification accuracies. N=50 for per class (chance baseline 20%), except 'All 25 classes' N=250 (chance baseline 4%).

Class	LOO Classification	Monte Carlo Resampling
All 25 classes	24.8%	29.6%
1 day post eclosion	58%	68%
7 days post eclosion	52%	64%
14 days post eclosion	46%	54%
21 days post eclosion	48%	50%
28 days post eclosion	64%	70%
w^-	54%	54%
DJ-1$\alpha^{\Delta 72}$	38%	38%
DJ-1$\beta^{\Delta 93}$	52%	52%
PINK1^5	34%	50%
dLRRK^{ex1}	26%	34%

3.4.9 N-Way Classification Accuracy

The confusion matrix was used to establish the accuracy of our LDA model to classify *Drosophila* into their correct genotypic class. Again, we investigated the precision of our model when all 25 classes were included in the model, with a 4% chance baseline (1/25). All classifications were reported above chance, bar *PINK1*^{5} at 21 days of age. The highest accuracy was for

w^- at 1 day of age, where the model performed with 34.49% accuracy, whilst most other conditions were classified with ~25% accuracy. A profile of classification accuracies when all 25 classes are considered is presented in Figure 3.9.

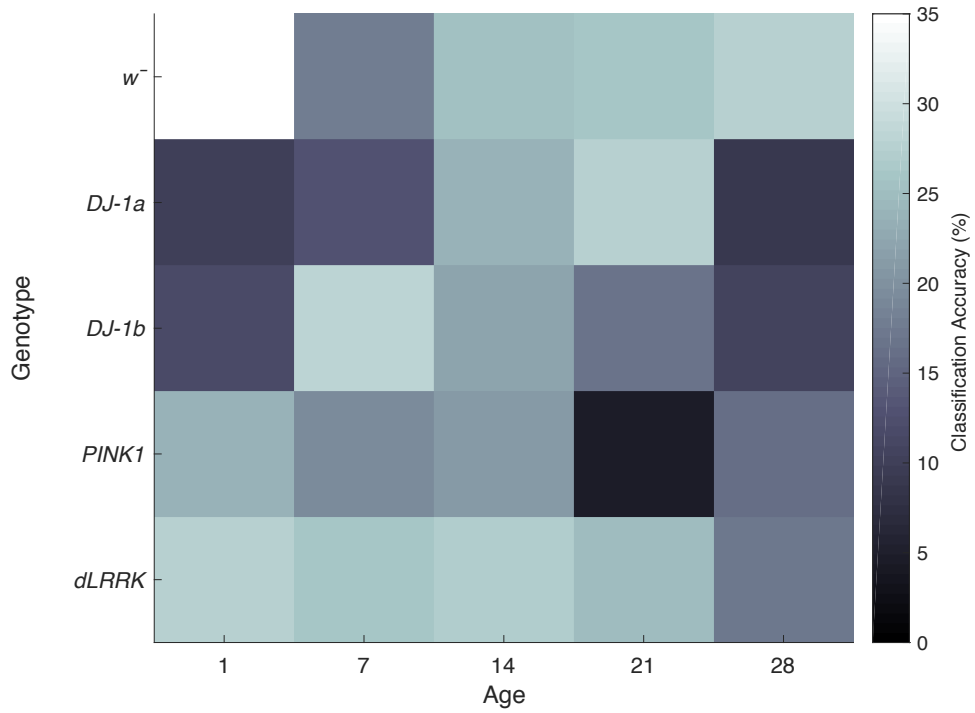

Figure 3.9 LDA can accurately discriminate between all 25 classes when they are included in the model. All classifications sit above 4% chance baseline, except for *PINK1*^{5} at 21 days of age.

Next, we assessed the ability of the classifier to accurately genotype *Drosophila* within each age group, thus, five genotypes at each age were included in the model, with a 20% chance baseline (1/5). Our classification accuracy is deduced by normalizing our confusion matrix by dividing by the number of flies in each condition (n=10). As illustrated in Figure 3.10, at 1 day of age our model could classify w^- control flies into their correct genotypic class

with 78.8% accuracy, whilst we could classify *DJ-1α*$^{\Delta 72}$ at 45.5% accuracy, *DJ-1β*$^{\Delta 93}$ at 52.9% accuracy, *PINK1*^{5} at 73.6% accuracy and *dLRRK*^{ex1} at 60.0% accuracy.

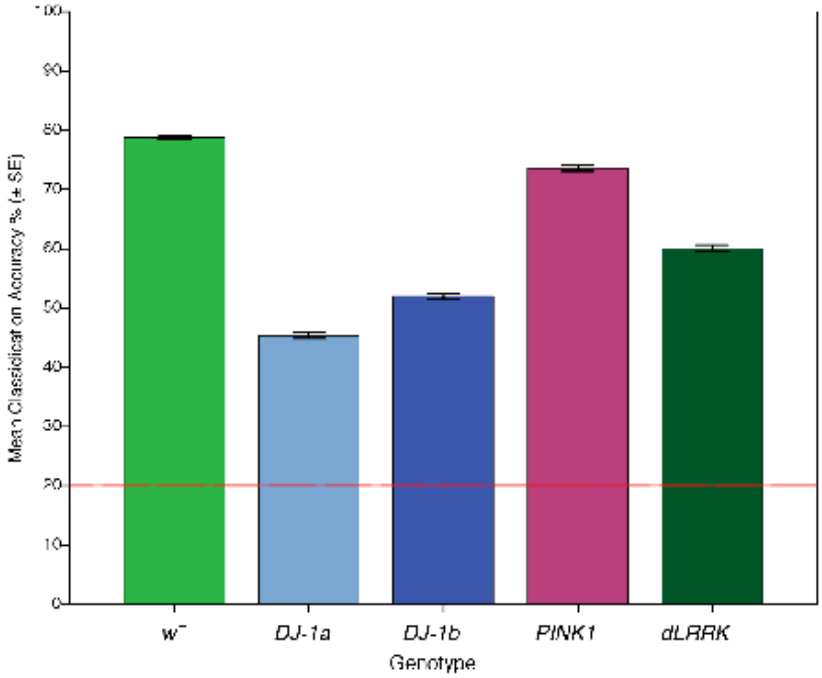

Figure 3.10 Classification of young flies by genotypic class using data from temporal contrast response profiles. Mean classification accuracies for N-way LDA of 5 genotypes at 1 day of age (n=10 per genotype). The chance baseline is set at 20%, with mean classification accuracies between 45.5% and 78.8%.

These accuracies shifted at seven days of age, with our model classifying *w*$^{-}$ with 29.8% accuracy, *DJ-1α*$^{\Delta 72}$ with 50.0% accuracy, *DJ-1β*$^{\Delta 93}$ with 64.7% accuracy, *PINK1*^{5} with 62.2% accuracy and *dLRRK*^{ex1} at 46.9% accuracy. At 14 days of age our model could accuracy classify *w*$^{-}$ at 50.0% accuracy, *DJ-1α*$^{\Delta 72}$ at 68.1% accuracy, *DJ-1β*$^{\Delta 93}$ at 50.3% accuracy, *PINK1*^{5}

at 36.4% accuracy and *dLRRK*^{ex1} at 29.1% accuracy. At 21 days of age with our model classified *w*$^{-}$ at 58.35% accuracy, *DJ-1*$\alpha^{\Delta 72}$ at 50.5% accuracy, DJ-1$\beta\Delta$93 at 50.2% accuracy, *PINK1*^{5} at 25.7% accuracy and *dLRRK*^{ex1} 53.8% accuracy. At 28 days of age our model classified *w*$^{-}$ with 53.7% accuracy, *DJ-1*$\alpha^{\Delta 72}$ with 71.5% accuracy, *DJ-1*$\beta^{\Delta 93}$ with 62.6% accuracy, *PINK1*^{5} with 55.1% accuracy and *dLRRK*^{ex1} at 46.35% accuracy.

3.4.10 N-Way Classification Accuracy: Age

Here, our LDA model was used to classify *Drosophila* mutants into their correct age within a single genotype, with a 20% chance baseline (1/5). Comparatively, the model was weaker in accurately classifying into age when compared to classifying into genotype, although all classifications exceeded chance baseline. Age N-Way classification accuracies for each genotype are presented in Table 3.2.

Table 3.2 N-Way classification of flies into their correct age differs between genotypes. All classes can be classified above 20% chance baseline, with the highest accuracy sitting at 81.3% for 1-day old w^{-} classifications (n=10).

	1 day	7 days	14 days	21 days	28 days
w^{-}	81.3%	29.5%	32%	53.5%	53.5%
DJ-1$\alpha^{\Delta 72}$	26.6%	34.1%	50.0%	29.7%	48.4%
DJ-1$\beta^{\Delta 93}$	55.3%	59.5%	51.0%	45.0%	57.3%
PINK1^{5}	39.7%	49.1%	35.0%	27.2%	49.3%

dLRRK^{ex1}	37.6%	23.7%	22.7%	30.2%	43.7%

Chance baseline: 20% (1/5)

3.4.11 Pairwise Classification Accuracy

To assess the accuracy of our model in classifying *Drosophila* between pairs of genotypes within each age group we bootstrapped our data through 1000 iterations of a two-way classification analysis. Here, we assess the accuracy of the algorithm estimation in classifying a fly from a pair of genotypes into its correct class. Classification is significantly above chance when fewer than 5% of the bootstrapped 2-way classification probabilities are .5 or greater.

As presented in Table 3.3, the algorithm classified one-day old *Drosophila* genotypes with accuracy between 73.7% - 94.1% ($p < .05$). Notably, all PD mutants could be accurately distinguished from w^-control flies.

Table 3.3 LDA can accurately compute pairwise classifications between PD and control genotypes at 1 day of age (n=10).

	w^-	*DJ-1*$\beta^{\Delta 93}$	*DJ-1*$\alpha^{\Delta 72}$	*dLRRK*^{ex1}
PINK1^5	94.1%*	84.7%*	78.8%*	88.9%*
w^-	-	86.3%*	75.8%*	77.6%*
DJ-1$\beta^{\Delta 93}$	-	-	57.9%	73.7%*
DJ-1$\alpha^{\Delta 72}$	-	-	-	65.3%

* = $p < .05$

As presented in Table 3.4, at 7 days of age the model had a reduction in the amount of significant comparisons, performing between 74.5% - 85.6% accuracy. At this age, the LDA could not accurately discriminate between any of the PD mutants and control flies.

Table 3.4 LDA had a reduction in total significant comparisons at 7 days of age, and cannot accurately discriminate between any of the PD mutants when compared against control flies (n=10).

	w^-	*DJ-1*$\beta^{\Delta 93}$	*DJ-1*$\alpha^{\Delta 72}$	*dLRRK*^{ex1}
PINK1^5	69.9%	74.7%*	76.1%*	85.6%*
w^-	-	60.8%	60.5%	63.3%
DJ-1$\beta^{\Delta 93}$	-	-	67.7%	76.3%*
DJ-1$\alpha^{\Delta 72}$	-	-	-	66.9%

* = $p < .05$

At 14 days of age there appeared to be an overall improvement in pairwise classifications with significant pairwise classifications between 78.0% - 81.3% accuracy, as illustrated in Table 3.5.

Table 3.5 LDA can accurately compute pairwise classifications between PD and control genotypes at 14 days of age (n=10). There are differences in accuracy when compared to 7- and 1-day old classifications.

	w^-	*DJ-1*$\beta^{\Delta 93}$	*DJ-1*$\alpha^{\Delta 72}$	*dLRRK*^{ex1}
PINK1^5	61.7%	57.8%	78.6%*	79.2%*
w^-	-	78.4%*	78.0%*	79.9%*
DJ-1$\beta^{\Delta 93}$	-	-	89.6%*	91.3%*
DJ-1$\alpha^{\Delta 72}$	-	-	-	52.1%

* = $p < .05$

This held at 21 days of age, where our pairwise classification accuracy reached between 75.2% - 85.1% for significant comparisons, as illustrated in Table 3.6, however there was a reduction in significant comparisons at this age.

Table 3.6 LDA can accurately compute pairwise classifications between PD and control genotypes at 21 day of age (n=10), however there are fewer significant comparisons compared to earlier ages.

	w^-	*DJ-1*$\beta^{\Delta 93}$	*DJ-1*$\alpha^{\Delta 72}$	*dLRRK*^{ex1}
PINK1^5	63.3%	65.2%	75.2%*	52.9%
w^-	-	78.4%*	77.4%*	69.4%
DJ-1$\beta^{\Delta 93}$	-	-	85.1%*	77.7%*

DJ-1$\alpha^{\Delta 72}$	-	-	-	60.6%

* = $p < .05$

In line with our peak in overall model accuracy, our model was most accurate in classifying between flies at 28 days of age, with all possible comparisons statistically significant and sitting between 72.7% and 86.2% accuracy (Table 3.7). Similar to one day old comparisons, all PD mutants could be accurately distinguished from w^- control flies at 28 days of age. We note that these statistics differ from the comparisons on the PCA simple effects analysis data, as will be addressed in our discussion.

Table 3.7 LDA accurately computes pairwise classifications between all genotypes at 28 days of age (n=10). All comparisons are significant and above 72.7% accuracy.

	w^-	*DJ-1*$\beta^{\Delta 93}$	*DJ-1*$\alpha^{\Delta 72}$	*dLRRK*^{ex1}
PINK1^5	78.9%*	78.7%*	79.7%*	73.7%*
w^-	-	86.2%*	81.0%*	75.6%*
DJ-1$\beta^{\Delta 93}$	-	-	88.4%*	83.6%*
DJ-1$\alpha^{\Delta 72}$	-	-	-	72.7%*

* = $p < .05$

3.5 Discussion

3.5.1 Abnormal gain control in early-onset PD Drosophila models

We have demonstrated that abnormal gain control occurs in young EOPD mutants; *DJ-1*$\alpha^{\Delta 72}$, *DJ-1*$\beta^{\Delta 93}$, and *PINK1*^{5}. *Drosophila* with these

mutations have significantly higher SSVEP response amplitudes when compared to w^- controls at day 1. Notably, there appears to be no difference between response amplitudes of 1-day old w^- controls and knockout of the fly LRRK2 homologue *dLRRK*^{ex1}. These results are consistent with previous studies, and point to a common phenotype of abnormal gain control occurring at a young age in the current studied EOPD mutants and the *LRRK2-G2019S* late-onset mutant (Afsari et al., 2014; West et al., 2015).

What common biological mechanism might explain these findings? Dopaminergic terminals are found in the *Drosophila* ommatidium, lamina, and medulla, where dopamine is thought to regulate contrast sensitivity, light adaptation, and circadian rhythms (Afsari et al., 2014; Chyb et al., 1999; Hirsh et al., 2010; Jackson et al., 2012; Nassel & Elekes, 1992). Thus, dopamine acts as a neuromodulator within the *Drosophila* visual system, effectively regulating neural response to visual excitation. PD-model flies may have less dopamine content, and/or fewer dopaminergic neurons, or disrupted dopamine signalling, though the reduction may depend on the environmental conditions (Navarro et al., 2014; Ng et al., 2012; Park et al., 2006; Wang et al., 2006). Any reduction in dopamine release will cause photoreceptors to respond faster and with greater amplitude (Chyb et al., 1999). This hyperactivity causes increased SSVEP amplitudes, manifesting as abnormal gain control. Humans, like flies, have retinal dopamine within the amacrine cells and inner border of the nuclear layer, where it is thought to be responsible for light adaptation, contour perception, and contrast sensitivity (Crooks &

Kolb, 1992; Dowling, 1979; Witkovsky, 2004). Human patients also show a reduction in retinal dopamine and report a range of low-level visual deficits, including poor contrast sensitivity and reduced light sensitivity (Archibald, Clarke, Mosimann, & Burn, 2011; Beitz, 2014; Chaudhuri & Schapira, 2009; Weil et al., 2016). These homologies in retinal structure, function, and disease pathology point to the possibility that prodromal gain control abnormalities occur in human PD patients.

The response profile of wild-type w^- *Drosophila* changes as a function of age. This genotype initially presented with comparatively low response amplitudes when compared to EOPD mutants. w^- response then increased between 1 and 7 days of age. This reflects the anatomical plasticity of the young *Drosophila* visual system. Young w^- flies are born with reduced visual sensitivity which then adapts to functional requirements, with visual maturity occurring between 4 - 7 days of age (Kral & Meinertzhagen, 1989). It is important to note that all *Drosophila* included in our study are white eyed, thus share the w^- mutation. The increased sensitivity to visual stimuli we have found in EOPD mutants, and mutants' unique developmental profiles, is due solely to the PD mutation.

3.5.2 Excitotoxicity as a pathological phenotype in Parkinson's disease

Initially, we saw no evidence of excitotoxic damage in the visual system of older PD flies. However, *Drosophila* in the lab experience a relatively stable visual environment: light levels are many orders of magnitude lower than those

in the outside world and they are modulated according to a strict 12hr:12hr LD cycle. We theorised that purposeful visual stimulation of the PD *Drosophila* visual system may be necessary to induce excitotoxicity in the lab. To increase neural demand for energy we exposed flies to a rich visual environment which contained irregular bursts of high intensity luminance modulations. This environment requires the photoreceptors both to change their firing rates and their mean sensitivity over relatively short time periods. Our hypothesis was that the abnormal gain control we observed in young EOPD flies would interact with an increase in neural activity to cause an excitotoxic cascade. Our data are consistent with this hypothesis – EOPD, but not w^{-} flies, showed reduced visual functionality after prolonged exposure to these visually demanding environments.

Our results provide evidence for an excitotoxic cascade in PD *Drosophila* mutants, with *DJ-1*$\alpha^{\Delta 72}$, *DJ-1*$\beta^{\Delta 93}$, and *PINK1*^{5} all showing a significant decrease in SSVEP amplitudes after seven days of visual stimulation, with a minimum of 50% reduction in response. Surprisingly, the response amplitudes of *dLRRK*^{ex1} mutants were also reduced, even though we did not observe abnormal gain control in this strain at one day of age.

We draw upon the previously established theory of excitotoxicity in PD to explain the biological processes underlying our observed visual loss. Here, abnormal gain control interacts with a visually induced increase in neural demand. This causes an increase in ionic flux across the cell membrane which

in turn results in extra demand for ATP from the ion exchange pumps. When mitochondria cannot meet this increased demand for ATP, they release reactive oxygen species (e.g. superoxide, hydrogen peroxide), so generating oxidative stress, which leads to autophagy, apoptosis and other forms of cell damage. This is then followed visual decline and eventual cell death (Hindle et al., 2013).

Mitochondrial dysfunction and oxidative stress appear to play a central role in PD pathogenesis (Bogaerts et al., 2008; Büeler, 2009; Henchcliffe & Beal, 2008; Schapira, 2008). The current experiment has investigated *Drosophila* PD mutations in genes whose human homologues are associated with EOPD. In both humans and flies, *DJ-1* encodes a small protein that is thought to protect against oxidative stress and assist in mitochondrial regulation by acting as a sensor for reactive oxidative species (ROS) (Oswald et al., 2016). Subsequently, loss-of-function mutations in *DJ-1* appear to increase cell death in response to oxidative stress. Further, animal studies have observed perturbations in dopamine release in *DJ-1* deficient animal models, although there is no physiological loss of dopamine neurons (Goldberg et al., 2005; Martella et al., 2011; Menzies, Yenisetti, & Min, 2005; Meulener et al., 2005; Pisani et al., 2006; Yang, Chen, Ding, Zhuang, & Kang, 2007). *PINK1* is a protein kinase with a mitochondrial targeting sequence and acts to maintain mitochondrial homeostasis in dopaminergic neurons (Park et al., 2006). Likewise, studies in *PINK1* animal models have found evidence for abnormal mitochondrial morphology and impaired dopamine release (Clark et

al., 2006; Kitada et al., 2007; Park et al., 2006). Thus, the protein products of both *DJ-1* and *PINK1* both play roles in the regulation of cellular energy production. However, loss-of-function mutations on these genes negatively impact mitochondria in different ways. Our data provide additional support for the hypothesis that mitochondrial impairment plays a role in the pathogenesis of genetic PD.

3.5.3 Classification of Drosophila PD genotype

Previously, we demonstrated that discriminant analysis is a useful tool that can accurately classify PD *Drosophila* into their correct genotypic class at 1 day of age (West et al., 2015). We have now built upon this, establishing that variability within temporal contrast response profiles obtained from *Drosophila* can be included in an LDA to accurately classify *Drosophila* into their correct genotypic class at various ages with above chance accuracy. When all 25 classes were included in our model, our LOO classification accuracy sat at 24.8%, whilst our bootstrapped classification accuracy was 29.6% (chance baseline of 4%). The LDA model also performed well when classifying between five genotypes within a single age group. Highest classifications occurred at day 1 (Monte Carlo sampling accuracy of 68% and LLO accuracy of 58%) and 28 days of age (Monte Carlo sampling accuracy of 70% and LOO accuracy of 64%), with a baseline of 20%. This indicates that there are substantial differences between *Drosophila* genotypes at both one and 28 days of age.

When all 25 classes were included in our model, all classifications (except *PINK1*^{5}) perform above a 4% chance baseline, with most classifications occurring with ~25% accuracy. There is substantial variation between EOPD *Drosophila* visual response throughout their lifespan, indicating that EOPD mutations have unique effects on *Drosophila* visual pathways throughout their lifespan. After our data were partitioned into five genotypes for each age group, we could classify *Drosophila* into their correct genotypic class with 29.8% - 78.8% accuracy over all possible age groups, with no classifications falling under the statistical chance baseline of 20%. Our results illustrate that mutants can be accurately classified into their correct genotypic class beyond one day of age, indicating there are subtle differences in how EOPD mutations affect *Drosophila* neural gain control, as will be discussed.

Although the N-Way classification accuracy decreased when the algorithm was required to classify *Drosophila* into their correct age within a single genotype, our model still performed above chance baseline. This is surprising considering the results of our first experiment, where, for the most part, within genotype responses did not significantly differ over time. Our analysis was run on a reduced number of genotypes and flies n=10 and five genotypes, rather than n=20 and 10 genotypes as per West et al. (2015), yet our model produced a consistently high classification accuracy, even when all 25 classes were included in the model. In West et al., (2015), we varied temporal and spatial frequency but kept contrast fixed. We observed relatively

little dependence on spatial frequency up to a hard cut-off that was associated with spatial sampling limits. Our use of contrast rather than spatial frequency in the experiments described here allows us to measure the full contrast sensitivity profile of each genotype and age, increasing the sensitivity of our assay to establish multivariate visual biomarkers in PD *Drosophila*. Further, our assay, when combined with LDA, is sensitive enough to detect small differences in the effect of EOPD mutations on *Drosophila* neural gain control. Our initial analysis found a substantial difference between w^- and EOPD mutants at 1 day of age, however our LDA results indicate that these mutations have their own subtle effects on neural gain control across *Drosophila* lifespan. Our findings carry an important implication. As noted, *DJ-1* acts as a ROS sensor, whilst *PINK1* acts to maintain mitochondrial homeostasis in dopaminergic neurons (Lavara-Culebras, Muñoz-Soriano, Gómez-Pastor, Matallana, & Paricio, 2010; Oswald et al., 2016; Park et al., 2006). The ability of our LDA to accurately distinguish between mutations on these genes indicates each mutation uniquely impacts the underlying cellular processes thereby causing a subtle, dissimilar neural responses across *Drosophila* lifespan, that then results in a common pathogenic outcome of visual loss and cell death.

A key benefit of using *Drosophila* as disease model is their convenience for early-stage drug testing due to their fecundity and fast generation time. It is advantageous to have phenotypic expression of PD mutations at early stages of *Drosophila* lifespan as this supports their utility as an initial model for

the rapid testing of neuroactive drugs that have the potential to treat human disease. Like *Drosophila*, perturbations in contrast sensitivity occur in human PD patients due to reduced retinal dopamine (Harnois & Di Paolo, 1990). Our current findings may correspond to the changes seen in human PD patients, although there is obvious difficulty in assessing whether a prodromal abnormal gain control occurs in the early stages of pre-genotyped PD patients. We believe that it may be possible for LDA to classify human PD patients genotype based on multivariate SSVEP response profiles as measured by electroencephalogram (EEG). This would have the potential to assist in early PD diagnosis, genotypic classification, and disease expression. Our next step is to investigate *Drosophila* response to additional low-level visual parameters such as chromatic contrast and orientation to deduce whether a similar biomarker can be established in human PD patients.

3.6 Conclusion

Together, our experiments have uncovered abnormal gain control and an excitotoxic cascade as a common pathological phenotype in three EOPD mutations, *DJ-1*$\alpha^{\Delta 72}$, *DJ-1*$\beta^{\Delta 93}$, and *PINK1*^{5}. In addition to furthering the link between abnormal gain control and excitotoxicity in genetic forms of PD, our findings have further built upon the utility of LDA in genotyping *Drosophila* based on multivariate response profiles. Further, we have illustrated that there are variations in how these EOPD mutations affect neural gain control across *Drosophila* lifespan, indicating that these mutations have unique effects upon underlying cellular processes that lead to a common outcome – visual loss

and cell death. Overall, it appears that these PD related mutations are heterochronic: in young flies, mutations lead to stronger neural signalling (increased sensory response may be beneficial in escaping behaviour) but are detrimental in older flies (a loss of vision would hinder escape behaviour). Should these findings in fly models prove applicable to the human situation, it would suggest that prodromal PD may be linked to changes in central nervous system processing that could, potentially, confer advantages in early life at the cost of degenerative disease in old age (Himmelberg, West, Wade, & Elliott, 2017).

3.7 Appendix A3

Table A3.1 Simple Effects Analysis: p-values at 1 day of age.

	w^-	*DJ-1*$\beta^{\Delta 93}$	*DJ-1*$\alpha^{\Delta 72}$	*dLRRK*^{ex1}
*PINK1*5	$p <$. 001*	p = .724	p = .048*	$p <$ .001*
w^-	-	$p <$ .001*	p = .006*	p = .302
DJ-1$\beta^{\Delta 93}$	-	-	p = .892	p = .083
DJ-1$\alpha^{\Delta 72}$	-	-	-	p = .852

Table A3.2 Simple Effects Analysis: p-values at 7 days of age.

	w^-	*DJ-1*$\beta^{\Delta 93}$	*DJ-1*$\alpha^{\Delta 72}$	*dLRRK*^{ex1}
*PINK1*5	p = .208	p = .158	p = .185	p = .004*
w^-	-	p = .208	p = 1.000	p = 1.000
DJ-1$\beta^{\Delta 93}$	-	-	p = 1.000	p = .940
DJ-1$\alpha^{\Delta 72}$	-	-	-	p = .917

Table 3A.3 Simple Effects Analysis: p-values at 14 days of age.

	w^-	*DJ-1*$\beta^{\Delta 93}$	*DJ-1*$\alpha^{\Delta 72}$	*dLRRK*^{ex1}
*PINK1*5	p = 1.000	p = .221	p = .042*	p = .019*
w^-	-	p = .064	p = .156	p =.080
DJ-1$\beta^{\Delta 93}$	-	-	$p <$ .001*	$p <$ .001*
DJ-1$\alpha^{\Delta 72}$	-	-	-	p = 1.000

Table A3.4 Simple Effects Analysis: p-values at 21 days of age.

	w^{-}	*DJ-1β*$^{\Delta 93}$	*DJ-1α*$^{\Delta 72}$	*dLRRK*^{ex1}
*PINK1*5	*p* = .897	*p* =. 737	*p* = .440	*p* = .862
w^{-}	-	*p* = .052	*p* = .999	*p* =1.0
DJ-1β$^{\Delta 93}$	-	-	*p* = .006*	*p* = .042*
DJ-1α$^{\Delta 72}$	-	-	-	*p* = 1.000

Table A3.5 Simple Effects Analysis: p-values at 28 days of age.

	w^{-}	*DJ-1β*$^{\Delta 93}$	*DJ-1α*$^{\Delta 72}$	*dLRRK*^{ex1}
*PINK1*5	*p* = .515	*p* = 1.000	*p* = .010*	*p* = .275
w^{-}	-	*p* = .440	*p* = .753	*p* = 1.000
DJ-1β$^{\Delta 93}$	-	-	*p* = .007*	*p* = .222
DJ-1α$^{\Delta 72}$	-	-	-	*p* = .937

Table A3.6 Simple Effects Analysis: p-values for *w*$^{-}$ *Drosophila*.

	7 days	14 days	21 days	28 days
1 day	*p* = .001*	*p* < .001*	*p* = .05*	*p* < .001*
7 days	-	*p* = .811	*p* = 1.000	*p* = 1.000
14 days	-	-	*p* = .372	*p* =.991
21 days	-	-	-	*p* = .951

Table A3.7 Simple Effects Analysis: p-values for *DJ-1α*$^{\Delta 72}$ *Drosophila*

	7 days	14 days	21 days	28 days
1 day	$p = 1.000$	$p = 1.000$	$p = 1.000$	$p = 1.000$
7 days	-	$p = .988$	$p = .938$	$p = .988$
14 days	-	-	$p = 1.000$	$p = 1.000$
21 days	-	-	-	$p = 1.000$

Table A3.8 Simple Effects Analysis: p-values for *DJ-1β*$^{\Delta 93}$ *Drosophila*

	7 days	14 days	21 days	28 days
1 day	$p = .988$	$p = .005$*	$p = .691$	$p = .507$
7 days	-	$p < .001$*	$p = .178$	$p = .099$
14 days	-	-	$p = .427$	$p = .609$
21 days	-	-	-	$p = 1.000$

Table A3.9 Simple Effects Analysis: p-values for *PINK1*^{5} *Drosophila*

	7 days	14 days	21 days	28 days
1 day	$p = 1.000$	$p = 1.000$	$p = .768$	$p = 1.000$
7 days	-	$p = 1.000$	$p = .698$	$p = 1.000$
14 days	-	-	$p = .923$	$p = 1.000$
21 days	-	-	-	$p = .634$

Table A3.10 Simple Effects Analysis: p-values for *dLRRK*^{ex1} *Drosophila*

	7 days	14 days	21 days	28 days
1 day	$p = .998$	$p = .997$	$p = .852$	$p = .242$
7 days	-	$p = 1.000$	$p = .999$	$p = .733$
14 days	-	-	$p = .1.000$	$p = .806$
21 days	-	-	-	$p = .993$

Chapter 4

Classification of α-synuclein Parkinson's disease rodents using chromatic SSVEP measurements.

4.1 Abstract

Biomarkers for Parkinson's disease (PD) tend to be classical motor symptoms that occur in the mid to late stages of disease. Evidence suggests that PD causes changes in visual processing in humans and animal models. This may be a useful biomarker for PD. Previously, we have applied machine learning classification techniques to electrophysiological measurements of visual processing in *Drosophila* PD mutants to establish a new visual biomarker. Here, we extend this research by asking whether we can identify a visual biomarker in a rodent model of PD overexpressing α-synuclein, using chromatically defined SSVEPs measured via the electroencephalogram (EEG). We use a support vector machine (SVM) classifier to assess whether we can accurately classify simulated rats into PD or control across 8 different ages, using responses from different electrode configurations. The SVM was able to accurately classify the presence or absence of α-synuclein using visual response across the majority of ages using different electrode configurations, indicating that the SSVEP is sensitive to the presence of the PD-causing gene product. Further, we were able to classify responses from the left versus right superior colliculus (SC) *within* both α-synuclein and control rats, indicating that interhemispheric differences are strong relative to any hemisphere-specific

change that might be caused by the α-synuclein gene itself. Our findings suggest that the overexpression of α-synuclein results in changes to the rodent SSVEP, and thus neural signalling, with such changes evident across lifespan. Our data are the first to establish a visual biomarker in a rodent model of PD and may suggest a similar biomarker can be found in human PD patients.

4.2 Introduction

Parkinson's Disease (PD) is the second most common progressive neurodegenerative disorder, affecting ~0.2 - 3.0% of the population, and is characterised by the pathological degeneration of dopaminergic neurons in the pars compacta of the substantia nigra (Clarke, 2007; de Rijk et al., 1997). The progression of PD is characterised using Braak staging, in which six stages of PD symptomology are associated with progressive pathology to neurological structures (Braak et al., 2003). Early stages of PD are typically characterized by secondary non-motor symptoms, such as those in the visual and olfactory domain, while the classic motor-related PD symptoms occur in mid-stages of PD (Meissner, 2012; Stern & Siderowf, 2010). Thus, it is common for clinicians to establish the presence of PD late into the disease's progression as diagnosis is typically dependent on the presence of detectable motor symptoms.

A range of changes in visual functioning have been found to occur in PD patients, including progressive deterioration in colour vision, changes in

the chromatic VEP, impaired motion discrimination, and abnormal contrast sensitivity (Armstrong, 2011; Diederich, Raman, Leurgans, & Goetz, 2002; Hutton et al., 1993; Price, Feldman, Adelberg, & Kayne, 1992; Sartucci et al., 2012; Sartucci & Porciatti, 2006; Trick, Kaskie, & Steinman, 1994). Recent research has found changes in low-level vision in fly models of PD. Studies have shown increased contrast sensitivity as an early visual biomarker in young *LRRK2-G2019S* transgene PD *Drosophila*, and this abnormality could be normalized using novel drug treatments (Afsari et al., 2014). This research has expanded to include machine learning classification techniques that allow one to investigate subtle differences in visual processing, and subsequently neural signalling, that occur as a result of PD. Previously, we established a visual biomarker in a three *Drosophila* models of early-onset PD (*DJ-1*$\alpha^{\Delta 72}$, *DJ-1*$\beta^{\Delta 93}$, and *PINK1*^{5}), where a linear discriminant analysis (LDA) classifier could accurately classify *Drosophila* into their correct age and genotype based on multivariate spatial and temporal contrast visual response profiles measured from retina (Himmelberg et al., 2018; West et al., 2015). We aim to establish the utility of machine learning classification as a tool to identify visual biomarkers in animal models of disease. Such biomarkers can be used as a novel and sensitive way of testing new therapeutic drugs that aim to alter disease progression, and define cross-species biomarkers that could be translated to human PD (Schapira, Chaudhuri, & Jenner, 2017).

Here, we ask whether we can identify a visual biomarker in rat model of PD overexpressing α-synuclein, using chromatically defined SSVEPs

measured from four regions of the rat cortex via the electroencephalogram (EEG). We use a support vector machine (SVM) classifier to assess whether we can accurately classify rats into PD or control at 8 different ages, using responses from different electrode configurations. Further, to assess interhemispheric differences, we ask whether the SVM can accurately classify EEG responses within rat genotype into the hemisphere from which it occurred (i.e. left or right superior colliculus (SC) of a control rat)?

We asked five questions. First, can the SVM accurately classify between α-synuclein rats and control rats, when responses from all electrodes from both classes are included in the analysis? The ability to distinguish between these two classes suggests significant variation in response properties between these genotypes across the cortex. Second, can the SVM accurately classify between α-synuclein and control rats, when only responses from the (PD-virus treated) left SC in α-synuclein rats and the (vehicle only treated) left SC in control rats are included in the analysis? Here, the ability to distinguish between these two classes suggests significant variation in response properties due the condition of α-synuclein virus, which is localised in the left SC of α-synuclein rats. Third, can the SVM accurately classify between α-synuclein and control rats, when only responses from the (untreated) right SC in α-synuclein rats and the (untreated) right SC in control rats are included in the analysis. The ability to distinguish between these two classes suggests systemic effects of the α-synuclein gene are detectable in the opposite hemisphere to the virus injection.

Next, we assess interhemispheric differences *within* rat class. Fourth, we ask whether the SVM can accurately classify between responses from the (PD-virus treated) left SC and the (untreated) right SC within α-synuclein rats. Finally, we ask if we can accurately classify between responses from the (treated) left SC and (untreated) right SC within control rats. The ability to use SSVEP responses to distinguish between hemispheres within control rats suggests interhemispheric differences due to an effect of injection (rather than PD-virus) or alternatively, indicates interhemispheric biases in the rodent visual system.

Overall, we found that the SVM was generally accurate in classifying across the comparisons tested at all ages, indicating that the rodent SSVEP is sensitive to both the overexpression of α-synuclein and the hemisphere from which it is measured.

4.3 Methods

4.3.1 Animals and Stereotaxic Surgery

Animal experimentation was carried out in accordance with the European Communities Council Directive (86/609/EEC) and in accordance with Danish law on laboratory animals. 26 female Sprague-Dawley (SD) rats, weighing 225g at arrival, were used in the study. Rats were anesthetized using hypnorm in saline and midazolam in a 2:1:1 relation (equivalent to fentanyl 157 μg/kg) and placed in a stereotaxic frame. Local anaesthetic (mercain) was injected prior to incision. A small drill was used to make seven holes in total:

above the substantia nigra pars compacta (SNc) (AP: -5.5, ML: +2.0 DV: -7.2) of the left hemisphere, and electrodes implanted bilaterally in the SC (AP: -6.0, ML: ±1.0, DV:-3.5) and visual cortex (AP: -6.0, ML: ±4.0), and a reference at (AT: +8.0, ML: -2.0), and a ground at (AP: -2.0, ML: +4.0).

Electrodes with a 15mm mounting screw (E363/20/2.4/S, plastics1) were inserted into the visual cortex, reference, and ground holes. Stranded electrodes with a 25mm mounting screw (E363/3/Spc, plastics1) were placed in the SC. Rats were randomly assigned into one of two conditions, α-synuclein or null, with 13 rats in each group. The α-synuclein group received an injection of adeno-associated virus (AAV) containing human *SNCA* (*hSNCA*) into the left substantia nigra pars compacta (SNc), whereas the control group received an injection of an empty AAV vehicle. Specifically, the α-synuclein rats were injected with 3.0 µl of rAAV2/5 viral vector (30x1010 GC) (Vector biolabs, Malvern, PA, USA) using a 32G Hamilton cannula with an injection rate of 0.2 µl/min. The right hemisphere received no treatment. The electrodes were gathered in a plastic pedestal (plastics1) making a female plug, as a chronic implant on their heads, and attached using dental cement (Relyx).

For each rat, this procedure took 90 – 120 minutes and the procedure for all rats was completed over 9 days. Female rats were chosen as the lesion develops over 10 weeks and males substantially grow in size, whereas females grow less and would not need their food restricted, which would

induce stress. Rats were left to recover for 2 weeks. Steady state visually evoked potential (SSVEP) recordings were made at eight time points throughout an 11-week period, counted from the last day of surgery (3 weeks, 5 weeks, 6 weeks, 7 weeks, 8 weeks, 9 weeks, 10 weeks, and 11 weeks). Henceforth, we refer to the weeks after surgery as 'age'.

4.3.2 Stimuli

Rats were presented with a flickering luminance stimulus that had a square wave modulation at 14 Hz. Each presentation run lasted 100 seconds. The stimulus was presented at 5 wavelength conditions– red (20 lx, 6320-625 nm), green (20 lx, 525-530 nm), blue (20 lx, 455 - 460 nm), ultra violet (20 lx, 405 nm), and white (20 lx, 400 - 700 nm). Stimuli were presented using 5050 SMD LEDs. Lux was measured using an LED luxmeter (Extech) located in the bottom of the cage.

4.3.3 Data collection

Rats were placed in a homecage of Plexiglas and a topbox and then placed inside a larger Faraday cage. The LEDs were placed at 40cm above the base of the cage and illuminated the entire Faraday cage. The rats were plugged in using (363 plug, plastics1). As the female plug is threaded, it is possible to fasten the plugs during the recording. SSVEPs were recorded for 100s using Spike2 (CED), while the animals were awake and behaving. This data was then exported to MATLAB 2018a for further analysis.

4.4 Analysis

4.4.1 Fourier Transform

The periodic modulation of a steady state visually evoked potential (SSVEP) stimulus evokes a phase locked, periodic time course which is best analysed in the frequency domain, rather than the time domain (Norcia et al., 2015). The frequency of the input stimulus (in this case, a flickering light at 14Hz) determines the response frequency, with narrowband peaks at frequencies related to the stimulus frequency. The input stimulus causes a response at the stimulus frequency itself (denoted as 1*f*, which for our stimulus, occurred at 14Hz) and additional responses at multiples of this frequency, referred to as harmonics (i.e. 2*f* at 28Hz, 3*f* at 42Hz). Thus, complex-valued Fourier amplitudes were computed for the first harmonic (1*f*, 14Hz) and the second harmonic (2*f*, 28Hz), and these two harmonics were used for further analysis. For more information on Fourier Transform please see *2.2.2: Fourier Transform*.

4.4.2 EEG data processing

Data were analysed within each age group and EEG samples were processed using MATLAB 2018a. For each of the 13 α-synuclein rats and each of the 13 control rats, we took a 100s EEG sample from the 4 separate electrodes (henceforth referred to as; left SC, left visual cortex, right SC, and right visual cortex). Each sample was recorded in response to a 14Hz stimulus that was presented at the 5 different wavelengths and comprised of 100 1s

bins (with a sampling rate of 1000Hz). In Figure 4.1A we present an example of an averaged EEG time course across a 1s bin in response to the 14Hz stimulus. We clipped the first 5s and the final 5s of each EEG sample to remove any major onset transients and adaptation effects, thus retaining 90 1s bins of EEG data per rat for each electrode and wavelength, at each age. Next, these data were transformed into the power spectrum by running a Fourier transform (FT) on each individual, unaveraged, 1s bin. The Fourier transform produced a complex number – we retained the real number reflecting the amplitude of the 1s bin and discarded the phase information as SSVEP phase originates from the summation of many waveforms and may be considered inaccurate. As presented in Figure 4.1B, peaks occurred at multiples of our input frequency, namely, 1*f* (14Hz) and 2*f* (28Hz). Thus, we retained the data from these two frequencies as our frequencies of interest for further analysis.

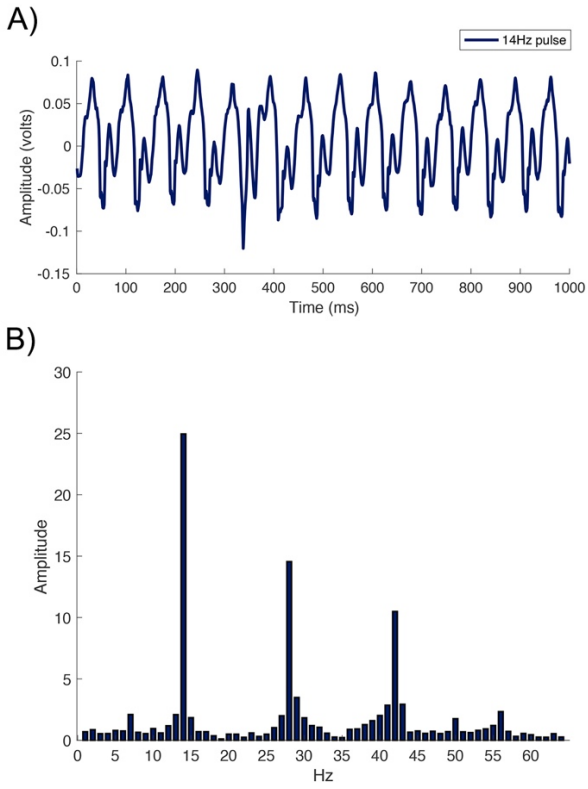

Figure 4.1 EEG data is collected in the time domain then transformed into the frequency domain using the FT. In A), we present an example of the average EEG time course across a 1000ms bin taken from the right SC of a 3-week-old control rat. There are 14 peaks across the 1000ms bin, reflecting the 14Hz temporal frequency of our stimulus. In B), we present this data in the power spectrum after applying the FT. Peaks occur at multiples of our input harmonic – at 14Hz, 28Hz, and 42Hz (1*f*, 2*f*, and 3*f*, respectively).

To filter our data, we took a measure of noise by computing the average power amplitudes in the four frequency bins above and below the two frequencies of interest (14 and 28Hz). To create a signal to noise (SNR) estimate, we compared the Fourier amplitude at 1*f* and 2*f* to the root mean square (RMS) of the noise calculated from the local side bins. We then

removed any data that had a SNR lower than 1. Therefore, all data retained for further analysis had a Fourier amplitude that was larger than the average noise across the neighbouring bins of 1*f* and 2*f* on the power spectrum.

4.4.3 Machine Learning Features

Our goal was to classify different rat phenotypes and electrode configurations based on multiple features of the SSVEP assay. Additional analysis found that there was no significant difference in responses when comparing between colour conditions, thus we did not attempt a multiclass classification of responses into their correct colour for the purpose of this experiment (Freja Gam Østergaard, personal communication, Jan 15, 2019). For each of the 4 electrodes we had a combination of 5 illumination wavelengths and 2 harmonics (1*f* and 2*f*); a total of 40 potential features per rat, with 90 bins of data containing each feature. We had 13 rats in each treatment group (α-synuclein or control). It is possible to simply apply a machine learning classifier to these two groups and compute an overall classification accuracy, however this can lead to issues of overfitting. To circumvent these issues, we bootstrapped our classification procedure to perform multiple classification iterations on groups of 'synthetic' rats by sampling data from the group-level population. For more information on overfitting please see *2.3.5 Issues: Overfitting.*

4.4.4 Bootstrapping procedure

We bootstrapped our classification estimates by repeatedly sampling (without replacement) from the pool of retained Fourier amplitudes, corresponding to 1s bins of our data. For each of the 4 electrodes, this sampling pool contained a maximum of 1170 Fourier amplitude bins (computed from 13 rats x 90 1s bins). Each bin of data was organised to contain the Fourier amplitude data from the 2 harmonics at each of the 5 wavelengths (thus 10 features within each bin). We randomly permutated through these bins, assigning 90 random 1s bins from each feature. These 90 1s bins were then averaged together along each feature to create a single synthetic rat. For each run of the SVM, this was repeated to create 13 unique synthetic α-synuclein rats and 13 synthetic control rats with 10 features per electrode. We normalised responses by z-scoring the data across each synthetic rat. The z-score of each feature was entered into the SVM classifier and labelled with the class that the data corresponded too, α-synuclein or control. Thus, for each run of the SVM we included 13 synthetic α-synuclein rats and 13 synthetic control rats with 40 features each, assuming the inclusion of all electrodes. We ran unique variations of these synthetic rats through 1000 bootstrapped runs of the SVM classifier to derive a mean classification accuracy and corresponding significance value. The mean classification accuracy was deemed significant if less than 5% of the 1000 iterations fell below a 50% chance baseline, equivalent to a *p*-value of .05. In an additional analysis, we shuffled our rat labels on each bootstrapped run so that the labels

were randomized. If the SVM is working correctly, we would expect the mean classification accuracy of shuffled data to fall around chance (50%).

4.4.5 Support Vector Machine

The goal of the SVM is to find the hyperplane that best separates two classes of data (i.e. the line that best separates α-synuclein and control data). The SVM then uses this hyperplane (which may be non-linear, via the 'kernel trick') as classification boundary to assign new examples of data to either class, with the output being the accuracy of the SVM in classifying these new examples of data (Boser, Guyon, & Vapnik, 1992; Cortes & Vapnik, 1995; Lipo Wang, 2018). We bootstrapped a SVM classification analysis in MATLAB 2018a using the LIBSVM toolbox, Version 3.23 (Chang & Lin, 2011). The SVM had a radial basis kernel (RBK) function and a 5-sample k-fold cross validation, with 4 groups of data used as the training data and a single group used as the validation data for each run, again, to avoid issues of overfitting. For more information on SVM please see *2.3.3 Support vector machine*, and for more information on the RBK function please see *2.4.4 Radial Basis Function Kernel*.

4.5 Results

4.5.1 Classification between responses from α-synuclein rats and control rats with all electrodes

First, we assessed the accuracy of the SVM classifier in distinguishing between responses from α-synuclein rats and control rats within each age

group when all four electrodes from each class were included in the analysis. Thus, for each synthetic rat, 40 features were included in the classifier (4 electrodes, 5 wavelengths, and 2 harmonics). The average classification accuracy of 1000 bootstrapped runs at each week and corresponding significance values are presented in Table 4.1 and histograms of these bootstrapped accuracies (and shuffled bootstrapped accuracies) are visualised in Figure 4.2. The SVM was highly accurate in classifying between α-synuclein rats and control rats within each age, with classifications consistently reaching > 83% accuracy. As a precaution, we also ran the SVM with shuffled labels and found that average classification accuracies fell around 50% (dotted line in Figure 4.2) and were non-significant across all ages. These shuffled accuracies were similar, falling around 50% across all 5 analyses, indicating that the SVM was working as expected. We applied a kernel smoothing function estimate to these shuffled classification accuracies and have plotted this distribution in the black line across our histograms. Shuffled label classification accuracies and p-values are available in Appendix Table A4.1.

Table 4.1 Mean SVM classification accuracy at each age after 1000 bootstrapped runs, classifying α-synuclein rats and control rats into their correct class, when all electrodes are included in the analysis.

Week	Accuracy	p-value
3	83.71%**	$p < .001$
5	87.98%**	$p < .001$
6	92.28%**	$p < .001$
7	88.99%**	$p < .001$
8	86.79%**	$p < .001$
9	90.16%**	$p < .001$
10	92.96%**	$p < .001$
11	84.12%*	$p = .020$

** $p < .001$, * $p < .05$

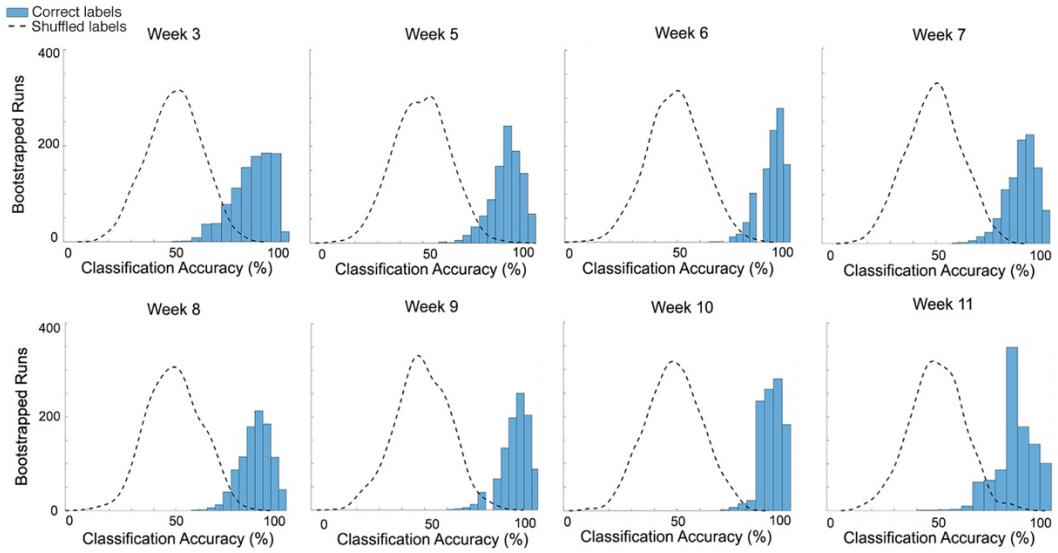

Figure 4.2 Histogram plots of classification accuracy across 1000 bootstrapped SVM classifications. The SVM is highly accurate in classifying between α-synuclein and control rats at each week when all electrodes are included in the analysis. We include a plot of classification accuracy after shuffling labels, where accuracies fall around the 50% baseline.

4.5.2 Classification between responses from the left SC in α-synuclein rats and the left SC in control rats

Both classes of rat received an injection of AAV into their left SC. The difference between classes was due solely to the payload of the AAV vector in the α-synuclein rats. Here, we assessed the ability of the SVM classifier in distinguishing between responses from α-synuclein rats and control rats within each age group, when only responses from the (treated) left SC of each class were included in the analysis. Thus, for each rat, 10 features were included in the SVM classifier (1 electrode, 5 wavelengths, and 2 harmonics). The average classification accuracy of 1000 bootstrapped runs at each week and

corresponding significance values are presented in Table 4.2 and histograms of these bootstrapped accuracies (and shuffled accuracies) are visualised in Figure 4.3. Using the left SC alone, the SVM was able to accurately classify between α-synuclein rats and control rats at all ages, except at week 3 (although this was closely approaching significance) and week 11.

Table 4.2 Mean SVM classification accuracy at each age after 1000 bootstrapped runs, comparing between the (treated) left SC electrode in α-synuclein rats and (treated) left SC in control rats.

Week	Accuracy	p-value
3	66.35%	$p = .055$
5	75.20%*	$p =. 006$
6	79.33%*	$p = .002$
7	74.56%*	$p = .007$
8	71.94%*	$p = .024$
9	75.63%*	$p = .018$
10	68.10%*	$p = .048$
11	60.83%	$p = .140$

** $p < .001$, * $p < .05$

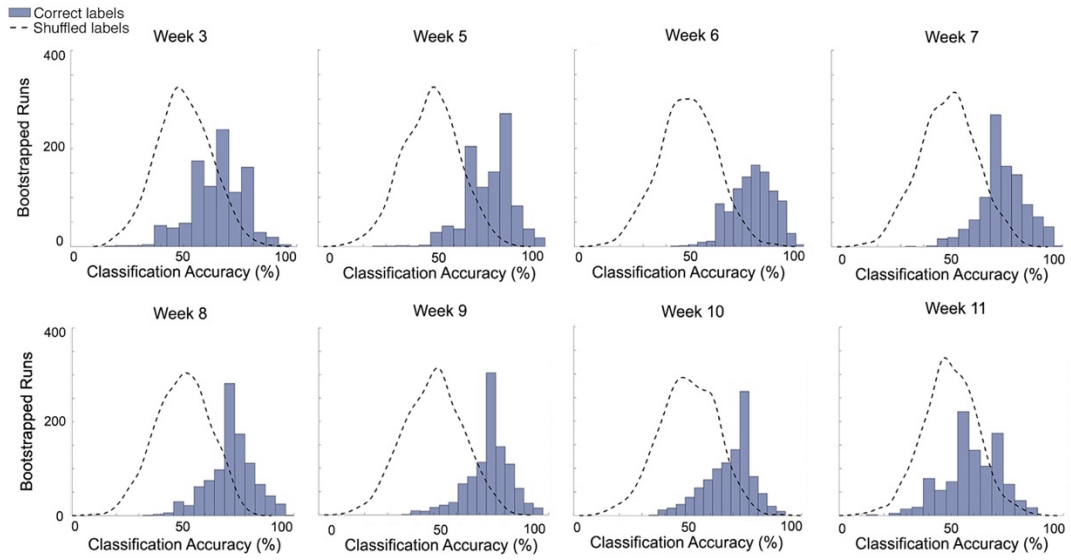

Figure 4.3 Histogram plots of classification accuracy across 1000 bootstrapped SVM classifications. The SVM is able to classify between α-synuclein and control rats using responses from the (treated) left SC, expect at weeks 3 and 11. We include a plot of classification accuracy after shuffling labels, where accuracies fall around the 50% baseline.

4.5.3 Classification between responses from the right SC in α-synuclein rats and the right SC in control rats

Next, we assessed the ability of the SVM classifier in distinguishing between responses from the α-synuclein rats and control rats within each age group, when only responses from the (untreated) right SC of each class were included in the analysis. Neither of these areas received any effect of injection or the AAV, thus differences in response may indicate changes long-range interhemispheric signalling due to the α-synuclein virus. For each rat, 10 features were included in the classifier (1 electrode, 5 wavelengths, and 2 harmonics). The average classification accuracy of 1000 bootstrapped runs at

each week and corresponding significance values are presented in Table 4.3 and histograms of these bootstrapped accuracies (and shuffled accuracies) are visualised in Figure 4.4. The SVM was able to accurately classify between α-synuclein rats and control rats at all ages, except at Week 5.

Table 4.3 Mean SVM classification accuracy at each age after 1000 bootstrapped runs, comparing between the (untreated) right SC electrode in α-synuclein rats and the (untreated) right SC electrode within control rats.

Week	Accuracy	p-value
3	71.10%*	$p = .014$
5	62.46%	$p = .112$
6	73.45%*	$p = .007$
7	76.76%*	$p = .004$
8	78.50%**	$p < .001$
9	75.37%*	$p = .008$
10	71.42%*	$p = .013$
11	75.68%*	$p = .006$

** $p < .001$, * $p < .05$

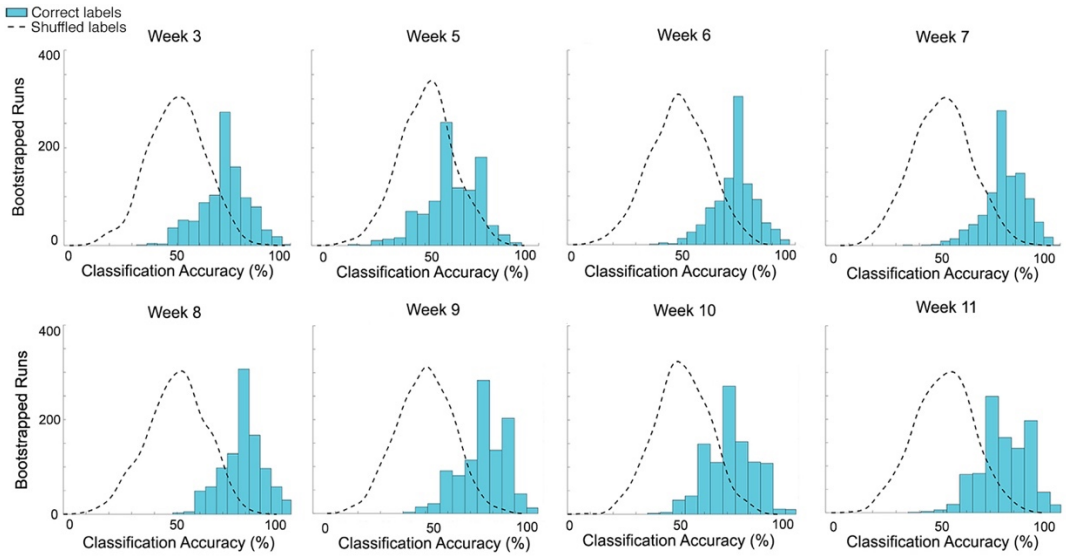

Figure 4.4 Histogram plots of classification accuracy across 1000 bootstrapped SVM classifications. The SVM is able to classify between α-synuclein and control rats using responses from the (untreated) right SC, expect at Week 5. We include a plot of classification accuracy after shuffling labels, where accuracies fall around the 50% baseline.

4.5.4 Classification between responses from the (treated) left SC and the (untreated) right SC within α-synuclein rats

Here, we aimed to test whether there is an overall difference in the left and right hemisphere of α-synuclein rats. If differences occur, this can suggest existing asymmetries in the rat visual system due to the site of injection, or possibly a real effect of the vector. To test this possibility, we assessed the accuracy of the SVM classifier in distinguishing between responses from the (treated) left SC and the (untreated) right SC of α-synuclein rats, within each age group. Thus, for each rat, 10 features were included in the classifier (1 electrode, 5 wavelengths, and 2 harmonics). The average classification

accuracy of 1000 bootstrapped runs at each week and corresponding significance values are presented in Table 4.4 and histograms of these bootstrapped accuracies (and shuffled accuracies) are visualised in Figure 4.5. The SVM was able to accurately classify between responses from the (treated) left and (untreated) right SC within α-synuclein rats, except for at 10 weeks of age (although this was approaching significance).

Table 4.4 Mean SVM classification accuracy at each age after 1000 bootstrapped runs, comparing between the (treated) left SC electrode and the (untreated) right SC electrode within α-synuclein rats.

Week	Accuracy	p-value
3	67.87%*	$p = .042$
5	81.46%**	$p < .001$
6	67.23%*	$p = .047$
7	77.17%*	$p = .002$
8	84.48%**	$p < .001$
9	69.52%*	$p = .036$
10	66.35%	$p = .062$
11	73.01%*	$p = .032$

** $p < .001$, * $p < .05$

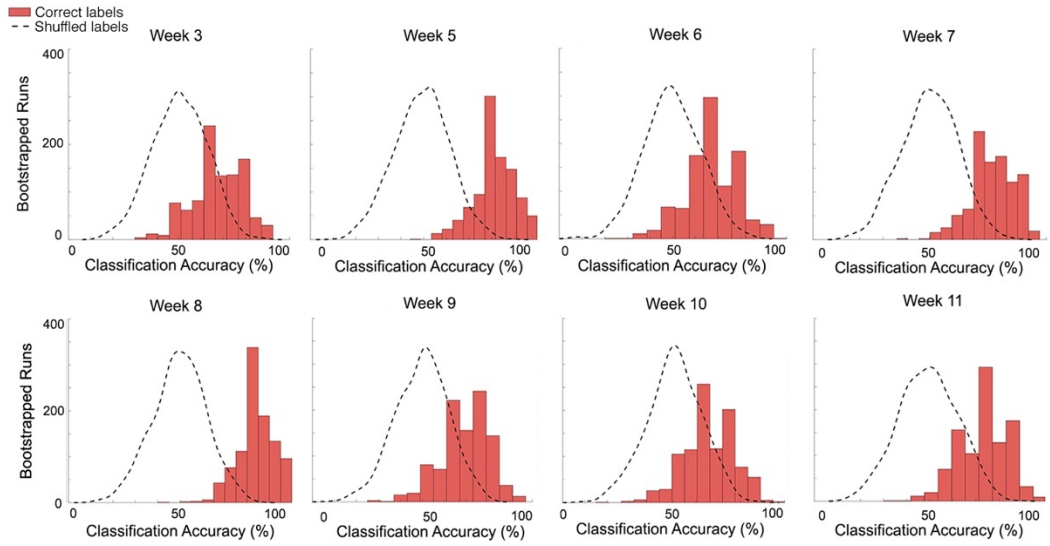

Figure 4.5 Histogram plots of classification accuracy across 1000 bootstrapped SVM classifications. The SVM is able to classify between the (treated) left SC and the (untreated) right SC within α-synuclein rats, expect at week 10. We include a plot of classification accuracy after shuffling labels, where accuracies fall around the 50% baseline.

4.5.5 Classification between responses from the (treated) left SC and the (untreated) right SC within control rats

As we found interhemispheric differences in SSVEP responses from α-synuclein rats, we repeated this analysis on control rats who did not receive any effect of α-synuclein. Here, we assessed the accuracy of the SVM classifier in distinguishing between responses from the (treated with empty vector) left SC and the (untreated) right SC of control rats within each age group. Thus, for each rat, 10 features were included in the classifier (1 electrode, 5 wavelengths, and 2 harmonics). The average classification accuracy of 1000 bootstrapped runs at each week and corresponding significance values are presented in Table 4.5 and histograms of these

bootstrapped accuracies (and shuffled accuracies) are visualised in Figure 4.6. At later ages, the SVM was able to accurately classify between responses from the (treated) left and (untreated) right SC within control rats, however the SVM classifications were non-significant at 3 and 5 weeks of age. In Figure 4.7, we present histogram plots comparing classification accuracies when comparing between responses from the (treated) left SC and the (untreated) right SC within α-synuclein rats, against the same analysis within control rats. There is little difference in performance between these two comparisons, except at Weeks 3 and 5, where the SVM is superior at classifying between the left and right SC in α-synuclein rats.

Table 4.5 Mean SVM classification accuracy at each age after 1000 bootstrapped runs, comparing between (treated) left SC and the (untreated) right SC electrode in control rats.

Week	Accuracy	p-value
3	67.52%	$p = .050$
5	55.64%	$p = .274$
6	67.41%*	$p = .041$
7	72.81%*	$p = .015$
8	78.13%*	$p = .004$
9	69.88%*	$p = .035$
10	67.89%*	$p = .044$
11	73.51%*	$p = .011$

** $p < .001$, * $p < .05$

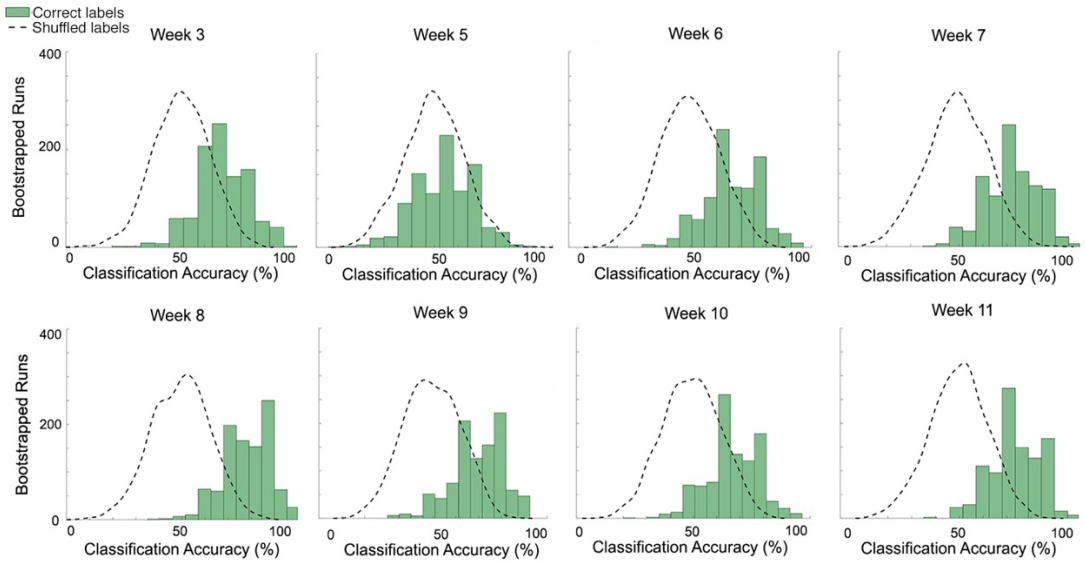

Figure 4.6 Histogram plots of classification accuracy across 1000 bootstrapped SVM classifications. The SVM is able to classify between the (treated) left SC and the (untreated) right SC within control rats from 6 weeks and beyond. We include a plot of classification accuracy after shuffling labels, where accuracies fall around the 50% baseline.

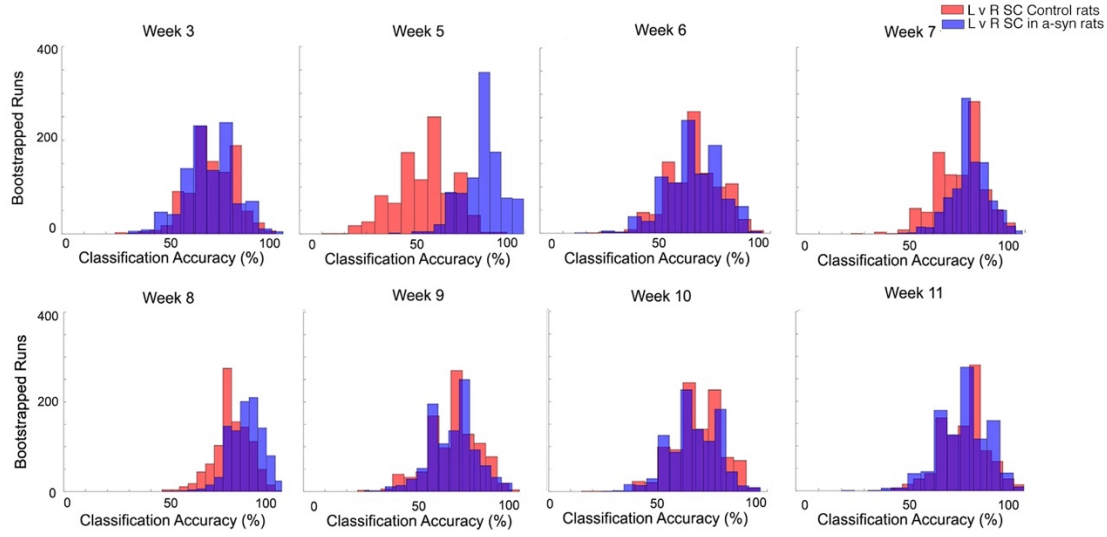

Figure 4.7 Histogram plots of classification accuracy across 1000 bootstrapped SVM classifications. In red we plot classification accuracies

comparing between the (treated) left SC and the (untreated) right SC in control rats, and in blue we plot the same for α-synuclein rats.

4.6 Discussion

Previously, we demonstrated that machine learning classifiers are a useful tool for establishing new visual biomarkers in *Drosophila* PD models (Himmelberg et al., 2018; West et al., 2015). Here, we asked whether we could use SSVEP response amplitudes from four different regions of the cortex to establish a similar visual biomarker in rat model of PD overexpressing α-synuclein. We used an SVM classifier to accurately classify α-synuclein and control rats into their correct genotype, using various electrode configuration across 8 ages. Further, the SVM classifier could accurately classify responses *within* rat class into which hemisphere SSVEPs were measured from. Our results suggest that the rodent SSVEP is sensitive to both the overexpression of α-synuclein across and the hemisphere from which it is measured, and such sensitivities persist across time.

4.6.1 Classification between α-synuclein and control rats when all electrodes are included in the SVM

First, we ran a full dataset with all electrodes included in the SVM to assess how well we could classify rats into either α-synuclein or control rats at each age group, with baseline performance at 50%. The SVM was able to classify rats into their correct genotype at all ages with very high accuracy – with the lowest accuracy occurring at Week 1 (83.71%) and the highest at Week 10 (92.96%). Further, the SVM generally performed better when data

from all electrodes were included in the analysis, even though the PD-virus was confined to the left SC of α-synuclein rats.

One reason for this may be that SVM accuracy tends to increase with increased features (in analysis there were 40 features, in all other analyses there were only 10). The fact that classification accuracy increases when more features are included in the SVM suggests that these additional features are relevant and contributing to classification accuracy, even though this additional data comes from untreated regions of the cortex (as will be further discussed). These results indicate that there are significant differences in visual response properties as a result of the overexpression of α-synuclein, and such differences may occur across the cortex. It is of note that these differences in SSVEP sensitivity occur as early as 3 weeks after the injection and persist across disease progression.

4.6.2 Classification of responses from the left SC in α-synuclein rats and the left SC in control rats

Next, we ran the SVM on responses from the left SC of α-synuclein rats and the left SC of control rats, at each age group. The difference between these two genotypes is purely due to the payload of the AAV vector which is injected into the left SC. We were able to classify rats into their correct genotype at most, but not all, ages – with the lowest accuracy occurring at Week 10 (68.10%) and the highest at Week 6 (79.33%). We were unable to classify between these two classes at Week 3 (66.35%) and at Week 11

(60.83%) – although these classification accuracies were above chance, they were not significant. One might expect the highest accuracy in this condition as we are solely comparing SSVEP responses from the region that directly received the PD virus (left SC in α-synuclein rats) with responses from the region that received no virus (left SC of control rats), with both electrodes receiving an effect of injection. However, this does not appear to be the case. One reason for slightly lower classification accuracies may be the reduced number of features included in the SVM, with only 10 features rather than 40. We theorised that regions of the cortex that do not show structural effects of the α-synuclein virus may still significantly differ due to changes in signalling, rather than changes in signalling being purely localised location of α-synuclein clusters (i.e. the left SC). Regardless, we were able to classify between α-synuclein and control rats between Week 5 and Week 10, indicating a direct effect of the AAV virus on SSVEP responses.

4.6.3 Classifying between α-synuclein and control rats using responses from the right SC in α-synuclein rats and the right SC in control rats

Although the vector was injected into the left SC, it is possible that the presence of the α-synuclein gene generates systemic effects that breach the opposing hemisphere of the SC and are detectable by the SVM classifier. This may occur either through the spreading of the virus across the brain, or alternatively because of changes in long-range neuronal signals that transfer information across hemispheres.

To test this, we ran the SVM on responses from the right SC of α-synuclein rats and the right SC of control rats, at each age group – comparing SSVEPs measured from two regions that did not directly receive the PD-virus. Here, the SVM was highly accurate in classifying rats into their correct genotype at all ages, except at Week 5. The lowest classification accuracy occurred at Week 3 (71.10%) and the highest was at Week 8 (78.50%). Thus, the ability of the SVM to classify between these two classes of data suggests that the overexpression of α-synuclein in the left hemisphere of the SC generates systemic effects, most likely through changes in long-range neuronal signalling, that then result in changes in the response properties in the opposing hemisphere. Further investigation identified that structural pathology, in the form of an abundance of α-synuclein, was restricted to the ipsilateral superior colliculus in which the AAV virus was injected (i.e. left SC only), with no inclusions on the contralateral hemisphere (Freja Gam Østergaard, personal communication, Jan 15, 2019). Here, we have found evidence for changes in functional visual processing that extend to responses in the opposing hemisphere of α-synuclein inclusions, suggesting changes in neural signalling. This is important, as PD symptomology is typically associated with progressive pathology to neurological structures and there is typically little structural change in the visual cortex although there are changes in visual processing. Thus, these findings show that cortical changes in visual processing (that may be particularly subtle, similar to our *Drosophila* research) may not necessarily be localised to structural pathology cortical regions involved in vision.

4.6.4 Classifying interhemispheric differences

We conducted two secondary analyses to ask whether there were interhemispheric differences *within* rat genotype. Here, we asked whether we distinguish between SSVEP responses from each hemisphere within α-synuclein rats. To test this, we ran the SVM on responses from the left and right SC of α-synuclein rats, at each age group. The SVM could accurately classify between responses from the left and right hemisphere at all weeks except Week 10 (although this was approaching significance) and we found that SVM had the highest classification accuracy at Week 5 (81.46%) and the lowest at Week 3 (67.87%).

At first, these results appear to indicate interhemispheric differences within the α-synuclein genotype due to the effect of the α-synuclein virus. This is surprising, considering our previous analysis suggests that one effect of the α-synuclein virus is that changes in neural signalling extend the contralateral hemisphere. However, an alternative explanation may be that there are differences in SSVEP due to asymmetries in the rat visual system, rather than any effect of α-synuclein, which restricts the reliability of classifications between hemispheres. Another alternative explanation may be that a functional change in response properties may be driven by an anatomical disruption linked to the injection procedure (i.e. the left SC receives an effect of injection, whether it is the AAV or the vehicle, while the right SC does not).

4.6.5 Interhemispheric differences: SVM classification between responses from the left SC and right SC within control rats

To test this alternative explanation, we ran the same analysis on control rats to test for interhemispheric differences that may be due to cerebral asymmetry that has previously been identified in the rat visual system, or alternatively, due to an effect of site of injection (Galaburda, Aboitiz, Rosen, & Sherman, 1986). Here, we found that the SVM was able to accurately distinguish between SSVEP responses from the left and right hemisphere from Week 6 to Week 11, but not early in life (Week 3 and 5). The SVM had the highest classification accuracy at Week 8 (78.13%) and lowest at Week 6 (67.41%). These results indicate that there are differences in the response properties of the left and right SC of control rats. Whether these are due to hemispheric asymmetry in the number of neurons, or anatomical disruption from the injection, is unknown. Notably, the SVM could not classify between responses from left and right SC in control rats at Week 3 and 5, however the identical classification was possible in α-synuclein at this age. Perhaps then, this is evidence of immediate effect of the AAV virus in young α-synuclein rats at a young age, while cerebral asymmetries could develop over time, leading to interhemispheric differences in rats at a later age that would override any effect of the α-synuclein virus. These findings highlight the importance of both functional and structural hemispheric asymmetries that occur in rats and should be considered in further studies.

4.6.6 Relevance to drug testing and future applications

It has been established that machine learning classifiers can accurately discriminate between PD fly models using SSVEP measurements (Himmelberg, West, Elliott, et al., 2018; West et al., 2015). Further, evidence indicates that new PD treatments can rescue visual functioning in similar fly models, although this is yet to be assessed using such classifiers (Afsari et al., 2014). There is clear benefit in combining these approaches to enhance early-stage drug research methods in animal disease models. The accuracy (or inaccuracy) of a highly sensitive classifier in differentiating between visual responses from a PD animal model that has been treated with a PD drug when compared to a control animal allows for the assessment of whether a treatment has rescued visual functioning (i.e. are the response between a drug treated disease model and a healthy animal *indistinguishable*?). Further, with evidence for visual biomarkers in a simple fly model of PD, and now a more complex rodent model, it may soon be possible to classify human PD patients into their correct genotype based on similar SSVEP responses (Himmelberg, West, Wade, et al., 2018).

4.7 Conclusion

To conclude, these analyses suggest that we can accurately classify responses from the left versus right SC in both α-synuclein and control rats. There is little difference in performance between these two comparisons, suggesting that interhemispheric differences are strong relative to any hemisphere-specific change that might be caused by the α-synuclein gene

itself, especially in later ages. Most importantly, we are also able to accurately classify the presence or absence of α-synuclein independently of hemisphere, indicating that the SSVEP is sensitive to the presence of the Parkinson's disease-causing gene product, as well as the hemisphere in which it is measured. These findings are beneficial for testing new therapeutic treatments for PD that aim to normalise neural responses.

4.8 Appendix A4

Table A4.1 Mean SVM classification accuracy at each age after 1000 bootstrapped runs, classifying α-synuclein rats and control rats into their correct class after labels have been shuffled, when all electrodes are included in the analysis.

Week	Accuracy	p-value
3	49.11%	$p = .455$
5	49.39%	$p = .462$
6	48.82%	$p = .476$
7	49.14%	$p = .457$
8	49.35%	$p = .462$
9	49.05%	$p = .479$
10	48.54%	$p = .498$
11	49.04%	$p = .471$

** $p < .001$, * $p < .05$

Chapter 5

Eccentricity-dependent temporal contrast tuning in human visual cortex measured with fMRI.

5.1 Abstract

Cells in the peripheral retina tend to have higher contrast sensitivity and respond at higher flicker frequencies than those closer to the fovea. Although this predicts increased behavioural temporal contrast sensitivity in the peripheral visual field, this effect is rarely observed in psychophysical experiments. It is unknown how temporal contrast sensitivity is represented across eccentricity within cortical visual field maps and whether such sensitivities reflect the response properties of retinal cells or psychophysical sensitivities. Here, we used functional magnetic resonance imaging (fMRI) to measure contrast sensitivity profiles at four temporal frequencies in five retinotopically-defined visual areas. We also measured population receptive field (pRF) parameters (polar angle, eccentricity, and size) in the same areas. Overall contrast sensitivity, independent of pRF parameters, peaked at 10Hz in all visual areas. In V1, V2, V3, and V3a, peripherally-tuned voxels had higher contrast sensitivity at a high temporal frequency (20Hz), while hV4 more closely reflected behavioural sensitivity profiles. We conclude that our data reflect a cortical representation of the increased peripheral temporal contrast sensitivity that is already present in the retina and that this bias must be compensated later in the cortical visual pathway.

5.2 Introduction

There is a mismatch between electrophysiological retinal measurements and psychophysical measurements of temporal contrast sensitivity across the visual field. Eccentricity-dependent differences in retinal temporal sensitivity originate in the cone photoreceptors – peripheral cones respond faster and are more sensitive to flicker when compared to those in the fovea (Sinha et al., 2017). These signals are filtered through the retinal ganglion cells (RGCs), where there is an increase in the proportion of parasol to midget RGCs with increasing retinal eccentricity (Connolly & van Essen, 1984; Dacey, 1993, 1994; Dacey & Petersen, 1992; De Monasterio & Gouras, 1975). Temporal frequency sensitivity is thought to be related to the relative activity of parasol to midget RGC populations which form the magnocellular and parvocellular pathway, respectively (Hammett, Thompson, & Bedingham, 2000; Harris, 1980). On average, RGCs in the periphery have larger receptive fields and cells with such receptive fields have increased contrast sensitivity (Dacey & Petersen, 1992; Enroth-Cugell & Shapley, 1973). Overall then, the peripheral retina has relatively more parasol cells, those cells integrate from larger portions of the retina, and they are fed by cones with brisker response kinetics (Dacey & Petersen, 1992; Enroth-Cugell & Shapley, 1973; Sinha et al., 2017). From such physiological differences we might expect subjects to be more sensitive to low contrast flickering stimuli in more peripheral regions of the visual field.

These predictions are not generally confirmed by psychophysical measurements of temporal contrast sensitivity across space. Previous research has found that psychophysical temporal contrast thresholds are approximately independent of visual field eccentricity (Koenderink et al., 1978; Virsu et al., 1982; Wright & Johnston, 1983). Although such thresholds (which by definition, occur at relatively low contrast) are independent of eccentricity, very low spatial frequencies might be an exception: previous papers report an increase in critical flicker frequency with increasing eccentricity (Hartmann, Lachenmayr, & Brettel, 1979; Rovamo & Raninen, 1984). How these eccentricity-dependent sensitivities to temporal contrast are represented in the visual cortex is currently unknown.

The early visual cortex is organised retinotopically; visual space is mapped topographically, with foveal receptive fields mapped towards the occipital pole and more peripheral receptive fields mapped in increasingly anterior areas of the cortex (Engel, Glover, & Wandell, 1997). Perhaps then, investigating sensitivity to temporal contrast across cortical space can help to explain the discrepancy between measurements of retinal and psychophysical temporal contrast sensitivity. Previous research has found centrally located sustained and peripherally located transient temporal channels in primary visual cortex, and these channels are thought to reflect responses from different classes of cells (Horiguchi, Nakadomari, Masaya, & Wandell, 2009). One might ask whether the relative weighting of response properties of peripheral retinal cells to temporal frequency and contrast is maintained in V1

and other early visual areas. One might also ask at what point in the cortical pathway is temporal contrast sensitivity filtered to reflect psychophysical sensitivity across space, rather than retinal sensitivity. One might expect such filtering to occur in higher-order visual areas that are typically specialized for complex feature identification computation and are less reliant on temporal frequency and contrast information.

How do measurements of cortical temporal contrast sensitivity differ across space, and how do such cortical sensitivities relate to behaviour? To answer this, we used fMRI to measure voxel contrast response functions (CRFs) at a range of temporal frequencies and plotted responses as a function of pRF eccentricity in different visual areas. Additionally, we obtained psychophysical temporal contrast threshold measurements in central and near-peripheral regions of visual space. Previous research has found that the optimal contrast sensitivity of the primate visual system is approximately 8Hz, thus we predicted that we would observe a similar peak contrast sensitivity, independent of eccentricity, in our psychophysical and fMRI data (Hawken, Shapley, & Grosof, 1996; Kastner et al., 2004; Singh, Smith, & Greenlee, 2000; Venkataraman, Lewis, Unsbo, & Lundström, 2017). Next, due to retinal biases, we predicted that in early visual areas, contrast sensitivity would be greater at a high temporal frequency in pRFs representing more peripheral locations of the visual field. Conversely, if cortical sensitivities are to shift to be more reflective of behaviour at some point in the visual cortex, it is predicted

that such areas will show no difference in temporal contrast sensitivity across pRF eccentricity.

5.3 Materials and Methods

5.3.1 Participants

Nineteen participants (mean ± SD age, 27.89 ± 5.72; 9 males) were recruited from the University of York. All participants had normal or corrected to normal vision. Each participant completed a 1-hour psychophysics session and two 1-hour fMRI sessions. In the first fMRI session, two high-resolution structural scans and six pRF functional runs were obtained. In the second fMRI session, 10 temporal contrast sensitivity (TCS) functional runs were obtained. All participants provided informed consent before participating in the study. Experiments were conducted in accordance with the Declaration of Helsinki and the study was approved by the ethics committees at the York NeuroImaging Centre and the University of York Department of Psychology.

5.3.2 Behavioural Psychophysics

5.3.2.1 Experimental Design

To investigate psychophysical temporal contrast sensitivity, we measured contrast detection thresholds for four temporal frequency conditions (1, 5, 10, and 20Hz) at two eccentricities (2° and 10°). 75% correct detection thresholds were obtained using a '2 Alternative Forced Choice' (2AFC) method using four randomly interleaved Bayesian staircases in separate eccentricity blocks (Kontsevich & Tyler, 1999). A single block of 200 trials (50

of each temporal frequency condition) was presented at either 2° or 10° from central fixation on the temporal visual field meridian. Participants were instructed to maintain fixation on a central cross and to respond, via keyboard press, whether the stimulus grating appeared on the left or right of fixation. Participants were informed via a toned 'beep' if their response was correct or incorrect. These responses were recorded using Psykinematix software (KyberVision, Montreal, Canada, psykinematix.com). After each response, a separate toned 'beep' was presented in conjunction with the fixation crossed briefly changing to 'o' then back to 'x' to signify the onset succeeding trial, which then began 500ms later. The first 10 trials were practice and not included in the analysis. The temporal frequency of the stimulus was randomized within each block. Participants completed each eccentricity condition block four times and responses were fit with Weibull functions of stimulus contrast. This resulted in four 75% contrast detection thresholds for each temporal frequency and eccentricity combination. For each condition, the average of these 4 thresholds was the final threshold.

5.3.2.2 Stimuli

Psychophysical stimuli (see Figure 5.1) were designed using Psykinematix software and were presented on a NEC MultiSync 200 CRT monitor running at 120Hz. Gamma correction was performed using a 'Spyder5Pro' (Datacolor, NJ, USA) display calibrator. Stimuli were circularly windowed sine wave gratings outlined with thin white circles to eliminate spatial uncertainty (Pelli, 1985). Grating spatial frequency was set to 1 cycle

per degree (cpd) and were presented for 500ms. At 2° eccentricity, the grating had a 0.5° radius. Using M-scaling to account for cortical magnification, at 10° eccentricity the stimulus had a 1.021° radius (Rovamo & Virsu, 1979).

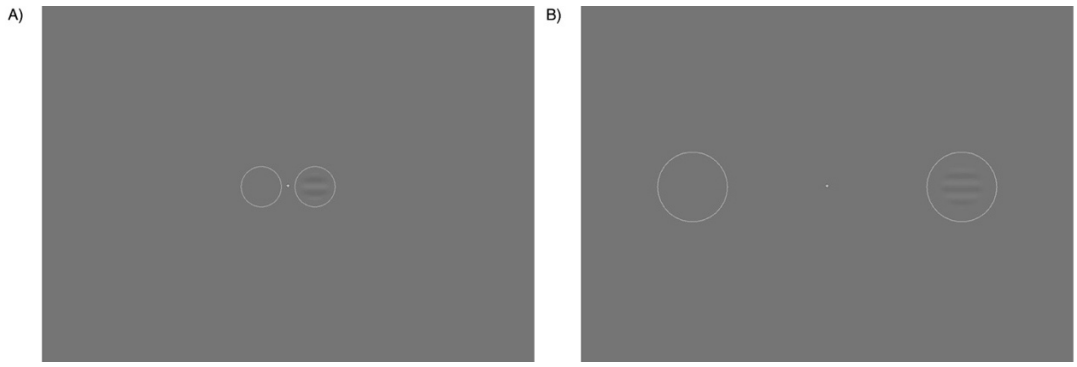

Figure 5.1 2AFC stimulus at two eccentricity conditions. In A) a flickering stimulus grating appears in the right circle at 2° eccentricity, while in B) the flickering stimulus grating appears in the right circle at 10° eccentricity. Participants must select which circle the grating appears in.

5.3.3 Functional neuroimaging

5.3.3.1 fMRI Stimulus Display

Stimuli were presented in the scanner using an PROpixx DLP LED projector (VPixx Technologies Inc., Saint-Bruno-de-Montarvile, QC, Canada) with a long throw lens that projected the image through the waveguide behind the scanner bore and onto an acrylic screen. The image presented had a resolution of 1920 x 1080 and a refresh rate of 120Hz. Participants viewed this screen at a viewing distance of 57cm using a mirror within the scanner. Gamma correction was performed using a customized MR-safe 'Spyder4' (Datacolor, NJ, USA) display calibrator.

5.3.3.2 fMRI Data Acquisition

Scans were completed on a GE Healthcare 3 Tesla Sigma HDx Excite scanner (GE Healthcare, Milwaukee, WI). Structural scans were obtained using an 8-channel head coil (MRI Devices Corporation, Waukesha, WI) to minimize magnetic field inhomogeneity. Functional scans were obtained with a 16-channel posterior head coil (Nova Medical, Wilmington, MA) to increase signal-to-noise in the occipital lobe.

5.3.3.3 Pre-processing of structural and functional scans

Two high-resolution, T1-weighted full-brain anatomical structural scans were acquired for each participant (TR, 7.8ms; TE, 3.0ms; TI, 450ms; voxel size, 1 x 1 x 1mm^3; flip angle, 20°; matrix size, 176 x 256 x 257). To improve grey-white matter contrast, the two T1 scans were aligned and then averaged together using FSL tool FLIRT (Jenkinson, Beckmann, Behrens, Woolrich, & Smith, 2012). This averaged T1 was automatically segmented using a combination of FreeSurfer (http://surfer.nmr.mgh.harvard.edu/) and FSL, and manual corrections were made to the segmentation using ITK-SNAP (http://www.itksnap.org/pmwiki/pmwiki.php) (Teo, Sapiro, & Wandell, 1997). At the beginning of each functional session, one 16-channel coil T1-weighted structural scan with the same spatial prescription as the functional scans was acquired to aid in the alignment of functional data to the T1-weighted anatomical structural scan.

Functional data were pre-processed and analysed using MATLAB 2016a and VISTA software (https://vistalab.stanford.edu/software/) (Vista Lab, Stanford University). Between and within scans motion correction was performed to compensate for any motion artefacts that occurred during the scan session. Any scans with >3mm movement were removed from the analysis. This resulted in the removal of one pRF run for two participants and one temporal contrast sensitivity scan for three participants. Functional runs were averaged across all scans. Next, we used mrVista tool rxAlign to co-register the 16-chanel coil T1-weighted structural scan to the 8-channel coil T1-weighted full-brain anatomical scan. First, we applied a manual alignment by using landmark points to bring the two volumes into approximate register. Next, we used a robust EM-based registration algorithm as described by Nestares & Heeger (2000) to fine tune the alignment. The final alignment was checked by eye to ensure that the automatic registration procedure optimised the fit. This alignment was used as a reference to align our functional data to our full-brain anatomical scan. These functional data were then interpolated to the anatomical segmentation.

5.3.3.4 Population Receptive Field Mapping Scans

pRF scan sessions consisted of six 6.5-minute pRF stimulus presentation runs collected using a standard EPI sequence (TR, 3000ms; TE, 30ms; voxel size, 2 x 2 x 2.5 mm^3, flip angle 20°; matrix size, 96 x 96 x 39). Here, a drifting pRF bar stimulus was used to obtain retinotopic maps and estimates of pRF parameters (Dumoulin & Wandell, 2008). A single bar (width

0.5°) was swept in one of eight directions within a circular aperture (10° radius) with each sweep lasting 48s. Using the conversion of visual angle to retinal eccentricity, 10° radius corresponds to mapping 2.83mm radius retinal space (Drasdo & Fowler, 1974). To stimulate a broad population of neurons, the pRF carrier consisted of pink noise at 5% contrast, where the noise pattern changed at 2Hz (see Figure 5.2). A 12s (4TR) dummy run was included at the beginning of each functional run to allow for the scanner magnetization to reach a steady state. To maintain fixation throughout the scan, participants completed an attentional task where they responded, via button press, when the orientation of the fixation cross changed. This task was set up so that on average, every 2 seconds there was a 30% chance of a change in the orientation of the fixation cross.

Figure 5.2 Example of the stimulus used to obtain pRF parameter estimates. The carrier is filled with pink noise that updates at 2Hz as it drifts across the screen in 8 directions within a circular aperture of 10° radius.

Using mrVista, pRF positions (i.e. eccentricity and polar angle parameters) and sizes were estimated for each voxel using the standard pRF model (Dumoulin & Wandell, 2008). In Figure 5.3 we present exemplar eccentricity, polar angle, and pRF size maps from one participant. Following the nomenclature of Wandell et al. (2007) we delineated five bilateral regions of interest (ROIs); V1, V2, V3, V3a, and hV4, by hand on cortical flat maps based on polar angle reversals for each participant (see Figure 5.3B).

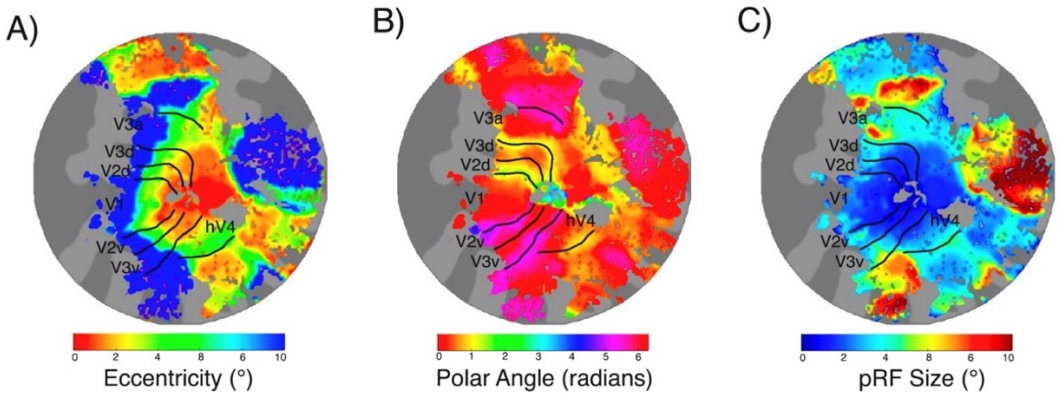

Figure 5.3 Exemplar left hemisphere retinotopic maps with ROI border overlays presented on flattened cortical representations for one subject. In A) we present eccentricity maps in which pRF eccentricity increases with distance from the fovea. In B) we present polar angle maps, with border overlays based on polar angle reversals. In C) we present pRF size maps, that show an increase in pRF size within and between ROIs.

5.3.3.5 Temporal Contrast Sensitivity (TCS) Functional Scans

5.3.3.5.1 Stimulus

To investigate voxel temporal contrast sensitivity, we presented participants with a vertically oriented contrast reversing sine grating within a circular aperture (10° radius). The stimulus was generated and presented using MATLAB 2016a and Psychtoolbox v.3.0.13 (David H. Brainard, 1997). We modulated both the contrast and temporal frequency of the grating. Within each functional run the sine wave grating was presented at 20 condition combinations of Michelson contrast (1, 4, 8, 16, and 64%) and temporal frequency flicker (1, 5, 10, and 20Hz) (Michelson, 1927). The spatial frequency of the grating was held at 1 cpd. Each stimulus condition was presented once per run and lasted 3 seconds. A baseline condition of mean luminance was presented for 3 seconds during each run. Here, a single contrast reversal was defined as one complete on-off cycle off the stimulus. A visual representation of the experimental design is illustrated in Figure 5.4.

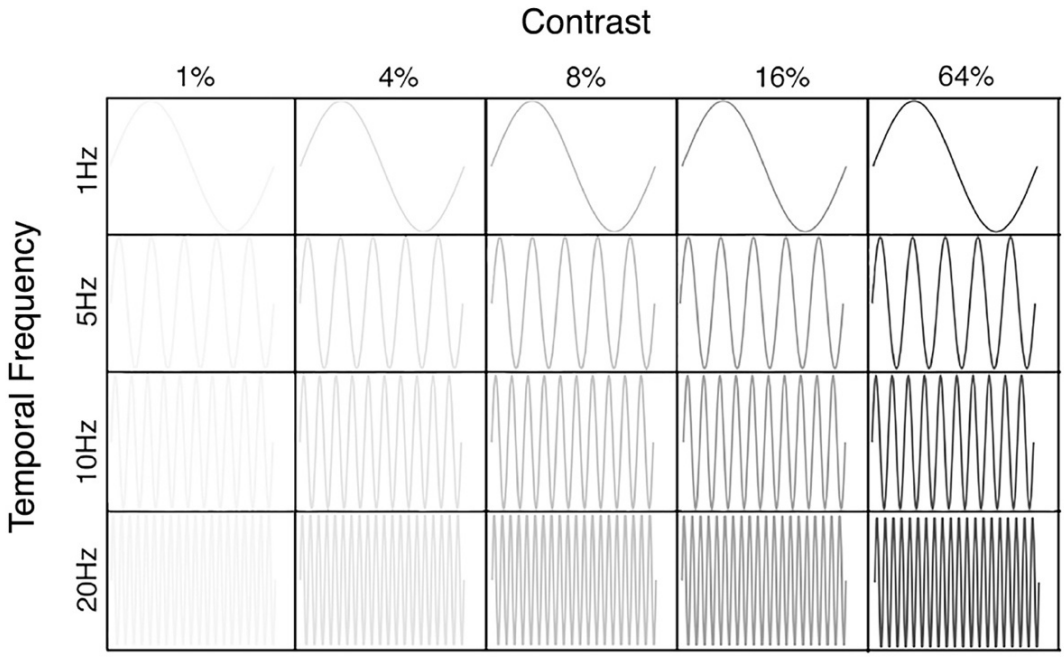

Figure 5.4 Visual representation of temporal contrast stimulus conditions. The sine wave grating sweeps through 20 temporal contrast conditions, with each condition being presented once per run for 3 s.

5.3.3.5.2 Data acquisition and analysis

TCS functional scan sessions consisted of ten 3.5-minute stimulus presentation runs collected using an almost identical EPI sequence to that used for the pRF mapping (TR, 3000ms; TE, 30ms; voxel size, 2 x 2 x 2.5 mm^3, flip angle 20°; matrix size, 96 x 96 x 39). The stimulus was presented using an event related design in which condition ordering was randomized within each run. A randomized interstimulus interval separated each condition and was jittered to last on average 6 seconds. Again, a 12 second (4TR) dummy run was included at the beginning of each functional run to allow for the scanner magnetization to reach a steady state. Participants completed the same attentional task as the pRF runs throughout the experiment.

TCS data were analysed using MATLAB 2016a and VISTA software. A general linear model (GLM) was implemented to test the contribution of stimulus condition to the BOLD time course (Friston et al., 1998). We used the default two-gamma Boynton HRF from SPM5 and fit the model to an averaged time course of BOLD signal changed for each stimulus condition by minimizing the sum of squared errors (RSS) between the predicted time series and the measured BOLD response. This resulted in 20 Beta weight estimates for each voxel, reflecting sensitivity to each stimulus condition.

5.3.4 Statistical Analysis

5.3.4.1 Plotting Beta Weights as a Function of pRF Parameters

Only pRF and TCS voxels with ≥10% variance explained were retained for further analysis. The pooled total voxel count for each ROI and the total voxels removed for falling below 10% variance explained are presented in Table 5.1. For each voxel within each participant's ROI, a pRF eccentricity value and a pRF size value was extracted from the pRF data. The same ROIs were then overlaid on each corresponding participants TCS data and 20 beta weights (1 beta weight per stimulus condition) were extracted for each voxel. Thus, each voxel was allocated 22 values: a pRF eccentricity value, a pRF size value, and 20 beta weights reflecting voxel sensitivity to each TCS stimulus condition. Polar angle values were not included in the analysis.

Table 5.1 Results of voxel thresholding. Voxels with less than 10% VE in both the pRF and the TCS data are removed from further analysis (N=19).

ROI	Pooled total voxels	< 10% VE	% removed
V1	77693	34314	44.16%
V2	76991	32555	42.28%
V3	70977	26907	37.81%
V3a	55659	23235	41.75%
hV4	25388	12589	49.59%

For each participant, beta weights were plotted as a function of pRF eccentricity; foveal, parafoveal, or peripheral. For each ROI, foveal pRFs were defined as being between 0.2° - 3.0° eccentricity, parafoveal pRFs were defined as being between 3.0° - 6.0° eccentricity, and peripheral pRFs were defined as being between 6.0° - 10.0° eccentricity. Visualisation of how these data are partitioned and their correspondence to visual space is illustrated in Figure 5.5.

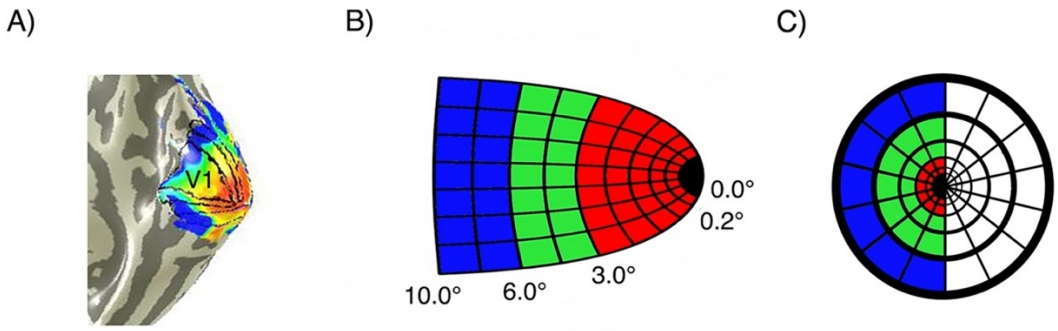

Figure 5.5 Voxels are binned into 3 gradients of eccentricity – foveal (red), parafoveal (green), and peripheral (blue). In A) we present an eccentricity map on a right hemisphere mesh of the visual cortex with overlaid hand drawn ROIs, noting the location of V1. B) shows how these voxel bins would be represented on a schematic model of right hemisphere V1. In C) we present how the voxel bins in B) would be spatially tuned (ignoring polar angle) across the contralateral visual field.

pRF size and eccentricity are highly related measures: average pRF sizes increase with eccentricity (Dumoulin & Wandell, 2008). For completeness, we additionally analysed our data as a function of pRF size to complement the eccentricity-based analysis. Each participant's beta weights were plotted as a function of pRF size; small or large. Receptive field sizes progressively increase as one moves up the visual hierarchy and what constitutes a 'small' or 'large' pRF will differ depending on ROI (Wandell et al., 2007). To account for this, within each ROI, 'small pRFs' were defined as having a size value between 0.25° (as a hard minimum) and the median pRF size, whilst 'large pRFs' were defined as a size value between the median and the maximum pRF size (with a maximum cut off of 10°). These normalized

pRF sizes are presented in Appendix Table A5.1 and the pRF size analysis is presented in the Appendix B5.1.

5.3.4.2 Contrast response functions

For each participant's ROIs, hyperbolic ratio functions were fitted at each of the four temporal frequencies for each eccentricity partition of data. We modelled contrast response using the following equation:

$$R(\mathrm{C}) = R_0 + R_{\max} \frac{c^n}{c_{50}^n + c^n}$$

Equation 5.1 Equation for fitting contrast response functions to fMRI data

Where C is stimulus contrast, R_0 is the baseline response, $R_{\max}$ is the maximum response rate, c_{50} is the semi saturation contrast, and the exponent, n, is the rate at which changes occur and was held at 2 (Albrecht & Hamilton, 1982; Boynton, Demb, Glover, & Heeger, 1999). This resulted in four contrast response functions (CRFs) per ROI at each eccentricity for each participant (i.e. each participant had four CRFs within V1 foveal, four CRFs within V1 parafoveal, and four CRFs within V1 peripheral).

From each CRF we extracted C_{50}, the contrast semisaturation point. This is the amount of contrast required to elicit half the maximum response of the CRF. A decrease in C_{50} results in a leftward shift in the CRF, indicating that less contrast is required to hit this 50% response, thus, is representative

of an increase in contrast sensitivity (Albrecht & Hamilton, 1982). Illustration of such a shift in C_{50} is presented in Figure 5.6.

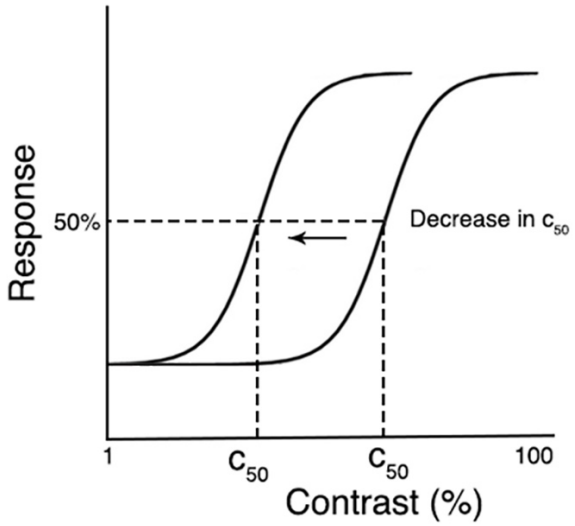

Figure 5.6 C_{50} plotted on two contrast response functions. C_{50} decreases when the CRF is shifted left, thus less contrast is needed to hit 50% of the full response, reflecting an increase contrast sensitivity.

5.3.4.3 Analysis - Repeated Measures ANOVAs

For our psychophysical experiment, we carried out a 4 (temporal frequency) x 2 (eccentricity) repeated measures ANOVA with 75% contrast detection thresholds as the dependent variable and looked at simple effects to compare between conditions. For our fMRI experiment we ran a 5 (ROI) x 4 (temporal frequency) x 3 (pRF eccentricity) repeated measures ANOVA with C_{50} as the dependent variable and looked at simple effects analyses to answer our targeted predictions.

5.3.4.4 Polynomial fits and bootstrapping

To find the temporal frequency at which contrast sensitivity peaks at each eccentricity and within each ROI (or for psychophysics, at the two visual field locations tested) we used MATLAB function 'bootstrp' to bootstrap 2000 second order polynomial fits (generated using MATLAB function 'polyfit') to the means of random permutations of our C_{50} data (fMRI) and contrast detection thresholds (psychophysics). These data were permutated using random sampling (19 draws) with replacement. We then found the mean of the zero points of the first derivatives of each of the 2000 second order polynomial fits. This point reflects the average level of temporal frequency at which contrast sensitivity peaks.

5.4 Results

Our psychophysical data were broadly consistent with those from previous studies indicating little difference in temporal frequency tuning between fovea and near-periphery, and an overall 'U' shaped temporal frequency threshold tuning function with a minimum contrast threshold (peak sensitivity) around 8Hz. In our imaging data, we found profound changes in C_{50} as a function of both temporal frequency and pRF eccentricity. First, we found all visual areas studied had an overall (i.e. ignoring any effects of eccentricity) peak in contrast sensitivity at 10Hz. Next, in early visual areas we found that pRFs representing the peripheral visual field had increased contrast sensitivity at a high temporal frequency (20Hz) when compared to pRFs representing the fovea – consistent with effects predicted from retinal

physiology. This difference disappeared in area hV4, where no consistent eccentricity-dependent difference in contrast sensitivity at any temporal frequency could be measured. We fed our 20Hz C_{50} measurements from all ROIs into a linear model and found that hV4 had the highest contribution to a fit of psychophysical contrast sensitivity. Overall, we find that contrast sensitivity in the periphery of V1, V2, V3, and V3a is increased at a high temporal frequency, but this sensitivity is lost in hV4 as cortical tuning becomes more similar that of the psychophysical observer. Here we present a summary of our results for our psychophysical and fMRI data. Supporting pRF size results are available in Appendix C5.

5.4.1 Psychophysical Results: Contrast sensitivity

A 2 x 4 repeated measures ANOVA was performed to assess whether there was a difference in psychophysical contrast detection thresholds between eccentricity and temporal frequency. Mauchly's test of Sphericity was violated for both the main effect of temporal frequency ($\chi^2(5) = 42.321$, $p < .001$) and the temporal frequency * eccentricity interaction effect ($\chi^2(5) = 11.619$, $p = .041$). Thus, a Greenhouse-Geisser correction was applied to the results of these effects.

The analysis found a significant main effect of temporal frequency ($p < .001$) and a significant eccentricity * temporal frequency interaction effect ($p < .001$). F-values and p-values are presented in Appendix Table A5.2. As illustrated in Figure 5.7A, contrast detection thresholds were higher at 1Hz

when presented at 2° eccentricity ($p < .000$). Conversely, at 20Hz, contrast detection thresholds were higher at 10° eccentricity ($p < .000$). Thresholds significantly differed as a function of temporal frequency across both eccentricities, except for comparing between 5Hz and 10Hz. All p-values are presented in Appendix Tables A5.3 and A5.4.

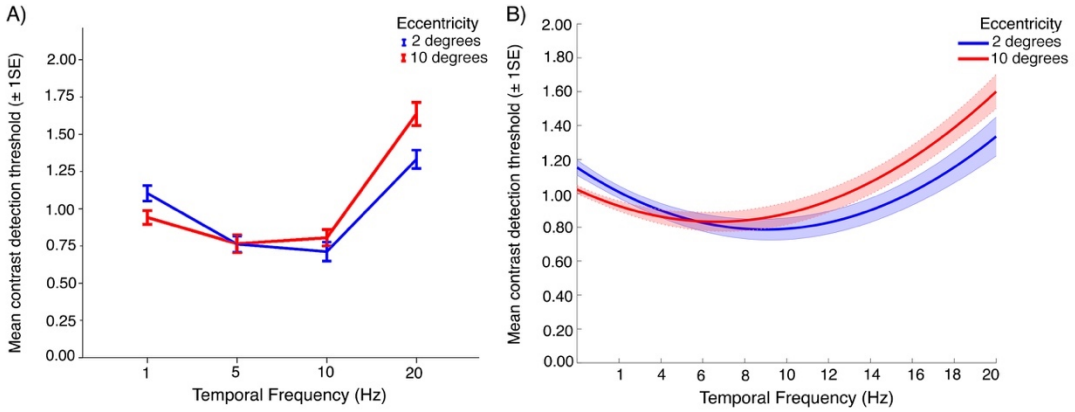

Figure 5.7 Psychophysical contrast detection thresholds plotted as a function of temporal frequency, at two eccentricities. In A) we present contrast detection thresholds plotted at four measured temporal frequencies at 2° and 10°. In B) we present bootstrapped fits to contrast detection thresholds plotted as a function of temporal frequency at 2° and 10°. Overall, there is little difference in sensitivity at each temporal frequency between fovea and near periphery.

5.4.1.1 Psychophysical temporal frequency optima

To find the temporal frequency at which contrast sensitivity peaks, we looked at the mean zero point of the first derivatives of bootstrapped polynomial fits to our psychological threshold data. At 2° eccentricity contrast

sensitivity peaked at 9Hz, while at 10° eccentricity contrast sensitivity peaked at 6.6Hz. Bootstrapped fits are presented in Figure 5.7B and mean zero points are presented in Appendix Table B5.1.

5.4.2 fMRI Results

A 5 x 4 x 3 repeated measures ANOVA was performed to assess whether there was a difference in contrast sensitivity between ROIs, temporal frequency, and eccentricity. Mauchly's test of Sphericity was violated for the main effect of ROI ($\chi^2(5) = 22.062$, $p = .009$) and the interaction effects for ROI * eccentricity ($\chi^2(35) = 52.540$, $p = .036$), ROI * temporal frequency ($\chi^2(77) = 121.003$, $p = .003$), and eccentricity * temporal frequency ($\chi^2(20) = 42.136$, $p = .003$). Thus, a Greenhouse-Geisser correction was applied to the results of these effects. The analysis found significant main effects for eccentricity ($p = .004$) and temporal frequency ($p = .007$). F-values, *p*-values, and effect sizes for main and interaction effects are presented in Appendix Table A5.5.

5.4.2.1 Contrast sensitivity peaks around 10Hz in all ROIs

First, we used a simple effects analysis to explore differences in contrast sensitivity by comparing between the four temporal frequencies, collapsed across pRF eccentricity, within each individual ROI. Sidak corrections were applied to all possible comparisons. As presented in Figure 5.8, V1, V2, V3, and V3a had significantly reduced C_{50} at 10Hz when compared to 1Hz and 20Hz ($p < .05$), reflecting increased contrast sensitivity at this temporal frequency. In hV4, C_{50} was significantly reduced at 10Hz when

compared to 20Hz (p = .004). P-values for these simple effects are presented in Appendix Table A5.6.

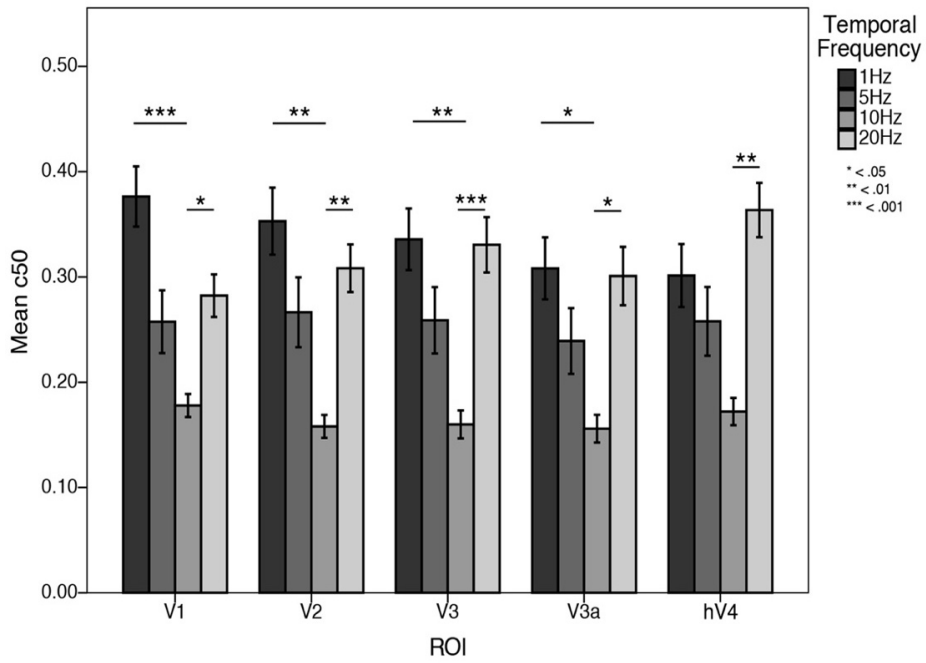

Figure 5.8 Mean C_{50} values plotted as a function of temporal frequency for each ROI. C_{50} is consistently reduced at 10Hz in all ROIs, indicating contrast sensitivity peaks at 10Hz in all regions tested.

5.4.2.2 fMRI temporal frequency optima

As we did with our psychophysical data, we looked at the mean zero point of the first derivatives of the bootstrapped polynomial fits to our C_{50} values to find, for each ROI and eccentricity, the temporal frequency at which contrast sensitivity peaks. These zero points are presented in Appendix Table B5.2 and examples of bootstrapped fits are illustrated in Figure 5.9. In V1 and V2, the optimal temporal frequency gradually increased with eccentricity. However, in V3 and V3a the optimal temporal frequency increased from foveal to parafoveal. In hV4 the optimal temporal frequency is essentially identical

between the foveal and parafovea. Fits to the data in the periphery of hV4 (see hV4 of Figure 5.9) were almost linear and no peak could be computed reliably. We attribute this to variability within the hV4 C_{50} estimates that were derived from the bootstrapping procedure. Thus, the peripheral hV4 fits presented here appear to differ when compared to the corresponding mean hV4 C_{50} values as presented in Figure 5.10.

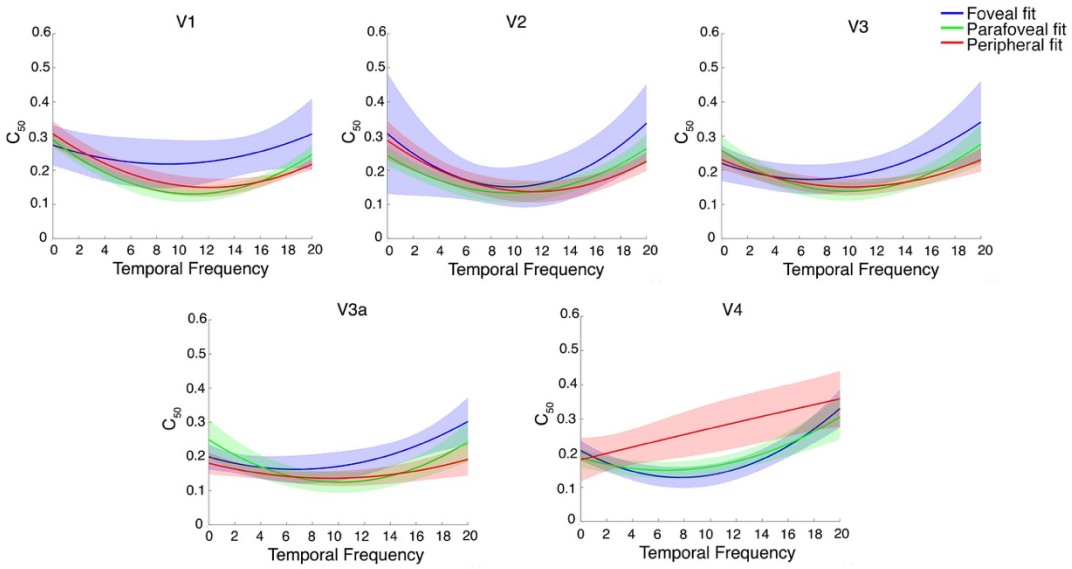

Figure 5.9 Examples of bootstrapped polynomial fits to C_{50} values plotted as a function of temporal frequency for each eccentricity in all ROIs. The solid line is a second-order bootstrapped polynomial fit to the data and the shaded outline is the standard deviation of 2000 permutations.

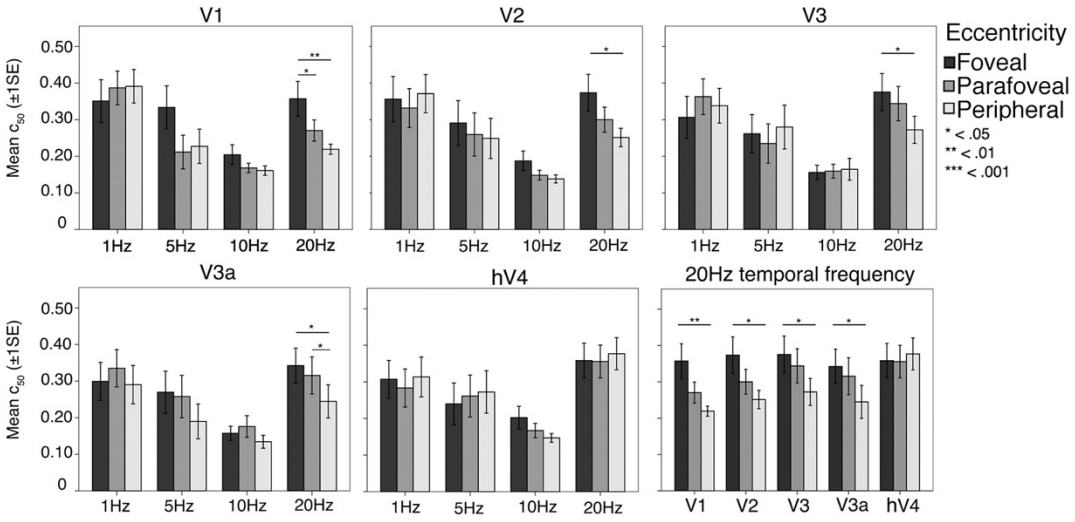

Figure 5.10 Mean C_{50} values plotted as a function pRF eccentricity at each temporal frequency, for each ROI. In V1-V3a, C_{50} is significantly reduced at 20Hz in peripheral pRFs, reflecting increased contrast sensitivity at 20Hz in the cortical periphery. This effect disappears in hV4, where C_{50} is flat across eccentricity at each temporal frequency.

5.4.2.3 Peripherally tuned pRFs have increased contrast sensitivity at 20Hz in V1, V2, V3, and V3a

A simple effects analysis was undertaken to explore differences in contrast sensitivity within each ROI at each temporal frequency, comparing between foveal, parafoveal, and peripherally tuned pRFs. Sidak corrections were applied to all possible comparisons. Mean C_{50} values at all temporal frequencies and at 20Hz alone are presented in Figure 5.10. We found eccentricity-dependent differences in contrast sensitivity at 20Hz. Namely, we found that in V1, V2, V3, and V3a, C_{50} at 20Hz was consistently decreased in peripherally tuned pRFs when compared to foveally tuned pRFs ($p < .05$), reflecting increased contrast sensitivity at a high temporal frequency in the

cortical periphery. There was no difference in contrast sensitivity as a function of eccentricity at 1, 5, or 10Hz, in any ROI. In Figure 5.11 we present a surface-based average (N=19) contrast sensitivity map at 20Hz, projected onto an inflated cortical mesh. Similar to previous psychophysical sensitivities, contrast sensitivity in hV4 was invariant across eccentricity at all temporal frequencies tested, including 20Hz. All p-values are presented in Appendix Table A5.7.

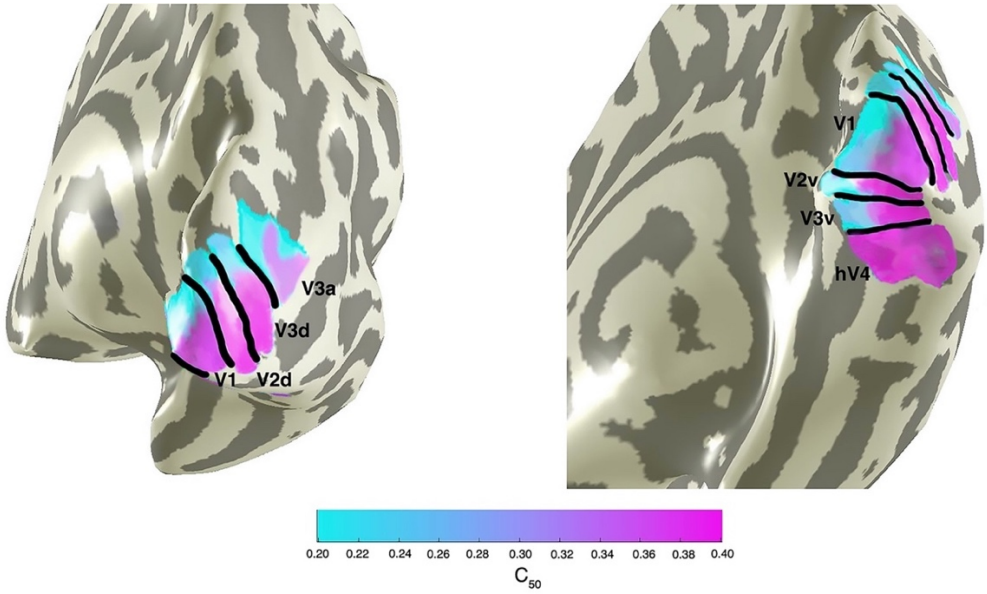

Figure 5.11 Mean contrast sensitivity maps at 20Hz projected onto a cortical mesh (N=19). Early visual field maps V1-V3a show decreasing C_{50} (indicating increasing contrast sensitivity) with increasing eccentricity, whilst contrast sensitivity in hV4 is invariant (and relatively low) across space.

5.4.3 Comparing psychophysical and fMRI contrast sensitivities

Unlike earlier visual areas, we found that contrast sensitivity at 20Hz in hV4 was relatively invariant across eccentricity. This finding is more similar to psychophysical sensitivities from our own and other behavioural studies that

report little difference in temporal contrast sensitivity across visual space (Koenderink et al., 1978; Virsu et al., 1982; Wright & Johnston, 1983). Next, we aimed to examine the relationship between psychophysical performance and fMRI signals driven by 20Hz stimuli. Here, we bootstrapped 1000 estimates of 20Hz fMRI C_{50} measurements from the fovea and periphery of each ROI, and fed this data into a linear model to assess how each ROI contributed to a fit of psychophysical contrast sensitivity at 20Hz. As illustrated in Figure 5.12, we found that C_{50} values from hV4 contributed proportionally more to our psychophysical measurements when compared to early visual areas, indicating that fMRI responses from this area best predict our psychophysical measurements. Bootstrapped beta weight statistics are available in Appendix Table B5.3.

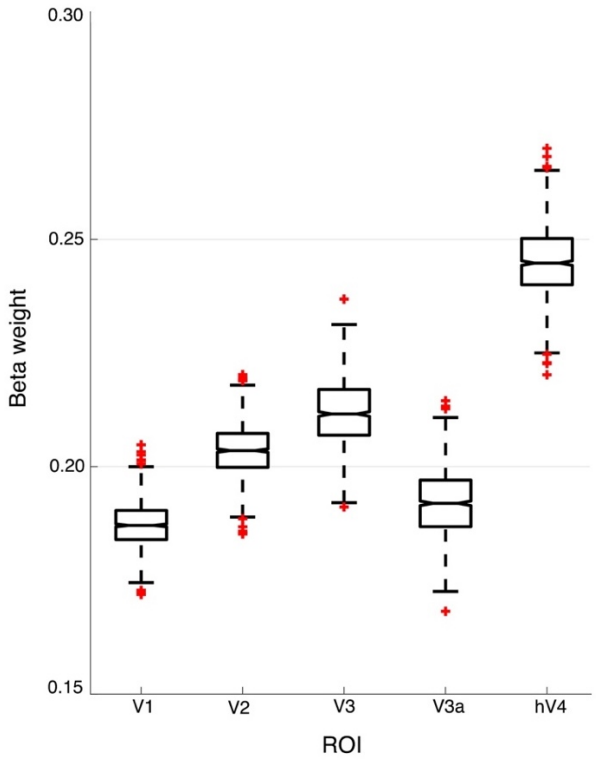

Figure 5.12 Median bootstrapped beta weights after predicting a fit of psychophysical contrast sensitivity using C_{50} measurements at 20Hz from each ROI. hV4 has the highest beta weight, indicating that this region is the best predictor of psychophysical contrast sensitivity at 20Hz.

5.5 Discussion

We have measured differences in psychophysical and cortical contrast sensitivity that occur as a function of temporal frequency and visual field eccentricity. Overall, our findings indicate that both psychophysical and cortical contrast sensitivity follow a 'U' shape function and is maximal between 8-12Hz across visual space. Further, in early visual areas there is a relative increase in contrast sensitivity at 20Hz in pRFs tuned to more peripheral regions of the visual field. We discuss these findings in light of the physiological bias towards faster visual processing and increased contrast

sensitivity in the peripheral retina. As we progressed up the visual pathway to visual area hV4, we observed an equalisation of temporal contrast sensitivity across eccentricity that was closer to psychophysical measurements, suggesting that the peripheral bias in retinal temporal contrast sensitivity disappears in this cortical area.

5.5.1 Peak psychophysical and fMRI contrast sensitivity

Previous research has typically measured the primate visual system's sensitivity to temporal frequency at a single level of contrast. These studies invariably identify a bandpass peak in temporal sensitivity occurring at approximately 8Hz (Hawken et al., 1996; Kastner et al., 2004; Kwong et al., 1992; Robson, 1966b; Singh et al., 2000; Venkataraman et al., 2017). Our approach was similar to these studies, except that we fit a CRF to a range of contrasts presented at different temporal frequencies, then defined our measurement of contrast sensitivity as 50% of the full CRF response (C_{50}). Our data showed a similar bandpass pattern. Peak psychophysical contrast sensitivity occurred at 9Hz and 6.6Hz at 2° and 10° eccentricity, respectively. Similarly, in our fMRI data we found contrast sensitivity generally peaked around 8Hz, with the critical frequency of this peak increasing between foveal and peripheral voxels. In this respect, the overall 'U' shape of our behavioural and cortical contrast sensitivity functions appears to be matched from a relatively early stage in the visual hierarchy.

Perhaps surprisingly, previous research has found little change in psychophysical temporal contrast sensitivity as a function of eccentricity (Koenderink et al., 1978; Rovamo & Raninen, 1984; Virsu et al., 1982). Although our own psychophysical data showed a slight decrease in temporal contrast sensitivity from the fovea to the near periphery, these differences were relatively small and may reflect difficulties in compensating precisely for cortical magnification effects or stimulus sizing in our own psychophysics (Granit & Harper, 1930; Hassan, Thompson, & Hammett, 2016).

5.5.2 Peripherally tuned pRFs have increased contrast sensitivity at 20Hz

Physiological biases in the response properties of retinal cells lead to increased temporal contrast sensitivity in more peripheral regions of the retina. Peripheral cones respond faster than foveal cones resulting in greater peripheral sensitivity to rapidly changing input (Sinha et al., 2017). There is also an eccentricity-dependent increase in the ratio of parasol to midget RGCs, and parasol cells are relatively more sensitive to high temporal frequencies and have increased contrast gain when compared to midget cells (Connolly & van Essen, 1984; Dacey, 1993, 1994; Dacey & Petersen, 1992; De Monasterio & Gouras, 1975; Schein & de Monasterio, 1987). At 10° eccentricity, measurements of temporal contrast sensitivity are thought to reflect more isolated functions of parasol RGCs (Croner & Kaplan, 1995; Gouras, 1968; Kaplan, Lee, & Shapley, 1990; Kaplan & Shapley, 1986). Signals passed from RGCs pass through the LGN, where the density of afferent parasol and midget RGCs is maintained, before being sent to primary

visual cortex (Connolly & van Essen, 1984; Schein & de Monasterio, 1987). Our data show that a sensitivity bias similar to that found in the retina and LGN is present in early visual cortex, with relatively increased contrast sensitivity at 20Hz in peripherally tuned voxels.

It is well known that neuronal spatial frequency sensitivity tends to be inversely related to temporal frequency sensitivity, thus, channels sensitive to low spatial frequencies are often sensitive to higher temporal frequencies (and vice versa). In addition, the sensitivity of these channels changes as a function of eccentricity (D'Souza, Auer, Frahm, Strasburger, & Lee, 2016; Henriksson, Nurminen, Hyvarinen, & Vanni, 2008; Kulikowski & Tolhurst, 1973; Shoham, Hübener, Schulze, Grinvald, & Bonhoeffer, 1997; Sun et al., 2007). Here, we report measurements made at a single spatial frequency (1 cpd). This frequency was chosen because it is well below the spatial resolution limit at the highest eccentricities measured, yet generates robust responses in the fovea (D'Souza et al., 2016; Henriksson et al., 2008; Welbourne, Morland, & Wade, 2018). It is possible that our results would change if a different spatial frequency was used: altering the base spatial frequency might, for example, alter the balance of parvo- to magnocellular cells contributing to the stimulus at each eccentricity, which would, in turn, alter the average temporal response properties (Levitt et al., 2001).

5.5.3 hV4 is similar to the psychophysical observer

Unlike earlier visual areas, we found that temporal contrast sensitivity does not significantly differ as a function of eccentricity in hV4. Specifically, there appears to be little bias towards higher temporal contrast sensitivity in more peripheral regions of hV4. Instead, temporal contrast sensitivity in hV4 is more reflective of the behavioural observer. After bootstrapping a linear model to assess the contribution of our 20Hz C_{50} data to a fit of psychophysical measurements, we found that hV4 had a proportionally greater contribution to psychophysical sensitivities when compared to all other visual areas. It may be that higher order areas become increasingly invariant to eccentricity-dependent differences in low-level features, including contrast and temporal frequency, and instead represent more complex stimulus aspects relating to shape, identity, and colour (Avidan et al., 2002; Felleman & Van Essen, 1991; Milner & Goodale, 1995; Perry & Fallah, 2014). For example, hV4 has previously been found to have a much coarser representation of spatial frequency and an increased tolerance to temporal dynamics when compared to earlier visual areas, suggesting these areas are less concerned with such low level visual properties (Henriksson et al., 2008; Zhou, Benson, Kay, & Winawer, 2017). In a similar vein, ventral regions local to hV4 that are concerned with global form and object representations such as FFA, PPA, VO, and LOC, have at times found to be invariant to lower level visual features, and fMRI responses within such regions can become impaired when stimuli are presented at high temporal frequencies (D'Souza, Auer, Strasburger, Frahm, & Lee, 2011; Grill-Spector et al., 1999; Jiang, Zhou, & He, 2007;

Kanwisher, 2010; Liu & Wandell, 2005; Mckeeff, Remus, & Tong, 2007; Vernon, Gouws, Lawrence, Wade, & Morland, 2016). Although this bias in retinal temporal contrast sensitivity is phased out by hV4, our data found that this area also responds optimally around 10Hz temporal frequency – perhaps inheriting this sensitivity bias from earlier regions.

5.6 Conclusion

Our experiments have found that in general, psychophysical and fMRI measurements of contrast sensitivity are relatively consistent and both peak around 8Hz. Next, pRFs in early visual areas that represent more peripheral regions of visual space show relatively increased contrast sensitivity at a high temporal frequency when compared to those in the cortical representation of the fovea. However, this bias in peripheral cortical contrast sensitivity disappears by hV4, suggesting a relative independence of temporal contrast sensitivity across space in this area. This independence is broadly consistent with behavioural measurements of temporal contrast sensitivity and suggests that neurons in area hV4 (and possibly other higher-order ventral regions) are relatively invariant to the eccentricity-dependent biases that are present in the early visual stream.

5.7 Appendix A5

Statistical output for pRF size normalisation statistics, ANOVA main effects, and simple effects analyses (*<.05, **<.01, ***<.001).

Table A5.1 Normalized pRF sizes for each ROI (N=19). For each ROI, small pRFs fall between the minimum and median pRF size, and large pRFs fall between median and maximum pRF size.

Visual Area	Min pRF size	Median pRF size	Max pRF size
V1	0.25°	1.72°	9.89°
V2	0.25°	2.06°	9.30°
V3	0.25°	2.89°	9.74°
V3a	0.25°	4.06°	10.0°
hV4	0.25°	4.7°	10.0°

Table A5.2 Tests of within-subject effects for psychophysical data. Temporal frequency and eccentricity as IVs, and contrast detection threshold as DV.

Source	df	F	pη²	p
Temporal Frequency (GG)	1.895	88.179	.830	.000***
Eccentricity	1	3.824	.175	.066
TF*Eccentricity (GG)	2.210	23.459	.566	.000***

Table A5.3 Simple effects comparisons for psychophysical data. Differences in contrast detection thresholds, comparing between two factors of eccentricity at each temporal frequency (N=19).

Temporal Frequency		10 degrees
1Hz	2 degrees	.000***
5Hz	2 degrees	.946
10Hz	2 degrees	.057
20Hz	2 degrees	.000***

Table A5.4 Simple effects comparisons for psychophysical data. Differences in contrast detection thresholds, comparing between four factors of temporal frequency at each eccentricity (N=19).

Eccentricity		5Hz	10Hz	20Hz
	1Hz	.000***	.000***	.023*
2 degrees	5Hz	-	.324	.000
	10Hz	-	-	.000***
	1Hz	.000***	.019*	.000***
10 degrees	5Hz	-	.277	.000***
	10Hz	-	-	.000**

Table A5.5 Tests of within-subject effects for fMRI data. ROI, eccentricity, and temporal frequency as IVs, and C_{50} as DV (N=19).

Source	df	F	*P*	power
ROI (GG)	2.749	.684	.554	.177
Eccentricity	2	6.403	.004**	.875
TF	3	4.466	.007**	.853
ROI*Eccentricity (GG)	4.334	2.158	.077	.838
ROI*TF (GG)	5.977	1.638	.145	.602
Eccentricity*TF (GG)	2.911	2.132	.110	.504
ROI*Eccentricity*TF	24	1.314	.148	.927

Table A5.6 Simple effects for fMRI data. Differences in C_{50}, comparing between four factors of temporal frequency within each ROI (N=19).

Visual Area		5Hz	10Hz	20Hz
V1	1Hz	.281	.000***	.295
	5Hz	-	.287	.999
	10Hz	-	-	.010*
V2	1Hz	.682	.006**	.960
	5Hz	-	.279	.990
	10Hz	-	-	.004**
V3	1Hz	.676	.007**	1.000
	5Hz	-	.449	.909

	10Hz	-	-	.007*
V3a	1Hz	.813	.045*	1.000
	5Hz	-	.642	.919
	10Hz	-	-	.037*
hV4	1Hz	.969	.124	.924
	5Hz	-	.595	.549
	10Hz	-	-	.004**

Table A5.7 Simple effects for fMRI data. Differences in C_{50}, comparing between three factors of eccentricity at each temporal frequency within each ROI (N=19).

			Parafoveal	Peripheral
V1	1Hz	Foveal	.913	.900
		Parafoveal	-	.994
	5Hz	Foveal	.072	.072
		Parafoveal	-	.963
	10Hz	Foveal	.284	.136
		Parafoveal	-	.358
	20Hz	Foveal	.026*	.008**
		Parafoveal	-	.061
	1Hz	Foveal	.993	.995
		Parafoveal	-	.763
	5Hz	Foveal	.827	.585

V2		Parafoveal	-	.763
	10Hz	Foveal	.302	.222
		Parafoveal	-	.214
	20Hz	Foveal	.319	.046*
		Parafoveal	-	.067
V3	1Hz	Foveal	.566	.922
		Parafoveal	-	.864
	5Hz	Foveal	.755	.893
		Parafoveal	-	.393
	10Hz	Foveal	.999	.996
		Parafoveal	-	.997
	20Hz	Foveal	.592	.034*
		Parafoveal	-	.086
V3a	1Hz	Foveal	.512	.938
		Parafoveal	-	.186
	5Hz	Foveal	.843	.191
		Parafoveal	-	.272
	10Hz	Foveal	.889	.610
		Parafoveal	-	.420
	20Hz	Foveal	.395	.016*
		Parafoveal	-	.033*
	1Hz	Foveal	.895	.997
		Parafoveal	-	.431

hV4	5Hz	Foveal	.957	.953
		Parafoveal	-	.995
	10Hz	Foveal	.481	.118
		Parafoveal	-	.174
	20Hz	Foveal	1.000	.928
		Parafoveal	-	.942

5.8 Appendix B5

Statistical output for bootstrapped psychophysics and fMRI data, and linear model results.

Table B5.1 Bootstrapped descriptive statistics psychophysical data (2000 iterations). Mean of the zero points of the first derivative of our bootstrapped fits to contrast threshold data, which is representative of the temporal frequency at which psychophysical contrast sensitivity peaks.

	Bootstrap Mean	Bootstrap Median	SD
2 degrees	9.00	8.92	.58
10 degrees	6.60	6.54	.57

Table B.2 Bootstrapped descriptive statistics for fMRI data (2000 iterations). Mean of the zero points of the first derivative of our bootstrapped fits to C_{50} data, which is representative of the temporal frequency at which fMRI contrast sensitivity peaks.

		Distribution Mean	Distribution Median
V1	Foveal	8.41	8.24
	Parafoveal	10.60	10.55
	Peripheral	12.10	12.03
V2	Foveal	7.59	7.34
	Parafoveal	9.10	9.06
	Peripheral	11.13	11.33
	Foveal	6.17	6.99

V3	Parafoveal	9.63	9.31
	Peripheral	9.53	9.47
V3a	Foveal	5.88	6.25
	Parafoveal	9.55	9.42
	Peripheral	9.16	9.02
hV4	Foveal	7.01	7.01
	Parafoveal	5.30	5.75
	Peripheral	-	-

Table B5.3 Bootstrapped beta weight estimates (1000 iterations) after feeding foveal and peripheral 20Hz C_{50} values into a linear model to assess how each ROI contributed to a fit of psychophysical contrast sensitivity.

ROI	Bootstrap Median Beta Weight
V1	0.18
V2	0.21
V3	0.22
V3a	0.19
hV4	0.24

5.9 Appendix C5

Both fMRI and electrophysiological research indicates that receptive field sizes generally become larger with increasing eccentricity (Wandell et al., 2007; Wandell & Winawer, 2015). In our own data we found that pRF size was positively correlated with visual field eccentricity in all ROIs (see Figure C5.1). In addition to an effect of pRF eccentricity, we asked whether similar biases in temporal contrast sensitivity would occur when we partitioned our data into pRF size. To investigate this, we partitioned our data into small and large pRF sizes to produce similar, although not identical, subsets of voxels and found similar effects when compared to pRF eccentricity partitioned data.

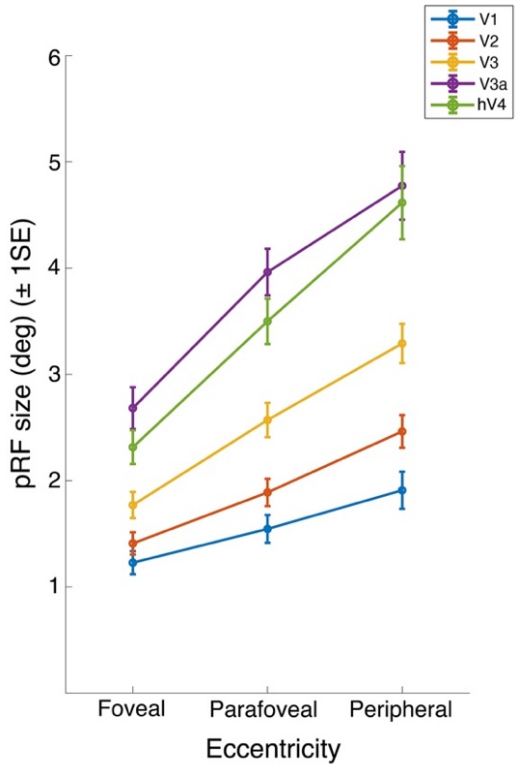

Figure C5.1 Average pRF sizes plotted against three levels of eccentricity. pRF sizes become larger as one moves towards the periphery.

Results

A 5 x 4 x 2 repeated measures ANOVA was performed to assess whether there was a difference in contrast sensitivity between ROIs, temporal frequency, and pRF size. Mauchly's test of Sphericity was violated for the main effect of ROI ($\chi2(9) = 20.736$, $p = .014$) and the interaction effects for pRF size * temporal frequency ($\chi2(5) = 14.710$, $p = .012$) and ROI * temporal frequency * pRF size ($\chi2(77) = 134.832$, $p < .000$). Thus, a Greenhouse-Geisser correction was applied to the results of these effects. The analysis found significant main effects of pRF size ($p < .000$), temporal frequency ($p = .003$), and a significant interaction effect between ROI * temporal frequency ($p < .000$). F-values, p-values, and effect sizes are presented in Table 5C.1.

Table 5C.1 Tests of within-subjects effects for fMRI C_{50} data. ROI, temporal frequency, and pRF size as IVs and C_{50} as DV (N=19).

	df	F	p	power
ROI (GG)	2.550	1.499	.231	.341
pRF size	1	21.651	.000***	.993
TF	3	5.261	.003**	.911
ROI*pRF size	4	.258	.904	.103
ROI*TF	12	3.442	.000***	.997
pRF Size*TF (GG)	2.080	3.004	.060	.559
ROI*pRF size*TF (GG)	6.363	1468	.192	.569

A simple effects analysis was undertaken to explore differences in contrast sensitivity within each ROI and at each temporal frequency, comparing between small and large pRF sizes. Sidak corrections were applied to all comparisons. Mean C_{50} values at all temporal frequencies and at 20Hz alone for small and large pRF sizes within each ROI are presented in Figure C5.2. Within all ROIs, C_{50} was significantly decreased in large pRFs compared to small pRFs at 20Hz ($p < .05$). Additionally, in V1 we found that C_{50} was decreased large pRFs at 10Hz ($p = .010$) and in V3a C_{50} was significantly decreased in large pRFs at 5Hz ($p = .016$). Our results here differed in hV4, where C_{50} was now significantly decreased in large pRFs compared to small pRFs at 20Hz ($p = .016$). All p-values are presented in Table C5.2.

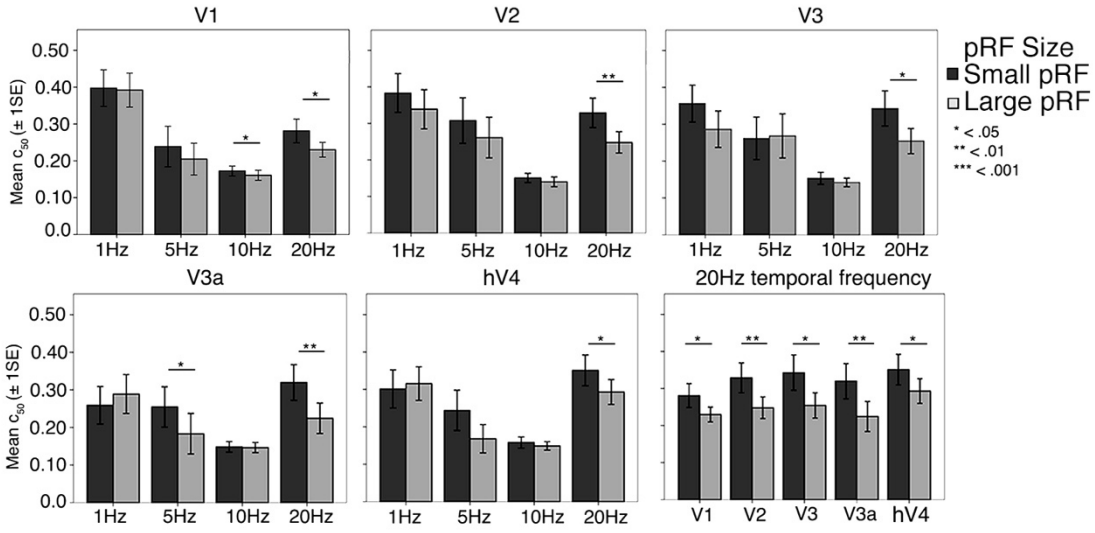

Figure C5.2 Mean C_{50} values plotted as a function of pRF size for each temporal frequency, in each ROI. In all ROIs, C_{50} in significantly reduced at 20Hz in larger pRF sizes.

Table C5.2 Simple effects for fMRI data. Differences in C_{50} for each ROI, comparing between small and large pRF sizes at each temporal frequency (N=19).

			Large
V1	1Hz	Small	.729
	5Hz	Small	.416
	10Hz	Small	.010*
	20Hz	Small	.028*
V2	1Hz	Small	.336
	5Hz	Small	.263
	10Hz	Small	.139
	20Hz	Small	.005**
V3	1Hz	Small	.200
	5Hz	Small	.735
	10Hz	Small	.198
	20Hz	Small	.013*
V3a	1Hz	Small	.336
	5Hz	Small	.016*
	10Hz	Small	.780
	20Hz	Small	.006**
hV4	1Hz	Small	.727
	5Hz	Small	.093
	10Hz	Small	.355

	20Hz	Small	.016*

Chapter 6

Measurements of achromatic and S-cone population receptive field (pRF) size across cortical depth in primary visual cortex.

6.1 Abstract

The receptive field size of a simple cell in primate visual cortex is linked with its spatial sensitivity. Within pre-cortical pathways, the spatial resolution of S-cone driven neurons in the koniocellular pathway is, on average, lower than that of the parvocellular pathway, which is driven by L- and M-cones. Here, we ask to what extent these differences in spatial sensitivity contribute to estimates of bulk neuronal population features in primary visual cortex, using population receptive field mapping (pRF) measurements derived from S-cone and achromatic mapping stimuli. If pRF measurements are dominated by simple cells, we might expect voxels to report larger receptive field sizes when mapped with S-cone isolating stimuli than when mapped with achromatic stimuli. Conversely, no difference in these pRF size estimates may indicate that pRF measurements are dominated by complex cells, whose sizes do not necessarily correspond to their spatial frequency tuning, or that such measurements represent a combination of factors including local cortical magnification, stimulus size, vascular network scales, cortical layers, and neuronal tuning. Increasing the fMRI sampling resolution may up-weight the contribution of neuronal factors underlying pRF measurements and reveal a

chromatic difference in pRF size. To test this, we used a high-field 7T fMRI scanner to test whether there are systematic differences in achromatic and S-cone pRF sizes using a one-dimensional difference of gaussian (DoG) pRF model that provides estimates of centre and surround pRF sizes. We report pRF sizes resolved at a voxel resolution of 0.70mm^3 across primary visual cortex. Surprisingly, after applying a linear regression to our data we found that pRF size estimates did not linearly increase with eccentricity for both S-cone and achromatic conditions. The average variance explained of our fits fell between 7.91% - 16.30%, indicating possible issues with SNR relative to SNR usually derived from 7T data. These results indicate potential issues with our stimulus sequence or stimulus design.

6.2 Introduction

The early human visual system begins with three chromoluminance channels that are derived from different combinations of cone photoreceptor signals that stem from the long (L), medium (M), and short (S) sensitive photoreceptor cones (Baylor, 1987; Hurvich & Jameson, 1957; Wandell, 1995). The achromatic luminance and red-green parvocellular pathways are driven by combinations of L and M cones, while the 'blue-yellow' (S-cone) pathway is driven by the difference between S-cones, and L- and M- cones combined (Stockman & Brainard, 2010). Psychophysical research has demonstrated differences in the spatial tuning of these pre-cortical pathways (Johnson, Van Hooser, & Fitzpatrick, 2010; Mullen, 1985; Poirson & Wandell, 1996; Webster, De Valois, & Switkes, 1990). The spatial resolution of the S-

cone pathway has a low pass peak <1 cycle per degree (cpd) due to the sparse density of S-cone photoreceptor cells within the retina and chromatic aberration from the optics, while the achromatic luminance pathway has a band-pass peak around 4 cpd (Webster et al., 1990). Further, the spatial frequency cut off of the S-cone system is much lower than the achromatic system, with a spatial frequency cut off at around 2 cpd (Humanski & Wilson, 1993; Williams, Sekiguchi, & Brainard, 1993).

In the primate visual cortex, the size of a simple cell's receptive field is correlated with its spatial sensitivity (Cleland, Harding, & Tilunay-Keesey, 1979; Enroth-Cugell & Freeman, 1987). Simple cells that are sensitive to isoluminant S-cone signals should have, on average, larger receptive field sizes when compared to simple cells that are sensitive to achromatic contrast. One might ask; to what extent do these differences in pre-cortical spatial sensitivity contribute to estimates of bulk neuronal population features in the visual cortex? One way of testing this is through functional magnetic resonance (fMRI) based measurements of population receptive field (pRF) size estimates using S-cone and achromatic mapping stimuli. These measurements provide estimates of the spatial location and spread of the population-averaged receptive fields in every part of the visual cortex. If these pRF measurements are dominated by simple cells, one might expect to find a correlation between pRF size and spatial frequency sensitivity: voxels should report larger receptive fields when mapped with S-cone isolating stimuli than when mapped with achromatic stimuli.

Recently, it has been found that population receptive field (pRF) sizes measured using a 3T fMRI scanner are independent of stimulus chromaticity (Welbourne et al., 2018). One explanation for this finding may be that pRF estimates are dominated by complex cells, whose receptive field sizes do not necessarily correspond to their spatial frequency tuning (Movshon et al., 1978). Alternatively, pRF size estimates may represent a combination of factors including neuronal tuning, local cortical magnification, stimulus size, vascular network scales, and cortical layers. Perhaps then, increasing the fMRI sampling resolution might up-weight the contribution of neuronal tuning factors underlaying pRF measurements and reveal a chromatic difference in pRF size.

Here, we increase our voxel resolution by using a high-field 7T fMRI scanner and ask whether there are systematic differences in achromatic and S-cone pRF sizes in primary visual cortex (V1). We hypothesise that pRF sizes measured using isoluminant S-cone stimuli should be, on average, larger than those measured using achromatic stimuli, if the response properties of a voxel are primarily dominated by simple linear cells. We report pRF sizes resolved at a voxel resolution of 0.70mm^3 across V1. We found that a linear regression accounted for a negligible amount of variance in pRF size for both achromatic and S-cone pRFs, indicating that our data was non-linear. Further inspection of the variance explained in of our pRF fits in V1 indicated complications with our data that that could not be resolved after conducting a series of further tests.

6.3 Methods

6.3.1 Participants

Three colour-normal trichromats (mean ±SD age, 28.5 ±1.8; 2 females, 1 male) were recruited for the study. All participants had normal or corrected to normal vision. All participants were experienced in retinotopic fMRI experiments. Each participant completed two fMRI sessions – one functional session and one short structural session. In the first session, 8 functional pRF runs were obtained (4 S-cone pRF runs and 4 luminance pRF runs). For one participant, a single S-cone scan was not included in the analysis due to excessive head motion. In the second session, a high resolution T1 structural scan was obtained. All participants provided informed consent before participating in the study. The experiment was conducted in accordance with the 1964 Declaration of Helsinki and the study was cleared by the ethics committee at the Spinoza Centre for NeuroImaging.

6.3.2 fMRI stimulus display

Stimuli were presented in the scanner using a 32-inch BOLDScreen LED display (Cambridge Research Systems). The screen had a display resolution of 1920 x 1080 and a refresh rate of 120Hz. Participants viewed this screen from within the scanner at a viewing distance of 210cm, using a mirror. Within the scanner room itself, spectral and gamma measurements from the RGB guns of the BOLDScreen were measured using a fibre optic cable and a 'Jaz' (Ocean Optics, FL) photospectrometer at 2nm resolution. These

measurements were then used to ensure that the BOLDScreen was calibrated to ensure correct cone isolation and a linear gamma.

6.3.3 Defining V1 and pRF modelling at standard resolution

V1 ROIs were obtained using data from a previous study on the same participants. This ROI subtended 10° of visual space and was obtained using conventional pRF mapping procedures as in previous studies (Dumoulin & Wandell, 2008). The V1 ROI was originally defined on a T1 anatomy with a voxel size of 1mm^3. Using FreeSurfer, we resampled this ROI onto the high resolution T1 anatomy with a voxel size of 0.65mm^3. The resampled ROI was carefully examined to ensure that it correctly covered voxels assigned to the grey matter of the calcarine sulcus of each participant.

6.3.4 Experiment and stimulus design

6.3.4.1 Isoluminance task

To ensure that the S-cone stimulus was isoluminant, each participant completed an S-cone minimum motion isoluminance task both outside and inside the scanner. This ensured that our S-cone stimulus was tailored to individual participants isoluminance points. Here, participants were asked to fixate on a central fixation cross while adjusting the colour of an S-cone drifting grating. This grating had a spatial frequency of 1 cpd, a drift rate of 1°/ second and a radius of 2°. The stimulus appeared at 2° eccentricity from the central fixation cross. The stimulus was presented in four quadrants of the screen that changed for each of the four trials (upper left, upper right, lower left, lower

right). Participants were instructed to use the button box to minimize the motion of the drifting grating. The point at which the drifting motion of the grating is minimized is deemed the isoluminant point of the stimulus (Anstis & Cavanagh, 1983). For each participant, the isoluminance point was recorded for each of the four trials, and the average value was used to specify the colour direction of the S-cone stimulus. Participants were given the opportunity to repeatedly practice this task outside the scanner and they then completed the task inside the scanner prior to scanning. The isoluminance point for all three participants was very similar, with mean theta values falling between 1.65 - 1.70.

6.3.4.2 pRF stimulus

The pRF stimulus consisted of a radially expanding and contracting ring aperture that contained an exposed checkerboard pattern that contrast reversed at 2Hz. The ring itself subtended 0.25° of visual angle and moved across the screen in 12 steps every 4s (1 TR), over the course of 42s. This stimulus was chosen as it would stimulate all pRFs at a given eccentricity at each TR. The ring expanded radially to a maximum of 3° eccentricity. This eccentricity was chosen as S-cone density peaks (~12% of total photoreceptors) on at the area of the retina corresponding to ~1.74° of visual space (Hendry & Reid, 2000). After each pass, there was a 20s (5TR) mean-luminance blank. The sequence of ring presentations was as follows: expand – contract – contract – expand, with the baseline condition occurring 4 times throughout the scan; after each pass of the ring. An example of the full stimulus

sequence over a single scan is presented in Figure 6.1C, with each image representing 1TR.

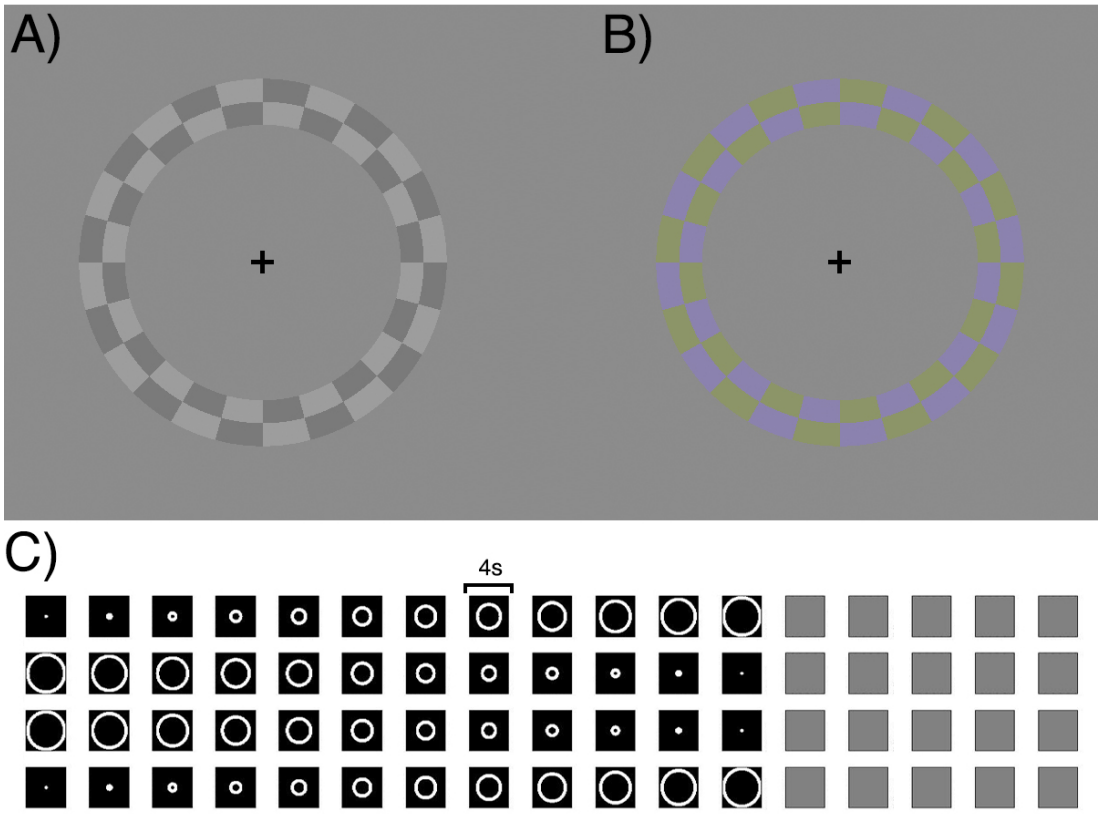

Figure 6.1 Example of the achromatic and S-cone pRF stimulus and the full stimulus sequence for one run. In A) we present the pRF ring in the achromatic condition, while in B) we present the pRF ring in the isoluminant s-cone condition. In C) we present the full expand-contract-contract-expand pRF ring stimulus sequence (moving left to right along each row) with each image representing the stimulus location during a 1 TR (4s). Note that the initial 16s luminance blank is removed from the data and sequence (total = 68 TRs).

The chromaticity condition (either S-cone or achromatic) of the stimulus was randomly interleaved within each run. In the achromatic condition (see Figure 6.1A), the pRF carrier contained root mean squared (RMS) contrast set

to 10%, while in the S-cone condition (see Figure 6.1B), the pRF carrier contained RMS contrast set to 30%. These contrast values are thought to equalize neuronal responses between achromatic and S-cone stimuli across V1 (Kane, Wade, & Ma-wyatt, 2011). The colour direction of the stimulus was specified using individual isoluminance values in MacLeod-Boynton colour space, using the 2° cone fundamental from Stockman and Sharpe (Stockman & Sharpe, 2000).

A 16s (4 TR) mean luminance blank was included at the beginning of each functional run to ensure the scanner magnetization had reached a steady state. These data were cropped before analysis to result in a total of 64TRs. To maintain fixation throughout the scan, participants completed an attentional task where they were required to respond, via button press, when the orientation of the black fixation cross changed. The task was set up so that on average, every 2s there was a 30% chance of a change in the orientation of the fixation cross.

6.3.5 fMRI Data Acquisition

Scans were completed on a Philips 7T Achieva scanner (Phillips, Best, NL) with a maximum gradient strength of 40mT/m and a slew rate of 200 T/m/s. A dual-channel volume transmit coil was used for all scans. Structural scans were obtained with a 32-channel head coil (Nova Medical, MA, USA). Functional scans were obtained with two custom built 16-channel high-density surface receive arrays (Petridou, Italiaander, Bank, & Siero, 2013, MRCoils

BV). These surface arrays were positioned adjacent so that the two arrays touched each other lengthwise but did not overlap. Participants were positioned within the scanner so that their occipital lobe was aligned with the centre between the arrays.

6.3.6 Pre-processing of high-resolution structural data

A high resolution T1-weighted full brain anatomical scan was acquired for each participant using an MP2RAGE sequence (TI1 = 800ms, TI2 = 2700ms, $TR_{MP2RAGE}$ = 5500ms, TR/TE = 6.2/2.3ms, flip angle α1 = 7, and α2 = 5, bandwidth = 403.7 Hz/pixel, acceleration factor using SENSE encoding = 3.5 x 1.3 (RL and AP respectively), resolution = 0.65mm^3, total scan time 9 min 57s) (Marques et al., 2010). This high-resolution T1 anatomy was automatically segmented using CBS Tools plugin for MIPAV software (https://www.cbs.mpg.de/institute/software/cbs-tools). Manual corrections were carefully applied to the automatic segmentation using ITK-SNAP (http://www.itksnap.org/pmwiki/pmwiki.php) to ensure the correct identification of grey and white matter (Teo et al., 1997). The high resolution at which our data were acquired allowed us to reconstruct a cortical depth profile across the grey matter of the cortex. The manually corrected segmentation was re-run through CBS Tools to generate a finely tuned cortical depth profile. This cortical depth profile identified the Euclidian distance of each grey matter voxel from the grey matter/white matter (GM/WM) surface in the T1 anatomy. Voxels on the pial surface border were identified with a distance value of 1, while those on the GM/WM border were identified with a value of 0. Voxels that were

identified as white matter were assigned a negative depth value. An example of the cortical depth map overlaid on a corresponding T1 anatomy is illustrated in Figure 6.2.

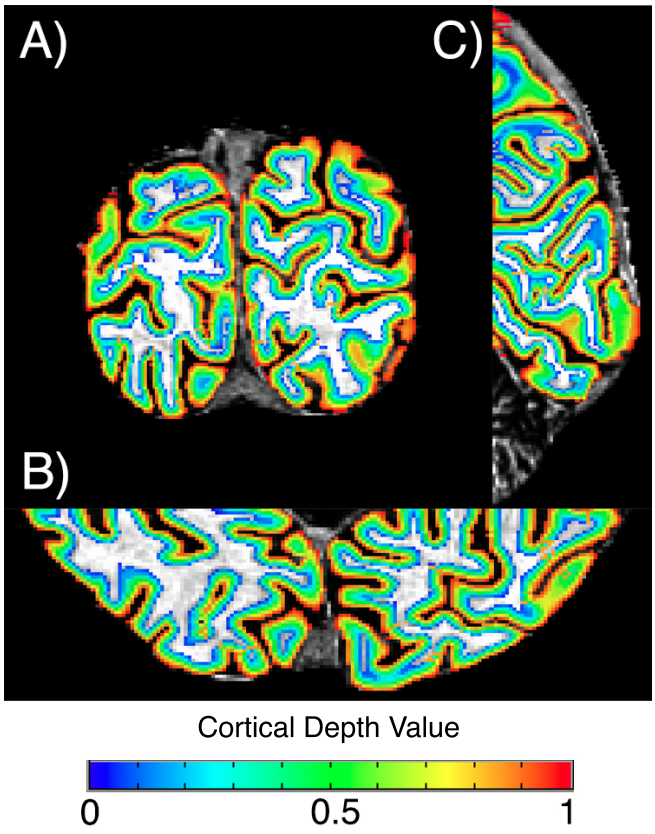

Figure 6.2 Cortical depth map overlaid on a high-resolution anatomy presented in three different views. Voxels that are classified as being closer towards the pial surface are coded in red (value = 1), whilst those classified as being towards the white/grey matter boarder are coded as blue (value = 0).

6.3.7 Pre-processing of high-resolution functional data

Functional data were acquired with a T2*-weighted 3-dimensional multi-shot EPI (TR/TE = 59/28ms, flip angle: 20°, acceleration factor using SENSE encoding: 3.5 (right-left) × 1.3 (anterior-posterior), echo planar factor: 27, bandwidth (phase-encode): 19.1Hz/pixel, voxel size = 0.70mm^3 isotropic, FOV

= 131 (right-left) × 120 (feet-head) × 24 (anterior - posterior) mm, 34 coronal slices, and 28% oversampling in the slice direction). Functional data were pre-processed using AFNI. In order to correct for geometric distortions in our EPIs, a top-up field with opposing phase encoding to our EPI data was computed at the end of each scan. The corresponding top-up field was applied to each EPI to correct geometric distortions. Next, between and within motion correction was performed to compensate for any motion artefacts that occurred during scanning and the linear trend of each voxels time series was removed. For each individual participant, motion-corrected (without top-up correction) functional runs were averaged across each condition produce a mean time series for both conditions, achromatic luminance and S-cone. Motion-corrected (with top-up correction) functional runs were averaged together to create a mean EPI 'amplitude anatomy' volume that was used to assist in aligning functional data to the high-resolution T1 anatomy.

We used a customized forward model to estimate 3 pRF parameters based of the stimulus sequence; pRF eccentricity, pRF centre size, and pRF surround size. For each mean EPI, the BOLD response of each voxel was predicted using a one-dimensional Difference of Gaussian (DoG) model (Zuiderbaan, Harvey, & Dumoulin, 2012). The DoG pRF model is defined by two Gaussian functions; the first representing a positive excitatory pRF centre, and the second representing an accompanying negative inhibitory pRF surround. Although this allows us to estimate the extend of a voxel's inhibitory surround, this was not of interest for the current study. Thus, we focused on

centre and surround sizes, and the average of these sizes as a representation of general 'pRF size'. For each voxel, the three parameters were estimated by minimizing the sum of squared errors (RSS) between the predicted and observed time series.

Next, we used the AFNI 'nudge' plugin to bring the amplitude anatomy EPI into approximate register with the high resolution T1. Following this, we used AFNI function `align_epi_anat` to run a double-pass alignment of the amplitude anatomy EPI to the structural data. The final alignment was checked by eye to ensure that the registration procedure optimised the fit. From this alignment we obtained a co-registration matrix. Finally, we applied the coregistration matrix and the top-up correction field to the pRF model and resampled the pRF data to the T1 anatomy. This effectively corrected our pRF data of spatial inhomogeneities while reregistering it to the T1 anatomy.

6.3.8 Plotting data as a function of eccentricity and cortical depth

Only voxels with ≥10% variance explained and those that fell within the V1 ROI were retained for further analysis. The voxel count for each individual participant and the total voxel count are presented in Table 6.1. To investigate any changes in pRF size across eccentricity (ignoring depth), we partitioned our data into six eccentricity bins (0.0° – 0.5°, 0.5° – 1.0°, 1.0 ° – 1.5°, 1.5° – 2.0°, 2.0° – 2.5°, and 2.5° – 3.0°), based on the eccentricity value for each voxel. We also binned our data into 5 layers of cortical depth based on cortical depth estimates for each voxel. This corresponds to ~0.5mm of cortical depth

per layer (with grey matter restricted between 0.0mm – 2.5mm of grey matter). For each participant, we used MATLAB function 'quant' to define the lower and upper boundary cortical depth values for each layer, effectively binning our data into 5 layers of cortical depth, with approximately equal voxels included in each of the layers. We note that separating our data into isolated lamina compartments can be problematic due to changes vasculature arrangement across cortical depth (Fracasso et al., 2016).

Table 6.1 V1 voxel count for each chromaticity condition after thresholding for ≥10% variance explained (N=3).

ROI	Total achromatic voxels	Total S-cone voxels
Participant 1	9678	8604
Participant 2	13613	9369
Participant 3	4572	5412
Total	27863	23389

6.3.9 pRF size data

First, we plotted pRF size (that is, the average of the centre and surround pRF sizes) as a function of eccentricity for both achromatic and S-cone pRFs, ignoring any effect of cortical depth. Following this, we plotted pRF size as a function of eccentricity, across cortical depth bins for both achromatic and S-cone pRFs. Finally, we split our data as both separate centre and surround pRF sizes for each condition and plotted these values as a function of eccentricity.

6.4 Results

On average, receptive field sizes increase monotonically with eccentricity, as reported by both neurophysiological and pRF studies in human and non-human primates (Alvarez, de Haas, Clark, Rees, & Schwarzkopf, 2015; Amano et al., 2009; Dumoulin & Wandell, 2008; J. Felleman & Van Essen, 1987; Fracasso et al., 2016; Haak, Cornelissen, & Morland, 2012; J. Levitt, Kiper, & Movshon, 1994; Wandell & Winawer, 2015; Welbourne et al., 2018; Zuiderbaan et al., 2012). Observation of our pRF plots indicated that size did not linearly increase with eccentricity, and a linear regression confirmed this. This conflicts with previous research and known physiology of the visual system. We also found that the average variance explained of our fits was lower than the variance explained from previous 7T pRF studies. These results suggest potential issues with our data, stimulus, or model.

6.4.1 How does pRF size change as a function of eccentricity across V1?

Inspection of our group mean pRF plots (see Figure 6.3A) found that pRF size (i.e. the average of centre and surround size) did not appear to linearly increase with eccentricity. Instead, pRF size showed an inverted 'U' shape as a function of eccentricity. Observation of the individual plots (Figure 6.3B-D) found similar relationship between size and eccentricity, with pRF sizes failing to linearly increase with eccentricity.

To test for linearity, we ran a linear regression on our group data. For the group luminance pRF data, a significant regression equation was found,

$F(1,25120) = 950.32$, $p < .000$, with $R^2 = .036$. The regression coefficients presented in Table 6.2 show a weak increase in luminance pRF size with eccentricity for the luminance condition. For the S-Cone pRF data, a significant regression equation was also found, $F(1,19119) = 12.21$, $p < .000$, with $R^2 = .001$, while the regression coefficients in Table 6.2 show that there was a decrease in S-cone pRF size with eccentricity. The variance explained of both regressions was negligible.

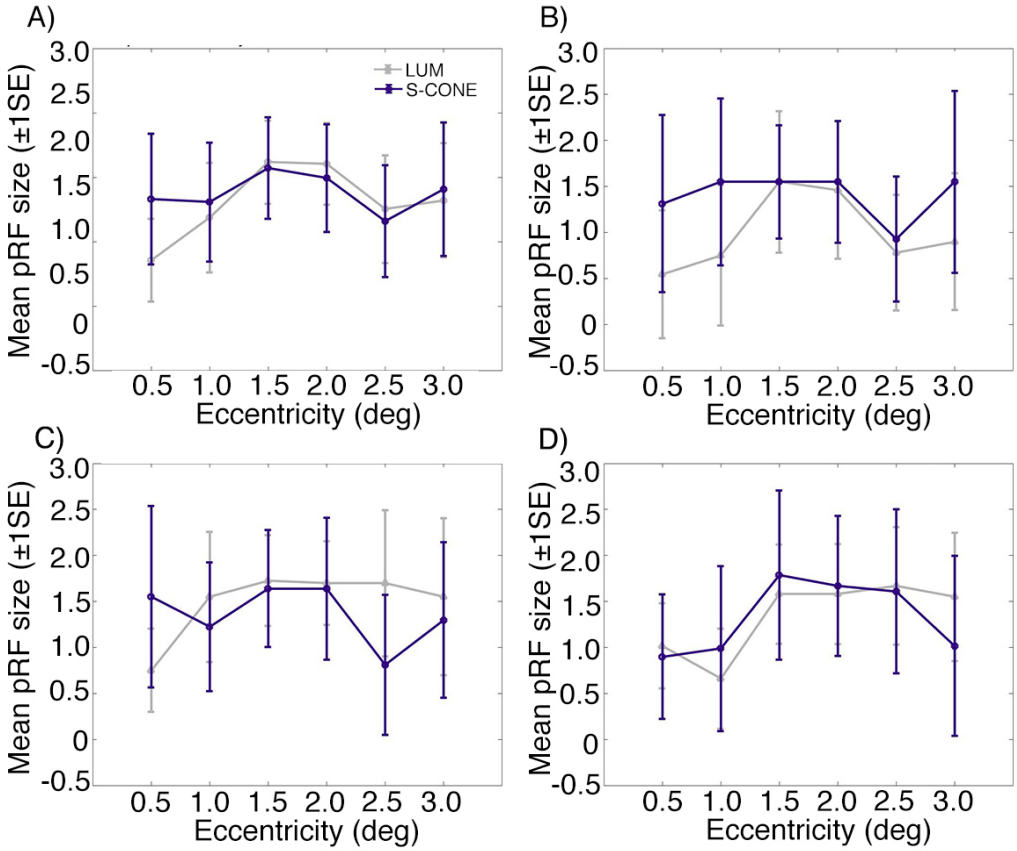

Figure 6.3 Mean pRF sizes as a function of eccentricity. In A) we present group means. In B) we present means at each eccentricity bin for participant 1. In C) we present means at each eccentricity bin for participant 2 and in D) we present means at each eccentricity bin for participant 3.

Table 6.2. Regression coefficients table for the group analysis.

Variable	B	Beta	*t*	*p*
Lum pRF Eccentricity	.172	.191	30.837	.000
S-Cone pRF Eccentricity	-.026	-.025	-3.494	.000

Dependent variable: pRF size

6.4.2 Verification of fitting procedure using centre-surround pRF sizes as a function of eccentricity

Next, we separated our pRF sizes into centre and surround size. Our goal was to test that the size of pRF centres are consistently smaller than surround size, as found in previous studies. This was tested as a verification of our pRF pipeline rather than any experimental difference, as this difference in size is imposed during the DoG fitting procedure (Fracasso et al., 2016; Zuiderbaan et al., 2012). Observation of the plots in Figure 6.4 show that both achromatic and S-cone centre sizes were smaller than surround sizes, although the centre and surround data towards the central eccentricities in Figure 6.4D are particularly close in size which may reflect issues with the data. It is worth noting that both centre and surround sizes appear to generally follow the *unexpected* non-linear trend, however they also follow an *expected* trend of centre sizes consistently smaller than surround sizes.

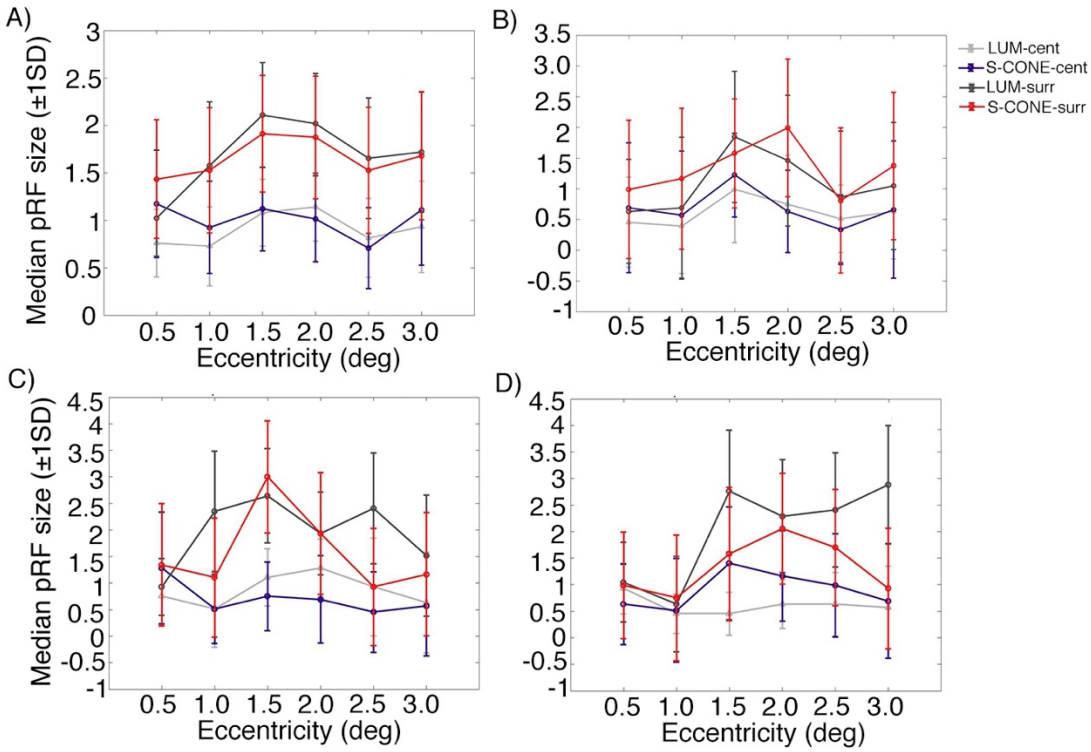

Figure 6.4 Mean centre and surround pRF sizes plotted as a function of eccentricity. Observation of the plots indicates that centre sizes are consistently smaller than surround sizes, as expected. In A) we present group means. In B) we present means at each eccentricity bin for participant 1. In C) we present means at each eccentricity bin for participant 2 and in D) we present means at each eccentricity bin for participant 3. We do not observe a trend of linearly increasing pRF size with eccentricity in either the group or individual data.

6.4.3 How does pRF size change as a function of eccentricity across V1 at different levels of cortical depth?

To assess the relationship between pRF size and eccentricity at each of the 5 layers of cortical depth, we plotted our eccentricity vs size data in individual lamina compartments. Again, we found that pRF size did not appear

to have a linear relationship with eccentricity at each level of cortical depth for the group means or for the individual participants (see Appendix A6 for data), further confirming issues with our data. As presented in Table 6.3, the variance explained of the linear regression model was negligible (although at times significant) and Table 6.4 shows inconsistency in the correlation coefficients. Overall, these data showed a similar inverted 'U' shape trend to when averaged across depth.

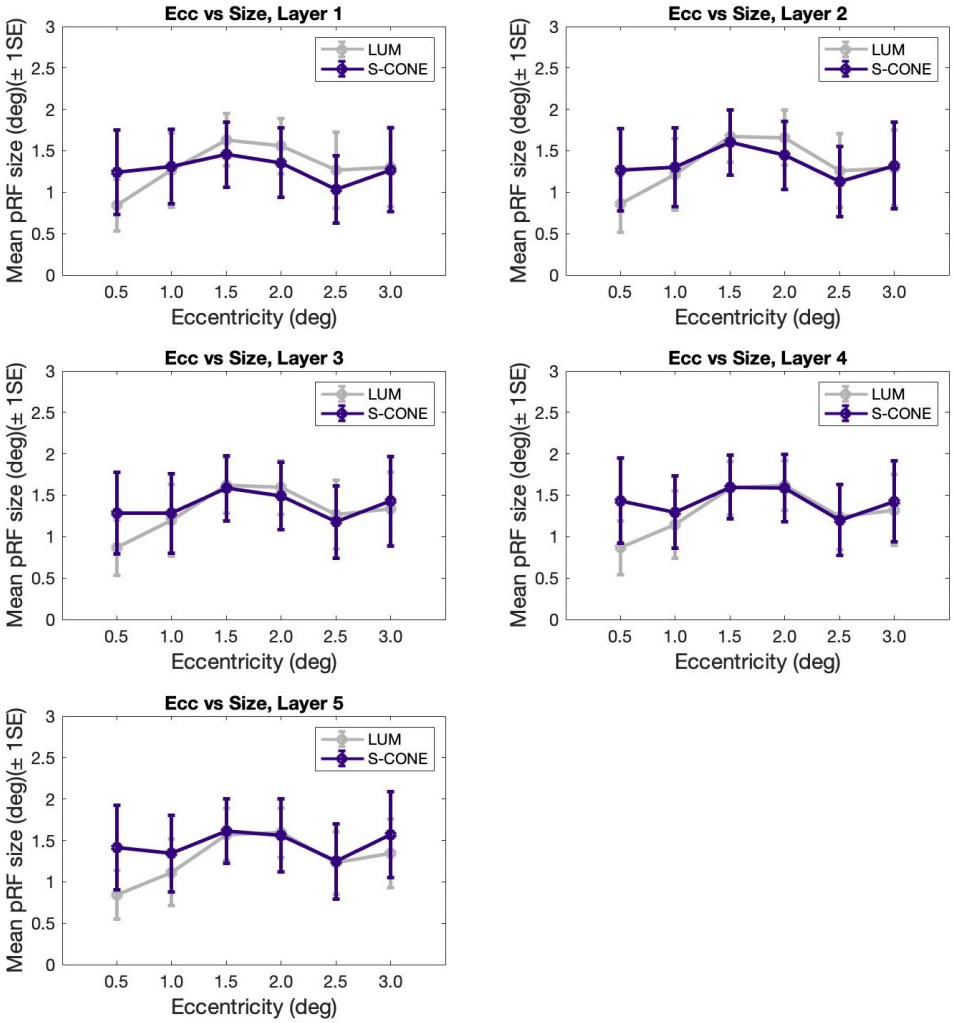

Figure 6.5 Mean pRF sizes plotted as a function of eccentricity at 5 levels of cortical depth, averaged across all participants (N=3). Layer 1 includes data towards the GM/WM border and layer 5 is towards the pial surface.

Table 6.3 Model summary table of linear regression analysis for group data at each layer of cortical depth. pRF eccentricity explains a very small amount of variance in pRF size in both achromatic luminance and S-cone conditions.

		R^2	*df*	*F*	*p*
Layer 1	Lum pRF eccentricity	.042	4815	209.94	.000
	S-Cone pRF eccentricity	.003	3611	11.03	.001
Layer 2	Lum pRF eccentricity	.027	4982	135.75	.000
	S-Cone pRF eccentricity	.002	3725	6.86	.009
Layer 3	Lum pRF eccentricity	.038	5079	199.68	.000
	S-Cone pRF eccentricity	.000	3870	1.57	.210
Layer 4	Lum pRF eccentricity	.026	5102	135.56	.000
	S-Cone pRF eccentricity	.002	3885	6.029	.014
Layer 5	Lum pRF eccentricity	.040	5132	215.46	.000
	S-Cone pRF eccentricity	.000	4019	.532	.466

Dependent variable: pRF size

Table 6.4. Regression coefficients table at each level of cortical depth, for group data. B coefficients indicate the trend of data, which is weakly positive for achromatic luminance pRF sizes, but weakly negative for S-cone pRF sizes.

		B	Beta	*t*	*p*
Layer 1	Lum pRF eccentricity	.187	.204	14.49	.000
	S-Cone pRF eccentricity	-.056	-.055	-3.321	.001
Layer 2	Lum pRF eccentricity	.157	.163	11.65	.000
	S-Cone pRF eccentricity	-.043	-.043	-2.62	.009
Layer 3	Lum pRF eccentricity	.217	.194	13.13	.000
	S-Cone pRF eccentricity	-.021	-.020	01.25	.210
Layer 4	Lum pRF eccentricity	.185	.161	11.64	.000
	S-Cone pRF eccentricity	-.041	-.039	-2.455	.014
Layer 5	Lum pRF eccentricity	.165	.210	14.68	.000
	S-Cone pRF eccentricity	.012	.012	.730	.466

Dependent variable: pRF size

6.4.4 Variance explained of fits

As presented in Figure 6.5 and Table 6.2, the variance explained of our pRF fits fell around 10% across all three participants. This is greatly lower when compared to pRF data from Fracasso et al. (2016), who found that the variance explained of similar pRF fits using submillimetre functional data fell around 55%, although they had a larger stimulus width, a high contrast checkerboard carrier, and averaged across twice as many scans than the

current study which would result in greater signal than our (relatively) less powerful stimulus.

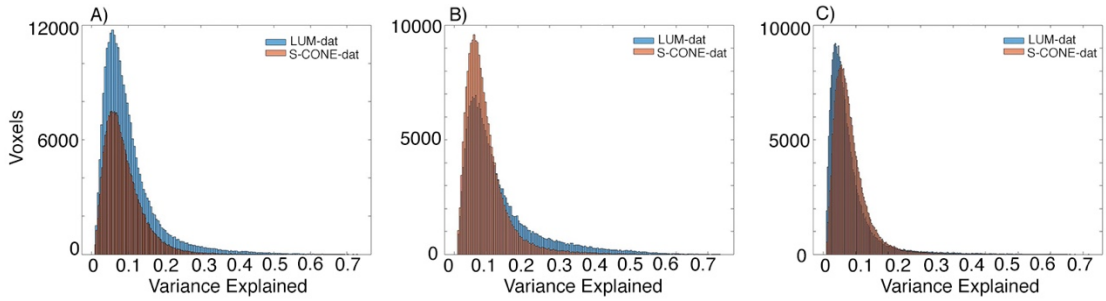

Figure 6.6 Histogram plots of variance explained of the V1 voxels for each participant. In A) we present the variance explained of V1 voxels in participant 1, while in B) we present the variance explained for participant 2, and C) for participant 3.

Table 6.5 Mean variance explained across V1 for each condition, for each participant. (above 1% VE).

	V1 Variance Explained	
	Achromatic luminance	S-Cone
Participant 1	11.53%	9.63%
Participant 2	16.30%	10.50%
Participant 3	8.00%	7.91%

6.5 Discussion

We have used high resolution 7T fMRI to measure S-cone and achromatic pRF size estimates in V1. Overall, we found that a linear model explained a negligible amount of variance in our data, indicating that pRF sizes did not increase with eccentricity for either achromatic or isoluminant S-cone

pRFs. This was similar at both the group and individual level, and after compartmentalizing our data into individual depth bins. However, we did find that, on average, mean pRF centre sizes were consistently smaller than pRF surround sizes, although these two parameters followed a similar non-linear trend. We discuss these findings while considering potential confounds to our data.

6.5.1 Accuracy of the DoG pRF model

An expanding and contracting ring stimulus is optimised for modelling pRF eccentricity and size estimates. This is important, as the repetition time for sub-millimetre fMRI is slow (TR=4 in the current study) and our time series contains a limited number of frames (a total of 72). Thus, a reduction in the number of pRF parameters to be estimated from the pRF model (i.e. removing polar angle and using a pRF ring) aims to maximize the number of degrees of freedom at this stage.

One might consider using the conventional pRF modelling pipeline in mrVista, where all 3 parameters (pRF size, eccentricity, and polar angle) are modelled. However, this would produce unreliable parameter estimates because no information about polar angle is available, in principle, in our dataset. Out of curiosity, we ran our data using the mrVista pRF model and found that the mrVista pRF fit indeed appeared to end much earlier than expected at the search-fit stage, while providing linearly *decreasing* pRF sizes when plotted against eccentricity (data not shown). This has been overcome

by our one-dimensional DoG pRF model, which relies on the grid-fit alone while giving the option to increase the grid sampling.

6.5.2 Stimulus sequence and timing

It is important to ensure that the pRF model matches the stimulus sequencing presented in the scanner. We re-checked our timings to ensure our stimulus timing was correct to the millisecond for each expansion and contraction of the ring, and each luminance blank. Next, we re-ran the pRF model using a different stimulus sequence under the assumption that there could have been an unseen delay in the stimulus trigger. Initially, a 16s (4 TRs) dummy run was included at the beginning of each functional run to allow for scanner magnetization to reach a steady state. This was included as a precaution, as the scanning sequence at the Spinoza Centre for NeuroImaging includes a warm up and dummy run sequence prior to triggering the stimulus. These data were cropped out before analysis, reducing our time series from 72 TRs to 68 TRs. We considered that there may have been problems with stimulus onset. Perhaps the stimulus presented in the first TR was the initial frame of the stimulus sequence (i.e. the first step of the ring expanding, rather than the first frame of the luminance blank). First, this would mean that our stimulus sequence did not match our pRF model. Second, this would mean that the stimulus ran overtime, and this may have not been accounted for due to the immediately preceding 'top up' scan that masked the stimulus running after the functional scan ended.

However, the pRF estimates were consistently worsened after making changes to the stimulus sequence. Likewise, any other alternative shifts the stimulus sequence resulted in a decrease in the variance explained of our fits and increased the variance of the pRF size estimates, indicating that there were no issues with our stimulus sequence nor timing. From further correspondence with Spinoza we could conclude that there were no issues with our stimulus timing.

6.5.3 Issues with stimulus design and SNR

Finally, we have considered stimulus design. The main features of our stimulus were modelled from the pRF stimulus used in the preceding lamina paper (Fracasso et al., 2016). However, some key differences may influence our pRF estimates. First, our pRF stimulus was small in size, expanding up to 3.0° radius with a pRF ring width of 0.25°, as opposed to Fracasso et al. (2016) who had a pRF ring width of 0.5° and expanded to ~4°. We chose this smaller bar size as it would allow us to resolve smaller pRFs, and this is important in analysing across cortical depth. Second, we used relatively low (yet theoretically response-equated) stimulus contrasts, 10% contrast for achromatic and 30% contrast for S-cone. We chose these contrast values both to equalise neuronal responses and to avoid the possibility of luminance leaking into the S-cone stimulus. Conversely, Fracasso et al. (2016) used a high contrast achromatic checkerboard that would produce much larger signal than our own stimulus. Indeed, the variance explained from a high achromatic contrast 2Hz carrier was, on average, around 55%. This is far higher than our

own variance explained, which fell around 10%. Third, our stimulus was viewed at a distance of 210cm in the scanner (from eyes to display), while for Fracasso et al. (2016) the stimulus was viewed at a distance of 35cm. Our stimulus sizing was adjusted to account for both distance and screen size and resolution, however the luminance of the screen at this distance may have some effect of SNR. Finally, our participants completed 3-4 runs of each stimulus condition, while Fracasso et al. (2016) completed 6-9 runs of the stimulus. The reduction in runs, combined with our small voxel size, may lead to a decrease in SNR.

It may be that the small voxel size ($0.7mm^3$) of our data has lead to a decrease in SNR, thus requiring the stimulus to provide more impact (i.e. wider bar, increased contrast, closer to display, and more scans) to produce accurate pRF sizes. Perhaps then, our pRF size estimates are due small differences in our stimulus design rather than any modelling or sequence problems. This is supported by the greatly reduced variance explained of our pRF fits.

In short, many factors might have been combined to lower the signal amplitude that we measured in our scans. We suspect that the noisy fits we measure are a direct result of these combined factors. One might consider re-tuning our stimulus to increase the fMRI response it produces. When used in conjunction with the DoG pRF model, an expanding ring stimulus with a larger width of 0.5° and doubled contrast for both conditions may increase the power

of the stimulus and thus increase the fMRI signal. Further, for our 2Hz square-wave contrast-reversing stimulus, it has been suggested that temporal non-linearities in the S-cone system may result in internal luminance artifacts (Mullen, Yoshizawa, & Baker, 2003; Yoshizawa, Mullen, & Baker, 2000). Such artifacts may affect the selectivity of our S-cone stimulus, and in further experimentation should consider a reduction in temporal flicker to avoid this.

6.6 Conclusion

Our experiment has failed to replicate a fundamental result in visual neuroscience; increasing pRF size with increasing eccentricity for both achromatic and isoluminant S-cone stimulus conditions. Further analyses have ruled out trivial timing problems that may have occurred with the stimulus sequence or fitting. Instead, the relatively low variance explained of our pRF fits suggests potential issues with SNR and possibly the stimulus design. Our stimulus may not be powerful enough to produce large enough fMRI responses, which is already reduced in 7T fMRI due to the sub-millimetre voxel size. These factors must be considered in future research that aims to use 7T fMRI up weight the contribution of neuronal response to pRF mapping.

6.7 Appendix A6 Individual participant plots across cortical depth

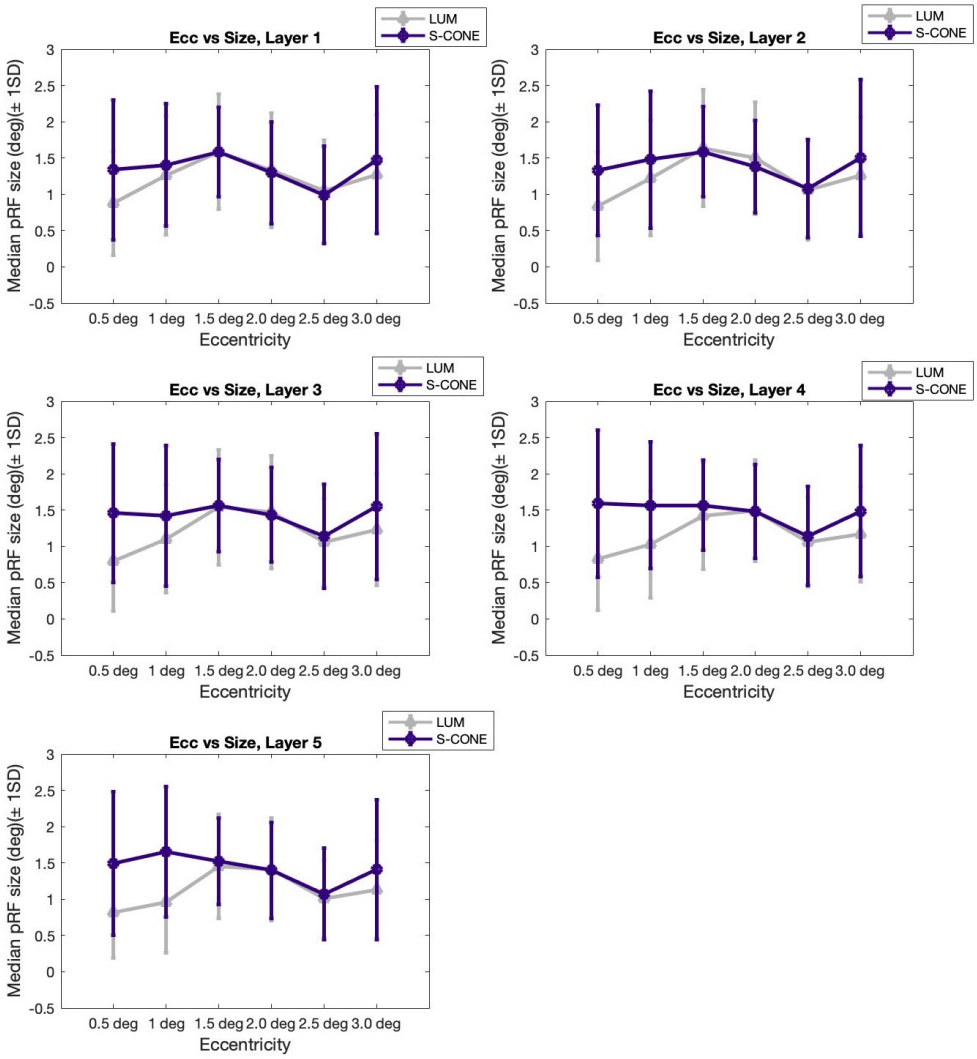

Figure A6.1 Mean pRF sizes plotted as a function of eccentricity at 5 levels of cortical depth for participant 1. Layer 1 includes data towards GM/WM border and layer 5 is data towards pial surface. pRF sizes appear to decrease with increasing eccentricity for both conditions, across all layers.

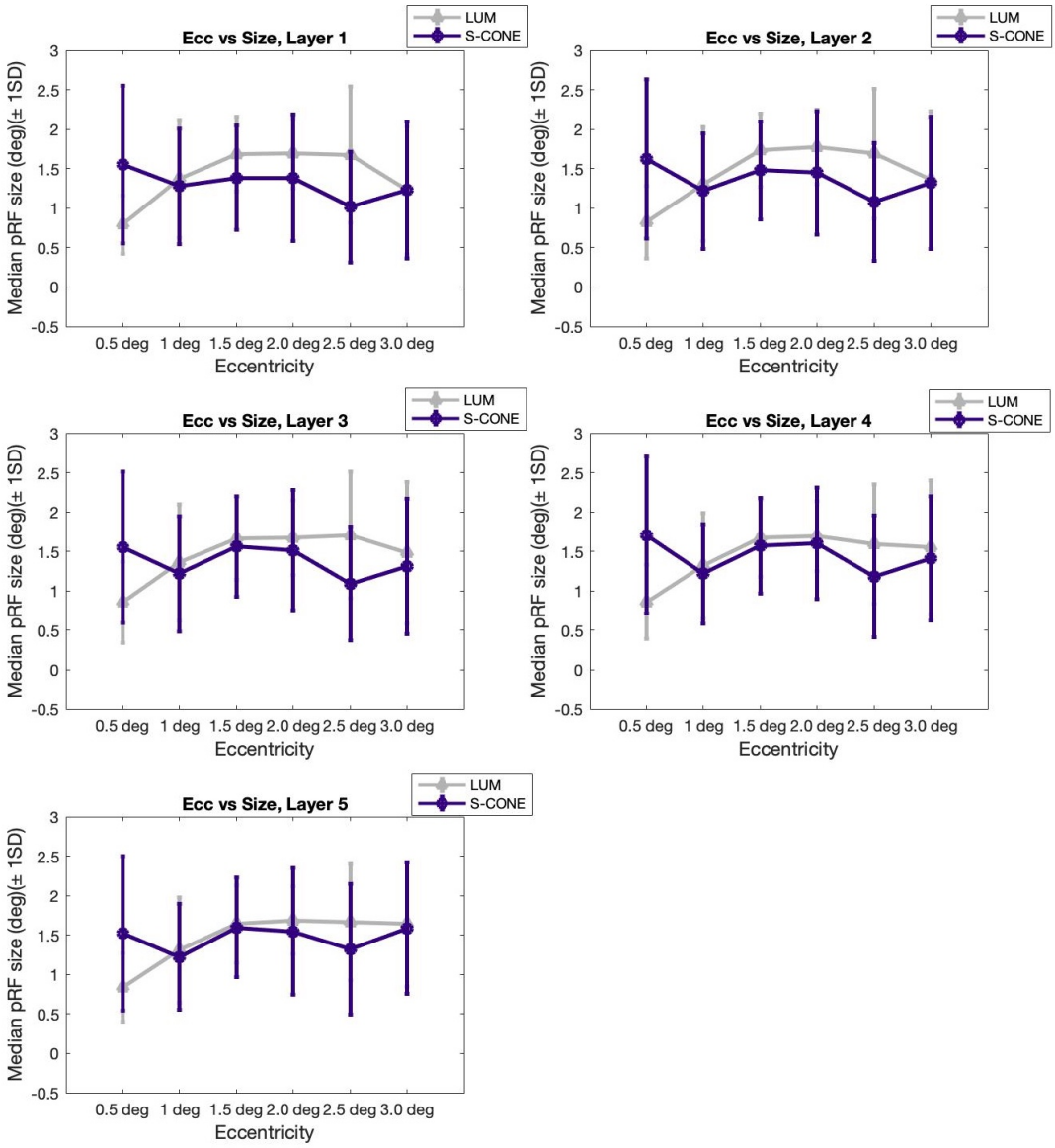

Figure A6.2 Mean pRF sizes plotted as a function of eccentricity at 5 levels of cortical depth for participant 2. Layer 1 includes data towards GM/WM border and layer 5 is data towards pial surface. pRF size gradually decreases with increasing eccentricity across all layers.

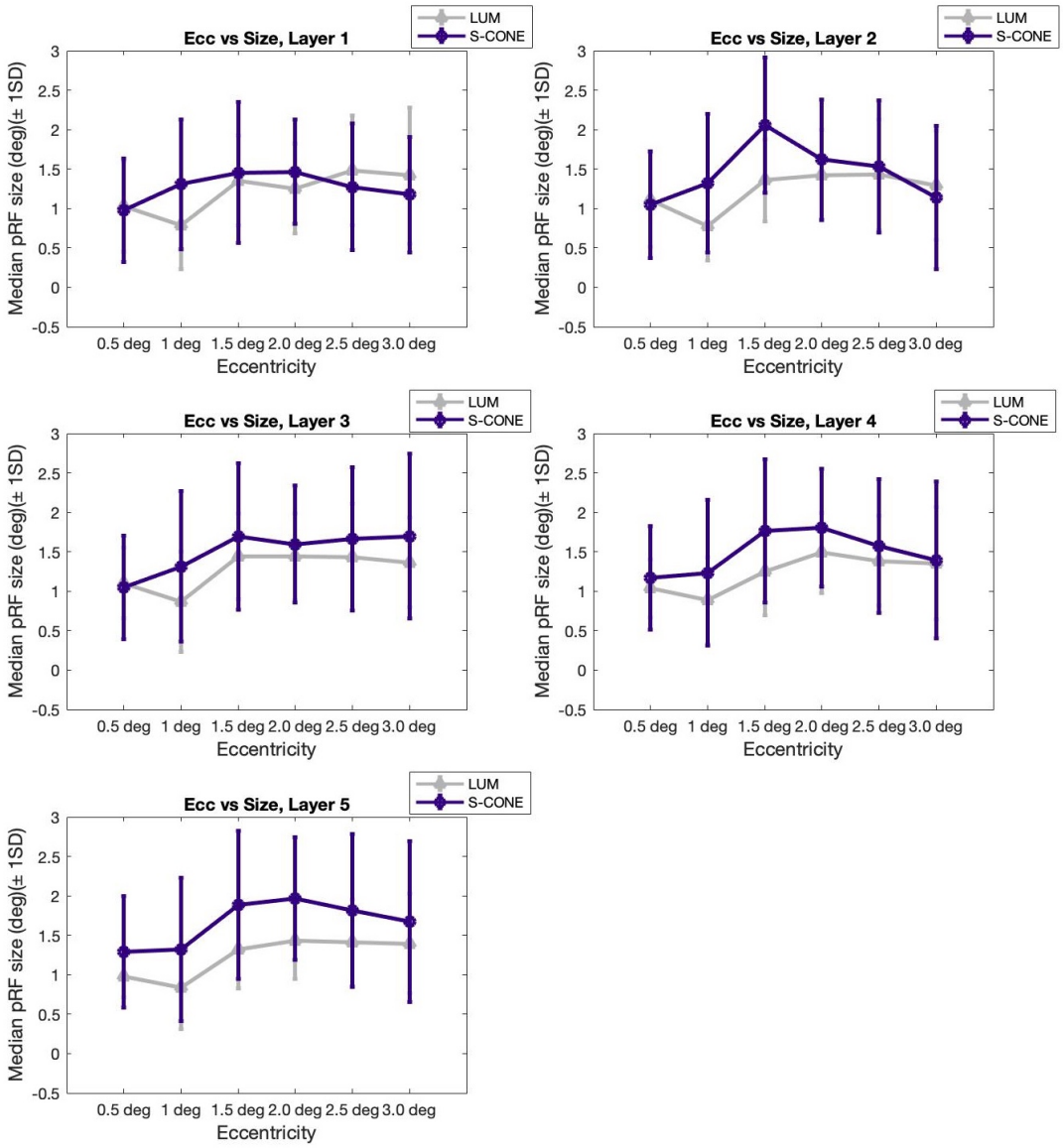

Figure A6.3 Mean pRF sizes plotted as a function of eccentricity at 5 levels of cortical depth for participant 3. Layer 1 includes data towards GM/WM border and layer 5 is data towards pial surface. There is no (or a very small) linear relationship between pRF size and eccentricity for this participant.

Chapter 7

Conclusions.

7.1 Overview of the thesis findings

The four experiments in this thesis are organised under two themes. In the first two studies we used electrophysiological neuronal population measurements to investigate how visual processing changes in response to PD mutations using *Drosophila* and rodent models of PD. In the second two studies, we used fMRI to investigate how low-level visual processes associated with pre-cortical pathways (the magnocellular and S-cone pathways) are represented in the healthy human cortex. The four experiments described in this thesis make novel contributions in their findings and in the methods used.

First, we identified the mechanism of excitotoxicity in *Drosophila* with mutations on genes known to be linked to EOPD in humans. We found that young PD mutants show increased contrast sensitivity, pointing to a common phenotype of abnormal gain control occurring in EOPD mutants and the *LRRK2-G2019S* late-onset mutant (Afsari et al., 2014). Visual loss occurred in such mutants, but only after increasing neural demand by applying photic stress. Following this, we used a LDA classifier to test whether we could accurately classify flies into their correct mutation and age, based on multivariate visual response profiles. We found that the classifier was highly accurate in pairwise classifications, leave-one-out classifications, and a N-way

classification with all 25 classes included. The ability of the classifier to accurately distinguish between PD mutants indicates that each mutation uniquely impacts the underlying cellular processes thereby causing subtle, dissimilar neural responses across lifespan, that result in the same pathogenic outcome; cell death and visual loss.

Second, this investigation was extended to a rodent model overexpressing *α-synuclein*. To establish a new visual biomarker for PD in a rodent model, we used a support vector machine (SVM) classifier to test whether we could classify SSVEP measurements recorded from the brain of PD rodents. The SVM was able to classify the presence or absence of *α-synuclein* independently of hemisphere, across disease progression. However, we found that we were able to accurately classify between hemisphere in both control and PD rats. These findings indicate that the SSVEP is sensitive to the presence of the PD-causing gene product, as well as the hemisphere from which it is measured, and such differences persist across disease progression. These findings, and methods, will be beneficial for testing new therapeutic treatments that aim to rescue neural changes that occur due to PD.

Third, fMRI and psychophysical methods were used to investigate how measurements of cortical temporal contrast sensitivity differ across visual space, and how such cortical sensitivities relate to behaviour. We found that both fMRI and psychophysical measurements of contrast sensitivity

consistently peak around 8Hz. However, pRFs in early visual areas that are tuned to peripheral regions of the visual field had increased contrast sensitivity at a high temporal frequency when compared to those in the fovea. This peripheral bias was not evident in area hV4, indicating a relative independence of temporal contrast sensitivity across eccentricity in this area. Using a linear model, we found that psychophysical measurements were best predicted by fMRI measurements in hV4. These data indicate that eccentricity-dependent retinal sensitivities to temporal contrast are present in the early visual cortex, however hV4 appears to be invariant to such eccentricity-dependent biases and is instead more similar to behavioural sensitivity.

Finally, high-resolution fMRI was used to test for systematic differences in achromatic and isoluminant S-cone pRF size estimates. Differences in the spatial resolution of these two pathways suggest that S-cone pRF sizes should be, on average, larger than luminance pRF sizes. We investigated whether such differences exist in primary visual cortex, with the initial intention to explore possible differences as a function of cortical depth. Unfortunately, we could not replicate the common effect of increasing pRF size with increasing eccentricity for either the S-cone or luminance pRFs. These results indicate that complications may have occurred due to an interaction between our stimulus and the small voxel size of our scans, which led to a reduction in SNR and poorer pRF fits.

7.2 Future work

The investigation of visual processing in animal models of disease can reveal important information about neural changes that occur, however, we eventually need to translate these findings to the human condition. The PD experiments in this thesis give reason to suggest that a similar cross-species visual biomarker may arise in human PD patients. Indeed, previous research (see *1.3.2 Visual abnormalities in PD*) has found visual changes in PD patients. The translation of our current research to human patients is, in theory, simple; repeat the similar SSVEP studies on PD patients and test whether a machine learning classifier can accurately classify between PD patients and healthy humans at different stages of disease progression.

We have found evidence for excitotoxicity as a pathological mechanism in *Drosophila* PD models. There is evidence that humans who develop PD tend to have jobs with higher socioeconomic status, while those with lower socioeconomic status report a lower incidence of PD (Beard et al., 2017). The work reported here may have some bearing on this finding: here, and in previous research, it has been found that young PD flies have stronger and faster neural responses (Afsari et al., 2014; M. M. Himmelberg et al., 2018). Perhaps then, increased visual processing, and possibly faster neural signalling, may provide people at risk of PD with advantages younger in life, before the later neurodegeneration and onset of classical PD symptoms (Himmelberg et al., 2017). However, investigating an excitotoxic mechanism in human PD patients would be exceedingly difficult. This would require

accurate genotyping from a very young age and longitudinal testing, virtually across the entire lifespan, with a large number of participants.

Although the ultimate goal of testing animal models of disease is to translate findings to the human condition, they are not without their own benefits. Specifically, there is utility in combining electrophysiological measurements recorded from animal models of disease with machine learning classification algorithms to test the efficacy of new drugs that aim to rescue neural signalling. Here, the *inability* of a classifier to distinguish between response from a healthy and drug treated animal model of disease provides a highly sensitive (and accurate) measure of visual restoration. Indeed, this is currently an avenue of research, where two LRRK2 kinase inhibitors, PFE360 and BMPBB-32, are being tested on the *Drosophila* and rodent models used in the current study.

In *Chapter 5: Eccentricity-dependent temporal contrast tuning in human visual cortex measured with fMRI*, we have developed an experimental paradigm that measures contrast sensitivity in the human visual cortex. Perturbations in contrast sensitivity have been found in electrophysiological measurements taken from *Drosophila* PD models and in psychophysical measurements human PD patients (Afsari et al., 2014; Bodis-wollner et al., 1987; Bulens et al., 1987; Himmelberg et al., 2018; Hutton et al., 1993). Thus, may be possible to apply this sensitive paradigm to investigate the loci of similar visual cortical changes that might occur in patients with neurological

disease (with a higher spatial sensitivity than, say, EEG). Future research that aims to investigate how visual processing is compromised by neurological (or even retinal) disease may rely on our paradigm to produce a sensitive measure of cortical contrast sensitivity. From a theoretical standpoint, the investigation of healthy visual pathways, from retina to cortex, to behaviour, is limited by the ability to take invasive physiological measurements from the retinal cells of humans. Recently, the Image System Engineering Toolbox for Biology (ISETBIO) has allowed for calculating the properties of the front of end biological visual systems. Thus, it may be possible advance our current research by using such tools to simulate both normal and abnormal retinal processing as a function of eccentricity (or perhaps polar angle) and investigate how such processes align with fMRI and psychophysical measurements.

7.3 Conclusion

This thesis has investigated low-level visual processing in health and disease using population electrophysiological recordings from animal models of PD, and fMRI measurements in healthy humans. We have established a new visual biomarker of abnormal gain control and excitotoxicity in three PD *Drosophila* mutants, and we have shown the utility of sensitive SSVEP methods and machine learning classification techniques in both *Drosophila* and rodent models of PD. Following this, we have used fMRI to show that pre-cortical pathways that are sensitive to temporal contrast are similarly represented across eccentricity in early human visual cortex. Finally, we have

made pRF measurements in primary visual cortex using submillimetre fMRI. Although these measurement appear inaccurate, such findings will inform the methods of future research that will continue to investigate the spatial properties of chromatic pathways in the visual cortex.

References

Abeliovich, A., Schmitz, Y., Fariñas, I., Choi-Lundberg, D., Ho, W.-H., Castillo, P. E., … Rosenthal, A. (2000). Mice Lacking α-Synuclein Display Functional Deficits in the Nigrostriatal Dopamine System. *Neuron*, *25*(1), 239–252. http://doi.org/https://doi.org/10.1016/S0896-6273(00)80886-7

Adams, A. D., & Forrester, J. M. (1968). The projection of the rat's visual field on the cerebral cortex. *Experimental Physiology*, *53*(3), 327–336. http://doi.org/10.1113/expphysiol.1968.sp001974

Adams, M. D., Celniker, S. E., Holt, R. A., Evans, C. A., Gocayne, J. D., Amanatides, P. G., … Venter, J. C. (2000). The Genome Sequence of Drosophila melanogaster. *Science*, *287*(5461), 2185–2195. http://doi.org/10.1126/science.287.5461.2185

Afsari, F., Christensen, K. V., Smith, G. P., Hentzer, M., Nippe, O. M., Elliott, C. J. H., & Wade, A. R. (2014). Abnormal visual gain control in a Parkinson's disease model. *Human Molecular Genetics*, *23*(17), 12. http://doi.org/10.1038/nrn2619

Albrecht, D. G., & Hamilton, D. B. (1982). Striate cortex of monkey and cat: contrast response function. *Journal of Neurophysiology*, *48*(1), 217–237. http://doi.org/0022-3077/82/0000-0000$01.25

Alvarez, I., de Haas, B., Clark, C. A., Rees, G., & Schwarzkopf, D. S. (2015). Comparing different stimulus configurations for population receptive field mapping in human fMRI. *Frontiers in Human Neuroscience*, *9*(February), 96. http://doi.org/10.3389/fnhum.2015.00096

Amano, K., Wandell, B. A., & Dumoulin, S. O. (2009). Visual Field Maps, Population Receptive Field Sizes, and Visual Field Coverage in the Human MT+ Complex. *Journal of Neurophysiology*, *102*(5), 2704–2718. http://doi.org/10.1152/jn.00102.2009

Anatal, A., Bandini, F., Keri, S., & Bodis-Wollner, I. (1998). Visuo-cognitive dysfunctions in Parkinson's disease. *Clinical Neuroscience*, *5*(2), 147–152.

Anderson, P. C., & Daggett, V. (2008). Molecular basis for the structural instability of human DJ-1 induced by the L166P mutation associated with Parkinson's disease. *Biochemistry*, *47*(36), 9380–9393. http://doi.org/10.1021/bi800677k

Andretic, R., Kim, Y.-C., Jones, F. S., Han, K.-A., & Greenspan, R. J. (2008). Drosophila D1 dopamine receptor mediates caffeine-induced arousal. *Proc. Natl. Acad. Sci. U. S. A.*, *105*(51), 20392–20397. http://doi.org/10.1073/pnas.0806776105

Angelucci, A., & Bressloff, P. C. (2006). Contribution of feedforward, lateral and feedback connections to the classical receptive field center and extra-classical receptive field surround of primate V1 neurons. *Progress in Brain Research*, *154*(A), 92–120. http://doi.org/10.1016/S0079-6123(06)54005-1

Anstis, S., & Cavangh, P. (1983). Minimum Motion Technique for Judging Equiluminance. In J. D. Mollon & L. T. Sharpe (Eds.), *Colour Vision: Psychophysics and Physiology* (pp. 156–166). London: Academic Press.

Archibald, N. K., Clarke, M. P., Mosimann, U. P., & Burn, D. J. (2011). Visual

symptoms in Parkinson's disease and Parkinson's disease dementia. *Movement Disorders*, *26*(13), 2387–2395. http://doi.org/10.1002/mds.23891

Armstrong, R. A. (2011). Visual symptoms in Parkinson's disease. *Parkinson's Disease*, *2011*. http://doi.org/10.4061/2011/908306

Avidan, G., Harel, M., Hendler, T., Ben-bashat, D., Zohary, E., Papanikolaou, A., … Smirnakis, S. M. (2002). Contrast Sensitivity in Human Visual Areas and Its Relationship to Object Recognition. *Journal of Neurophysiology*, *87*(6), 3102–3116. http://doi.org/10.1152/jn.2002.87.6.3102

Barbato, L., Rinalduzzi, S., Laurenti, M., Ruggieri, S., & Accornero, N. (1994). Color VEPs in Parkinson's disease. *Electroencephalogr Clin Neurophysiol.*, *92*(2), 169–172. http://doi.org/10.1016/0168-5597(94)90057-4

Baylor, D. A. (1987). Photoreceptor signals and vision. Proctor lecture. *Invest Opthalmol Vis Sci*, *28*(1), 34–49.

Beal, M. F., Brouillet, E., Jenkins, B. G., Ferrante, R. J., Kowall, N. W., Miller, J. M., … Hyman, B. T. (1993). Neurochemical and histologic characterization of striatal excitotoxic lesions produced by the mitochondrial toxin 3-nitropropionic acid. *The Journal of Neuroscience : The Official Journal of the Society for Neuroscience*, *13*(October), 4181–4192.

Beard, J. D., Steege, A. L., Ju, J., Lu, J., Luckhaupt, S. E., & Schubauer-Berigan, M. K. (2017). Mortality from Amyotrophic Lateral Sclerosis and Parkinson's Disease Among Different Occupation Groups — United

States, 1985–2011. *MMWR. Morbidity and Mortality Weekly Report*, *66*(27), 718–722. http://doi.org/10.15585/mmwr.mm6627a2

Beitz, J. M. (2014). Parkinson's disease: a review. *Frontiers in Bioscience (Scholar Edition)*, *6*, 65–74. http://doi.org/10.2741/S415

Bodis-wollner, I., Marx, M. S., Mitra, S., Bobak, P., Mylin, L., & Yahr, M. (1987). Visual dysfunction in parkinson's disease: Loss in spatiotemporal contrast sensitivity. *Brain*, *110*(6), 1675–1698. http://doi.org/10.1093/brain/110.6.1675

Bogaerts, V., Theuns, J., & Van Broeckhoven, C. (2008). Genetic findings in Parkinson's disease and translation into treatment: A leading role for mitochondria? *Genes, Brain and Behavior*. http://doi.org/10.1111/j.1601-183X.2007.00342.x

Bohon, K. S., Hermann, K. L., Hansen, T., & Conway, B. R. (2016). Representation of Perceptual Color Space in Macaque Posterior Inferior Temporal Cortex (the V4 Complex). *ENeuro*, *3*(4). http://doi.org/10.1523/ENEURO.0039-16.2016

Bonifati, V., Rohé, C. F., Breedveld, G. J., Fabrizio, E., De Mari, M., Tassorelli, C., … Oostra, B. A. (2005). Early-onset parkinsonism associated with PINK1 mutations. *Neurology*, *65*(1), 87 LP-95. http://doi.org/10.1212/01.wnl.0000167546.39375.82

Bonin, V., Histed, M. H., Yurgenson, S., & Reid, R. C. (2011). Local diversity and fine-scale organization of receptive fields in mouse visual cortex. *The Journal of Neuroscience : The Official Journal of the Society for Neuroscience*, *31*(50), 18506–18521.

http://doi.org/10.1523/JNEUROSCI.2974-11.2011

Boser, B., Guyon, I., & Vapnik, V. (1992). A Training Algorithm for Optimal Margin Classifiers. In *Proceedings of the 5th Annual ACM Workshop on Computational Learning Theory* (pp. 144–152). ACM Press. http://doi.org/10.1145/130385.130401

Boynton, G. M., Demb, J. B., Glover, G. H., & Heeger, D. J. (1999). Neuronal basis of contrast discrimination. *Vision Research*, *39*(2), 257–269. http://doi.org/10.1016/S0042-6989(98)00113-8

Braak, H., Del Tredici, K., Rüb, U., De Vos, R. A. I., Jansen Steur, E. N. H., & Braak, E. (2003). Staging of brain pathology related to sporadic Parkinson's disease. *Neurobiology of Aging*, *24*(2), 197–211. http://doi.org/10.1016/S0197-4580(02)00065-9

Brainard, D. H. (1997). The Psychophysics Toolbox. *Spatial Vision*, *10*(4), 433–436. http://doi.org/10.1163/156856897X00357

Brainard, D. H., & Stockman, A. (2010). Colorimetry. In M. Bass, C. DeCusatis, V. Enoch, J., Lakshminarayanan, & G. Li (Eds.), *The Optical Society of America Handbook of Optics, 3rd edition, Volume III: Vision and Vision Optics* (3rd ed., p. 10.1-10.56). New York: McGraw-Hill.

Büeler, H. (2009). Impaired mitochondrial dynamics and function in the pathogenesis of Parkinson's disease. *Experimental Neurology*. http://doi.org/10.1016/j.expneurol.2009.03.006

Bulens, C., Meerwaldt, J. D., Van Der Wildt, G. J., & Keemink, C. J. (1986). Contrast sensitivity in Parkinson's disease. *Neurology*, *36*(8), 1121–1125. Retrieved from http://www.scopus.com/inward/record.url?eid=2-s2.0-

0022494898&partnerID=40&md5=775dc8fdf7c6dacc574e8bf93bca8215

Bulens, C., Meerwaldt, J. D., Van der Wildt, G. J., & Van Deursen, J. B. P. (1987). Effect of levodopa treatment on contrast sensitivity in Parkinson's disease. *Annals of Neurology*, *22*(3), 365–369. http://doi.org/10.1002/ana.410220313

Busse, L., Wade, A. R., & Carandini, M. (2009). Representation of Concurrent Stimuli by Population Activity in Visual Cortex. *Neuron*, *64*(6), 931–942. http://doi.org/10.1016/j.neuron.2009.11.004

Cadenhead, K. S., Dobkins, K., McGovern, J., & Shafer, K. (2013). Schizophrenia spectrum participants have reduced visual contrast sensitivity to chromatic (red/green) and luminance (light/dark) stimuli: New insights into information processing, visual channel function, and antipsychotic effects. *Frontiers in Psychology*, *4*(AUG), 1–8. http://doi.org/10.3389/fpsyg.2013.00535

Campbell, F. W., & Green, D. G. (1965). Optical and retinal factors affecting visual resolution. *The Journal of Physiology*, *181*, 576–593. http://doi.org/10.1113/jphysiol.1965.sp007784

Campbell, F. W., & Robson, J. G. (1968). Application of fourier analysis to the visibility of gratings. *The Journal of Physiology*, *197*(3), 551–566. http://doi.org/10.1113/jphysiol.1968.sp008574

Canet-Avilés, R. M., Wilson, M. A., Miller, D. W., Ahmad, R., McLendon, C., Bandyopadhyay, S., … Cookson, M. R. (2004). The Parkinson's disease protein DJ-1 is neuroprotective due to cysteine-sulfinic acid-driven mitochondrial localization. *Proceedings of the National Academy of*

Sciences, *101*(24), 9103 LP-9108. http://doi.org/10.1073/pnas.0402959101

Carandini, M. (2006). What simple and complex cells compute. *Journal of Physiology*, *577*(2), 463–466. http://doi.org/10.1113/jphysiol.2006.118976

Carandini, M., & Heeger, D. (1994). Summation and division by neurons in primate visual cortex. *Science (New York, N.Y.)*, *264*(5163), 1333–1336. http://doi.org/10.1126/science.8191289

Carandini, M., & Heeger, D. J. (2011). Normalization as a canonical neural computation. *Nature Reviews Neuroscience*. http://doi.org/10.1038/nrn3136

Carandini, M., Heeger, D. J., & Movshon, J. A. (1997). Linearity and normalization in simple cells of the macaque primary visual cortex. *The Journal of Neuroscience : The Official Journal of the Society for Neuroscience*, *17*(21), 8621–8644.

Carroll, J., Neitz, J., & Neitz, M. (2002). Estimates of L:M cone ratio from ERG flicker photometry and genetics. *Journal of Vision*, *2*(8), 531–542. http://doi.org/10.1167/2.8.1

Chang, C., & Lin, C. (2011). LIBSVM -- A Library for Support Vector Machines. *ACM Transactions on Intelligent Systems and Technology*, *2*(3), 1–27. http://doi.org/10.1145/1961189.1961199

Chaudhuri, K. R., & Schapira, A. H. (2009). Non-motor symptoms of Parkinson's disease: dopaminergic pathophysiology and treatment. *The Lancet Neurology*. http://doi.org/10.1016/S1474-4422(09)70068-7

Chouhan, A. K., Guo, C., Hsieh, Y. C., Ye, H., Senturk, M., Zuo, Z., … Shulman, J. M. (2016). Uncoupling neuronal death and dysfunction in Drosophila models of neurodegenerative disease. *Acta Neuropathologica Communications*, *4*(1), 62. http://doi.org/10.1186/s40478-016-0333-4

Chyb, S., Hevers, W., Forte, M., Wolfgang, W. J., Selinger, Z., & Hardie, R. C. (1999). Modulation of the light response by cAMP in Drosophila photoreceptors. *The Journal of Neuroscience : The Official Journal of the Society for Neuroscience*, *19*(20), 8799–8807.

Clark, I. E., Dodson, M. W., Jiang, C., Cao, J. H., Huh, J. R., Seol, J. H., … Guo, M. (2006a). Drosophila pink1 is required for mitochondrial function and interacts genetically with parkin. *Nature*, *441*(7097), 1162–1166. http://doi.org/10.1038/nature04779

Clark, I. E., Dodson, M. W., Jiang, C., Cao, J. H., Huh, J. R., Seol, J. H., … Guo, M. (2006b). Drosophila pink1 is required for mitochondrial function and interacts genetically with parkin. *Nature*, *441*(7097), 1162–6. http://doi.org/10.1038/nature04779

Clarke, C. E. (2007). Parkinson's disease. *BMJ (Clinical Research Ed.)*, *335*(7617), 441–5. http://doi.org/10.1136/bmj.39289.437454.AD

Cleland, B. G., Harding, T. H., & Tilunay-Keesey, U. (1979). Visual resolution and receptive field size: examination of two kinds of cat retinal ganglion cell. *Science*, *205*(4410), 1015–1017. http://doi.org/10.1126/science.472720

Connolly, M., & van Essen, D. (1984). The representation of the visualfield in parvocellular and magnocellular layers in the lateral geniculate nucleus in

the macque monkey. *The Journal of Comparative Neurology*, *226*(4), 544–564. http://doi.org/10.1002/cne.902260408

Conway, B. R., Moeller, S., & Tsao, D. Y. (2007). Specialized Color Modules in Macaque Extrastriate Cortex. *Neuron*, *56*(3), 560–573. http://doi.org/10.1016/j.neuron.2007.10.008

Cortes, C., & Vapnik, V. (1995). Support-Vector Networks. *Machine Learning*, *20*, 273–297. http://doi.org/10.1023/A:1022627411411

Croner, L. J., & Kaplan, E. (1995). Receptive fields of P and M ganglion cells across the primate retina. *Vision Research*, *35*(1), 7–24. http://doi.org/10.1016/0042-6989(94)E0066-T

Crooks, J., & Kolb, H. (1992). Localization of GABA, glycine, glutamate and tyrosine hydroxylase in the human retina. *Journal of Comparative Neurology*, *315*(3), 287–302. http://doi.org/10.1002/cne.903150305

D'Souza, D., Auer, T., Frahm, J., Strasburger, H., & Lee, B. B. (2016). Dependence of chromatic responses in V1 on visual field eccentricity and spatial frequency: an fMRI study. *Journal of the Optical Society of America. A*, *33*(3), 53–64. http://doi.org/10.1364/JOSAA.33.000A53

D'Souza, D., Auer, T., Strasburger, H., Frahm, J., & Lee, B. B. (2011). Temporal frequency and chromatic processing in humans : An fMRI study of the cortical visual areas. *Journal of Vision*, *11*(2011), 1–17. http://doi.org/10.1167/11.8.8

Dacey, D. M. (1993). The mosaic of midget ganglion cells in the human retina. *Journal of Neuroscience*, *13*(12), 5334–55. http://doi.org/10.1523/JNEUROSCI.13-12-05334.1993

Dacey, D. M. (1994). Physiology, morphology and spatial densities of identified ganglion cell types in primate retina. In *Higher-order processing in the visual system* (pp. 12–34). London: Ciba Foundation.

Dacey, D. M., & Petersen, M. R. (1992). Dendritic field size and morphology of midget and parasol ganglion cells of the human retina. *Proceedings of the National Academy of Sciences of the United States of America*, *89*(20), 9666–9670. http://doi.org/10.1073/pnas.89.20.9666

De Monasterio, F. M., & Gouras, P. (1975). Functional properties of ganglion cells of the rhesus monkey retina. *Journal of Physiology*, *25*(1), 167–195. http://doi.org/10.1113/jphysiol.1975.sp011086

de Rijk, M. C., Tzourio, C., Breteler, M. M., Dartigues, J. F., Amaducci, L., Lopez-Pousa, S., … Rocca, W. A. (1997). Prevalence of parkinsonism and Parkinson's disease in Europe: the EUROPARKINSON Collaborative Study. European Community Concerted Action on the Epidemiology of Parkinson's disease. *Journal of Neurology, Neurosurgery, and Psychiatry*, *62*(1), 10–5. http://doi.org/10.1136/jnnp.62.1.10

Deegan, J. F., & Jacobs, G. H. (1993). On the Identity of the Cone Types of the Rat Retina. *Experimental Eye Research*, *56*(3), 375–377. http://doi.org/10.1006/exer.1993.1049

Deng, H., & Yuan, L. (2014). Genetic variants and animal models in SNCA and Parkinson disease. *Ageing Research Reviews*, *May*, 161–176. http://doi.org/10.1016/j.arr.2014.04.002

Derrington, A. M., & Lennie, P. (1984). Spatial and temporal contrast sensitivities of neurones in lateral geniculate nucleus of macaque. *The*

Journal of Physiology, *357*, 219–240. http://doi.org/10.1113/jphysiol.1984.sp015498

Diederich, N. J., Raman, R., Leurgans, S., & Goetz, C. G. (2002). Progressive worsening of spatial and chromatic processing deficits in Parkinson disease. *Archives of Neurology*, *59*(8), 1249–1252. http://doi.org/10.1001/archneur.59.8.1249

Dolph, P., Nair, A., & Raghu, P. (2011). Electroretinogram recordings of Drosophila. *Cold Spring Harbour Protoc*, *1*(1). http://doi.org/10.1101/pdb.prot5549

Dowling, J. E. (1979). A new retinal neurone - the interplexiform cell. *Trends in Neurosciences*, *2*(C), 189–191. http://doi.org/10.1016/0166-2236(79)90076-6

Drasdo, N., & Fowler, C. W. (1974). Non-linear projection of the retinal image in a wide-angle schematic eye. *British Journal of Ophthalmology*, *58*(8), 709–714. http://doi.org/10.1136/bjo.58.8.709

Dubner, R., & Zeki, S. M. (1971). Response properties and receptive fields of cells in an anatomically defined region of the superior temporal sulcus in the monkey. *Brain Research*, *35*(2). http://doi.org/10.1016/0006-8993(71)90494-X

Dumoulin, S. O., & Wandell, B. A. (2008). Population receptive field estimates in human visual cortex. *Neuroimage*, *39*(2), 647–660. http://doi.org/10.1016/j.neuroimage.2007.09.034.

Ebrey, T., & Koutalos, Y. (2001). Vertebrate Photoreceptors. *Progress in Retinal and Eye Research*, *20*(1), 49–94.

Ellis, E. M., Gauvain, G., Sivyer, B., & Murphy, G. J. (2016). Shared and distinct retinal input to the mouse superior colliculus and dorsal lateral geniculate nucleus. *Journal of Neurophysiology*, *116*, 602–610. http://doi.org/10.1152/jn.00227.2016

Engel, S. A., Glover, G. G., & Wandell, B. A. (1997). Retintopic organization in human visual cortex and the spatial precision of functional MRI. *Cereb Cortex*, *7*(2), 181–192. http://doi.org/10.1093/cercor/7.2.181

Enroth-Cugell, C., & Freeman, A. W. (1987). The receptive-field spatial structure of cat retinal Y cells. *Journal of Physiology*, *384*(1), 49–79. http://doi.org/10.1113/jphysiol.1987.sp016443

Enroth-Cugell, C., & Shapley, R. M. (1973). Adaptation and dynamics of cat retinal ganglion cells. *The Journal of Physiology*, *233*(2), 271–309. http://doi.org/10.1113/jphysiol.1973.sp010308

Espinoza, S. G., & Hardy, T. C. (1983). Retinotopic organization of striate and extrastriate visual cortex in the hooded rat. *Brain Research*, *272*(1), 137–144. http://doi.org/10.1016/0006-8993(83)90370-0

Felleman, D. J., & Van Essen, D. C. (1991). Distributed hierachical processing in the primate cerebral cortex. *Cerebral Cortex*, *1*(1), 1–47. http://doi.org/10.1093/cercor/1.1.1

Felleman, J., & Van Essen, D. (1987). Receptive field properties of neurons in area V3 of macaque monkey extrastriate cortex. *Journal of Neurophysiology*, *57*(4), 889–920. http://doi.org/10.1152/jn.1987.57.4.889

Fellman, D. J., & Van Essen, D. C. (1991). Distributed hierarchical processing

in the primate cerebral cortex. *Cerebral Cortex*, *1*, 1–47. http://doi.org/10.1093/cercor/1.1.1

Fischbach, K. F., & Dittrich, A. P. M. (1989). The optic lobe of Drosophila melanogaster. I. A Golgi analysis of wild-type structure. *Cell and Tissue Research*, *258*(3), 441–475. http://doi.org/10.1007/BF00218858

Fisher, R. A. (1936). The use of multiple measures in taxonomic problems. *Annals of Eugenics*, *7*(2), 179–188. http://doi.org/10.1111/j.1469-1809.1936.tb02137.x

Fracasso, A., Petridou, N., & Dumoulin, S. O. (2016). Systematic variation of population receptive field properties across cortical depth in human visual cortex. *NeuroImage*, *139*, 427–438. http://doi.org/10.1016/j.neuroimage.2016.06.048

Friston, K. J., Fletcher, P., Josephs, O., Holmes, A., Rugg, M. D., & Turner, R. (1998). Event-Related fMRI: Characterizing Differential Responses. *NeuroImage*, *7*(1), 30–40. http://doi.org/10.1006/nimg.1997.0306

Galaburda, A. M., Aboitiz, F., Rosen, G. D., & Sherman, G. F. (1986). Histological asymmetry in the primary visual cortex of the rat: Implications for mechanisms of cerebral asymmetry. *Cortex: A Journal Devoted to the Study of the Nervous System and Behavior*, *22*(1), 151–160.

Glickfeld, L. L., Reid, R. C., & Andermann, M. L. (2014). A mouse model of higher visual cortical function. *Current Opinion in Neurobiology*, *24*(1), 28–33. http://doi.org/10.1016/j.conb.2013.08.009

Goldberg, M. S., Pisani, A., Haburcak, M., Vortherms, T. A., Kitada, T., Costa, C., … Shen, J. (2005). Nigrostriatal dopaminergic deficits and hypokinesia

caused by inactivation of the familial parkinsonism-linked gene DJ-1. *Neuron*, *45*(4), 489–496. http://doi.org/10.1016/j.neuron.2005.01.041

Goldsmith, T. H., Barker, R. J., & Cohen, C. F. (1964). Sensitivity of visual receptors of carotenoid-depleted flies: A vitamin A deficiency in an invertebrate. *Science*, *146*(3640), 65–67. http://doi.org/10.1126/science.146.3640.65

Gouras, P. (1968). Identification of cone mechanisms in monkey ganglion cells. *Journal of Physiology*, *199*(3), 533–547. http://doi.org/10.1113/jphysiol.1968.sp008667

Granit, R., & Harper, P. (1930). Comparative studies on the peripheral and central retina. II. Synaptic reactions in the eye. *American Journal of Physiology*, *95*(1), 211–228. http://doi.org/10.1152/ajplegacy.1930.95.1.211

Grill-Spector, K., Kushnir, T., Edelman, S., Avidan, G., Itzchak, Y., & Malach, R. (1999). Differential processing of objects under various viewing conditions in the human lateral occipital complex. *Neuron*, *24*(1), 187–203. http://doi.org/10.1016/S0896-6273(00)80832-6

Haak, K. V., Cornelissen, F. W., & Morland, A. B. (2012). Population receptive field dynamics in human visual cortex. *PLoS ONE*, *7*(5), 1–8. http://doi.org/10.1371/journal.pone.0037686

Hammett, S. T., Thompson, P. G., & Bedingham, S. (2000). The dynamics of velocity adaptation in human vision. *Current Biology*, *10*(18), 1123–1126. http://doi.org/10.1016/S0960-9822(00)00698-9

Hardie, R. (1985). Functional Organization of the Fly Retina. In H. Autrum, D.

Ottoson, E. R. Perl, R. F. Schmidt, H. Shimazu, & W. D. Willis (Eds.), *Progress in Sensory Physiology* (5th ed., pp. 1–79). Berlin, Heidelberg: Springer.

Hardie, R. C., & Raghu, P. (2001a). Visual transduction in Drosophila. *Nature*, *413*, 186. Retrieved from https://doi.org/10.1038/35093002

Hardie, R. C., & Raghu, P. (2001b). Visual transduction in Drosophila. *Annual Review of Cell and Developmental Biology*, *15*(6852), 186–193. http://doi.org/10.1038/35093002

Harnois, C., & Di Paolo, T. (1990). Decreased dopamine in the retinas of patients with Parkinson's disease. *Investigative Ophthalmology and Visual Science*, *31*(11), 2473–2475.

Harris, M. G. (1980). Velocity specificity of the flicker to pattern sensitivity ratio in human vision. *Vision Research*, *20*(8), 687–691. http://doi.org/10.1016/0042-6989(80)90093-0

Hartline, H. K. (1938). The response of single optic nerve fibers of the vertebrate eye to illumination of the retina. *American Journal of Physiology*, *121*, 400–415.

Hartmann, E., Lachenmayr, B., & Brettel, H. (1979). The peripheral critical flicker frequency. *Vision Research*, *19*(9), 1019–1023. http://doi.org/10.1016/0042-6989(79)90227-X

Hassan, O., Thompson, P., & Hammett, S. T. (2016). Perceived speed in peripheral vision can go up or down. *Journal of Vision*, *16*(6), 1–7. http://doi.org/10.1167/16.6.20.doi

Hawken, M. J., Shapley, R. M., & Grosof, D. H. (1996). Temporal-frequency

selectivity in monkey visual cortex. *Visual Neuroscience*, *13*(1996), 477–492. http://doi.org/10.1017/S0952523800008154

Henchcliffe, C., & Beal, M. F. (2008). Mitochondrial biology and oxidative stress in Parkinson disease pathogenesis. *Nature Clinical Practice. Neurology*, *4*(11), 600–609. http://doi.org/10.1038/ncpneuro0924

Hendry, S. H. C., & Reid, R. C. (2000). The koniocellular pathway in primate vision. *Annual Review of Neuroscience*, *23*, 127–153. http://doi.org/10.1146/annurev.neuro.23.1.127

Henriksson, L., Nurminen, L., Hyvarinen, A., & Vanni, S. (2008). Spatial frequency tuning in human retinotopic visual areas. *Journal of Vision*, *8*(10), 1–13. http://doi.org/10.1167/8.10.5

Hernandez, D. G., Reed, X., & Singleton, A. B. (2016). Genetics in Parkinson disease: Mendelian versus non-Mendelian inheritance. *Journal of Neurochemistry*. http://doi.org/10.1111/jnc.13593

Himmelberg, M. M., West, R. J. H., Elliott, C. J. H., & Wade, A. R. (2018). Abnormal visual gain control and excitotoxicity in early-onset Parkinson's disease Drosophila models. *Journal of Neurophysiology*, *119*(3), 957–970. http://doi.org/10.1152/jn.00681.2017

Himmelberg, M. M., West, R. J. H. H., Wade, A. R., Elliott, C. J. H. H., West, R. J. H. H., Elliott, C. J. H. H., & Wade, A. R. (2018). A perceptive plus in Parkinson's disease. *Movement Disorders*, *33*(2), 27240. http://doi.org/10.1002/mds.27240

Himmelberg, M. M., West, R. J. H., Wade, A. R., & Elliott, C. J. H. (2017). A perspective plus on Parkinson's disease. *Movement Disorders*.

Hindle, S., Afsari, F., Stark, M., Adam Middleton, C., Evans, G. J. O., Sweeney, S. T., & Elliott, C. J. H. (2013). Dopaminergic expression of the Parkinsonian gene LRRK2-G2019S leads to non-autonomous visual neurodegeneration, accelerated by increased neural demands for energy. *Human Molecular Genetics*, *22*(11), 2129–2140. http://doi.org/10.1093/hmg/ddt061

Hindle, S., Afsari, F., Stark, M., Middleton, C., Evans, G. J. O., Sweeney, S. T., & Elliott, C. J. H. (2013). Dopaminergic expression of the Parkinsonian gene LRRK2-G2019S leads to non-autonomous visual neurodegeneration, accelerated by increased neural demands for energy. *Human Molecular Genetics*, *22*(11), 2129–2140. http://doi.org/10.1093/hmg/ddt061

Hirsh, J., Riemensperger, T., Coulom, H., Ich??, M., Coupar, J., & Birman, S. (2010). Roles of Dopamine in Circadian Rhythmicity and Extreme Light Sensitivity of Circadian Entrainment. *Current Biology*, *20*(3), 209–214. http://doi.org/10.1016/j.cub.2009.11.037

Hofbauer, A., & Campos-Ortega, J. A. (1990). Proliferation pattern and early differentiation of the optic lobes in Drosophila melanogaster. *Roux's Archives of Developmental Biology*, *198*(5), 264–274. http://doi.org/10.1007/BF00377393

Hofbauer, A., & Dräger, U. C. (1985). Depth segregation of retinal ganglion cells projecting to mouse superior colliculus. *Journal of Comparative Neurology*, *234*(4), 465–474. http://doi.org/10.1002/cne.902340405

Horiguchi, H., Nakadomari, S., Masaya, M., & Wandell, B. A. (2009). Two

temporal channels in human V1 identified using fMRI. *Neuroimage*, *47*(1), 273–280. http://doi.org/10.1016/j.neuroimage.2009.03.078

Hotta, Y., & Benzer, S. (1969). Abnormal Electroretinograms in Visual Mutants of Drosophila. *Nature*, *222*(5191), 354–356. http://doi.org/10.1038/222354a0

Hubel, D. N., & Wiesel, T. N. (1962). Receptive fields, binocular interaction and functional architecture in the cat's visual cortex. *Journal of Physiology*, *160*(1), 106–154. http://doi.org/10.1523/JNEUROSCI.1991-09.2009

Humanski, R. A., & Wilson, H. R. (1993). Spatial-frequency adaptation: Evidence for a multiple-channel model of short-wavelength-sensitive-cone spatial vision. *Vision Research*, *33*(5–6), 665–675. http://doi.org/10.1016/0042-6989(93)90187-2

Humphrey, N. K. (1968). Responses to visual stimuli of units in the superior colliculus of rats and monkeys. *Experimental Neurology*, *20*(3), 312–340. http://doi.org/https://doi.org/10.1016/0014-4886(68)90076-9

Hurvich, L., & Jameson, D. (1957). An opponent-process theory of color vision. *Psychological Review*, *64*(6), 384–404.

Hutton, T. J., Morris, J. L., & Elias, J. W. (1993). Levodopa improves spatial contrast sensitivity in Parkinson's disease. *Archives of Neurology*, *50*(7), 721–724. http://doi.org/10.1001/archneur.1993.00540070041012

Inezman, A. J. Modern Multivariate Statistical Techniques: Regression, Classification and Manifold Learning (2008).

Ito, S., & Feldheim, D. A. (2018). The Mouse Superior Colliculus: An Emerging

Model for Studying Circuit Formation and Function . *Frontiers in Neural Circuits* . Retrieved from https://www.frontiersin.org/article/10.3389/fncir.2018.00010

Izenman, A. J. (2008). *Modern Multivariate Statistical Techniques*. New York: Springer-Verlag.

Jackson, C. R., Ruan, G.-X., Aseem, F., Abey, J., Gamble, K., Stanwood, G., … McMahon, D. G. (2012). Retinal Dopamine Mediates Multiple Dimensions of Light-Adapted Vision. *Journal of Neuroscience*, *32*(27), 9359–9368. http://doi.org/10.1523/JNEUROSCI.0711-12.2012

James, G., Witten, D., Hastie, T., & Tibshirani, R. (2013). *An Introduction to Statistical Learning,*. New York: Springer-Verlag. http://doi.org/10.1007/978-1-4614-7138-7

Jeffries, A. M., Killian, N. J., & Pezaris, J. S. (2014). Mapping the primate lateral geniculate nucleus: A review of experiments and methods. *Journal of Physiology Paris*, *108*(1), 3–10. http://doi.org/10.1016/j.jphysparis.2013.10.001

Jenkinson, M., Beckmann, C. F., Behrens, T. E. J., Woolrich, M. W., & Smith, S. M. (2012). Fsl. *NeuroImage*, *62*(2), 782–790. http://doi.org/10.1016/j.neuroimage.2011.09.015

Jiang, Y., Zhou, K., & He, S. (2007). Human visual cortex responds to invisible chromatic flicker. *Nature Neuroscience*, *10*(5), 657–662. http://doi.org/10.1038/nn1879

Johnson, E. N., Van Hooser, S. D., & Fitzpatrick, D. (2010). The Representation of S-Cone Signals in Primary Visual Cortex. *Journal of*

Neuroscience, *30*(31), 10337–10350. http://doi.org/10.1523/JNEUROSCI.1428-10.2010

Jolliffe, I. T., & Cadima, J. (2016). Principal component analysis : a review and recent developments Subject Areas : Author for correspondence :

Jones, R. D., & Donaldson, I. M. (1995). Fractionation of visuoperceptual dysfunction in Parkinson's disease. *Journal of Neurological Sciences*, *131*(1), 43–50. http://doi.org/10.1016/0022-510X(95)00043-2

Jones, R. D., Donaldson, I. M., & Timmings, P. L. (1992). Impairment of high-contrast visual acuity in Parkinson's disease. *Movement Disorders*, *7*(3), 232–238. http://doi.org/10.1002/mds.870070308

Kane, A., Wade, A., & Ma-wyatt, A. (2011). Delays in using chromatic and luminance information to correct rapid reaches. *Journal of Vision*, *11*(10), 1–18. http://doi.org/10.1167/11.10.3.Introduction

Kanwisher, N. (2010). Functional specificity in the human brain: A window into the functional architecture of the mind. *Proceedings of the National Academy of Sciences*, *107*(25), 11163–11170. http://doi.org/10.1073/pnas.1005062107

Kaplan, E., Lee, B. L., & Shapley, R. M. (1990). New Views of Primate Retinal Functions. In N. . Osborne & G. J. Chader (Eds.), *Progress in retinal research* (pp. 273–335). Elmsford, NY: Pergamon Press.

Kaplan, E., & Shapley, R. (1986). The primate retina contains two types of ganglion cells, with high and low contrast sensitivity. *Proceedings of the National Academy of Sciences of the United States of America*, *83*(8), 2755–2757. http://doi.org/https://doi.org/10.1073/pnas.83.8.2755

Kastner, S., O'Connor, D. H., Fukui, M. M., Fehd, H. M., Herwig, U., & Pinsk, M. A. (2004). Functional imaging of the human lateral geniculate nucleus and pulvinar. *J Neurophysiol*, *91*(1), 438–448. http://doi.org/10.1152/jn.00553.2003

Kitada, T., Pisani, A., Porter, D. R., Yamaguchi, H., Tscherter, A., Martella, G., … Shen, J. (2007). Impaired dopamine release and synaptic plasticity in the striatum of PINK1-deficient mice. *Proc.Natl.Acad.Sci.U.S.A*, *104*(0027–8424 (Print)), 11441–11446. http://doi.org/10.1073/pnas.0702717104

Klien, C., & Westenberger, A. (2012). Genetics of Parkinson's Disease. *Cold Spring Harbor Perspectives in Medicine*, *2*(1), 91–100. http://doi.org/10.1101/cshperspect.a008888

Koenderink, J. J., Bouman, M. A., Bueno, A. E., & Slappendel, S. (1978). Perimetry of contrast detection thresholds of moving spatial sine wave patterns. I. The near peripheral visual field (eccentricity 0°–8°). *Journal of the Optical Society of America*, *68*(6), 845–849. http://doi.org/10.1364/JOSA.68.000845

Kontsevich, L. L., & Tyler, C. W. (1999). Bayesian adaptive estimation of psychometric slope and threshold. *Vision Research*, *39*(16), 2729–2737. http://doi.org/10.1016/S0042-6989(98)00285-5

Kral, K., & Meinertzhagen, I. a. (1989). Anatomical plasticity of synapses in the lamina of the optic lobe of the fly. *Philosophical Transactions of the Royal Society of London. Series B, Biological Sciences*, *323*(1214), 155–183. http://doi.org/10.1098/rstb.1989.0004

Kuhn, M., & Johnson, K. (2013). *Applied Predictive Modeling* (1st ed.). New York: Springer-Verlag.

Kulikowski, J. J., & Tolhurst, D. J. (1973). Psychophysical evidence for sustained and transient detectors in human vision. *The Journal of Physiology*, *232*(1), 149–162. http://doi.org/10.1113/jphysiol.1973.sp010261

Kwong, K. K., Belliveau, J. W., Chesler, D. A., Goldberg, I. E., Weisskoff, R. M., Poncelet, B. P., … Turner, R. (1992). Dynamic magnetic resonance imaging of human brain activity during primary sensory stimulation. *Proceedings of the National Academy of Sciences of the United States of America*, *89*(12), 5675–5679. http://doi.org/10.1073/pnas.89.12.5675

Lavara-Culebras, E., Muñoz-Soriano, V., Gómez-Pastor, R., Matallana, E., & Paricio, N. (2010). Effects of pharmacological agents on the lifespan phenotype of Drosophila DJ-1β mutants. *Gene*, *462*(1–2), 26–33. http://doi.org/10.1016/j.gene.2010.04.009

Lennie, P., Krauskopf, J., & Sclar, G. (1990). Chromatic mechanisms in striate cortex of macaque. *The Journal of Neuroscience : The Official Journal of the Society for Neuroscience*, *10*(2), 649–669. http://doi.org/10.1523/JNEUROSCI.10-02-00649.1990

Levitt, J. B., Schumer, R. A., Sherman, S. M., Spear, P. D., & Movshon, J. A. (2001). Visual response properties of neurons in the LGN of normally reared and visually deprived macaque monkeys. *Journal of Neurophysiology*, *85*(5), 2111–29. Retrieved from http://www.ncbi.nlm.nih.gov/pubmed/11353027

Levitt, J., Kiper, D., & Movshon, A. (1994). Receptive fields and functional architecture of macaque V2. *Journal of Neurophysiology*, *71*(6), 2517–2542. http://doi.org/10.1152/jn.1994.71.6.2517

Liu, G., Zhang, C., Yin, J., Li, X., Cheng, F., Li, Y., … Yu, S. (2009). α-Synuclein is differentially expressed in mitochondria from different rat brain regions and dose-dependently down-regulates complex I activity. *Neuroscience Letters*, *454*(3), 187–192. http://doi.org/https://doi.org/10.1016/j.neulet.2009.02.056

Liu, J., & Wandell, B. A. (2005). Specializations for Chromatic and Temporal Signals in Human Visual Cortex. *Journal of Neuroscience*, *25*(13), 3459–3468. http://doi.org/10.1523/JNEUROSCI.4206-04.2005

Livingstone, M. ., & Hubel, D. . (1984). Anatomy and physiology of a color system in the primate visual cortex. *Journal of Neuroscience*, *4*(1), 309–356. http://doi.org/10.1523/JNEUROSCI.04-01-00309.1984

Longo, F., Russo, I., Shimshek, D. R., Greggio, E., & Morari, M. (2014). Genetic and pharmacological evidence that G2019S LRRK2 confers a hyperkinetic phenotype, resistant to motor decline associated with aging. *Neurobiology of Disease*, *71*, 62–73. http://doi.org/10.1016/j.nbd.2014.07.013

Lücking, C. B., & Brice, A. (2000). Alpha-synuclein and Parkinson's disease. *Cellular and Molecular Life Sciences CMLS*, *57*(13), 1894–1908. http://doi.org/10.1007/PL00000671

Luo, L., Callaway, E. M., & Svoboda, K. (2008). Genetic dissection of neural circuits. *Neuron*, *57*(5), 634–660.

http://doi.org/10.1016/j.neuron.2008.01.002

Malgieri, G., & Eliezer, D. (2008). Structural effects of Parkinson's disease linked DJ-1 mutations. *Protein Science : A Publication of the Protein Society*, *17*(5), 855–868. http://doi.org/10.1110/ps.073411608

Mandemakers, W., Morais, V. A., & Strooper, B. De. (2007). A cell biological perspective on mitochondrial dysfunction in Parkinson disease and other neurodegenerative diseases. *J Cell Sci*, *120*(Pt 10), 1707–1716. http://doi.org/10.1242/jcs.03443

Marques, J. P., Kober, T., Krueger, G., Zwaag, W. Van Der, Van de Moortele, P.-F., & Gruetter, R. (2010). MP2RAGE , a self bias-field corrected sequence for improved segmentation and T1-mapping at high field. *NeuroImage*, *49*(2), 1271–1281. http://doi.org/10.1016/j.neuroimage.2009.10.002

Marshak, D. W. (2010). Retinal Ganglion Cells: Anatomy. In *Encyclopedia of Neuroscience*. http://doi.org/10.1016/B978-008045046-9.00897-4

Martella, G., Madeo, G., Schirinzi, T., Tassone, A., Sciamanna, G., Spadoni, F., … Bonsi, P. (2011). Altered profile and D2-dopamine receptor modulation of high voltage-activated calcium current in striatal medium spiny neurons from animal models of Parkinson's disease. *Neuroscience*, *177*, 240–251. http://doi.org/10.1016/j.neuroscience.2010.12.057

Martin, L. J., Pan, Y., Price, A. C., Sterling, W., Copeland, N. G., Jenkins, N. A., … Lee, M. K. (2006). Parkinson's Disease α-Synuclein Transgenic Mice Develop Neuronal Mitochondrial Degeneration and Cell Death. *The Journal of Neuroscience*, *26*(1), 41 LP-50.

http://doi.org/10.1523/JNEUROSCI.4308-05.2006

Martinez-Vicente, M., & Vila, M. (2013). Alpha-synuclein and protein degradation pathways in Parkinson's disease: A pathological feed-back loop. *Experimental Neurology*, *247*, 308–313. http://doi.org/https://doi.org/10.1016/j.expneurol.2013.03.005

Matikainen-Ankney, B. A., Kezunovic, N., Mesias, R. E., Tian, Y., Williams, F. M., Huntley, G. W., & Benson, D. L. (2016). Altered Development of Synapse Structure and Function in Striatum Caused by Parkinson's Disease-Linked LRRK2-G2019S Mutation. *The Journal of Neuroscience : The Official Journal of the Society for Neuroscience*, *36*(27), 7128–41. http://doi.org/10.1523/JNEUROSCI.3314-15.2016

Mckeeff, T. J., Remus, D. A., & Tong, F. (2007). Temporal Limitations in Object Processing Across the Human Ventral Visual Pathway. *Journal of Neurophysiology*, *98*(1), 382–393. http://doi.org/10.1152/jn.00568.2006.

Meissner, W. G. (2012). When does Parkinson's disease begin? From prodromal disease to motor signs. *Rev Neurol.*, *168*, 809–814. http://doi.org/10.1016/j.neurol.2012.07.004

Menzies, F. M., Yenisetti, S. C., & Min, K. T. (2005). Roles of Drosophila DJ-1 in survival of dopaminergic neurons and oxidative stress. *Current Biology*, *15*(17), 1578–1582. http://doi.org/10.1016/j.cub.2005.07.036

Meulener, M., Whitworth, A. J., Armstrong-Gold, C. E., Rizzu, P., Heutink, P., Wes, P. D., … Bonini, N. M. (2005). Drosophila DJ-1 mutants are selectively sensitive to environmental toxins associated with Parkinson's disease. *Current Biology*, *15*(17), 1572–1577.

http://doi.org/10.1016/j.cub.2005.07.064

Michelson, A. (1927). *Studies in Optics*. University of Chicago Press.

Milner, A. ., & Goodale, M. . (1995). The visual brain in action. Oxford, UK: Oxford University Press.

Ming, W., Palidis, D. J., Spering, M., & McKeown, M. J. (2016). Visual contrast sensitivity in early-stage parkinson's disease. *Investigative Ophthalmology and Visual Science*, *57*(13), 5696–5704. http://doi.org/10.1167/iovs.16-20025

Montell, C. (1999). Visual transduction in Drosophila. *Annu. Rev. Cell Dev. Biol.*, *15*, 231–268. http://doi.org/10.1146/annurev.cellbio.15.1.231

Montell, C. (2012). Drosophia visual transduction. *Trends in Neuroscience*, *35*(6), 356–363. http://doi.org/10.1016/j.tins.2012.03.004

Morante, J., & Desplan, C. (2004). Building a projection map for photoreceptor neurons in the Drosophila optic lobes. *Seminars in Cell and Developmental Biology*, *15*(1), 137–143. http://doi.org/10.1016/j.semcdb.2003.09.007

Mortiboys, H., Furmston, R., Bronstad, G., Aasly, J., Elliott, C., & Bandmann, O. (2015). UDCA exerts beneficial effect on mitochondrial dysfunction in LRRK2(G2019S) carriers and in vivo. *Neurology*, *85*(10). http://doi.org/10.1212/WNL.0000000000001905.

Movshon, J. A., & Newsome, W. . (1996). Visual Response Properties of Striate Cortical Neurons Projecting to Area MT in Macaque Monkeys. *The Journal of Neuroscience*, *16*(23), 7733 LP-7741. Retrieved from http://www.jneurosci.org/content/16/23/7733.abstract

Movshon, J. A., Thompson, I. D., & Tolhurst, D. J. (1978). Receptive field organization of complex cells in the cat's striate cortex. *J. Physiol.*, *283*(1), 78–100.

Mullen, K. T. (1985). The contrast sensitivity of human colour vision to red-green and blue-yellow chromatic gratings. *Journal of Physiology*, *359*(381–400). http://doi.org/10.1113/jphysiol.1985.sp015591

Mullen, K. T., Yoshizawa, T., & Baker, C. L. (2003). Luminance mechanisms mediate the motion of red-green isoluminant gratings: The role of "temporal chromatic aberration." *Vision Research*, *43*(11), 1237–1249. http://doi.org/10.1016/S0042-6989(03)00115-9

Murphy, D. D., Rueter, S. M., Trojanowski, J. Q., & Lee, V. M.-Y. (2000). Synucleins Are Developmentally Expressed, and α-Synuclein Regulates the Size of the Presynaptic Vesicular Pool in Primary Hippocampal Neurons. *The Journal of Neuroscience*, *20*(9), 3214 LP-3220. http://doi.org/10.1523/JNEUROSCI.20-09-03214.2000

Nakamura, K., Nemani, V. M., Azarbal, F., Skibinski, G., Levy, J. M., Egami, K., … Edwards, R. H. (2011). Direct membrane association drives mitochondrial fission by the Parkinson disease-associated protein alpha-synuclein. *The Journal of Biological Chemistry*, *286*(23), 20710–20726. http://doi.org/10.1074/jbc.M110.213538

Nassel, D. R., & Elekes, K. (1992). Aminergic neurons in the brain of blowflies and Drosophila: dopamine- and tyrosine hydroxylase-immunoreactive neurons and their relationship with putative histaminergic neurons. *Cell Tissue Res.*, *267*, 147–167.

Navarro, J. A., Heßner, S., Yenisetti, S. C., Bayersdorfer, F., Zhang, L., Voigt, A., … Botella, J. A. (2014). Analysis of dopaminergic neuronal dysfunction in genetic and toxin-induced models of Parkinson's disease in Drosophila. *Journal of Neurochemistry*, *131*(3), 369–382. http://doi.org/10.1111/jnc.12818

Nériec, N., & Desplan, C. (2016). From the eye to the brain: Development of the Drosophila visual system. *Curr Top Dev Biol*, *116*, 247–271. http://doi.org/10.1016/bs.ctdb.2015.11.032.

Nestares, O., & Heeger, D. J. (2000). Robust multiresolution alignment of MRI brain volumes. *Magnetic Resonance in Medicine*, *43*(5), 705–715. http://doi.org/10.1002/(SICI)1522-2594(200005)43:5<705::AID-MRM13>3.0.CO;2-R

Ng, C.-H., Guan, M. S. H., Koh, C., Ouyang, X., Yu, F., Tan, E.-K., … Lim, K.-L. (2012). AMP Kinase Activation Mitigates Dopaminergic Dysfunction and Mitochondrial Abnormalities in Drosophila Models of Parkinson's Disease. *Journal of Neuroscience*, *32*(41), 14311–14317. http://doi.org/10.1523/JNEUROSCI.0499-12.2012

Niell, C. M., & Stryker, M. P. (2008). Highly selective receptive fields in mouse visual cortex. *The Journal of Neuroscience : The Official Journal of the Society for Neuroscience*, *28*(30), 7520–7536. http://doi.org/10.1523/JNEUROSCI.0623-08.2008

Norcia, A. M., Appelbaum, L. G., Ales, J. M., Cottereau, B. R., & Rossion, B. (2015). The steady-state visual evoked potential in vision research: A review. *Journal of Vision*, *15*(6), 4. http://doi.org/10.1167/15.6.4.doi

Ogden, D. (1994). Microelectrode electronics. In D. Ogden (Ed.), *Microelectrode Techniques*. Cambridge: Company of Biologists.

Ong, C., Yung, L. ., Cai, Y., Bay, B., & Baeg, G. (2015). Drosophila melanogaster as a model organism to study nanotoxicity AU - Ong, Cynthia. *Nanotoxicology*, *9*(3), 396–403. http://doi.org/10.3109/17435390.2014.940405

Oswald, M. C. W., Brooks, P. S., Zwart, M. F., Mukherjee, A., Ryan, J. H., Morarach, K., … Landgraf, M. (2016). Reactive Oxygen Species Regulate Neuronal Structural Plasticity, *3*. http://doi.org/http://dx.doi.org/10.1101/081968

Otsuna, H., & Ito, K. (2006). Systematic Analysis of the Visual Projection Neurons of Drosophila melanogaster. I. Lobula-Specific Pathways. *The Journal of Comparative Neurology*, *497*, 928–958. http://doi.org/10.1002/cne.21015

Pak, W. L. (1966). Drosophila in Vision Research. *Investigative Ophthalmology*, *3*(12).

Pandey, U. B., & Nichols, C. D. (2011). Human disease models in Drosophila melanogaster and the role of the fly in therapeutic drug discovery. *Pharmacological Reviews*, *63*(2), 411–36. http://doi.org/10.1124/pr.110.003293

Pankratz, N., Pauciulo, M. W., Elsaesser, V. E., Marek, D. K., Halter, C. A., Wojcieszek, J., … Investigators, P. S. G.-P. (2006). Mutations in DJ-1 are rare in familial Parkinson disease. *Neuroscience Letters*, *408*(3), 209–213. http://doi.org/10.1016/j.neulet.2006.09.003

Park, J., Lee, S. B., Lee, S. B., Kim, Y., Song, S., Kim, S., … Chung, J. K. (2006). Mitochondrial dysfunction in Drosophila PINK1 mutants is complemented by parkin. *Nature*, *441*(7097), 1157–1161. http://doi.org/10.1038/nature04788

Parkinson, J. (2002). An Essay on the Shaking Palsy. *The Journal of Neuripsychiatry and Clinical Neurosciences*, *13*(2), 223–236.

Paulk, A., Millard, S. S., & van Swinderen, B. (2013). Vision in Drosophila: Seeing the world through a model's eyes. *Annual Review of Entomology*, *58*, 313–332. http://doi.org/10.1146/annurev-ento-120811-153715

Pelli, D. G. (1985). Uncertainty explains many aspects of visual contrast detection and discrimination. *Journal of the Optical Society of America, A, Optics, Image & Science*, *2*(9), 1508–1532. http://doi.org/10.1364/JOSAA.2.001508

Pelli, D. G., & Bex, P. (2013). Measuring contrast sensitivity. *Vision Research*, *90*, 10–14. http://doi.org/10.1016/j.visres.2013.04.015

Perry, C. J., & Fallah, M. (2014). Feature integration and object representations along the dorsal stream visual hierarchy. *Frontiers in Computational Neuroscience*, *8*(84), 1–17. http://doi.org/10.3389/fncom.2014.00084

Petridou, N., Italiaander, M., Bank, B. L. Van De, & Siero, J. C. W. (2013). Pushing the limits of high-resolution functional MRI using a simple high-density multi-element coil design. *NMR In Biomedicine*, *26*, 65–73. http://doi.org/10.1002/nbm.2820

Pisani, A., Martella, G., Tscherter, A., Costa, C., Mercuri, N. B., Bernardi, G.,

… Calabresi, P. (2006). Enhanced sensitivity of DJ-1-deficient dopaminergic neurons to energy metabolism impairment: Role of Na+/K+ ATPase. *Neurobiology of Disease*, *23*(1), 54–60. http://doi.org/10.1016/j.nbd.2006.02.001

Poirson, A. B., & Wandell, B. A. (1996). Pattern-color separable pathways predict sensitivity to simple colored patterns. *Vision Research*, *36*(4), 515–526. http://doi.org/10.1016/0042-6989(96)89251-0

Polyak, S. L. (1941). *The Retina*. Illinois: The University of Chicago Press.

Polymeropoulos, M. H., Higgins, J. J., Golbe, L. I., Johnson, W. G., Ide, S. E., Iorio, G. Di, … Duvoisin, R. C. (1996). Mapping of a Gene for Parkinson's Disease to Chromosome 4q21-q23. *Science*, *274*(5290), 1197 LP-1199. http://doi.org/10.1126/science.274.5290.1197

Ponzo, V., Di Lorenzo, F., Brusa, L., Schirinzi, T., Battistini, S., Ricci, C., … Koch, G. (2017). Reply Letter to “Does motor cortex plasticity depend on the type of mutation in the LRRK2 gene? *Movement Disorders*, *32*(6), 949.

Powell, J. (2013). Progress and Prospects in Evolutionary Biology (Vol. 1). USA: Oxford University Press.

Price, M. J., Feldman, R. G., Adelberg, D., & Kayne, H. (1992). Abnormalities in color vision and contrast sensitivity in Parkinson’s disease. *Neurology*, *42*, 887–890. http://doi.org/10.1212/WNL.42.4.887

Prusky, G. T., & Douglas, R. M. (2004). Characterization of mouse cortical spatial vision. *Vision Research*, *44*(28), 3411–3418. http://doi.org/https://doi.org/10.1016/j.visres.2004.09.001

Qiu, X., Kumbalasiri, T., Carlson, S. M., Wong, K. Y., Krishna, V., Provencio, I., & Berson, D. M. (2005). Induction of photosensitivity by heterologous expression of melanopsin. *Nature*, *433*, 745. Retrieved from https://doi.org/10.1038/nature03345

Radhakrishna, R. C. (1948). The Utilization of Multiple Measurements in Problems of Biological Classification. *Journal of the Royal Statistical Society. Series B (Methodological)*, *10*(2), 159–203.

Recasens, A., & Dehay, B. (2014). Alpha-synuclein spreading in Parkinson's disease. *Frontiers in Neuroanatomy*, *8*, 159. http://doi.org/10.3389/fnana.2014.00159

Regan, D. (1966). Some characteristics of average steady-state and transient respones evoked by modulated light. *Electroencephalography and Clinical Neurophysiology*, *20*(3), 238–248.

Reiter, L. T., Potocki, L., Chien, S., Gribskov, M., & Bier, E. (2001). A Systematic Analysis of Human Disease-Associated Gene Sequences In. *Genome Research*, 1114–1125. http://doi.org/10.1101/gr.169101.sophila

Rister, J., Pauls, D., Schnell, B., Ting, C. Y., Lee, C. H., Sinakevitch, I., … Heisenberg, M. (2007). Dissection of the Peripheral Motion Channel in the Visual System of Drosophila melanogaster. *Neuron*, *56*(1), 155–170. http://doi.org/10.1016/j.neuron.2007.09.014

Robson, J. G. (1966a). Spatial and Temporal Contrast-Sensitivity Functions of the Visual System. *Journal of the Optical Society of America*, *56*(8), 1141. http://doi.org/10.1364/JOSA.56.001141

Robson, J. G. (1966b). Spatial and Temporal Contrast-Sensitivity Functions of

the Visual System. *Journal of the Optical Society of America*, *56*(8), 1141–1142. http://doi.org/10.1364/JOSA.56.001141

Rockland, K. S., & Pandya, D. N. (1979). Laminar origins and terminations of cortical connections of the occipital lobe in the rhesus monkey. *Brain Research*, *179*(1), 3–20. http://doi.org/10.1016/0006-8993(79)90485-2

Rogaeva, E., Johnson, J., Lang, A. E., Gulick, C., Gwinn-Hardy, K., Kawarai, T., … Singleton, A. B. (2004). Analysis of the PINK1 Gene in a Large Cohort of Cases With Parkinson Disease. *Archives of Neurology*, *61*(12), 1898–1904. http://doi.org/10.1001/archneur.61.12.1898

Roorda, A., & Williams, D. R. (1999). The arrangement of the three cone classes in the living human eye. *Nature*, *397*(6719), 520–522. http://doi.org/10.1038/17383

Roote, J., & Prokop, A. (2013). How to design a genetic mating scheme: a basic training package for Drosophila genetics. *G3 (Bethesda, Md.)*, *3*(2), 353–358. http://doi.org/10.1534/g3.112.004820

Rovamo, J., & Raninen, A. (1984). Critical flicker frequency and M-scaling of stimulus size and retinal illuminance. *Vision Research*, *24*(10), 1127–1131. http://doi.org/10.1016/0042-6989(84)90166-4

Rovamo, J., & Virsu, V. (1979). An estimation and application of the human cortical magnification factor. *Experimental Brain Research*, *37*(3), 495–510. http://doi.org/10.1007/BF00236819

Sanes, J. R., & Masland, R. H. (2015). The Types of Retinal Ganglion Cells: Current Status and Implications for Neuronal Classification. *Annual Review of Neuroscience*, *38*(1), 221–246. http://doi.org/10.1146/annurev-

neuro-071714-034120

Sang, J. H. (1982). A handbook of Drosophila development. *Trends in Biochem Sci.*, *7*, 341–342. http://doi.org/10.1016/0968-0004(82)90276-6

Sartucci, F., Orlandi, G., Bonuccelli, U., Borghetti, D., Murri, L., Orsini, C., … Porciatti, V. (2012). Chromatic pattern-reversal electroretinograms (ChPERGs) are spared in multiple system atrophy compared with Parkinson's disease. *Neurol Sci*, *26*(6), 395–401. http://doi.org/10.1016/j.dcn.2011.01.002.The

Sartucci, F., & Porciatti, V. (2006). Visual-evoked potentials to onset of chromatic red-green and blue-yellow gratings in Parkinson's disease never treated with L-dopa. *Journal of Clinical Neurophysiology*, *23*(5), 431–435. http://doi.org/10.1097/01.wnp.0000216127.53517.4d

Schapira, A. H. (2008). Mitochondria in the aetiology and pathogenesis of Parkinson's disease. *The Lancet Neurology*. http://doi.org/10.1016/S1474-4422(07)70327-7

Schapira, A. H. V., Chaudhuri, K. R., & Jenner, P. (2017). Non-motor features of Parkinson disease. *Nature Reviews Neuroscience*, *18*(7), 435–450. http://doi.org/10.1038/nrn.2017.62

Schein, S. J., & de Monasterio, F. M. (1987). Mapping of retinal and geniculate neurons onto striate cortex of macaque. *Journal of Neuroscience*, *7*(4), 996–1009. http://doi.org/10.1523/JNEUROSCI.07-04-00996.1987

Seabrook, T. A., Burbridge, T. J., Crair, M. C., & Huberman, A. D. (2017). Architecture, Function, and Assembly of the Mouse Visual System. *Annual Review of Neuroscience*, *40*, 499–538.

http://doi.org/10.1146/annurev-neuro-071714-033842

Shendelman, S., Jonason, A., Martinat, C., Leete, T., & Abeliovich, A. (2004). DJ-1 is a redox-dependent molecular chaperone that inhibits alpha-synuclein aggregate formation. *PLoS Biology*, *2*(11), e362–e362. http://doi.org/10.1371/journal.pbio.0020362

Shoham, D., Hübener, M., Schulze, S., Grinvald, A., & Bonhoeffer, T. (1997). Spatio-temporal frequency domains and their relation to cytochrome oxidase staining in cat visual cortex. *Nature*. http://doi.org/10.1038/385529a0

Siddiqui, I. J., Pervaiz, N., & Abbasi, A. A. (2016). The Parkinson Disease gene SNCA: Evolutionary and structural insights with pathological implication. *Scientific Reports*, *6*, 1–11. http://doi.org/10.1038/srep24475

Silva, M. F., Faria, P., Regateiro, F. S., Forjaz, V., Januário, C., Freire, A., & Castelo-Branco, M. (2005). Independent patterns of damage within magno-, parvo- and koniocellular pathways in Parkinson's disease. *Brain*, *128*(10), 2260–2271. http://doi.org/10.1093/brain/awh581

Singh, K. D., Smith, A. T., & Greenlee, M. W. (2000). Spatiotemporal Frequency and Direction Sensitivities of Human Visual Areas Measured Using fMRI. *NeuroImage*, *12*(5), 550–564. http://doi.org/10.1006/nimg.2000.0642

Single, S., Haag, J., & Borst, A. (1997). Dendritic computation of direction selectivity and gain control in visual interneurons. *The Journal of Neuroscience : The Official Journal of the Society for Neuroscience*, *17*(16), 6023–6030.

Sinha, R., Hoon, M., Baudin, J., Okawa, H., Wong, R. O. L., & Rieke, F. (2017). Cellular and Circuit Mechanisms Shaping the Perceptual Properties of the Primate Fovea. *Cell*, *168*(3), 413–426.e12. http://doi.org/10.1016/j.cell.2017.01.005

Sloan, M., Alegre-Abarrategui, J., Potgieter, D., Kaufmann, A. K., Exley, R., Deltheil, T., … Wade-Martins, R. (2016). LRRK2 BAC transgenic rats develop progressive, L-DOPA-responsive motor impairment, and deficits in dopamine circuit function. *Human Molecular Genetics*, *25*(5), 951–963. http://doi.org/10.1093/hmg/ddv628

Smith, S. L., & Häusser, M. (2010). Parallel processing of visual space by neighboring neurons in mouse visual cortex. *Nature Neuroscience*, *13*(9), 1144–1149. http://doi.org/10.1038/nn.2620

Solomon, S. G., & Lennie, P. (2007). The machinery of colour vision. *Nature Reviews Neuroscience*, *8*, 276. Retrieved from https://doi.org/10.1038/nrn2094

Soma, S., Shimegi, S., Suematsu, N., Tamura, H., & Sato, H. (2013). Modulation-Specific and Laminar-Dependent Effects of Acetylcholine on Visual Responses in the Rat Primary Visual Cortex. *PLoS ONE*, *8*(7). http://doi.org/10.1371/journal.pone.0068430

Stern, M. B., & Siderowf, A. (2010). Parkinson's at risk syndrome: Can Parkinson's disease be predicted? *Movement Disorders*, *25*, S89–S93. http://doi.org/10.1002/mds.22719

Stockman, A., & Brainard, D. H. (2010). Color vision mechanisms. In M. Bass, C. DeCusatis, J. Enoch, V. Lakshminarayanan, G. Li, C. Macdonald, …

E. van Stryland (Eds.), *The Optical Society of America Handbook of Optics, 3rd edition, Volume III: Vision and Vision Optics*. New York: Hill, McGraw. Retrieved from http://www.researchgate.net/publication/228358887_Color_vision_mechanisms

Stockman, A., & Sharpe, L. T. (2000). The spectral sensitivities of the middle- and long-wavelength-sensitive cones derived from measurements in observers of known genotype. *Vision Research*, *40*, 1711–1737. http://doi.org/10.1016/S0042-6989(00)00021-3

Strausfeld, N. J. (1976). Mosaic Organizations, Layers, and Visual Pathways in the Insect Brain. In F. Zettler & R. Weiler (Eds.), *Neural Principles in Vision* (pp. 245–279). Berlin: Springer-Verlag.

Sun, P., Ueno, K., Waggoner, R. A., Gardner, J. L., Tanaka, K., & Cheng, K. (2007). A temporal frequency-dependent functional architecture in human V1 revealed by high-resolution fMRI. *Nature Neuroscience*, *10*(11), 1404–1406. http://doi.org/10.1038/nn1983

Surmeier, D. J., Obeso, J. A., & Halliday, G. M. (2017). Parkinson's Disease Is Not Simply a Prion Disorder. *Journal of Neuroscience*, *37*(41). http://doi.org/https://doi.org/10.1523/JNEUROSCI.1787-16.2017

Teo, P. C., Sapiro, G., & Wandell, B. A. (1997). Creating connected representations of cortical gray matter for functional MRI visualization. *IEEE Transactions on Medical Imaging*, *16*(6), 852–863. http://doi.org/10.1109/42.650881

Trick, G. L., Kaskie, B., & Steinman, S. B. (1994). Visual impairment in

Parkinson's disease: deficits in orientation and motion discrimination. *Optometry and Vision Science : Official Publication of the American Academy of Optometry*, *71*(4), 242–245. http://doi.org/10.1097/00006324-199404000-00002

Tyler, C. W., Apkarian, P., & Nakayama, K. (1978). Multiple spatial-frequency tuning of electrical responses from human visual cortex. *Experimental Brain Research*, *33*(3–4), 535–550. http://doi.org/10.1007/BF00235573

Tyler, C. W., Likova, L. T., Chen, C.-C., Kontsevich, L. L., Schira, M. M., & Wade, A. R. (2005). Extended Concepts of Occipital Retinotopy. *Current Medical Imaging Reviews*, *1*, 319–329. http://doi.org/10.2174/157340505774574772

Ugur, B., Chen, K., & Bellen, H. J. (2016). *Drosophila* tools and assays for the study of human diseases. *Disease Models & Mechanisms*, *9*(3), 235–244. http://doi.org/10.1242/dmm.023762

Vapnik, V. (1995). *The Nature of Statistical Learning Theory*. New York: Springer-Verlagy.

Venkataraman, A. P., Lewis, P., Unsbo, P., & Lundström, L. (2017). Peripheral resolution and contrast sensitivity: Effects of stimulus drift. *Vision Research*, *133*, 145–149. http://doi.org/10.1016/j.visres.2017.02.002

Vernon, R. J. W., Gouws, A. D., Lawrence, S. J. D., Wade, A. R., & Morland, A. B. (2016). Multivariate Patterns in the Human Object-Processing Pathway Reveal a Shift from Retinotopic to Shape Curvature Representations in Lateral Occipital Areas, LO-1 and LO-2. *Journal of Neuroscience*, *36*(21), 5763–5774.

http://doi.org/10.1523/JNEUROSCI.3603-15.2016

Virsu, V., Rovamo, J., Laurinen, P., & Näsänen, R. (1982). Temporal Contrast Sensitivity Magnification and Cortical Magnification. *Nature*, *22*(9), 1211–1217. http://doi.org/10.1016/0042-6989(82)90087-6

Volta, M., Beccano-Kelly, D. A., Paschall, S. A., Cataldi, S., MacIsaac, S. E., Kuhlmann, N., … Milnerwood, A. J. (2017). Initial elevations in glutamate and dopamine neurotransmission decline with age, as does exploratory behavior, in LRRK2 G2019S mice. *Elife*, *20*(6). http://doi.org/10.7554/eLife.28377

Wandell, B. ., Dumoulin, S. O., & Brewer, A. A. (2007). Visual field maps in human cortex. *Neuron*, *56*(2), 366–383. http://doi.org/10.1016/j.neuron.2007.10.012

Wandell, B. A. (1995). *Foundations of vision*. Sunderland, MA: Sinauer Associates, Inc. http://doi.org/10.1039/c1pp90008k

Wandell, B. A., Brewer, A. ., & Dougherty, R. F. (2005). Visual field map clusters in human cortex. *Philosophical Transactions of the Royal Society of London. Series B, Biological Sciences*, *360*(1456), 693–707. http://doi.org/10.1098/rstb.2005.1628

Wandell, B. A., & Winawer, J. (2015). Computational neuroimaging and population receptive fields. *Trends in Cognitive Sciences*, *19*(6), 349–357. http://doi.org/10.1016/j.tics.2015.03.009

Wandell, B. A., Winawer, J., & Kay, K. N. (2015). *Computational Modeling of Responses in Human Visual Cortex*. *Brain Mapping* (Vol. 1). Elsevier Inc. http://doi.org/10.1016/B978-0-12-397025-1.00347-X

Wang, D., Qian, L., Xiong, H., Liu, J., Neckameyer, W. S., Oldham, S., … Zhang, Z. (2006). Antioxidants protect PINK1-dependent dopaminergic neurons in Drosophila. *Proceedings of the National Academy of Sciences of the United States of America*, *103*(36), 13520–5. http://doi.org/10.1073/pnas.0604661103

Wang, L. (2018). *Support Vector Machines: Theory and Applications (Studies in Fuzziness and Soft Computing)*. Berlin: Springer-Verlag.

Wang, L., Sarnaik, R., Rangarajan, K., Liu, X., & Cang, J. (2010). Visual receptive field properties of neurons in the superficial superior colliculus of the mouse. *The Journal of Neuroscience : The Official Journal of the Society for Neuroscience*, *30*(49), 16573–16584. http://doi.org/10.1523/JNEUROSCI.3305-10.2010

Webster, M. ., De Valois, K. ., & Switkes, E. (1990). Orientation and spatial-frequency discrimination for luminance and chromatic gratings. *Journal of the Optical Society of America A*, *7*(6), 1034–1049. http://doi.org/10.1364/JOSAA.7.001034

Weil, R. S., Schrag, A. E., Warren, J. D., Crutch, S. J., Lees, A. J., & Morris, H. R. (2016). Visual dysfunction in Parkinson's disease. *Brain*, *139*(11), 2827–2843. http://doi.org/10.1093/brain/aww175

Welbourne, L. E., Morland, A. B., & Wade, A. R. (2018). Population receptive field (pRF) measurements of chromatic responses in human visual cortex using fMRI. *NeuroImage*, *167*(May 2017), 84–94. http://doi.org/10.1016/j.neuroimage.2017.11.022

Wells, G. L. (1934). The visual cells of the white rat. *Journal of Comparative*

Psychology, *18*(3), 363–366. http://doi.org/10.1037/h0070869

West, R. J. H., Elliott, C. J. H., & Wade, A. R. (2015). Classification of Parkinson's Disease Genotypes in Drosophila Using Spatiotemporal Profiling of Vision. *Scientific Reports*, *5*(October), 16933. http://doi.org/10.1038/srep16933

Williams, D., Sekiguchi, N., & Brainard, D. (1993). Color, contrast sensitivity, and the cone mosaic. *Proc. Natl. Acad. Sci. U. S. A.*, *90*(20), 9770–9777.

Witkovsky, P. (2004). Dopamine and retinal function. *Documenta Ophthalmologica*. http://doi.org/10.1023/B:DOOP.0000019487.88486.0a

Wolkstein, M., Atkin, A., & Bodis-Wollner, I. (1980). Contrast sensitivity in retinal disease. *Ophthalmology*, *87*(11), 1140–1149. http://doi.org/10.1016/S0161-6420(80)35112-9

Wright, M. J., & Johnston, A. (1983). Spatiotemporal contrast sensitivity and visual field locus. *Vision Research*, *23*(10), 983–989. http://doi.org/10.1016/0042-6989(83)90008-1

Yang, W., Chen, L., Ding, Y., Zhuang, X., & Kang, U. J. (2007). Paraquat induces dopaminergic dysfunction and proteasome impairment in DJ-1-deficient mice. *Human Molecular Genetics*, *16*(23), 2900–2910. http://doi.org/10.1093/hmg/ddm249

Yoshizawa, T., Mullen, K. T., & Baker, C. L. (2000). Absence of a chromatic linear motion mechanism in human vision. *Vision Research*, *40*(15), 1993–2010. http://doi.org/10.1016/S0042-6989(00)00069-9

Zhang, F., Aravanis, A. M., Adamantidis, A., de Lecea, L., & Deisseroth, K. (2007). Circuit-breakers: optical technologies for probing neural signals

and systems. *Nature Reviews Neuroscience*, *8*, 577. Retrieved from https://doi.org/10.1038/nrn2192

Zhou, J., Benson, N. C., Kay, K., & Winawer, J. (2017). Compressive Temporal Summation in Human Visual Cortex. *The Journal of Neuroscience*, 1724–17. http://doi.org/10.1523/JNEUROSCI.1724-17.2017

Zuiderbaan, W., Harvey, B. M., & Dumoulin, S. O. (2012). Modeling center – surround configurations in population receptive fields using fMRI. *Journal of Vision*, *12*(3), 1–15. http://doi.org/10.1167/12.3.10.Introduction